Silicate weathering and the habitability of temperate, rocky planets

Robert J. Graham

Jesus College

University of Oxford

A thesis submitted for the degree of

Doctor of Philosophy

2022

For my parents, Edwin Eugene Graham and Christina Jo Riley Graham. I will never be able to express the depth of gratitude I feel for the unwavering love, support, and kindness you have provided me every day of my life. I owe every positive aspect of my life to you two.

At the equinox when the earth was veiled in a late
rain, wreathed with wet poppies, waiting spring,
The ocean swelled for a far storm and beat its
boundary, the ground-swell shook the beds of
granite.
I gazing at the boundaries of granite and spray, the
established sea-marks, felt behind me
Mountain and plain, the immense breadth of the
continent, before me the mass and doubled stretch of
water
I said: You yoke the Aleutian seal-rocks with the
lava and coral sowings that flower the south,
Over your flood the life that sought the sunrise faces
ours that has followed the evening star.
The long migrations meet across you and it is
nothing to you, you have forgotten us, mother.
You were much younger when we crawled out of the
womb and lay in the sun's eye on the tideline.
It was long and long ago; we have grown proud since
then and you have grown bitter; life retains
Your mobile soft unquiet strength; and envies
hardness, the insolent quietness of stone.
The tides are in our veins, we still mirror the stars,
life is your child, but there is in me
Older and harder than life and more impartial, the
eye that watched before there was an ocean.
That watched you fill your beds out of the
condensation of thin vapor and watched you change
them,
That saw you soft and violent wear your boundaries
down, eat rock, shift places with the continents.
Mother, though my song's measure is like your
surf-beat's ancient rhythm I never learned it of you.
Before there was any water there were tides of fire,
both our tones flow from the older fountain.

Continent's End
Robinson Jeffers

Acknowledgments

There are many people who contributed to this work and to my well-being over the past few years in ways both large and small, and I know I will not be able to thank them all individually.

I would like to thank Raymond Pierrehumbert for his guidance and mentorship throughout graduate school. Ray granted me near-absolute freedom to explore any topic that interested me, while providing advice and direction to ensure I did not get too lost wandering down blind alleys. Everyone in Ray's research group was consistently wonderful and supportive, and I would like to specifically thank some of the post-docs who helped me along. Sarah Rugheimer, who was also my Jesus College advisor, was always there to chat about science or the travails of the PhD life whenever I needed it, and she also gave me many wonderful opportunities to hang out with her cat Pippin. Tim Lichtenberg also frequently provided scientific and career advice during our collaborations, and he and his wife Lola also repeatedly gave me the privilege of caring for their cat, Whisper. Shami Tsai also provided valuable scientific advice and knowledge, and he always served as a formidable foe in board games.

I would also like to thank Dorian Abbot, Fred Ciesla, and Tiffany Shaw. Each provided me with the tools and opportunities I needed to develop my research abilities during my time as an undergraduate at the University of Chicago.

Finally, I thank my parents Edwin and Christina Graham, to whom I have dedicated this thesis.

The next subsections acknowledge contributions to the projects presented as Chapters 2 through 5 in this thesis.

Chapter 2

From publication: The author thanks Ray Pierrehumbert, Dorian Abbot, Michael Foote, and Sarah Rugheimer for useful discussions over the course of the writing of this article. Ray, Dorian, Sarah, and two anonymous reviewers are acknowledged for their helpful comments on various versions of the article. Lastly, I would like to make note of a study by Robin Wordsworth (Wordsworth, 2021) that was published while this paper was under review and independently arrives at similar insights from a different angle.

Chapter 3

I acknowledge Ray Pierrehumbert as a coauthor on the published version of this Chapter (Graham & Pierrehumbert, 2020). He served as a sounding board as I developed the ideas that resulted in this paper, and he read and critiqued multiple drafts.

From publication: We thank Dorian Abbot, Edwin Kite, Tim Lichtenberg, Ramses Ramirez, and an anonymous reviewer for insightful comments and suggestions that improved various versions of this manuscript. RJG thanks the participants at the Rocky Worlds Workshop in Cambridge and the Bornö School on Climate and Conditions for Life on Early Earth and Other Planets for thoughtful discussions on some of the issues covered in this study. RJG acknowledges scholarship funding from the Clarendon Fund and Jesus College, Oxford. RTP is supported by European Research Council Advanced Grant EXOCONDENSE (#740963).

Chapter 4

I acknowledge Tim Lichtenberg and Ray Pierrehumbert as coauthors on the published version of this article (Graham et al., 2022b). I also acknowledge Ryan Boukrouche for contributing to the paper. Tim and Ryan wrote parts of the code that I used to calculate atmospheric temperature structure in this chapter, though I derived the lapse rate equation used in the code (Graham et al., 2021) and made substantial contributions to the writing of the code as well. Tim served as a sounding board for ideas related to the paper, suggested discussion points, read several drafts of the paper, gave many suggestions to improve the writing, helped make the figures look nice, and created the lovely final schematic figure. Ray served as a sounding board as I was developing the ideas that resulted in this paper.

From publication: RJG acknowledges scholarship funding from the Clarendon Fund and Jesus College, Oxford. TL was supported by a grant from the Simons Foundation (SCOL Award No. 611576). RTP is supported by European Research Council Advanced Grant EXOCONDENSE (Grant 740963). This AEThER publication is also funded in part by the Alfred P. Sloan Foundation under grant G202114194. We thank Robin Wordsworth, Jim Kasting, and an anonymous reviewer for helpful reviews that significantly strengthened the paper.

Chapter 5

I acknowledge Ray Pierrehumbert as a co-author on the planned submission of this paper. Ray and I repeatedly discussed the ideas that resulted in this paper, and Ray read a draft of it and gave various pieces of advice to improve the writing and structure.

Abstract

Through the climate-dependence of silicate weathering, the carbonate-silicate cycle is thought to provide a powerful negative feedback on atmospheric CO_2 that has maintained clement surface conditions on Earth almost continuously for 4 billion years in the face of profound environmental change. The fundamental role played by silicate weathering in sustaining long-term habitability on Earth has led to the hypothesis that sufficiently "Earth-like" exoplanets may have their climates regulated by the same process. This allows the definition of a "circumstellar habitable zone" around a star, where planets with carbonate-silicate cycling could in principle adjust CO_2 to levels that prevent runaway glaciation or extreme surface warmth. This definition of the habitable zone has become a major organizing principle in exoplanetary astronomy, guiding telescope design and target prioritization. This thesis will deploy coupled models of exoplanetary climate, ocean chemistry, and silicate weathering to examine the implications and validity of the assumption that Earth-like planets can regulate their climates with silicate weathering throughout the putative habitable zone.

In the Introduction (Chapter 1), I review the habitable zone concept, qualitatively describe the carbonate-silicate cycle and the stabilizing negative feedback on climate that it provides, go over the evidence for the importance of the cycle and feedback in Earth history, and describe how these concepts have been applied to evaluate exoplanet carbon cycling in various modeling studies. In Chapter 2, I apply a global-mean climate model and a global-mean ocean chemistry model to show that climate and ocean pH on exoplanets throughout most of the habitable zone will be insensitive to CO_2 perturbations of sizes that have caused catastrophes in Earth's past if we assume the carbonate-silicate cycle adjusts CO_2 to high levels on exoplanets receiving low instellation. In Chapter 3, I conduct the first simulations of exoplanet weathering to account for the crucial impact of

weathering zone clay precipitation, which leads to large changes in predicted climate behavior compared to previous models that neglected this effect. In particular, I find a much larger climate sensitivity to parameters like land fraction and outgassing in the more complex weathering model, and large sensitivity to parameters like lithology and soil thickness that previous models were too crude to evaluate. This suggests climate control by silicate weathering on exoplanets (and, perhaps, the Earth) may be less efficient than previously assumed. In Chapter 4, I model weathering and climate at various instellations under extremely high CO_2 conditions to demonstrate that the carbonate-silicate cycle can behave as a positive feedback on climate when CO_2's Rayleigh scattering effect begins to outweigh its greenhouse effect, converting the molecule into a planetary coolant at high pressures. This may lead to the accumulation of oceans of liquid CO_2 and CO_2 clathrate hydrates under outgassing and instellation conditions that also support stable, temperate, low-CO_2 climate equilibria, implying a novel form of climate hysteresis and bistability for Earth-like planets in the outer reaches of the HZ. Finally, in Chapter 5, I drive weathering models with precipitation and temperature fields from a 3D global climate model to demonstrate that surface energy budget strongly constrains hydrology and therefore weathering behavior for planets with high CO_2 at low instellations, if the impact of clay formation in the weathering zone is accounted for. Contrary to expectations from the modern Earth, precipitation rates can actually fall with increasing CO_2 and surface temperature when planets begin to bump up against these surface energy budget constraints. This allows silicate weathering to become a destabilizing feedback at lower CO_2 levels and higher instellations than those required for the scattering-based destabilization mechanism described in Chapter 4, and may mean that low-instellation planets are very susceptible to runaway CO_2 accumulation and attendant catastrophic warming or surface CO_2 condensation.

Overall, the work presented in this thesis suggests that the efficacy of the silicate weathering feedback at maintaining clement environments on exoplanets throughout the classical circumstellar habitable zone remains an open question, which may have broad implications for our current strategies for remotely detecting life beyond Earth.

Contents

List of Figures

Chapter 1

Introduction

Consciousness? The learned astronomer
Analyzing the light of most remote star-swirls
Has found them—or a trick of distance deludes his prism—
All at incredible speeds fleeing outward from ours.
I thought, no doubt they are fleeing the contagion
Of consciousness that infects this corner of space.
For often I have heard the hard rocks I handled
Groan, because lichen and time and water dissolve them,
And they have to travel down the strange falling scale
Of soil and plants and the flesh of beasts to become
The bodies of men; they murmur at their fate
In the hollows of windless nights, they'd rather be anything
Than human flesh played on by pain and joy,
They pray for annihilation sooner, but annihilation's
Not in the book yet.

Excerpt from *Margrave*
Robinson Jeffers

1.1 What makes a planet habitable?

In 2022, the James Webb Space Telescope (JWST) (Gardner et al., 2006) Transiting Exoplanet Community Early Release Science Team announced the first detection of CO_2 in an exoplanetary atmosphere (Early et al., 2022). Although the CO_2 molecules in question are floating in the atmosphere of WASP-39b, a thoroughly inhospitable gas giant with an equilibrium temperature in excess of 1000 K and an orbital period of only 4 days, the detection still constitutes an important symbolic step toward the eventual characterization of the atmospheres of temperate, potentially inhabited Earth-like planets. As the most abundant non-condensing greenhouse gas in Earth's atmosphere, CO_2 is the primary reason Earth is not currently covered in ice (Lacis et al., 2010), and, for reasons discussed in detail in Section 1.2, it has likely played this crucial role throughout Earth's 4 billion year history as a habitable planet (see also e.g. Charnay et al., 2020). The molecule's significance in the maintenance of habitability in the Earth system, its abundance on our solar system's other terrestrial planets Venus (92 bars) and Mars (6 millibars) (Pierrehumbert, 2010a), and its expected general importance as a constituent of outgassing from silicate magmas (Gaillard & Scaillet, 2014) have given CO_2 a central place in one of the fundamental hypotheses guiding the search for life beyond Earth, the concept of the classical "circumstellar habitable zone" (HZ) (Kasting et al., 1988, 1993; Kopparapu et al., 2013).

The most widely-used limits of the HZ coincide with the range of orbits or instellations over which an Earth-mass planet with an atmosphere consisting of an adjustable amount of CO_2, 1 bar of N_2, and saturated H_2O can maintain stable bodies of liquid water on its surface (Kasting et al., 1993; Kopparapu et al., 2013). Of course, surface water is not a pre-requisite for habitability as such; life can exist in subsurface H_2O reservoirs (e.g. Lingam & Loeb, 2019), and there may be exotic forms of biology that do not require water as a solvent (e.g. Bains, 2004). Rather than attempting to exhaustively include all possible biospheres, this definition of "habitability" focuses attention on ocean-bearing planets that are thought to be the most likely to support large Earth-like biospheres robust enough to produce detectable biosignatures (Kasting et al., 2014; Domagal-Goldman & Kopparapu, 2018). This terminology has been criticized (e.g. Tasker et al., 2017; Moore et al., 2017; Stevenson, 2018), but the field seems to have settled upon it for better or for worse. Thus, the inner edge of the HZ is associated with uncontrolled evaporation of surface water, and the outer edge is associated with its uncontrolled freezing.

The inner edge is traditionally defined as the instellation at which either a "moist greenhouse" state or a "runaway greenhouse" state would occur on Earth or an Earth-like exoplanet with little or no atmospheric CO_2, and a significant quantity of work has been carried out to determine the conditions that trigger these transitions (e.g. Ingersoll, 1969; Kasting et al., 1984a; Kasting, 1988a; Kasting et al., 1993; Kopparapu et al., 2013; Leconte et al., 2013a; Wolf & Toon, 2014; Kopparapu et al., 2014; Yang et al., 2014; Wolf & Toon, 2015; Kopparapu et al., 2016; Popp et al., 2016; Kodama et al., 2018, 2019; Ramirez, 2020a; Chaverot et al., 2022). A moist greenhouse state is thought to occur on a planet with an Earth-like surface pressure when the global-mean surface temperature reaches approximately 350 K, warm enough to moisten the upper atmosphere, leading to an H_2O-rich stratosphere that drives geologically rapid ($\sim$ 4 billion years (Ga)) oceanic loss through photodissociation of water molecules and escape of their hydrogen (Kasting et al., 1984a; Kasting, 1988b; Kasting et al., 1993; Pierrehumbert, 2010a; Wolf & Toon, 2014; Kasting et al., 2015; Popp et al., 2016; Ramirez, 2020a). The even-more-extreme runaway greenhouse can occur when elevated instellation drives a planet's surface temperature high enough for water vapor to become a dominant atmospheric constituent, at which point the surface pressure of the atmosphere is controlled by the (exponential in temperature) Clausius-Clapeyron relation (e.g. Pierrehumbert, 2010a). Eventually, outgoing longwave radiation decouples from surface temperature because of the rapid accumulation of highly opaque water vapor at the base of the atmosphere with any heating, triggering a positive feedback loop that drives uncontrolled warming until the ocean completely evaporates into the atmosphere (e.g. Ingersoll, 1969; Nakajima et al., 1992; Goldblatt & Watson, 2012; Goldblatt et al., 2013; Leconte et al., 2013a). Temperature stabilizes (often in the thousands of Kelvin, hot enough to melt the planetary surface) when the surface heats to the point that radiation can escape to space through shortwave window regions in the H_2O spectrum or when the dry adiabat penetrates deeply enough into the upper atmosphere (Boukrouche et al., 2021). The precise conditions under which moist or runaway greenhouse climate states occur are still debated, with significant differences between models depending on dimensionality, surface water inventory and distribution, and planetary properties (Ingersoll, 1969; Nakajima et al., 1992; Kasting et al., 1984a; Abe et al., 2011; Goldblatt & Watson, 2012; Goldblatt et al., 2013; Leconte et al., 2013a; Yang et al., 2014; Wolf & Toon, 2014; Kodama et al., 2018, 2019; Ramirez, 2020a). This means that the "inner edge" of the habitable zone is so porous as to be better termed an "inner sponge," but the most sophisticated models for Earth-like planets around Sun-like stars seem to converge on inner edge orbital distances between 0.92 and 1 au, i.e. orbits quite close to that of the Earth (Leconte et al., 2013a; Wolf & Toon, 2015; Ramirez, 2020a).

The outer edge of the classical HZ is generally defined as the instellation below which an Earth-like ocean-bearing planet with an atmospheric composition of N_2-CO_2-H_2O is unable to maintain a surface temperature high enough to avoid global glaciation with adjustments to its atmospheric CO_2 content (Kasting et al., 1993; Kopparapu et al., 2013). Although CO_2 is a net warming agent at low partial pressures, it is also a relatively efficient Rayleigh scatterer (see e.g. Pierrehumbert, 2010a, for a tabulation of scattering coefficients), which means that atmospheres with multiple bars of CO_2 display a high albedo and thus reflect away a large fraction of impinging starlight, an effect that competes with the molecule's greenhouse effect. Further, at high enough partial pressure ($p$$CO_2$), CO_2 will begin to condense and release latent heat in the upper atmosphere, reducing the atmospheric lapse rate and throttling its greenhouse effect (Kasting, 1991; Pierrehumbert, 2010a). Thus, with enough CO_2, the combined effects of upper atmospheric CO_2 condensation and Rayleigh scattering swamp the warming effect entirely, such that further additions of CO_2 to an atmosphere will cool the planetary surface (e.g. Kasting et al., 1993). This implies the existence of a maximum possible surface temperature from CO_2 warming at any given instellation and suggests a definition of the outer edge of the HZ as the instellation at which the maximum temperature attainable by CO_2 coincides with the minimum temperature that avoids global glaciation on a given planet; any change in CO_2 (in either direction) or reduction in instellation at this "maximum greenhouse limit" would plunge a planet into a "snowball state" (Kasting et al., 1993; Tajika, 2007; Kopparapu et al., 2013; Kadoya & Tajika, 2019). The impacts of CO_2 ice clouds in this realm are unclear–early work presumed they would increase planetary albedo, moving the outer edge of the HZ closer to the star (Kasting et al., 1993); later two-stream radiative transfer calculations suggested the clouds imparted a strong greenhouse effect via efficient infrared scattering (Forget & Pierrehumbert, 1997; Pierrehumbert & Erlick, 1998); most recently, multistream radiative transfer calculations have suggested the clouds may only have a small net radiative effect (Kitzmann, 2016, 2017). Further, to my knowledge, the optical properties of liquid CO_2 have not been measured, precluding evaluation of the impact of liquid CO_2 clouds on the radiative properties of thick CO_2 atmospheres (Graham et al., 2022b). With these uncertainties in mind, the standard clear-sky estimate for the outer edge around a Sun-like star is an instellation of about 36% of modern-day Earth, i.e. an orbit of 1.67 au (Kopparapu et al., 2013; Ramirez, 2018).

It is important to note that the HZ boundaries are dependent on stellar type (Kopparapu et al., 2013). One reason for this is that Wien's displacement law dictates that the light emitted by hotter, higher-mass (e.g. F-type) stars is bluer (shorter wavelength), while that emitted by cooler, lower-mass stars (e.g. M- or K-type) is redder (longer wavelength), leading to changes in the interaction of stellar radiation with planetary atmospheres due to the wavelength-dependent nature of scattering and absorption by matter (Wien, 1897; Pierrehumbert, 2010a; Kopparapu et al., 2013). Thus, holding atmospheric and surface properties constant, the albedo of a planet will tend to increase with the mass and temperature of its parent star, moving both the inner and outer edge of the HZ to higher instellations (demonstrated by the slope of the "Conservative Habitable Zone" boundaries in Fig. 1.1). An opposing effect may also come into play for planets orbiting in the HZs of cool, low-mass M-stars, some of which are expected to spin down into synchronous orbits with the same hemisphere always directed at the star due to powerful gravitational tides induced by much smaller orbital distances for a given instellation (e.g. Pollard, 1979; Leconte et al., 2015). 3D GCM simulations of such slow rotators have suggested that they may be able to maintain temperate surface climates closer to their stars than 1D radiative-convective column models suggest, since massive, high-albedo cloud decks should be generated by the vigorous convection sustained at the planetary substellar point, offsetting the reduction in albedo from the redder stellar spectrum (Yang et al., 2013, 2014; Kopparapu et al., 2016), though the actual extent of this effect is still debated (Kopparapu et al., 2017; Lefèvre et al., 2021). In any case, unless otherwise noted, the rest of the thesis will generally deal with planets rotating at an Earth-like rate and irradiated by a Sun-like stellar spectrum.

These HZ boundaries have come to occupy an important place within exoplanetary astronomy. The increasingly frequent discoveries of rocky exoplanets in the HZs around other stars (some displayed in Fig. 1.1) are treated as significant events, with such planets regarded as prime targets for characterization with future telescopes (e.g. Wordsworth et al., 2010b; Borucki et al., 2013; Quintana et al., 2014; Barstow & Irwin, 2016; Anglada-Escudé et al., 2016; Gillon et al., 2016, 2017; Gilbert et al., 2020). The HZ boundaries and the exoplanets discovered within them also serve as fundamental inputs for statistically estimating the fraction of stars bearing "Earth-analogues," a number often referred to as $\eta_\oplus$ (see e.g. Catanzarite & Shao, 2011; Gaidos, 2013; Kopparapu, 2013a; Petigura et al., 2013; Foreman-Mackey et al., 2014; Dressing & Charbonneau, 2015; Burke et al., 2015; Gaidos et al., 2016; Mulders et al., 2018; Lopez & Rice, 2018; Pascucci et al., 2019; Neil & Rogers, 2020, though some calculations use slightly modified HZ definitions, or include multiple definitions). Based on early data from the Kepler (Borucki et al., 2008) survey, many of these early studies suggested that a large proportion of stars will bear rocky planets in their HZs, with $\eta_\oplus$ estimates often falling between ≈20% (Dressing & Charbonneau, 2015) and ≈50% (Kopparapu, 2013a), but subsequent work has revised that number downward, sometimes by orders of magnitude, by accounting for the pollution of the early estimates by "stripped cores," i.e. formerly volatile-rich planets that lost their volatile envelopes during the prolonged high-luminosity pre-main sequence phase

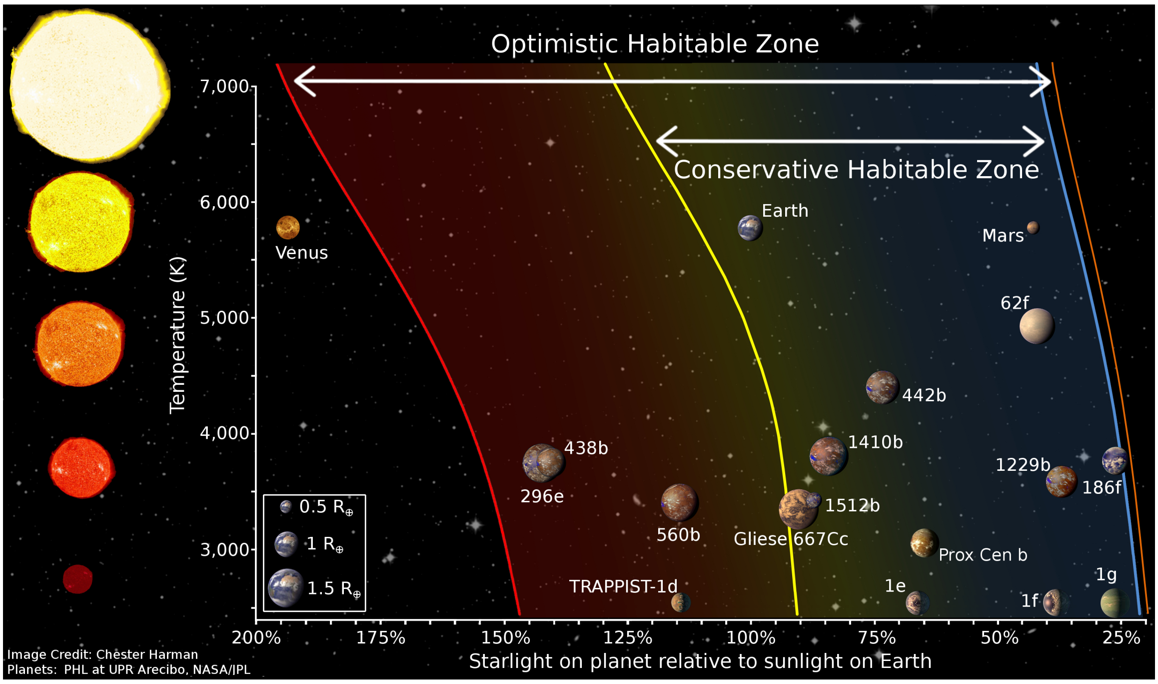

Figure 1.1: **Schematic showing the instellation boundaries of the HZ as a function of stellar temperature**. The classical HZ discussed in the text is labeled "Conservative Habitable Zone." The figure also includes a more optimistic HZ based on the locations of early Mars and Venus, under the assumption that these planets were habitable in their early histories (e.g. Way et al., 2016; Kite, 2019). HZ boundaries are cast in terms of fraction of instellation received by Earth and curve toward the star with increased stellar temperature due to the expected increase in Rayleigh scattering albedo for planets orbiting bluer stars. Some exoplanets discovered in the HZ that are close to Earth's size are plotted at locations corresponding to the temperature of their parent star and instellation of their orbit. Credit: Chester Harman, `http://web.archive.org/web/20160808133813/https://sites.psu.edu/ceh5286/images/`

cool stars experience (Lopez & Rice, 2018; Pascucci et al., 2019; Neil & Rogers, 2020) (though the potential for continued habitability of such dessicated planets is an active topic of research: Leconte et al., 2013b; Ding & Wordsworth, 2020; Moore & Cowan, 2020). The value of $\eta_\oplus$, in turn, is an important input in the design of potential future telescope missions like HabEx (Gaudi et al., 2020), LUVOIR (Team et al., 2019), and LIFE (Quanz et al., 2021). Thus, since $\eta_\oplus$ scales with the width of the HZ, and smaller values of $\eta_\oplus$ require correspondingly larger telescopes to observe a given number of "Earth-analogues," the HZ width becomes directly relevant to the allocation of billions of dollars in funding by space agencies creating future telescopes (e.g. Dressing & Charbonneau, 2013; Kasting & Harman, 2013; Batalha, 2014; Léger et al., 2015; Stark et al., 2015; Ramirez, 2018; Team et al., 2019; Gaudi et al., 2020; Quanz et al., 2021).

A definition of the HZ centered on the warming abilities of CO_2 may seem arbitrary. Early HZ concepts (Huang, 1959; Hart, 1978, 1979) neglected large adjustment of CO_2 with instellation, resulting in much narrower HZ widths. Conversely, atmospheric modeling in subsequent decades has suggested that with a suitable potpourri of gases, there is no obvious hard lower limit to the amount of instellation that could maintain liquid water on the surface of a planet (e.g. Abe et al., 2011; Pierrehumbert & Gaidos, 2011; Zsom, 2015), and with a bit of geothermal heating and a thick enough hydrogen atmosphere, no instellation at all is necessary (Stevenson, 1999; Abbot & Switzer, 2011). However, without some stabilizing negative feedback regulating the partial pressure of a given greenhouse gas in the atmosphere, the question of whether a given planet has enough of the gas to maintain temperatures above freezing is largely a matter of luck (e.g. Kite & Ford, 2018; Mol Lous et al., 2022). This is the basic insight underpinning the focus on CO_2 in the HZ concept: there *is* a negative feedback process in the Earth system that is thought to regulate CO_2's partial pressure in the atmosphere, such that Earth's surface climate is stabilized in a temperate range on long timescales, even in the face of changing boundary conditions like the volcanic outgassing rate, the luminosity of the sun, or the concentrations of other greenhouse gases (Walker et al., 1981; Kasting, 2019). I will generally refer to this process as the **silicate weathering feedback**, and it seems to emerge naturally as a consequence of the physics and chemistry governing the **carbonate-silicate cycle**, suggesting that it may plausibly operate on exoplanets with sufficiently similar compositions, environments, and histories to those of the Earth (e.g. Kasting et al., 1988).

1.2 The carbonate-silicate cycle and the silicate weathering feedback

1.2.1 The cycle

Today, sans humans, the primary control on the level of CO_2 in Earth's atmosphere is thought to be the carbonate-silicate cycle, a set of interlocking H_2O-mediated processes that cycle inorganic carbon between the atmosphere, ocean, crust, and interior of the planet, first proposed by an obscure French metallurgist named Jacques-Joseph Ebelmen in 1845 and promptly ignored (Ebelmen, 1845; Berner, 2012). A century later, Urey (1952) hit upon the fundamentals again, so the net, schematic chemical description of the cycle is often labeled the "Urey reaction" or "Ebelmen-Urey reaction" (Pierrehumbert, 2010a):

$$CaSiO_3(s) + CO_2(g) \leftrightarrow CaCO_3(s) + SiO_2(s) \tag{1.1}$$

where the rightward direction represents the net reaction of CO_2 with silicate minerals (represented by wollastonite, $CaSiO_3$) on the land and seafloor to produce silica (SiO_2) and carbonate minerals (e.g. $CaCO_3$) that precipitate onto the seafloor, and the leftward direction represents the thermal decomposition of subducted or buried carbonates back into CO_2 through metamorphism and volcanism. The calcium atoms found in Earth's silicates and carbonates on average share a stable isotopic fingerprint throughout the geologic record, which implies that the two types of mineral share a common pool of calcium that cycles between them, providing strong evidence that the above equation accurately describes the Earth system, at least qualitatively (Blättler & Higgins, 2017). However, in actuality, the forward and backward branches of the reaction occur separately in space and time and thus are not in chemical equilibrium, preventing the use of the equilibrium equation to quantitatively predict the Earth's atmospheric $p\mathrm{CO}_2$ (e.g. Kasting, 2019). Further, many other species of mineral are involved in this process, including clays and other varieties of silicate, with important consequences for the rates at which various relevant reactions proceed (e.g. Winnick & Maher, 2018). Equation 1.2.1 is only a useful schematic for a very complex set of processes unfolding across a massive range of spatial and temporal scales.

A more detailed (though still highly idealized) illustration of the carbonate-silicate cycle is provided in Figure 1.2. Rainwater, rendered acidic by the dissolution and speciation of atmospheric CO_2 into carbonic acid (H_2CO_3) (Zeebe & Wolf-Gladrow, 2001), falls onto continents and islands made of silicate minerals. The acidic rain water dissolves the silicates into components like Ca^{2+}, Mg^{2+}, and SiO_2, which are subsequently washed to the ocean in rivers (e.g. Mackenzie & Garrels, 1966a; Gaillardet et al., 1999). In the ocean, divalent cations (ions with +2 charge, acting as alkalinity), primarily Ca^{2+} along with some Mg^{2+}, react with oceanic carbonate ions (CO_3^{2-}) that are in equilibrium with atmospheric CO_2 through the seawater carbonate speciation system (Zeebe & Wolf-Gladrow, 2001) to produce carbonate minerals like $CaCO_3$ and $MgCO_3$. Eventually these minerals precipitate from the ocean, a process that occurs on the modern Earth due to the action of plankton that constitute their bodies from oceanic carbon, but which would also occur in the absence of biology once the ocean became supersaturated enough with respect to the carbonate phases

Figure 1.2: **An illustration of the carbonate-silicate cycle.** Rain rendered acidic by atmospheric CO_2 dissolves silicate minerals in a process called weathering, whereupon rivers carry the alkaline dissolution products to the ocean, driving the precipitation of carbonate minerals in a net process that at steady-state removes a mole of CO_2 from the atmosphere-ocean system for every mole of carbonate precipitated onto the seafloor. These minerals are eventually subducted into the Earth's interior and thermally decomposed, whereupon the CO_2 is released back into the atmosphere and the cycle is closed. See also Section 1.2. Art credit: Jenny Leibundgut

(Siever, 1968; Pierrehumbert, 2010a), though the kinetic controls on abiotic carbonate precipitation under these conditions are poorly understood (Strauss & Tosca, 2020). Most precipitated carbonates re-dissolve before they reach the seafloor due to the pressure-dependence of their saturation threshold, but some make it to the bottom, becoming a component of the sediments on parts of the seafloor (Kasting, 2019). Thus the weathering of silicates and subsequent seafloor deposition of carbonates that form from the weathering products acts as a net sink of inorganic carbon in the atmosphere-ocean system, ultimately removing CO_2 from the atmosphere. These seafloor carbonates are then subducted into the Earth's interior by the action of plate tectonics (Sleep & Zahnle, 2001; Müller et al., 2022), eventually reaching depths with high enough temperatures and pressures that they undergo metamorphic decarbonation, reproducing the original silicates and degassing the resultant CO_2 back into the atmosphere, completing the cycle (though the total outgassing rate also includes CO_2 contributions from Earth's mantle, not just metamorphic decarbonation, e.g. Catling & Kasting, 2017; Stewart et al., 2019).[1] As the primary geologic sink of CO_2 degassed at Earth's surface, seafloor carbonate deposition driven by the weathering of crustal silicate minerals is thought to play a fundamental role in the long-term regulation of climate on Earth throughout deep time (Walker et al., 1981; Maher & Chamberlain, 2014; Krissansen-Totton et al., 2018; Penman et al., 2020) and, more speculatively, on Earth-like, terrestrial, ocean-bearing exoplanets (Kasting et al., 1988, 1993; Abbot et al., 2012; Kopparapu et al., 2013; Rushby et al., 2018; Graham & Pierrehumbert, 2020; Lehmer et al., 2020b).

1.2.2 The (continental) feedback

The stabilizing negative feedback alluded to in Section 1.1 emerges as a consequence of the chemistry and physics of the silicate weathering step in the carbonate-silicate cycle. Because of the temperature- and $p\mathrm{CO}_2$-dependence of silicate dissolution kinetics (Walker et al., 1981) and the temperature-dependence of the hydrology driving the process (Maher & Chamberlain, 2014), the weathering of silicates at Earth's surface appears to be climate-dependent, accelerating under warmer conditions and slowing under cooler conditions (represented by the positive slope of the blue weathering curve with respect to CO_2 in the schematic Fig. 1.3). If we consider a planet that initially starts with a silicate weathering rate that consumes less CO_2 than is supplied by outgassing (V, Fig. 1.3), i.e. a planet in the purple zone with $p\mathrm{CO}_2 < P$ in Fig. 1.3, CO_2 will accumulate, the planetary surface will warm, and the silicate weathering rate will increase. Eventually the CO_2 will reach a value (P, Fig. 1.3) that warms the surface enough to bring the rate of sequestration of CO_2 from the atmosphere by weathering into balance with the input of CO_2 by outgassing, stabilizing atmospheric CO_2 content and surface climate. Similarly, a planet initialized with enough CO_2 to drive weathering rates higher than outgassing rates (the pink zone of Fig. 1.3,

[1]It remains unclear whether plate tectonics and subduction are strictly necessary for the operation of the carbonate-silicate cycle; some work suggests that Earth spent a long period of its early history as a single-plate world (Moore & Webb, 2013), and modeling of resurfacing on geologically active stagnant lid planets suggests they might be able to efficiently bury carbonates to depths large enough for decarbonation reactions to proceed in the absence of subduction, allowing the cycle to operate even in the absence of plate tectonics (Foley & Smye, 2018; Foley, 2019).

with $pCO_2 > P$) would experience net loss of CO_2, cooling the surface and slowing weathering until it equalled outgassing.

In this way, the balance between silicate weathering and CO_2 outgassing determines a quasi-stable equilibrium for Earth's climate. Perturbations are met with imbalances in the carbon cycle that tend to drive the atmosphere in a direction that opposes and suppresses the perturbations. For example, a change to outgassing will tend to move the pCO_2 level, weathering rate, and climate in the corresponding direction by forcing an initially balanced carbon cycle to evolve until weathering again equals outgassing, with increases in CO_2 flux leading to warming and reductions leading to cooling (e.g. Godderis & Donnadieu, 2019, and see Fig. 1.4 for a schematic illustration). Similarly, holding outgassing constant, an increase in the luminosity of a planet's parent star will tend to warm its surface, increasing the planet's weathering rate beyond its outgassing rate (assuming its carbon cycle was initially in balance), forcing CO_2 to fall and cooling the planet until weathering is again equal to outgassing (see Fig.1.5). As the Sun displayed only $\approx$70% of its present luminosity 4.5 Ga (Sagan & Mullen, 1972; Bahcall et al., 2001), the weathering-driven adjustment of pCO_2 in response to increasing instellation has likely played a fundamental role in Earth's ability to maintain a clement climate across almost this entire period (Walker et al., 1981; Charnay et al., 2020).

1.2.3 The evidence

Although doubts have periodically been raised about its functioning (e.g. Raymo, 1992; Edmond & Huh, 2003) there is substantial geochemical evidence across multiple timescales for the operation of the silicate weathering feedback in Earth's history. For example, present-day measurements of the degree of weathering of rocks across the world demonstrate a strong correlation between apparent weathering intensity and mean annual temperature (Deng et al., 2022). Stepping back a bit further, ice cores directly preserve a record of the past million years of atmospheric CO_2 in their bubbles, and these samples demonstrate long-term stability in CO_2's concentration over this time period (Zeebe & Caldeira, 2008; Yan et al., 2021). This necessitates either the operation of a powerful negative feedback to maintain balance between the influx and outflux of carbon to the atmosphere or hundreds of thousands of years of inordinate luck, since a small imbalance between volcanism and weathering sustained across this timescale would rapidly drive the climate into inhospitably hot or cold states (Berner & Caldeira, 1997; Broecker & Sanyal, 1998). Statistical analysis

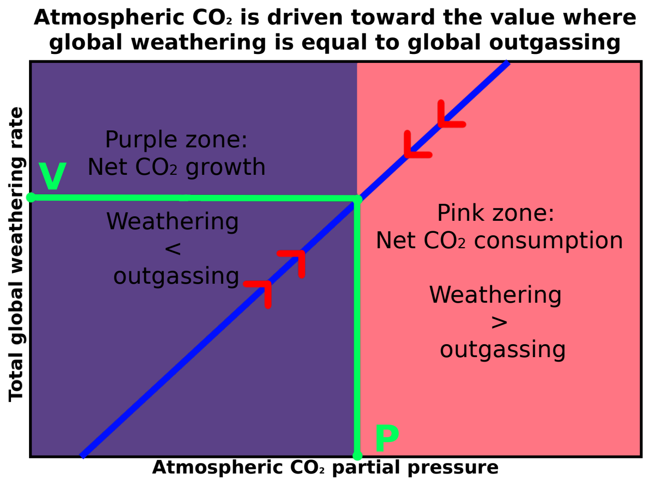

Figure 1.3: **Schematic demonstrating the stabilizing effect of the carbonate-silicate cycle**. The blue curve represents the total global weathering rate as a function of atmospheric CO_2 for a planet at a given instellation. If pCO_2 is smaller than the value indicated by the green P (i.e. if pCO_2 falls in the purple side of the plot), the global weathering rate will sequester CO_2 more slowly than volcanic outgassing (represented by the green V) supplies it to the atmosphere. This forces pCO_2 to grow, as represented by the rightward orientation of the red arrows in the purple zone, which drives the weathering rate higher, as represented by the arrows' upward orientation. The converse is true in the pink zone, where pCO_2 >P and weathering exceeds outgassing, drawing down CO_2. P is the only CO_2 partial pressure where the weathering rate is in equilibrium with the outgassing rate V, and the system will tend to stabilize at $pCO_2=P$ as long as the outgassing rate (V) and instellation (which determines the location of the blue curve) don't change.

of temperature anomalies recorded by paleothermometer datasets across the Pleistocene (2 million years) and Cenozoic (66 million years) demonstrate the operation of stabilizing feedbacks in the climate system on timescales between 4 thousand years and 400 thousand years (Arnscheidt & Rothman, 2022), with the upper range of stabilization consistent with estimates that Earth's silicate weathering feedback operates on a $\approx 200-400$ thousand year timescale (Colbourn et al., 2015).

In sedimentary records stretching back tens of millions of years, isotopes thought to be derived from erosional processes that accompany silicate weathering display approximate long-term stability (Willenbring & Von Blanckenburg, 2010; Caves et al., 2016; Caves Rugenstein et al., 2019; von Blanckenburg et al., 2022) (as required by the long-term equality between the weathering rate and the CO_2 degassing rate), but with pulses that map onto climate fluctuations that would be predicted to drive tran-

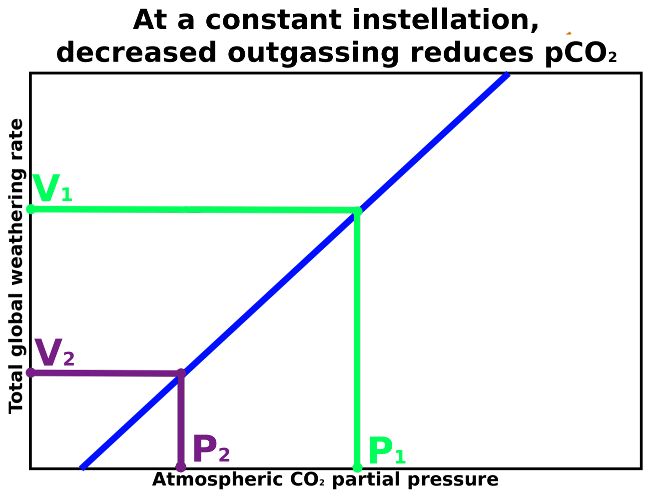

Figure 1.4: **Schematic diagram of total global weathering rate vs. atmospheric CO_2 partial pressure demonstrating how volcanic outgassing qualitatively affects CO_2 content under a climate-dependent carbonate-silicate cycle.** The blue curve is the total global weathering rate as a function of atmospheric CO_2. For an atmosphere to maintain a stable CO_2 content, CO_2 must be removed by weathering at a rate equal to the rate at which it is added by outgassing. Thus a given weathering value on the y-axis is equivalent to the outgassing rate required to sustain a given CO_2 level, given the assumed climate-dependence of weathering (i.e. the assumed shape and position of the blue curve). The positive slope of the blue curve means that global weathering (and thus global CO_2 sequestration) becomes faster as CO_2 increases and surface temperatures rise. Point P_1 (green) is the CO_2 partial pressure that would drive a weathering rate balancing a volcanic outgassing rate of V_1 (green). A smaller volcanic outgassing rate, i.e. V_2 (purple) $< V_1$, is balanced by a smaller weathering rate, which is maintained by a cooler climate with a smaller $p\mathrm{CO}_2$ of P_2 (purple)$< P_1$. An increase or reduction in outgassing leads to an increase or reduction in CO_2 content respectively, all else being equal, with the sensitivity of global climate to outgassing rate thus determined by the shape of the blue weathering curve, which can itself be thought of as the sensitivity of global weathering to climate.

sient increases or decreases in weathering until re-equilibration with outgassing (Korte et al., 2003; Cohen et al., 2004; Pogge von Strandmann et al., 2013, 2017; van der Ploeg et al., 2018), suggesting responsiveness of weathering rates to global climate, a necessity for the existence of a negative feedback. On the 100-million-year timescale, a large compilation of CO_2 data from the past 420 million years demonstrates that the long-term average atmospheric CO_2 concentration has adjusted downward over that period from ≈2000 ppmv to ≈280 ppmv pre-industrially (Foster et al., 2017).

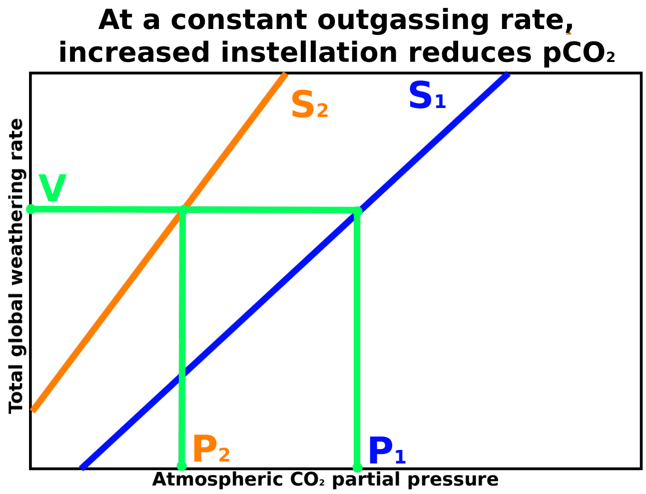

Figure 1.5: **Schematic diagram of total global weathering rate vs. atmospheric CO_2 partial pressure demonstrating how changing instellation qualitatively affects CO_2 content under a climate-dependent carbonate-silicate cycle.** The blue curve is the total global weathering rate as a function of atmospheric CO_2 for a planet irradiated by an instellation of S_1. The orange curve represents the weathering rates for a planet with instellation $S_2 > S_1$. Under higher instellations, a planet requires less CO_2 to achieve the same surface temperatures and weathering rates, which is why the orange curve shifts to the left (lower $p\mathrm{CO}_2$) relative to the blue curve. Thus, assuming the outgassing rate (green V) is independent of instellation (which ought to hold over the range of instellations we are interested in), increasing instellation from S_1 to $S_2 > S_1$ shifts the equilibrium $p\mathrm{CO}_2$ from P_1 to $P_2 < P_1$.

Although the trend is noisy (see the jagged portion of the black line in the CO_2 reconstruction in Fig. 1.6), Foster et al. (2017) find that the solar forcing from the gradual brightening of the Sun over the same period has been almost entirely cancelled out by the reduction in CO_2 greenhouse forcing on million-year timescales, in line with the operation of a climate-dependent negative feedback stabilizing surface temperature as in Fig. 1.5. And although the CO_2 record becomes increasingly ambiguous as we move deeper into the past, the feedback is also thought to be responsible for maintaining the much higher levels of atmospheric CO_2 ($\mathcal{O}(0.01-0.1\mathrm{bars})$) billions of years ago that have been inferred from studies of paleosols, micrometeorite oxidation, and seawater pH (e.g. Kanzaki & Murakami, 2015; Halevy & Bachan, 2017; Catling & Zahnle, 2020; Lehmer et al., 2020a; Payne et al., 2020; Huang et al., 2021) during the Archean and Proterozoic Eons (see Fig. 1.6). Such high levels of CO_2 likely occurred in response to a combination of substantially reduced irradiation from the

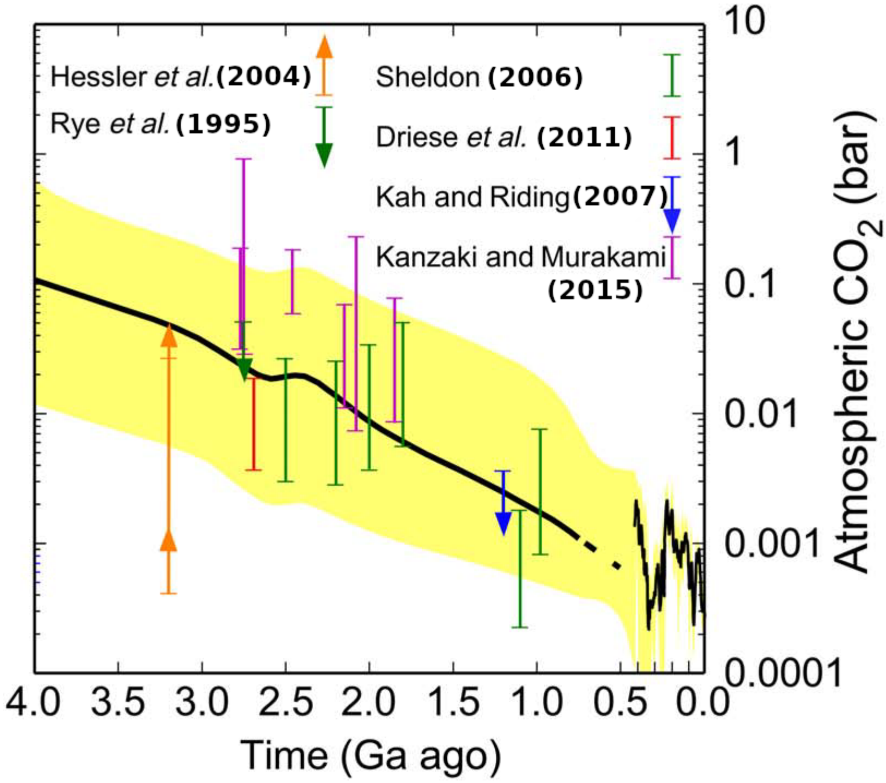

Figure 1.6: **Reconstructing 4 billion years of atmospheric $p\mathrm{CO_2}$ evolution.** Most of the black curve represents the median CO_2 evolution inferred from an inverse carbon cycle model (Krissansen-Totton et al., 2018), with yellow shading indicating that model's 95% confidence intervals; the final 420 million years of the curve are drawn from a CO_2 reconstruction from proxy estimates (Foster et al., 2017). Archean and Proterozoic Eon proxy estimates from Rye et al. (1995); Hessler et al. (2004); Sheldon (2006); Kah & Riding (2007); Driese et al. (2011); Kanzaki & Murakami (2015) are superimposed, with symbols as labeled on the plot. This CO_2 evolution is generally attributed to the response of the carbonate-silicate cycle to the gradual brightening of the Sun. Modified from Figure 3 in Catling & Zahnle (2020) under Creative Commons Attributions License 4.0 (CC BY).

Sun (Sagan & Mullen, 1972; Walker et al., 1981; Bahcall et al., 2001), greater CO_2 outgassing (Dasgupta, 2013), and reduced continental area (e.g. Johnson & Wing, 2020)–making this mechanism the likely solution to the so-called "Faint Young Sun problem" (Charnay et al., 2020).

A note on possible feedbacks from basalt carbonatization (seafloor weathering) and authigenic ocean-bottom clay formation (reverse weathering)

So far, I have focused on the continental silicate weathering component of the carbonate-silicate cycle, but there are other important parts of the carbon cycle that have recently been argued to play roles similar to that of the continental weathering feedback. Here, I will briefly review two of them: "seafloor weathering" and "reverse weathering." The magnitude (and even the direction) of the contribution of these processes to Earth's climate stability is uncertain, so they are excluded from the calculations I will present in the rest of this work, but their possible importance should still be noted as either process could substantially affect the behaviors and mechanisms I will go on to discuss throughout the thesis.

Seafloor weathering is the label applied to the conversion of (silicate) basalts on the seafloor into carbonate minerals through basalt dissolution, release of Ca^{2+} ions, and reaction of those ions with dissolved inorganic carbon flowing through pores and cracks in the seafloor in a process analogous to carbon sequestration by continental silicate weathering (e.g. Coogan & Gillis, 2018b). Abundant evidence demonstrates that large quantities of carbonate minerals are stored in seafloor basalt porespace, suggesting the possibility that this process serves as a large carbon sink (Alt & Teagle, 1999). Early modeling work focused on the potential direct pH- or $p\mathrm{CO}_2$-dependence of this process, with debate over whether such a dependence might lead to a significant climatic negative feedback (Francois & Walker, 1992; Caldeira, 1995; Sleep & Zahnle, 2001). A direct temperature-dependence of basalt carbonatization has also been suggested based on laboratory experiments directly measuring basalt dissolution (e.g. Brady & Gislason, 1997) as well as geochemical data showing secular variations in uptake of carbon into basaltic porespace that appear to map onto background temperature (Gillis & Coogan, 2011; Coogan & Gillis, 2013; Coogan & Dosso, 2015; Coogan & Gillis, 2018a), which would also contribute directly to any negative feedback behavior. However, it is unclear whether the calcium in these carbonates was sourced directly from the surrounding basalts or was supplied to the ocean by continental weathering, with some estimates indicating 70-85% of the calcium in these porespace carbonates is derived from continents (Alt & Teagle, 1999), which would reduce the importance of basalt dissolution as a carbon sink, since continental weathering would still be the main driver. While the continental silicate weathering feedback is generally held to dominate as a carbon sink today (Li & Elderfield, 2013; Isson et al., 2020), modeling studies (Mills et al., 2014; Krissansen-Totton & Catling, 2017; Krissansen-Totton et al., 2018) and analysis of Archean rocks (Nakamura & Kato, 2004) suggest that longterm variations in exposed landmass and area of exposed basalts on the seafloor may have driven large changes in the relative importances of continental and seafloor weathering throughout Earth history.

The other potential carbon cycle feedback that will be neglected throughout the rest of the thesis is authigenic clay formation on the seafloor, also known as "reverse weathering," a process originally proposed to explain an apparent imbalance between oceanic in- and outfluxes of bicarbonate and silica from streams and rivers (Mackenzie & Garrels, 1966a,b). Reverse weathering can be represented schematically (as in Trower & Fischer, 2019) for our purposes by:

$$\text{Cations} + \text{SiO}_2\ (\text{aq}) + \text{Al(OH)}_3 \rightarrow \text{smectite} + \text{H}^+ + \text{H}_2\text{O} \tag{1.2}$$

representing the reaction of silicate dissolution products to form siliceous clay and release acidity, with no net CO_2 consumption, in direct competition with the role of silicate dissolution products in driving the precipitation of silica and carbonates, thereby sequestering CO_2 (e.g. equation 1.2.1). Thus reverse weathering decreases the amount of carbonate precipitation expected from the products of a given amount of silicate weathering, reducing the efficiency of weathering at CO_2 drawdown, leading to the suggestion that changes to reverse weathering have played roles in various carbon cycle perturbations (Dunlea et al., 2017; Li et al., 2021; Isson et al., 2022).

Because the Precambrian oceans lacked creatures that could utilize oceanic SiO_2 (diatoms, radiolaria, silicaflagellolates, and sponges, e.g. Maliva et al., 1989; Siever, 1992) silica concentrations were much higher, as reflected in the massive secular reduction in chert (SiO_2) deposits (Maliva et al., 1989; Siever, 1992; Maliva et al., 2005) and progressive changes in the silicon and lithium isotope records (Trower & Fischer, 2019; Kalderon-Asael et al., 2021). Of most interest to us, silica saturation likely drove much more efficient reverse weathering during the Precambrian, since silicon is a component of all clays (e.g. Isson & Planavsky, 2018). Since this clay formation process competes with carbonate deposition for silicate dissolution products, greater reverse weathering would tend to hold CO_2 at higher levels (Trower & Fischer, 2019; Isson et al., 2020). Isson & Planavsky (2018) suggested that these silica-rich conditions might have induced reverse weathering to produce a negative feedback on climate complementing the silicate weathering feedback, since clay formation is faster at high pH (i.e. low CO_2), meaning silicate weathering's efficiency at driving carbonate deposition would fall as CO_2 fell, producing a stronger overall carbon cycle response to CO_2 reductions than the silicate weathering feedback alone. Some tentative support for this scenario has emerged from Bayesian inverse carbon modeling (Krissansen-Totton & Catling, 2020). However, most studies seem to have neglected the possibility that reverse weathering accelerates under higher temperatures (as suggested by Higgins & Schrag, 2015, to explain secular change in Mg isotopes in seawater during the Cenozoic), which would actually allow clay formation to act as a positive, destabilizing feedback on climate by reducing silicate weathering's efficacy under warmer temperatures, particular under the silica-heavy conditions of the Precambrian. This is an important possibility that might have relevance for exoplanet climate, since many exoplanet oceans might be expected to lack biosilicifiers and thus display increased susceptibility to widespread authigenic clay formation. I plan to address this crucial open question in the future, but for the rest of the thesis, reverse weathering is presumed to be negligible.

1.2.4 Silicate weathering beyond Earth?

As noted, the hypothesis that silicate weathering induces CO_2 concentrations to adjust in a way that tends to stabilize planetary climate on Earth-like worlds with land and water oceans is the fundamental premise underlying the concept of the circumstellar HZ (Kasting et al., 1988, 1993; Kopparapu et al., 2013). As such, a growing handful of studies have applied simple models of the weathering feedback in attempts to understand how exoplanet climates might be expected to vary on planets throughout the HZ, and this thesis falls within that tradition. Kite et al. (2011); Edson et al. (2011) found interesting suggestions of instability in the carbon cycles of synchronously rotating planets. GCM simulations have been argued to suggest a "sweet spot" in planetary rotation rate somewhat slower than Earth's that maximizes the efficacy of the silicate weathering feedback (Jansen et al., 2019). In global-mean simulations, Abbot et al. (2012) found that planetary land fraction should not have a large impact on the operation of the feedback above a coverage of about 1%, but under "waterworld" conditions with minimal land, the feedback would fail and CO_2 would accumulate to high levels and make a planet inhospitably hot. That study also found that seafloor weathering does not provide an effective climate buffer, but some subsequent studies have examined the potential impact of a directly temperature-dependent seafloor weathering flux and and found that it may buffer climate as effectively as continental weathering (Hayworth & Foley, 2020; Chambers, 2020). However, their seafloor weathering formulations may be overly simplistic (Hakim et al., 2021).

A series of studies (Tajika, 2007; Kadoya & Tajika, 2014; Menou, 2015; Abbot, 2016; Haqq-Misra et al., 2016; Paradise & Menou, 2017; Kadoya & Tajika, 2019) have predicted that if silicate weathering displays a strong direct pCO_2 dependence (rather than, or in addition to, a temperature dependence), rapidly rotating planets in the outer reaches of the HZ may have difficulty sustaining non-glaciated climates. This is because the CO_2 necessary to attain a given temperature grows at lower instellations, implying more rapid weathering rates for a given temperature, implying that a given outgassing rate should be balanced by weathering from lower equilibrium surface temperatures at lower instellations. At low enough instellation and/or low enough outgassing rates, silicate weathering will draw CO_2 down to levels that cause glaciation, dramatically slowing weathering, allowing CO_2 to accumulate to levels high enough that the planet deglaciates (unless CO_2 begins to condense on the surface before the surface ice begins to melt, halting further accumulation, e.g. Turbet et al., 2017; Kadoya & Tajika, 2019). After deglaciation, weathering would rapidly accelerate, drawing down CO_2 and plunging the planet back into a snowball state, primed to go through the process again in an oscillatory mechanism nicknamed "limit cycling" (Haqq-Misra et al., 2016). This concept has even used in attempts to explain the puzzling intermittent habitability of early Mars (Batalha et al., 2016; Hayworth et al., 2020). Seafloor weathering may prevent the escape from these snowball states and prevent limit cycling for some planets (Chambers, 2020). Synchronously rotating planets, because of their strong resistance to glaciation at the substellar point under HZ instellations (Pierrehumbert, 2010b; Checlair et al., 2017), do not suffer from this proposed carbon cycle instability (Checlair et al., 2019a).

Finally, if we take seriously the possibility that the carbonate-silicate cycle is operating on exoplanets, then certain trends in environmental properties might be remotely detectable with future telescope missions, simultaneously serving as a test of the existence of the silicate weathering feedback on other worlds and as a test of the usefulness of the HZ concept. For example, the reconstructed time evolution of Earth's CO_2 from Catling & Zahnle (2020) that I reproduced in Fig. 1.6 is equivalent to an inverse correlation between pCO_2 and instellation (i.e. solar luminosity, which at 4 Ga was only 74% of today's value, Bahcall et al., 2001), driven by the reaction of the carbon cycle to stellar brightening demonstrated in Fig. 1.5. Assuming you are a biological human reading this in the 21st century, it is unlikely you will live long enough to observe CO_2 evolution trends for individual terrestrial exoplanets across a billion years of observations (Pearce & Raftery, 2021). However, on much shorter timescales it should become possible to loosely constrain atmospheric CO_2 mixing ratios for a handful of nearby exoplanets within their respective HZs, potentially allowing identification of the anti-correlation between TOA instellation and CO_2 that is predicted based on the carbonate-silicate cycle (Bean et al., 2017; Checlair et al., 2019b; Lehmer et al., 2020b; Checlair, 2021). The most comprehensive examinations of the possibility of detecting the weathering feedback have simulated observations of large numbers of HZ exoplanets by NASA's HabEx (Gaudi et al., 2020) and LUVOIR (Team et al., 2019) space telescope concepts at varying CO_2 and instellation to determine the number of observations needed to confidently distinguish between the null hypothesis of randomly distributed pCO_2 vs. a weathering-induced CO_2/instellation pattern (Lehmer et al., 2020b; Checlair, 2021). With various assumptions about instrumental noise and the potential for carbon cycle variability, these studies found that HabEx and LUVOIR-B (the small version of the LUVOIR telescope) are unlikely to detect and characterize enough planets to reveal the feedback, but that the LUVOIR-A concept would likely succeed (Lehmer et al., 2020b; Checlair, 2021).

Other properties predicted by the silicate weathering hypothesis for planets within the HZ and beyond its inner and outer edges suggest other possibilities for identifying statistical signatures of the operation of the carbonate-silicate cycle using exoplanet observations. As described in Section 1.1, ocean-bearing exoplanets orbiting closer to their star than the inner edge of the HZ are expected to undergo the runaway greenhouse process (e.g. Kopparapu et al., 2013). Before photolysis strips away their water, planets in the runaway greenhouse state with fully evaporated oceans are expected to have significantly thicker atmospheres than their temperate counterparts with equivalent quantities of water in the condensed phase (e.g. Goldblatt, 2015). For ocean masses between 0.1 and 100× that of Earth's oceans, this effect increases a planet's apparent radius by between 5% and 17%, meaning there may be an observable jump in planetary radius across the inner edge of the HZ if silicate weathering successfully maintains low CO_2 levels and temperate conditions at instellations lower than the inner edge (Turbet et al., 2019; Turbet, 2019; Turbet et al., 2020). After these steam atmospheres are eroded by H_2O photolysis and subsequent hydrogen escape, a common expectation is for CO_2 outgassing to continue in the complete absence of silicate weathering, allowing for the build-up of thick, hot, dry atmospheres with high pCO_2 and high albedo similar to that of Venus, suggesting the possibility of a sharp gradient in CO_2 across the inner edge of the HZ, detectable by differences in albedo (Graham & Pierrehumbert, 2020) or CO_2 concentration (Turbet, 2019) between temperate and post-runaway states. Beyond the outer edge of the HZ, CO_2 surface condensation is expected to become a major sink of outgassed CO_2, which would lead to rapid reductions in pCO_2 as instellations fall beyond the HZ (Turbet, 2019). Water vapor may also be detectable in the atmospheres of exoplanets within the HZ, but not beyond its inner and outer edges, where, respectively, surface water is expected eventually to be photolyzed and lost to space or trapped under a frozen crust (Bean et al., 2017), though the cloudiness of synchronously rotating planets may decrease water vapor's detectability substantially for HZ planets orbiting M-stars, preventing JWST from contributing to this effort (Komacek et al., 2020; Suissa et al., 2020). Finally, if detectable life does exist elsewhere, and if the distribution of detected biosignatures (observations that indicate the presence of life, e.g. Schwieterman et al., 2018) lines up with the theorized extent of the HZ, that will also represent strong, indirect evidence that the carbonate-silicate cycle is involved in stabilizing climates on many Earth-like planets.

1.3 Chapter summaries

As we have seen, a great deal of modeling, theory, and geochemical data support the notion that the carbonate-silicate cycle and the silicate weathering feedback have been fundamental in the maintenance of Earth's habitability throughout its history, and these facts have given rise to the suggestion that this process may operate on similar worlds orbiting other stars. Because this hypothesis has become an organizing principle in much of the thinking behind the search for life beyond Earth, there is ample reason to revisit the purported stabilizing abilities of the silicate weathering feedback for exoplanets under a variety of planetary boundary conditions.

In this work, I will focus on modeling the interplay between the continental silicate weathering feedback, planetary climate, and the long-term maintenance of planetary habitability. I will approach these issues using planetary climate models coupled to idealized models of relevant components of planetary carbon cycles (oceanic carbonate speciation in Chapter 2 and continental silicate weathering in subsequent chapters). As the chapters progress, I will deploy increasingly sophisticated climate models, moving from pre-existing zero-dimensional polynomial fits of outgoing longwave radiation and albedo (Chapters 2 and 3) to two-stream radiative transfer calculated with a one-dimensional column model (Chapter 4) to fully dynamical three-dimensional climate calculations with coupled radiative transfer (Chapter 5). Although I will begin the thesis with a chapter arguing for some degree of optimism about the habitability of high-CO_2 planets in the outer reaches of the HZ, the subsequent chapters will increasingly suggest a drearier picture, highlighting the potential for carbon-cycle-induced climatic instability and runaway CO_2 accumulation for planets receiving somewhat less instellation than the Earth.

1.3.1 Chapter 1: High $p\mathrm{CO_2}$ reduces sensitivity to $\mathrm{CO_2}$ perturbations on temperate, Earth-like planets throughout most of habitable zone

This chapter (published as Graham, 2021) will start from the baseline assumption that an efficient silicate weathering feedback adjusts $p\mathrm{CO_2}$ to maintain moderate surface temperatures on Earth-like planets throughout the HZ. From this starting point, I will use simple global-mean polynomial models of climate and ocean carbonate chemistry to point out that both surface temperature and ocean pH should become increasingly insensitive to additions of a given mass of $\mathrm{CO_2}$ to the atmosphere for planets at low instellations with correspondingly higher background $p\mathrm{CO_2}$. Many of Earth's mass extinctions and climate catastrophes seem to have been caused by the warming and ocean acidification that accompanied geologically sudden additions of atmospheric $\mathrm{CO_2}$, so this result suggests that planets with large $\mathrm{CO_2}$ inventories from the combined effect of the carbonate-silicate cycle and reduced instellation will be less sensitive to these killing mechanisms and thus perhaps more quiescent and hospitable for biospheres. I will go on to discuss potential implications of this perspective for understanding some facets of exoplanetary habitability and Earth's deep (high-$p\mathrm{CO_2}$) past.

1.3.2 Chapter 2: Thermodynamic and energetic limits on continental silicate weathering strongly impact the climate and habitability of wet, rocky worlds

Here (published as Graham & Pierrehumbert, 2020), I will couple the same polynomial climate model from Chapter 2 to a pair of models of continental silicate weathering to examine the implications of each formulation for predictions of planetary climate in the HZ. One of the weathering models will be based in the original formulation of the silicate weathering feedback from Walker et al. (1981, WHAK), which has dominated studies of Earth weathering for 40 years and was the only continental silicate weathering formulation applied in any exoplanet climate study until this one. The second weathering formulation that will be applied in this study is based in more recent models that attempt to account for the crucial impact of the formation of secondary silicate minerals (clays, usually) while primary silicates are dissolving during the weathering process (Maher & Chamberlain, 2014, MAC). This caps the concentration of weathering products in runoff due to chemical equilibration between dissolving primary silicates and precipitating clays, leading to a much stronger dependence of weathering fluxes on hydrology compared to the behavior that emerges from the WHAK model, under which weathering rates are assumed to be governed by the kinetics of silicate dissolution. It will turn out that MAC weathering leads to a large climate sensitivity in response to changes in outgassing rate and land fraction, contrasting strongly with the relative insensitivity to those parameters displayed in WHAK weathering/climate models. The MAC formulation also allows for more explicit representation of the impacts of variations in lithology and surface properties on weathering rates, and the simulations that will be presented here suggest that Earth-like climates will display strong sensitivity to those parameters as well. Overall, the more physically and chemically realistic MAC formulation of weathering seems to lead to a less effective negative feedback on climate than predictions based on WHAK might have suggested, generally resulting in a larger spread in plausible stable climate states at a given instellation.

1.3.3 Chapter 3: CO_2 ocean bistability on terrestrial exoplanets

This study (published as Graham et al., 2022b) will deploy the MAC weathering formulation from Chapter 3 along with improved climate modeling with real gas radiative transfer from the SOCRATES column model to argue that planets orbiting at low instellations within the HZ of F-stars and G-stars (but not M-stars), even with water oceans and active carbonate-silicate cycles, may be able to accumulate oceans of liquid CO_2 and/or CO_2 clathrate hydrates that can remain stable for geologic timescales. I will demonstrate that this behavior occurs because of CO_2's Rayleigh scattering effect, which at very high pCO_2 helps convert the gas into a planetary coolant, transforming silicate weathering from a stabilizing negative feedback into a destabilizing positive feedback, allowing outgassed CO_2 to build in the atmosphere until surface condensation becomes a new sink and the atmospheric content stabilizes. This can occur even when stable, temperate, low-CO_2 climate equilibria exist with the same instellation, CO_2 outgassing rate, and weathering parameters, implying that this constitutes a novel form of climatic bistability and hysteresis for Earth-like exoplanets at low instellations.

1.3.4 Chapter 4: Sluggish hydrology under dim suns: energetically-limited precipitation and silicate weathering

In the fourth chapter, which will be submitted soon, I will use global climate model (GCM) simulations to examine the impact of realistic precipitation patterns and surface temperature distributions on continental weathering rates (both WHAK and MAC) under different instellations and background atmospheres. I will find that under low-pCO$_2$, high-instellation conditions like those on the modern Earth, both WHAK and MAC result in negative feedback, i.e. in both cases the global weathering rate will increase with background pCO$_2$, allowing for climate stabilization and matching the traditional picture of continental silicate weathering. However, in the case of CO_2-dominated atmospheres at low instellations, it will turn out that the predictions of WHAK and MAC diverge drastically because of an energetic limit on global rainfall rates that is set by the surface energy budget of a planet. At low instellations, planets are restricted to lower precipitation rates, and for planets that have approached this energetic limit, I will demonstrate that accumulation of CO_2 can actually reduce rainfall and weathering rates in the MAC formulation, even while surface temperatures continue to rise, in contrast to WHAK weathering, which will display strong increases in weathering rates with CO_2 regardless of the energetic limit. So, I will argue that if the MAC formulation is an accurate picture of silicate weathering, then planets at low instellations in the HZ may be in serious danger of runaway CO_2 accumulation due to the failure of their weathering feedbacks, which can lead either to extremely hot surface temperatures or oceans of condensed CO_2 at the surface. These conclusions will thus strengthen and extend the conclusions of the preceding two chapters, suggesting that more-accurate modeling of silicate weathering may imply severe carbon cycle hysteresis for exoplanets under a range of conditions, potentially leading to termination of habitability for many worlds.

Chapter 2

High pCO_2 reduces sensitivity to CO_2 perturbations on temperate, Earth-like planets throughout most of habitable zone

Some say the world will end in fire,
Some say in ice.
From what I've tasted of desire
I hold with those who favor fire.
But if it had to perish twice,
I think I know enough of hate
To say that for destruction ice
Is also great
And would suffice.

Fire and Ice
Robert Frost

Abstract

Note: This chapter was published as Graham (2021). The nearly logarithmic radiative impact of CO_2 means that planets near the outer edge of the liquid water habitable zone (HZ) require $\sim 10^6$ x more CO_2 to maintain temperatures conducive to standing liquid water on the planetary surface than their counterparts near the inner edge. This logarithmic radiative response also means that atmospheric CO_2 changes of a given mass will have smaller temperature effects on higher pCO_2 planets. Ocean pH is linked to atmospheric pCO_2 through seawater carbonate speciation and calcium carbonate dissolution/precipitation, and the response of pH to changes in pCO_2 also decreases at higher initial pCO_2. Here, we use idealized climate and ocean chemistry models to demonstrate that CO_2 perturbations large enough to cause catastrophic changes to surface temperature and ocean pH on low-pCO_2 planets in the innermost region of the HZ are likely to have much smaller effects on planets with higher pCO_2. Major bouts of extraterrestrial fossil fuel combustion or volcanic CO_2 outgassing on high-pCO_2 planets in the mid-to-outer HZ should have mild or negligible impacts on surface temperature and ocean pH. Owing to low pCO_2, Phanerozoic Earth's surface environment may be unusually volatile compared to similar planets receiving lower instellation.

2.1 Introduction

Transient perturbations to the carbon cycle that draw down or release large quantities of CO_2 are known to have played a central role in Earth's climatic history and the evolution of life. Many of the major and minor extinction events of the Phanerozoic Eon are thought to have been caused in part by global heating and ocean acidification from the CO_2 spewed by the eruptions of massive volcanic systems called large igneous provinces (LIPs) (Kidder & Worsley, 2010; Sobolev et al., 2011; Bond & Wignall, 2014; Bond & Grasby, 2017; Ernst & Youbi, 2017). The most extreme known example of this phenomenon is the Permian-Triassic extinction, which wiped out up to 96% of marine species and likely resulted from the eruption of the Siberian Traps LIP through a large organic carbon deposit (Benton, 2018). Conversely, cooling periods throughout the Phanerozoic have been driven by tropical arc-continent collisions and flood basalt eruptions, each of which can trigger CO_2 drawdown by exposing fresh silicates to the surface that are subsequently weathered (Ernst & Youbi, 2017; Macdonald et al., 2019). Pulses of CO_2 consumption may also have served as triggers or preconditions for one or more of the Snowball Earth glaciations that occurred at the ends of the Archean and Proterozoic eons (Donnadieu et al., 2004; Cox et al., 2016; Somelar et al., 2020). Furthermore, ongoing anthropogenic CO_2 emission is comparable to that of other major carbon release events during the Phanerozoic (Foster et al., 2018), though much more rapid, and the consequences for human civilization and the biosphere would be severe if the flood of CO_2 were allowed to continue until depletion of all fossil fuel resources (Ramirez et al., 2014).

The above helps make it clear that the Earth's habitability is fundamentally influenced – in some cases, threatened – by large, rapid carbon cycle perturbations (Rothman, 2017). This motivates a broader analysis of these events to understand their potential importance for the habitability of Earth-like planets in general. Are failed Earths that were heated or frozen by CO_2 perturbations until sterilized of complex life common in the galaxy?

On Earth, the sequestration of CO_2 by the temperature-dependent chemical conversion of silicate minerals on the continents and seafloor into carbonate minerals is thought to have acted as a first-order negative feedback on climate over geologic timescales (Walker et al., 1981; Coogan & Gillis, 2013; Maher & Chamberlain, 2014; Graham & Pierrehumbert, 2020). Under a cooling trend, silicate weathering slows down, allowing CO_2 from volcanic outgassing to build to higher levels and oppose the cooling, and the opposite happens in response to warming. This stabilizing feedback modulates climate on 10^5 to 10^6 year time intervals (Colbourn et al., 2015). Control of CO_2 partial pressure via the silicate weathering feedback is likely a primary reason the planet has remained habitable for the past 4 billion years (Ga) (Walker et al., 1981), despite an initial solar luminosity of about 70% of its modern value and a $(1-0.7)/0.7 \approx 40\%$ increase in luminosity over the same period (Sagan & Mullen, 1972; Charnay et al., 2020). When the sun was dimmer, pCO_2 was higher because of the feedback, and the increase in solar brightness has been slow enough for weathering to draw down CO_2 and maintain climate in a quasi-steady-state with respect to evolving luminosity.

A working hypothesis that underlies the concept of the classical habitable zone (HZ) (the circumstellar region where N2-CO_2-H2O atmospheres can provide enough warming to maintain stable surface liquid water) is that at least some Earth-like exoplanets within the HZ of their stars can support a silicate weathering feedback like Earth's (Kasting et al., 1988, 1993; Kopparapu et al., 2013). This would imply that this subpopulation of rocky planets will display a trend in pCO_2 vs. incoming stellar radiation ("instellation"), with planets that receive less instellation within the HZ generally building up thicker pCO_2 atmospheres to compensate for the cooling at lower luminosity (Bean et al., 2017). This would allow for the maintenance of liquid water on the surfaces of Earth-like planets for longer periods of time and over a much wider range of conditions than would otherwise be likely.

The radiative forcing response to CO_2 is approximately logarithmic, meaning a progressively larger CO_2 change is required in order to produce a given amount of forcing as the background CO_2 level increases (Pierrehumbert, 2010a; Huang & Bani Shahabadi, 2014) (the deviation from logarithmic behavior at high pCO_2 due to self-broadening does not materially affect this point, see e.g. Fig. 1). This means that the pCO_2 required to maintain surface temperatures above freezing rises rapidly as instellation falls, going from parts per million of a bar in the inner portion of the HZ to bars or tens of bars in the mid-to-outer reaches. Given this huge gradient in pCO_2 for N_2-CO_2-H2O atmospheres across the HZ, changes in CO_2 that might cause catastrophe in the inner-HZ should have much smaller impacts in the outer-HZ because of the logarithmic forcing effect. For example, a LIP that suddenly increased the atmospheric CO_2 concentration on an inner-HZ planet from a few hundred parts per million by volume (ppmv) to a few thousand ppmv would likely cause severe warming and (in the presence of life) a mass extinction, but adding the same mass of CO_2 to an atmosphere in the outer-HZ that already had a pCO_2 of a few bars would result in a negligible change in surface temperature.

In this article, we use an idealized climate model to quantify the variation in temperature impact of transient carbon perturbations to the atmospheres of Earth-like planets with different $p\mathrm{CO_2}$ values at a range of instellations throughout the HZ. We also apply a basic model of carbonate equilibrium and calcium carbonate buffering in the sea to estimate the extent of ocean acidification from these perturbations, another of the important killing mechanisms in mass extinctions caused by LIPs on Earth (Benton, 2018). In Section 2.2, we introduce the models used in the article. In Section 3, we present the results of the calculations, demonstrating extreme climate resilience to carbon cycle perturbations for temperate planets in the mid-to-outer reaches of the HZ. In section 4, we discuss caveats and implications of these results, and in section 5 we summarize and conclude the study.

2.2 Modeling & Methods

2.2.1 Energy balance climate model

To investigate the climate sensitivity of Earth-like planetary climate to carbon cycle perturbations at varying instellations, we examine the changes to global-mean surface temperature from atmospheric $\mathrm{CO_2}$ increases equivalent to 5000 gigatonnes of carbon (GtC) and 50,000 GtC. A perturbation of 5000 GtC is on the order of the size of perturbation that caused the Paleocene-Eocene Thermal Maximum (McInerney & Wing, 2011) and is approximately equal to estimates of total global hydrocarbon resources (which includes both accessible and currently-inaccessible reservoirs of fossil fuels) (Rogner, 1997; Ramirez et al., 2014). A perturbation of 50,000 GtC is of the same order of magnitude as the carbon release caused by the Siberian Traps during the Permian-Triassic mass extinction (Svensen et al., 2009). We use an "inverse climate modeling" approach, as described in (e.g. Kasting, 1991), to calculate the initial pre-perturbation climate in each case: the surface temperature and $p\mathrm{CO_2}$ are first assumed, which allows calculation of the albedo and outgoing longwave radiation (OLR), which can together be used to calculate the effective stellar flux (S_{eff}); the ratio of incoming stellar flux, S, on a given planet to modern Earth's insolation of S_{earth}=1368 W m^{-2}) required to sustain the assumed global-mean temperature-$p\mathrm{CO_2}$ combination under the assumption of global-mean energy balance:

$$S_{\mathrm{eff}} = \frac{S}{S_{earth}} = \frac{4 \times OLR\,(T, pCO_2)}{S_{earth} \times (1 - a\,(T, pCO_2))} \tag{2.1}$$

where $a(T,\ p\mathrm{CO_2})$ is the planetary albedo and all other symbols have been introduced above. This highly idealized, global-mean approach is justified for this study because the climate effect we demonstrate results from the basic, qualitative behavior of atmospheric CO_2. To calculate OLR as a function of $p\mathrm{CO}_2$ and global-mean sur-

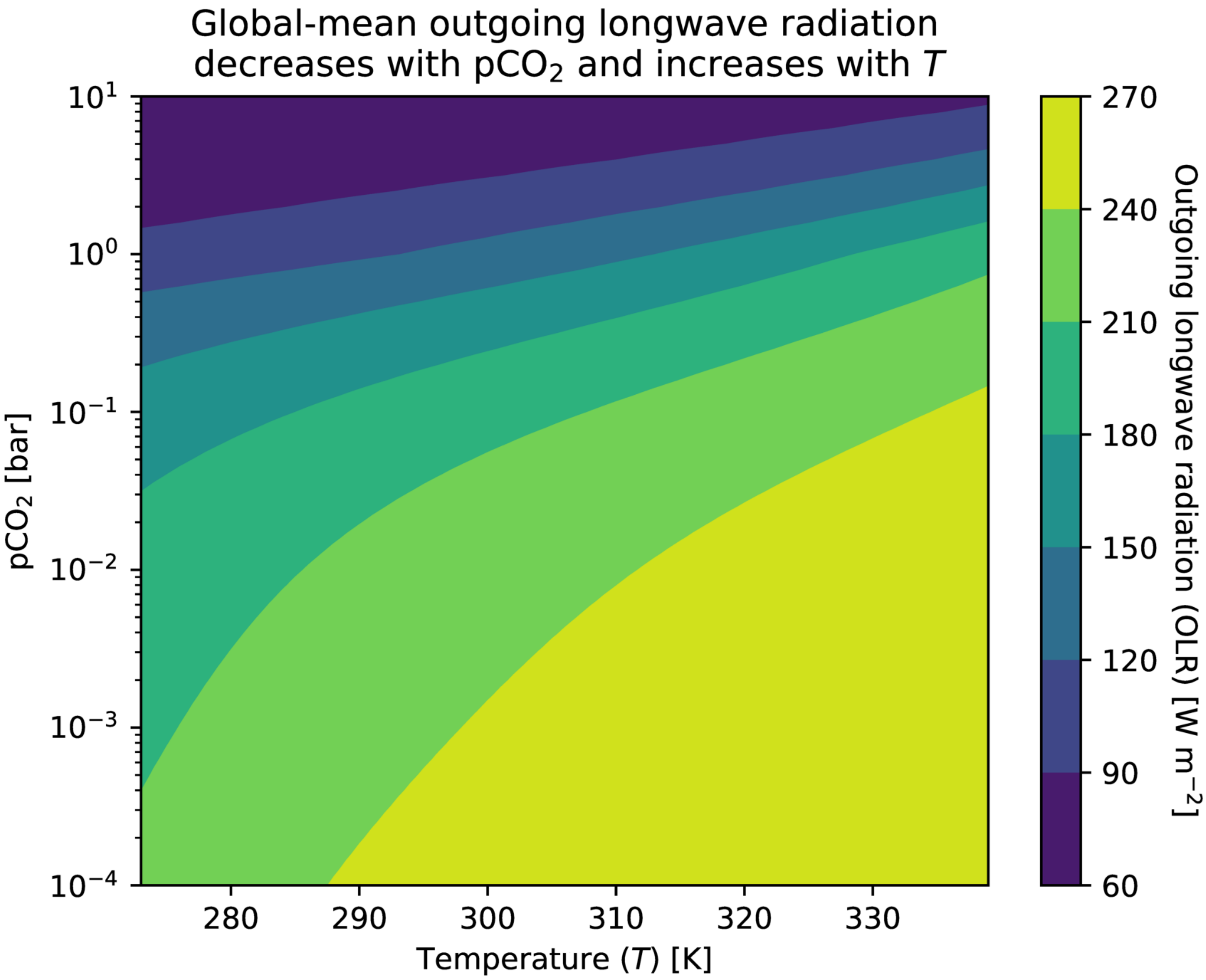

Figure 2.1: **OLR as a function of $p\mathrm{CO}_2$ and global-mean surface temperature** T. OLR, outgoing longwave radiation.

face temperature, we apply a piecewise 6th-degree polynomial function developed by Kadoya & Tajika (2019) to approximate simulations of an N_2-CO_2-H_2O atmosphere by the 1D radiative-convective column model used in Haqq-Misra et al. (2016). The fit can accurately (with error $\leq$ 3.3 W m^{-2}) reproduce the column model's OLR output for 10^{-5} bar $< p\mathrm{CO}_2 <$ 10 bar and 150 K $<$ T $<$ 350 K. For all $p\mathrm{CO}_2$ and T,

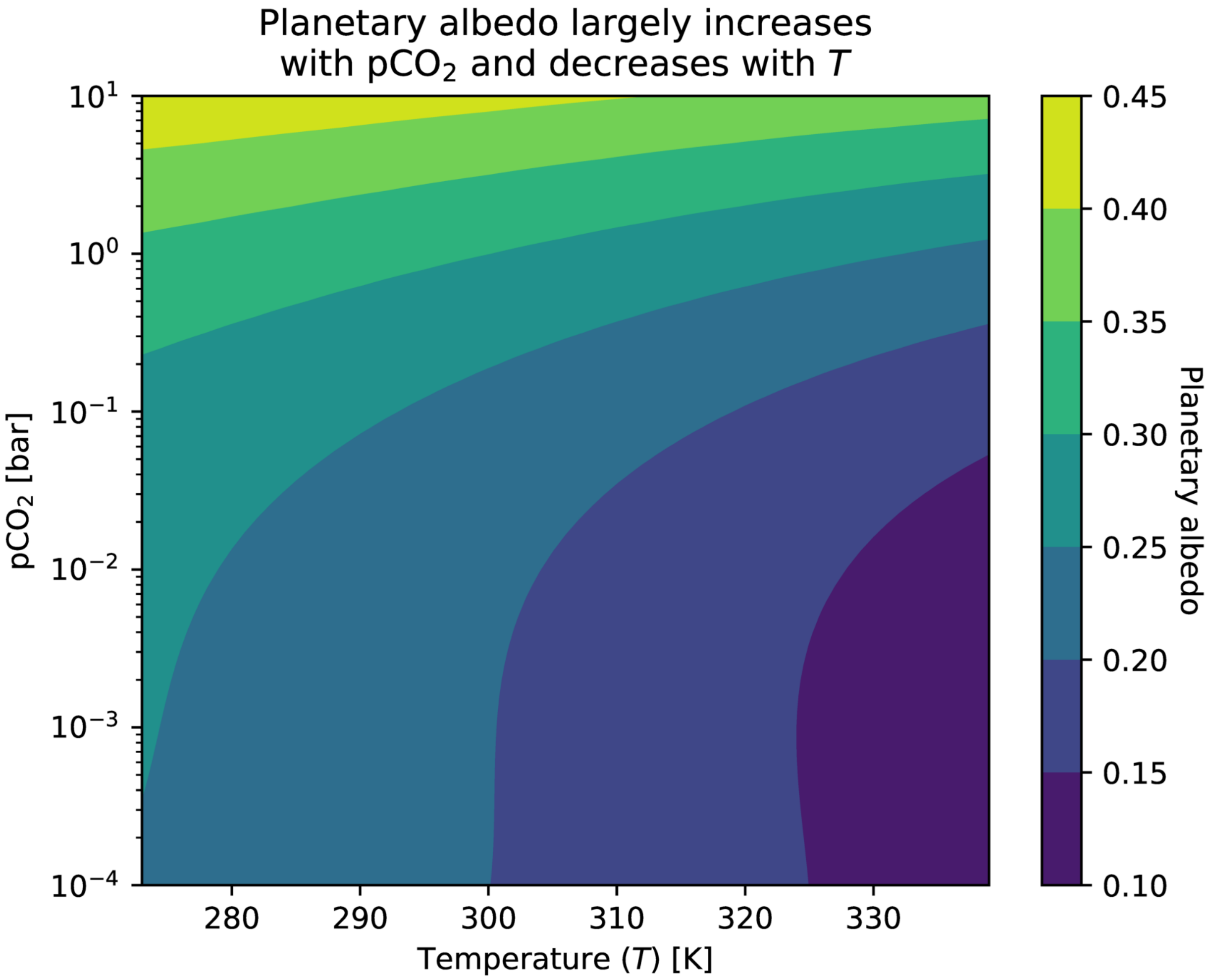

Figure 2.2: **Planetary albedo as a function of $p\mathrm{CO}_2$ and global-mean surface temperature T.**

the atmosphere has a constant $p\mathrm{N}_2 = 1$ bar and is saturated with $\mathrm{H_2O}$. OLR output from this model is plotted as a function of temperature over the range 273 K < T < 340 K and $p\mathrm{CO}_2$ over the range 10^{-4} bar $< p\mathrm{CO}_2 <$ 10 bar in Fig. 2.1. In matrix form, the equation is:

$$OLR\,(T, p\mathrm{CO}_2) = I_0 + TB\boldsymbol{\Upsilon}^t \tag{2.2}$$

$$T = \begin{pmatrix}1 \; \xi \; \xi^2 \; \xi^3 \; \xi^4 \; \xi^5 \; \xi^6\end{pmatrix} \tag{2.3}$$

$$\boldsymbol{\Upsilon} = \begin{pmatrix}1 \; \upsilon \; \upsilon^2 \; \upsilon^3 \; \upsilon^4\end{pmatrix} \tag{2.4}$$

where T is the surface temperature in Kelvin, $p\mathrm{CO_2}$ is the partial pressure of $\mathrm{CO_2}$ in bars, and $\xi = 0.01\times(T\text{-}250)$. For $p\mathrm{CO_2} < 1$ bar

$$p = 0.2 \times \log_{10}(pCO_2) \tag{2.5}$$

$$\boldsymbol{B} = \begin{bmatrix} 87.8373 & -311.289 & -504.408 & -422.929 & -134.611 \\ 54.9102 & -677.741 & -1440.63 & -1467.04 & -543.371 \\ 24.7875 & 31.3614 & -364.617 & -747.352 & -395.401 \\ 75.8917 & 816.426 & 1565.03 & 1453.73 & 476.475 \\ 43.0076 & 339.957 & 996.723 & 1361.41 & 612.967 \\ -31.4994 & -261.362 & -395.106 & -261.600 & -36.6589 \\ -28.8846 & -174.942 & -378.436 & -445.878 & -178.948 \end{bmatrix} \tag{2.6}$$

and when $p\mathrm{CO_2}$ exceeds 1 bar, p and B are instead:

$$p = \log_{10}(p\mathrm{CO_2}) \tag{2.7}$$

$$\boldsymbol{B} = \begin{bmatrix} 87.8373 & -52.1056 & 35.2800 & -1.64935 & -3.43858 \\ 54.9102 & -49.6404 & -93.8576 & 130.671 & -41.1725 \\ 24.7875 & 94.7348 & -252.996 & 171.685 & -34.7665 \\ 75.8917 & -180.679 & 385.989 & -344.020 & 101.455 \\ 43.0076 & -327.589 & 523.212 & -351.086 & 81.0478 \\ -31.4994 & 235.321 & -462.453 & 346.483 & -90.0657 \\ -28.8846 & 284.233 & -469.600 & 311.854 & -72.4874 \end{bmatrix} \tag{2.8}$$

with symbols retaining their previous meanings. OLR is plotted as a function of temperature over the range 273 K < T < 340 K and $p\mathrm{CO_2}$ over the range 10^{-4} bar $< p\mathrm{CO_2} < 10$ bar in Fig. 2.1.

We calculate global-mean planetary albedo using another polynomial fit to radiative-convective model output for a planet orbiting a Sun-like star with T_{eff}=5800 K, sourced from the same model the OLR equation is fit to, though in this case the albedo parameterization comes from Haqq-Misra et al. (2016):

$$\begin{aligned} \alpha(t, a_s, \mu, \phi) = {} & A\mu^3 + B\mu^2 a_s + C\mu^2 t + D\mu^2\phi + E\mu^2 + F\mu a_s^2 + G\mu a_s t... \\ & + H\mu a_s\phi + I\mu a_s + J\mu t^2 + K\mu t\phi + L\mu t + M\mu\phi^2 + N\mu\phi... \\ & + O\mu + Pa_s^3 + Qa_s^2 t + Ra_s^2\phi + Sa_s^2 + T_0 a_s t^2 + Ua_s t\phi + Va_s t... \\ & + Wa_s\phi^2 + Xa_s\phi + Ya_s + Zt^3 + AAt^2\phi + ABt^2 + ACt\phi^2... \\ & + ADt\phi + AEt + AF\phi^3 + AG\phi^2 + AH\phi + \ AG \end{aligned} \tag{2.9}$$

where $t = \log_{10}(T)$, as is the surface albedo (taken to be 0.3 by default), μ is the cosine of the stellar zenith angle (taken to be $\frac{2}{3}$, the instellation-weighted average, following Cronin (2014)), and $\phi = \log_{10}(p\mathrm{CO_2})$. The coefficients A through AG in the equation can be downloaded as a tar.gz file made available by Haqq-Misra et al. (2016). The file includes coefficients for stars with stellar effective temperatures of 3400 K, 4600 K, 5800 K (which we use), and 7200 K, since different stellar spectra lead to different planetary albedos. The coefficient values used in this study (for a 5800 K G-star) are also listed in Table 2.1.

With boundary conditions characteristic of pre-industrial Earth, e.g. an instellation of S = 1368 W m^{-2} and pCO$_2$ = 280 × 10^{-6} bar, the model produces T = 309 K, significantly hotter than Earth's pre-industrial temperature of 285 K (Walker et al., 1981). This is at least partly because the model atmosphere is assumed to be saturated with water vapor, whereas Earth's atmosphere is held at global-mean relative humidities less than 1 due to regions of dry, subsiding air, allowing for more efficient radiation to space and thus cooler surface temperatures (e.g. Pierrehumbert, 1995). In addition, cloud feedbacks that can have important impacts on OLR and albedo are not included in this model. Cloud effects can alter long term climate and the relationship between pCO$_2$ and temperature at a given instellation on Earth-like planets (e.g. Goldblatt et al., 2021), but they are intrinsically 3-dimensional phenomena, so they require 3-D general circulation models to simulate. To ensure the simplifications noted above are minor for the purposes of this study, next we evaluate the sensitivity of the climate model to ensure it reproduces the relevant behavior of more sophisticated models. The steady-state global-mean temperature increase produced by a doubling of CO$_2$ is known as the equilibrium climate sensitivity (ECS) and is a common metric in studies of Earth climate. In more sophisticated climate models than the model used in this paper, the value of ECS is dependent on many processes in addition to the radiative effects of CO$_2$ (and H$_2$O), particularly the dynamics of low-lying, high-albedo clouds (Wolf et al., 2018; Schneider et al., 2019). Based on climate models of varying complexity, ECS on Earth may vary by an order of magnitude depending on background conditions, from ≈2 K to ≈20 K, with a general trend toward higher sensitivity as pCO$_2$ increases and a pronounced maximum at warm temperatures and intermediate pCO$_2$ that arises from low-lying cloud dissipation (Wolf et al., 2018) and clear-sky radiative feedbacks (Seeley & Jeevanjee, 2021). To ensure that the model in this paper produces reasonable climatic responses to CO$_2$ changes, we examine the temperature perturbations from pCO$_2$ doublings with initial pCO$_2$ values ranging from 10^{-4} bar to 5 bars (beyond which a CO$_2$ doubling takes the model outside of its range of validity in pCO$_2$ space), with each simulation initialized at T=273.15 K (see Fig. 2.3). The range of ECS values produced by our climate model is broadly consistent with the range of values in the literature (e.g. the

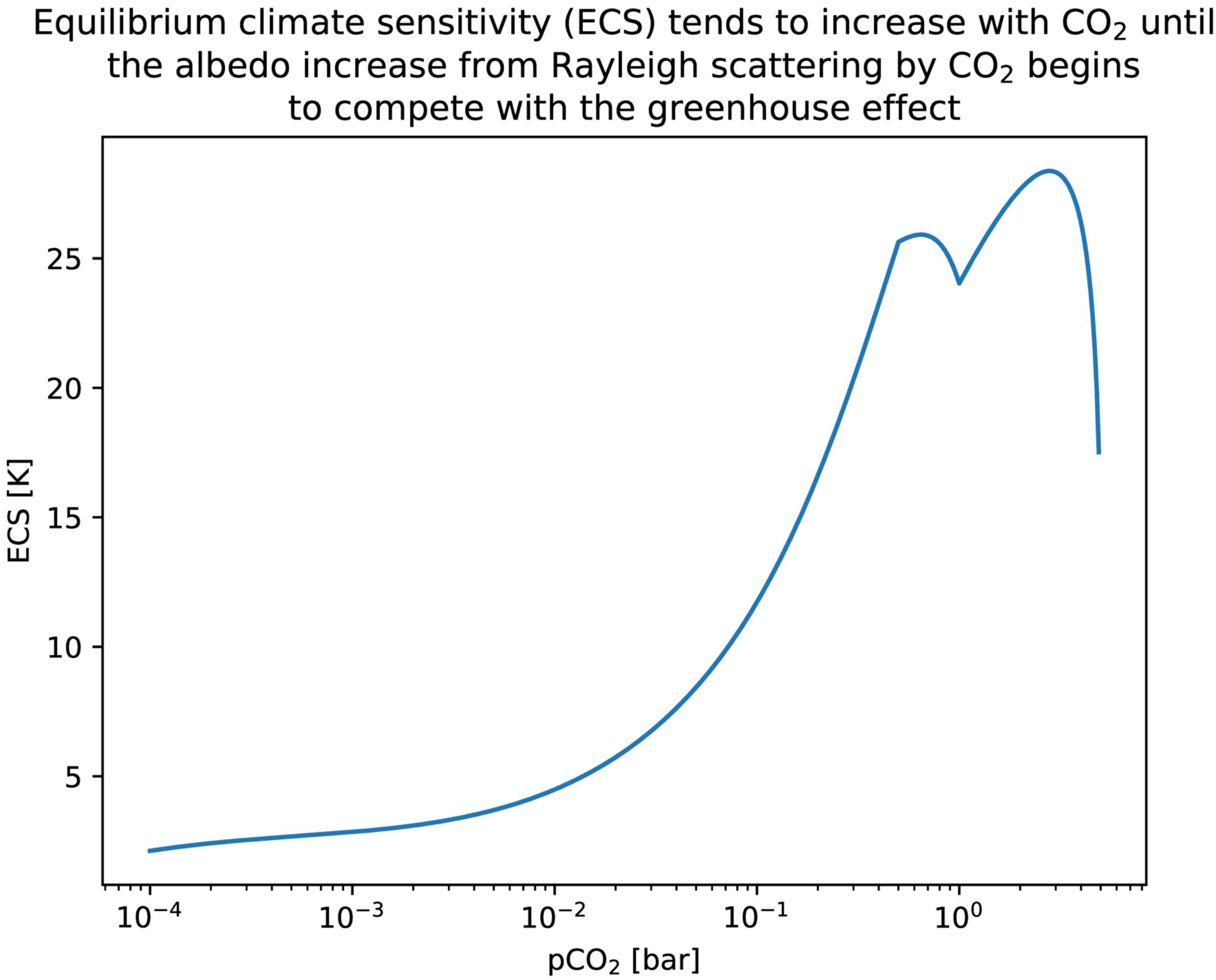

Figure 2.3: **ECS as a function of $p\mathrm{CO}_2$ for planets with initial T = 273.15 K.** ECS, equilibrium climate sensitivity.

ECS throughout Earth history is estimated to have varied between 2.6 K and 21.6 K by (Wolf et al., 2018), though there is no maximum at intermediate $p\mathrm{CO}_2$ since the calculations are all carried out with low initial temperatures. The model does reproduce the intermediate-$p\mathrm{CO}_2$ ECS maximum when initialized at T $\geq\approx$300 K, (not shown). At $p\mathrm{CO}_2 = 10^{-4}$ bar, ECS $\approx$ 2 K, which increases to a maximum of around 27 K near 2 bars. These numbers vary by a few degrees in either direction when the model is initialized from different temperatures, but the differences are small relative to the effects demonstrated in this study. The kink in the ECS that occurs at 1 bar is due to the discontinuity at $p\mathrm{CO}_2$= 1 bar in the OLR polynomial fit from Kadoya

& Tajika (2019) used in this climate model. CO_2's self-broadening increases ECS as background pCO_2 goes up, meaning the model's radiative behavior is not perfectly logarithmic (ECS would be constant in that case), but ECS varies by approximately an order of magnitude across five orders of magnitude of pCO_2, confirming the usefulness of the logarithmic approximation in discussing the model's behavior. ECS begins to decrease rapidly beyond about 2 bars because of the increasing relative impact of CO_2's Rayleigh scattering on the energy balance of the planet. If the curve were extended until ECS intercepted the x-axis, that point would define the "maximum greenhouse limit," beyond which the addition of CO_2 to the atmosphere would cool the planet (e.g. Kopparapu et al., 2013).

Label	Coefficient value	Label	Coefficient value
A	-4.41391620e-01	S	6.11699085e-01
B	-2.60017516e-01	T0	-2.33213410e+00
C	1.08110772e+00	U	2.56011431e-01
D	-3.93863286e-02	V	1.05912148e+01
E	-1.46383456e+00	W	-1.85772689e-02
F	9.91383779e-02	X	-7.55796861e-01
G	-1.45914724e+00	Y	-1.16485004e+01
H	-2.72769393e-02	Z	2.74062492e+01
I	3.99933641e+00	AA	5.46044241e-01
J	1.07231336e+00	AB	-2.05761674e+02
K	-1.04302521e-02	AC	5.57943359e-02
L	-6.10296439e+00	AD	-2.49880330e+00
M	2.69255204e-03	AE	5.14448995e+02
N	9.50143253e-02	AF	2.43702089e-03
O	7.37864216e+00	AG	-1.09384841e-01
P	1.28580729e-01	AH	2.92643187e+00
Q	-3.07800301e-01	AG	-4.27802455e+02
R	2.27715595e-02		

Table 2.1:

We first determine the S_{eff} necessary at a given pCO_2 to hold a planet's global-mean temperature at H_2O's freezing point, T=273.15 K, which serves as an approximate minimum temperature & pCO_2 for surface habitability at a given instellation. This is a conservative choice for addressing the question of the impact of carbon cycle perturbations, as it minimizes initial atmospheric CO_2, maximizing the impact of a given pCO_2 increase. Then, given the initial CO_2, we calculate the pCO_2 increase from the addition of a mass of CO_2 mCO_2:

$$\Delta p\mathrm{CO}_2 = \frac{\mu_{\mathrm{atm}}}{\mu_{\mathrm{CO}_2}} \frac{m_{\mathrm{CO2}} g}{4\pi {R_{\mathrm{earth}}}^2} \quad (2.10)$$

where $\Delta\ pCO_2$ is the change in CO_2 partial pressure, μ_{atm}, which varies with relative proportions of CO_2 and N_2 ($\mu_N 2$=28 g mol^{-1}), is the molar mass for the atmosphere as a whole, μ_{CO_2}=44 g mol^{-1} is the molar mass for CO_2, g=9.81 m s^{-2} is the acceleration due to gravity on Earth (we assume planets are the same size as Earth in this article), and R_{earth}=6.371 $\times 10^6$ m is the radius of the Earth. Finally, to calculate the temperature change ΔT from a perturbation, we simply add the $p\mathrm{CO}_2$ increase to the initial $p\mathrm{CO}_2$ and calculate the new temperature necessary to maintain energy balance at the original instellation (S).

2.2.2 Oceanic carbonate system and pH

To estimate the impact of the calculated changes to $p\mathrm{CO}_2$ and T on seawater pH, we assume the oceanic carbonate system is in equilibrium with atmospheric CO_2 and with calcium carbonate that buffers changes to pH by dissolving or precipitating. The following equations and constants are drawn from (Pierrehumbert, 2010a), but with the concentrations converted from units of [mol mol^{-1}] to units of [mol L^{-1}] through multiplication by a factor of 55.56 mol L^{-1}, the number of moles of liquid water per liter. All constants are set to values appropriate for an ocean depth of 3 km, with salinity approximately equal to 35 grams of salt per kilogram of water. The solubility equilibrium equation for CaCO3's dissociation into Ca^{2+} and $CO_3{}^{2-}$ is:

$$K_{sp} = \left[\mathrm{Ca}^{2+}\right]\left[\mathrm{CO}_3^{2-}\right] \tag{2.11}$$

where $K_{sp} = 7.90 \times 10^{-7}\mathrm{mol}^2\ \mathrm{L}^{-2}$ is $CaCO_3$'s solubility product and each bracketed chemical species represents the concentration of that chemical, written as a molarity. The equilibrium equation for the reaction H_2O + CO_2 (aq) $\leftrightarrow$ H^+(aq) + HCO^{3-} (aq) can be written:

$$K_1(T) = \frac{[\mathrm{H}^+]\left[\mathrm{HCO}_3^-\right]}{[\mathrm{CO}_2]} = K_{1,ref} \times \exp\left(-c_1\left(\frac{1}{T} - \frac{1}{298}\right)\right) \tag{2.12}$$

where $K_1(T)$ is the temperature-dependent equilibrium constant, $K_{1,\mathrm{ref}} = 1.32 \times 10^{-6}$ mol L^{-1} is the value of K_1 at 298 K, and $c_1 = 1218$ K is the temperature dependence of the reaction. The equilibrium equation for the reaction HCO_3 (aq) $\leftrightarrow$ H^+ (aq) + CO_3^{2-} (aq) can be written:

$$K_2(T) = \frac{[\mathrm{H}^+]\left[\mathrm{CO}_3^{2-}\right]}{\left[\mathrm{HCO}_3^-\right]} = K_{2,\mathrm{ref}} \times \exp\left(-c_2\left(\frac{1}{T} - \frac{1}{298}\right)\right) \tag{2.13}$$

where the symbols have the same meanings as before (for their respective reaction), $K_{2,\mathrm{ref}} = 8.95 \times 10^{-10}$ mol L^{-1}, and $c_2 = 2407$ K. Henry's law for CO_2 is written:

$$\mathrm{pCO_2} = k_\mathrm{H}\,[\mathrm{CO_2}] \tag{2.14}$$

where k_H= 29 bar L mol^{-1} is the Henry's law constant for CO_2, which relates its partial pressure to its concentration in water at equilibrium. Lastly, under the simplifying assumption that Ca^{2+} is the only source of alkalinity in the ocean, charge balance can be written:

$$2\left[\mathrm{Ca^{2+}}\right] = \left[\mathrm{HCO_3^-}\right] + 2\left[\mathrm{CO_3^{2-}}\right] + \frac{10^{-14}}{[\mathrm{H^+}]} - \left[\mathrm{H^+}\right] \tag{2.15}$$

where $\frac{10^{-14}}{[\mathrm{H^+}]}$ is equal to $[\mathrm{OH^-}]$. Combined and rearranged, the previous five equations produce a convenient fourth degree polynomial relating $[\mathrm{H^+}]$ to $p\mathrm{CO_2}$ and T:

$$\begin{aligned}2K_{sp}\left[\mathrm{H^+}\right]^4 + \frac{K_1(T)\,K_2(T)}{k_H}p\mathrm{CO_2}\left[H^+\right]^3 \ldots \\ - \left(\frac{K_1(T)^2K_2(T)}{{k_H}^2}p{\mathrm{CO_2}}^2 + \frac{K_1(T)\,K_2(T)}{k_H}10^{-14}p\mathrm{CO_2}\right)\left[H^+\right]\ldots \\ - 2\frac{K_1(T)^2K_2(T)^2}{{k_H}^2}p{\mathrm{CO_2}}^2 = 0\end{aligned} \tag{2.16}$$

which can be solved for $[\mathrm{H^+}]$ (and therefore pH, equal to -$\log_{10}[\mathrm{H^+}]$) numerically using the $p\mathrm{CO_2}$ and T output from the climate model. It is worth noting that we are implicitly assuming a higher mass of CO_2 enters the atmosphere-ocean system than $m_{\mathrm{CO_2}}$ alone by including ocean carbonate chemistry changes in response to atmospheric CO_2 because some carbon must be diverted into the ocean for changes to pH to occur. This effect becomes smaller as the initial $p\mathrm{CO_2}$ inventory increases farther from the star, since increasing CO_2 causes a larger and larger fraction of the total carbon in the atmosphere-ocean system to be partitioned into the atmosphere (Pierrehumbert, 2010a). With preindustrial Earth-like conditions of $p\mathrm{CO_2} = 280 \times 10^{-6}$ bar and $T = 285$ K, the model produces a pH of 8.32, which is reasonably close to Earth's preindustrial pH of 8.25 (Jacobson, 2005).

2.3 Results

In Section 2.3.1, we describe the temperature impact of increases in atmospheric CO_2 of 5000 GtC and 50,000 GtC on planets orbiting G-type stars throughout the HZ. In Section 2.3.2, we describe the change to oceanic pH from the same CO_2 increases.

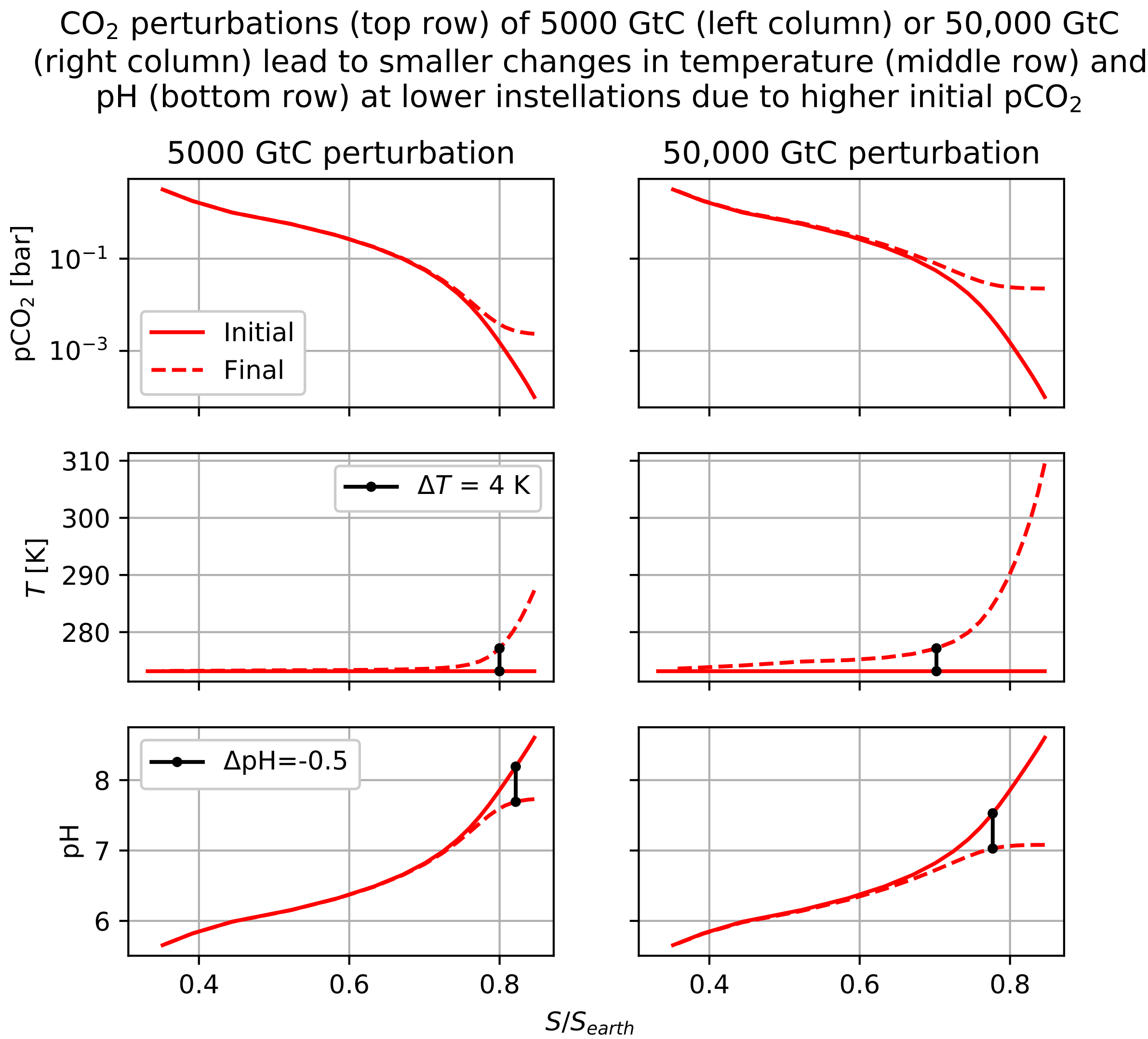

Figure 2.4: **Comparison of temperature-change and pH-change for CO_2 perturbations of 5000 GtC (left column) and 50,000 GtC (right column).** The x-axis in each case is the instellation relative to Earth's, $S_{\text{eff}} = \frac{S}{S_{\text{earth}}}$. The top row shows the pre-perturbation (solid curve) and post-perturbation pCO_2 (dashed curve) for planets that are initialized at $T = 273.15$ K. The middle row shows the temperature change from the CO_2 perturbations, with the solid and dashed curves representing the pre- and post-perturbation temperature values and the black line segment marking the point where the temperature change falls below 4 K. The bottom row shows the oceanic pH change from the CO_2 perturbations, with the solid and dashed curves representing the pre- and post-perturbation pH values and the black line segment marking where the magnitude of acidification falls below 0.5 pH units. GtC, gigatonnes of carbon.

2.3.1 Temperature change from CO_2 perturbations

For both the 5000 GtC perturbation and the 50,000 GtC perturbation, temperature changes go from very large in the inner portion of the HZ to negligibly small in the middle and outer reaches (see middle row of plots in Fig. 4). An initial pCO_2 inventory of 10-4 bar is the lowest used in this study, equivalent to a concentration of 100 parts per million by volume (ppmv) of CO_2 in a 1 bar N2 atmosphere, and this pCO_2 produces an initial T = 273.15 K at $S_{\rm eff}$ = 0.846. In this case the planet experiences a pCO_2 increase of more than an order of magnitude from the 5000 GtC injection, to 2.3×10^{-3} bar (2300 ppmv; see top-left panel of Fig. 2.4). This is accompanied by a temperature increase of 15 K (see mid-left panel of Fig. 4). In the 50,000 GtC case, the final pCO_2=$2.3{\times}10^{-2}$ bar (23,000 ppmv; top-right panel of Fig. 2.4), with a temperature increase of 36 K (mid-right panel of Fig. 2.4). For comparison, on Earth, LIP eruptions have been associated with temperature increases of up to 15 K (Ernst & Youbi, 2017).

At the outermost orbit evaluated in this study, $S_{\rm eff}$ is equal to 0.352 and a pCO_2 of 3.162 bars is necessary to initialize at T=273.15 K. For that configuration, a 5000 GtC injection elevates pCO_2 to 3.166 bars and increases the temperature by 0.04 K, a change approximately 3 orders of magnitude smaller than the change at the innermost orbit. A 50,000 GtC injection causes a temperature increase of 0.4 K and increases pCO_2 to 3.19 bars.

By choosing a semi-arbitrary level of ΔT as the threshold between a "large" and a "small" climate change, it's possible to define orbital boundaries beyond which planets inhabit "stability zones" where they experience small changes in response to CO_2 increases of a given size. Here, we use ΔT = 4 K as the threshold value separating large from small, as 4 K of heating by 2100 is a worst-case scenario for anthropogenic climate change which would lead to widespread environmental disaster (New et al., 2011). For the 5000 GtC CO_2 injection, $\Delta T \leq 4$ K at $S_{\rm eff} \leq 0.80$, where the initial pCO_2 was 1.5 $\times 10^{-3}$ bar. For planets orbiting a star with the Sun's properties where $S_{\rm eff}$ = 1 at an orbital radius of 1 astronomical unit (au), this translates to climate stability against 5000 GtC perturbations beyond an orbital distance of d=$\sqrt(\frac{1}{0.80})$ = 1.12 au (see boundary between the orange and yellow rings in Fig. 2.5). For the 50,000 GtC perturbation, climate stability occurs at $S_{\rm eff} \leq 0.70$ (with an initial pCO_2 of 5.4 $\times 10^{-2}$ bar), translating to an inner orbital distance of d=1.20 au for the 50,000 GtC stability zone (see boundary between yellow and green rings in top panel of Fig. 2.5).

The inner edge of the HZ for rapidly-rotating planets is usually defined as the instellation where climates are forced into either a "moist greenhouse" state (Kasting et al., 1984b) or a "runaway greenhouse" state (Ingersoll, 1969), given some assumptions about a planet's inventory and surface distribution of water. The moist greenhouse state occurs when a planet's stratosphere becomes wet, triggering efficient photodissociation and hydrogen loss that in time depletes a planet of its oceans (Kasting et al., 1984b). This can occur at a variety of instellations depending on background pCO_2 and the atmospheric history of the planet, with values as low as S_{eff}=1.03 to 1.05 recovered in GCM simulations of a rapidly rotating aquaplanet around a Sun-like star (Popp et al., 2016). The runaway greenhouse occurs when a planet's absorbed instellation exceeds the maximum OLR the planet can radiate in the presence of a condensed reservoir of greenhouse gas in vapor equilibrium with the atmosphere e.g. (e.g. Goldblatt & Watson, 2012), leading to uncontrollable warming until the condensable reservoir has evaporated. The runaway greenhouse limit is about $S = 375$ W m^{-2} for the Sun (Leconte et al., 2013b), which translates to S_{eff}=1.1 and d=0.95 au. As the runaway greenhouse is generally thought to occur closer to the star than the moist greenhouse, we will take the runaway limit as the inner edge of the HZ for our calculations. The outer edge of the HZ, where added CO_2 cools the planet below freezing instead of warming it, is at approximately d=1.67 au in our solar system (Kopparapu et al., 2013).

With the above choices of inner and outer HZ boundaries, the innermost ring of the HZ where planets are susceptible to both 5000 GtC and 50,000 GtC perturbations has a radial width of 0.17 au, whereas planets are safe from 5000 GtC perturbations over a 0.55 au range of radii, and planets are safe from both 5000 and 50,000 GtC perturbations across 0.47 au. An alternative visualization of the climate stability is provided in the bottom panels of Fig. 2.5, which show the temperature responses to the 5000 GtC (bottom-left panel) and 50,000 GtC (bottom-right panel) perturbations as functions of orbital radius. In the 5000 GtC case, the temperature response is less than 1 K throughout most of the HZ, while for the 50,000 GtC perturbation the response is still modest but stays above 1 K until near the outer edge of the HZ. So, throughout most of the classical HZ, temperate planets where CO_2 and H_2O are the dominant greenhouse gases will lie in stability zones where global surface temperature should only be mildly affected by transient carbon cycle perturbations of similar size to those that have repeatedly caused large, catastrophic swings in Earth's surface temperature during the Phanerozoic Eon, and potentially the Neoproterozoic. It is worth noting that if we had assumed a higher initial temperature and a correspondingly higher initial $p\mathrm{CO_2}$ at each luminosity, then the inner boundaries for the stable zones would be even closer to the star, so the choice of initializing at T=273.15 K is conservative. In any case, this calculation is meant to be illustrative; the same qualitative pattern emerges regardless of the choice of T, as long as CO_2 is assumed to be the dominant greenhouse gas offsetting the reduction in solar luminosity with orbital distance.

2.3.2 pH change from CO_2 perturbations

Similar to the temperature perturbation results, the change in pH from 5000 and 50,000 GtC atmospheric CO_2 mass injections is large only in the inner region of the HZ (see bottom row in Fig. 4). Initial pH is smaller at lower Seff because of higher initial $p\mathrm{CO_2}$ values. As S_{eff} decreases, so does the reduction in pH from a given CO_2 increase, going from a change of nearly 2 pH units (e.g. a 2 order-of-magnitude increase in $[H^+]$) under the 50,000 GtC increase at the innermost orbit to a change of less than one hundredth of a pH unit at the outermost orbit evaluated.

Stability zones for pH can be defined in the same way we defined them for temperature. In this case, we will use -0.5 pH units as the threshold between a "large" and "small" pH change, since that is the estimated level of oceanic pH reduction below the pre-industrial value in the year 2100 for a worst-case scenario of climate change, and represents a level of change that would pose a danger to many extant marine animal taxa (Wittmann & Pörtner, 2013). With that choice of threshold, under a 5000 GtC perturbation, the boundary between safety and vulnerability is at S_{eff} = 0.82, e.g. 1.10 au from the star when orbiting a host identical to our Sun, with an initial $p\mathrm{CO_2}$=4.6 $\times$ 10^{-4} bar (see black line segment in the bottom-left panel of Fig. 2.4). At 50,000 GtC, the boundary moves out to S_{eff}=0.78, or 1.13 au, with an initial $p\mathrm{CO_2}$=4.5 $\times 10^{-3}$ bar (black line segment in the bottom-right panel of Fig. 2.4). The pH stability zones for 5000 GtC and 50,000 GtC both lie closer to the star than their temperature-stability analogues, so in the rest of the article, "stability zone" will refer to the more conservative temperature-based zones.

2.4 Discussion

2.4.1 Mechanisms of catastrophe & mass extinction

Hyperthermals and potentially one or more of the snowball events in Earth's past were caused by transient carbon cycle perturbations, and these events strongly influenced the particular evolutionary path taken by the biosphere. Significant warming and/or ocean acidification, often as a result of the eruption of LIPs, is associated with most or all of the major mass extinctions in the Phanerozoic (Bond & Grasby, 2017; Lindström et al., 2017; Benton, 2018; Racki et al., 2018; Schoene et al., 2019; Bond & Grasby, 2020). The stability of global-mean surface temperature and ocean pH against transient carbon cycle perturbations on planets in the mid-to-outer reaches of the HZ suggests that such catastrophic climate events and mass extinctions may happen much less frequently for this class of Earth-like planet than they have on Earth. However, mass extinctions and climate perturbations can be caused by mechanisms other than temperature- and pH-change from CO_2 perturbations. It is worth examining the mechanisms underlying the catastrophes in Earth's past for context to understand the implications of the results in this paper.

A relevant category of catastrophic environmental processes is the set that can or must be triggered by an initial pulse of warming. Processes of this type have been important in past mass extinction events, and the resistance to CO_2-based temperature change on mid-outer HZ planets should make them less likely. Ocean anoxia is one such process. Ocean anoxia can be caused by increased continental weathering—a result of elevated temperature and/or $p\mathrm{CO}_2$—which washes nutrients into the oceans and causes eutrophication, leading to elevated oxygen consumption that depletes surrounding waters (Bond & Grasby, 2017). High surface temperatures can also directly cause anoxic events by productivity stimulation (Bond & Grasby, 2017) and enhanced ocean stratification (which reduces ocean ventilation) (Erbacher et al., 2001). However, productivity stimulation from the direct injection of nutrients into the ocean by seafloor LIP eruptions can also cause anoxia (Ernst & Youbi, 2017), so a lack of CO_2-based warming does not necessarily preclude anoxic conditions from occurring. Similarly, thermogenic methane release and consequent rapid warming can be caused by an initial pulse of CO_2 warming, but it can also be caused by the intrusion of LIP magmas into organic-rich sediments and coal beds (Bond & Grasby, 2017). A final example of this type is the depletion of the ozone layer, which leads to elevated surface ultraviolet fluxes and is suggested to have contributed to several mass extinctions via UV's ability to induce harmful elevated mutation rates (Beerling et al., 2007; Bond & Grasby, 2017; Marshall et al., 2020). Marshall et al. (2020) suggest that rapid warming may induce ozone loss via enhanced convective transport of ClO into the stratosphere, but other mechanisms have also been proposed to destroy the ozone layer, such as supernova-accelerated cosmic ray bombardment (Fields et al., 2020), organohalogen release by LIP volcanism (Beerling et al., 2007; Broadley et al., 2018), or proton bombardment from flaring by an active M-dwarf star (Segura et al., 2010; Tilley et al., 2019).

Along with increased resilience to hyperthermal-related disasters, these results suggest that planets in the mid-to-outer reaches of the HZ have reduced susceptibility to global glaciation from transient increases in weathering. Changes to lithology, continent location, mountain-building, and many other processes can all cause weathering to accelerate or decline (e.g. (e.g. Kump et al., 2000; Penman et al., 2020)), and workers have suggested that several partial (Macdonald et al., 2019) and global (Goddéris et al., 2003; Donnadieu et al., 2004; Cox et al., 2016) glaciations happened as a result of weathering acceleration. Just like CO_2 injection leads to smaller temperature increases under high background pCO_2, CO_2 sequestration leads to smaller temperature reductions under the same conditions, meaning this route to glaciation may be much less likely for high pCO_2 planets. Still, if excess weathering can be maintained on long enough timescales, "limit cycling" (the alternation between a warm climate state and a snowball climate state due to lack of stable weathering equilibrium (Mills et al., 2011; Kadoya & Tajika, 2014; Menou, 2015; Abbot, 2016; Haqq-Misra et al., 2016)) remains a possibility for these planets, since the CO_2 drawdown events from which mid-outer HZ planets are safe are transient pulses, not the quasi-permanent shifts to new carbon cycle equilibria required for limit cycle initiation. In addition, other non-weathering-related mechanisms like a rapid reduction in the level of a non-CO_2 greenhouse gas like methane (Kopp et al., 2005) or a rapid increase in albedo due to stratospheric aerosol injection (Macdonald & Wordsworth, 2017) have also been proposed to trigger glaciation (Arnscheidt & Rothman, 2020). However, the high Rayleigh scattering albedo (see Fig. 2.2) and consequent reduced sensitivity of planetary albedo to surface albedo in high-pCO_2 atmospheres means the ice-albedo feedback is less effective on these planets, since the growth of sea ice has less effect on the radiative balance of the planet under high pCO_2 (Pierrehumbert, 2010a; Von Paris et al., 2013). A set of calculations (not shown) that included a temperature-dependent surface albedo feedback using the formula in Wang & Stone (1980) yielded qualitatively identical behavior to the constant-surface-albedo calculations presented in this paper for both CO_2 increases and CO_2 decreases, confirming the basic result that climate stability increases with decreasing instellation.

There are also a variety of catastrophe-inducing mechanisms that are not triggered by carbon cycle perturbations or their downstream effects. The frequencies of these events should not be affected by the presence of high background $p\mathrm{CO}_2$. For example, extraterrestrial disaster sources like nearby supernovae (which may have a variety of negative impacts on atmospheric chemistry (e.g. Reid et al., 1978)), large asteroid/comet impacts (Alvarez et al., 1980; Hull et al., 2020), and stellar superflares (Lingam & Loeb, 2017) likely do not discriminate by background $p\mathrm{CO}_2$ levels. Similarly, global heavy metal poisoning by LIP volcanism (Lindström et al., 2019) should remain a possible killing mechanism regardless of background $p\mathrm{CO}_2$, though it is an interesting question whether this process alone could trigger a mass extinction without the additional environmental stressors from an accompanying hyperthermal episode. A variety of catastrophe triggers remain in play for mid-outer HZ planets despite the results of this study, but the main mass extinction mechanisms that have operated in Earth's past may be suppressed on these planets.

A corollary to the reasoning that planets at lower luminosity than the Earth are more stable to CO_2 perturbation-induced extinctions is that planets in the HZ receiving more instellation than Earth will be more susceptible to these perturbations because of their lower initial $p\mathrm{CO}_2$ (although it is worth noting that Earth's position near the inner edge of the HZ means that there is not much space for temperate planets to reside at higher instellations). This point is noted in a blog post by Alex Tolley, who suggests that the increased volatility might be a serious enough barrier to habitability to justify revising the inner edge of the HZ outward to a slightly greater distance from the star (Tolley, 2018). The same basic idea is elaborated by (Archer, 2016), who shows that anthropogenic climate change would be progressing even more rapidly if Earth had possessed a lower initial $p\mathrm{CO}_2$ when industrialization began and less rapidly if the initial $p\mathrm{CO}_2$ had been higher.

In line with the logic of Archer (2016) and analogous to the reasoning presented in the discussion of previous mass extinctions on Earth, the results in this paper also show that civilizations arising throughout a large proportion of the HZ would be placed in no danger of self-induced climate change by burning fossil fuels. Since 5000 GtC is an approximate upper-bound on the accessible fossil fuel inventory on Earth (Ramirez et al., 2014), civilizations arising anywhere beyond the inner boundary of the 5000 GtC stability zone will not face the degree of CO_2-based danger we face.

Civilizational die-off from industrialization and pollution (Frank et al., 2018) may be less of a danger on other worlds than it appears when extrapolating from Earth.

2.4.2 Does high pCO_2 preclude complex life?

A few studies have argued that high levels of atmospheric CO_2 may prevent the evolution of complex life on planets in the mid-outer reaches of the HZ (Bounama et al., 2007; Schwieterman et al., 2019; Ramirez, 2020b). With the assumption of some threshold CO_2 beyond which complex life is not able to evolve, this idea can be used to define a "habitable zone for complex life" (HZCL), where temperatures can be maintained above freezing under the proposed CO_2 constraint. These arguments are based on observed responses of some forms of multicellular Earth-life, usually mammals, to high CO_2, low pH, and/or high CO (which can build up to high levels in high-CO_2 atmospheres of planets orbiting cool M or K stars (Schwieterman et al., 2019)). It is important to note that the idea that CO might limit complex life is falsified by the fact that some extant invertebrates are invulnerable to CO's toxic effects because of their use of blood oxygen transport mechanisms that do not interact with CO (Howell, 2019). Similarly, it is plausible that the pH- and pCO_2-sensitivity of the organisms that have been studied are not results of fundamental constraints on complex life, but are instead results of the specific chemical machinery employed by particular Earth lineages, a point which is acknowledged in the studies that explore the HZCL idea (Schwieterman et al., 2019; Ramirez, 2020b).

Still, if complex life is limited by high pCO_2, this has interesting implications for the results in this study. Using the most conservative value for maximum pCO_2 that appears in (Bounama et al., 2007; Schwieterman et al., 2019; Ramirez, 2020b), 0.01 bar, produces an outer edge for the HZCL of S_{eff}=0.76 with the climate model used in this paper, implying an outer radius of $d = 1.15$ au. This means there is no overlap between this conservative choice of HZCL and the 50,000 GtC stability zone defined in this paper (see Section 2.3.1), and only a narrow ring of overlap with the 5000 GtC stability zone (1.15-1.12 = 0.03 au). So, if the tolerance of complex life for CO_2 is low, this would suggest that much of the complex life in the universe could face carbon cycle volatility comparable to what the Earth experienced during the Phanerozoic Eon, conditional on significant similarities to Earth in terms of tectonics, mantle processes, and surface processes.

Alternatively, if we take the value for the outer edge of the HZCL to be at the luminosity where pCO_2=0.1 bar and T=273.15 K, perhaps based on the argument from lipid solubility theory in Ramirez (2020b), the model used in this paper produces

S_{eff}=0.67 and $d = 1.22$ au. With a 1D latitudinally-dependent energy balance climate model, Ramirez (2020b) reports a slightly more distant boundary of $d = 1.27$ au with 1 bar background N_2. Our preference is for the latter value, since it comes from a more sophisticated model, in which case the HZCL encompasses the entire 5000 GtC stability zone, as well as a small ring with a width of 0.07 au in the interior portion for the 50,000 GtC stability zone. Higher choices of the toxic $p\text{CO}_2$ level lead to greater overlap with the 50,000 GtC stability zone. So, under the less conservative choices for maximum $p\text{CO}_2$, there is an optimal zone that allows for CO_2 levels that are high enough to reduce climate sensitivity to carbon cycle perturbations while being small enough to allow complex life to flourish. Planets in this zone might be considered "superhabitable" (Heller & Armstrong, 2014).

2.4.3 Implications for the distribution of biosignatures?

As mentioned in the introduction, the largest known extinction in Earth's history is the Permian-Triassic event, a crisis apparently triggered by the eruption of a LIP, which eliminated up to 96% of marine species (and a significant but potentially smaller fraction of species on land) (Bond & Wignall, 2014; Benton, 2018). Several other mass extinctions that eliminated most of the species on Earth at the time also coincided with LIP eruptions (Kidder & Worsley, 2010; Bond & Grasby, 2017). The severity and frequency of these mass extinctions in Earth history raises the question of whether they present a danger to the persistence of complex biospheres over geologic timescales – it is conceivable that the Permian-Triassic extinction might have wiped out 100% of macroscopic species had the event been somewhat more severe.

If large, productive oxygenic biospheres are difficult to maintain for long periods because of extinction events, planets with detectable O_2/O_3 biosignatures may be few and far between, and thus difficult to find with near-future telescope surveys (see (e.g. Kawashima & Rugheimer, 2019; Checlair et al., 2020) for discussions of next-generation O_2/O_3 biosignature detection). In a work addressing the question of the persistence of Earth-like biospheres in the face of extinction events, Tsumura (2020) models Earth's extinction history as a random multiplicative process, and his methodology leads him to conclude that the probability of life's survival on Earth from the time of its origin to the present day is only 15% (since it is likely extremely difficult to extinguish prokaryotic life, this result should appropriately be considered to apply only to complex, multicellular life, not life as a whole). Tsumura (2020) suggests that this value can be used in models attempting to estimate the prevalence of intelligent life in the universe.

The results in this article demonstrate that the calculations in Tsumura (2020) cannot be applied to infer the rate of complex life sterilization on Earth-like planets in general, even if they do accurately represent Earth itself. This is because the mechanisms that produced Earth's particular extinction history are strongly dependent on background atmospheric state, which is expected to systematically vary. In particular, the increased resilience to carbon cycle perturbations of planets in the mid-outer HZ implies that these planets will be much less susceptible to the primary form of mass extinction that has operated on Earth, suggesting a higher long-term survival fraction for complex biospheres that occupy the stability zones outlined in Section 2.3.

Overall, this discussion implies that O_2/O_3 biosignatures may be more common in the middle-outer reaches of the HZ compared to the innermost region due to reduced likelihood of extinction because of greater environmental stability under high-$p$$CO_2$ atmospheres. For planets orbiting F-, G- and early-K-type stars that display significant brightening on gigayear timescales, this might suggest an anti-correlation between stellar age and biosignature prevalence because the increase in luminosity pushes the location of stability zones farther and farther away from the star over time, moving a larger and larger fraction of planets into the less-stable, more-extinction-prone interior region of the HZ. This prediction is directly opposite that of Bixel & Apai (2020), who note that the appearance of detectable O_2/O_3 biosignatures on Earth occurred one to two billion years after the origin of life, suggesting that planets orbiting older stars may be better candidates for biosignature searches.

An identical point regarding safety from catastrophic sterilization can be made about the distribution of technosignatures (biosignatures that imply the presence of technological civilizations e.g.(e.g. Lin et al., 2014)). As noted in Section 2.4.1, analogues of anthropogenic climate change will be much less severe on planets in the stability zones defined in this paper, which suggests that civilizations on these planets may experience less stress from industrialization than those at higher instellations, perhaps allowing them to persist longer and increasing the likelihood of observable technosignatures in the stability zones.

Another wrinkle in this discussion is the possibility that non-sterilizing mass extinctions and climatic perturbations facilitate the emergence of novelty in the biosphere by freeing up or creating niches and restructuring ecosystems, perhaps allowing for greater complexity/biodiversity to be attained post-recovery (e.g. Wagner et al., 2006). An extreme example of this is the suggestion that the Neoproterozoic snowball Earth episodes triggered the emergence of animal multicellularity (Simpson, 2019, 2021). If climate perturbations do have a long-term positive effect on global biodiversity and novelty, then it is possible that planets in the stability zones will be less likely to have detectable biosignatures, depending on whether this effect is more important than the possibility of sterilization of complex life. However, the ecological and biogeochemical dynamics of post-catastrophe recovery are complex and poorly understood (Solé et al., 2002; Hull, 2015), and the paleontological data on the long-term impact of non-sterilizing catastrophes on global biodiversity is open to various interpretations (Michael Foote, personal communication).

So, biosignatures may be more likely in the high pCO_2 stability zones. This selection criterion can be used in conjunction with others, e.g. the HZCL (Schwieterman et al., 2019; Ramirez, 2020b), to rank and prioritize targets in the HZ for next-generation telescopes to probe in search of life. If decreased likelihood of catastrophe leads to a greater likelihood of detectable biosignatures, a large enough sample of O_2/O_3 detections might reveal a trend with a higher-than-expected fraction of biosignature detections at low instellations within the HZ.

2.4.4 Implications for Earth history?

Although there is still considerable debate about Earth's CO_2 levels throughout the past 4 Ga (e.g. Charnay et al., 2020), recent proxy constraints suggest that CO_2 partial pressure may have been approximately $1000\times$ its present value (perhaps 0.1-0.5 bar) in the late Archean (Lehmer et al., 2020a; Payne et al., 2020), with a gradual decline over the Proterozoic Eon driven by the response of weathering to a brightening Sun (Kanzaki & Murakami, 2015; Krissansen-Totton et al., 2018; Krissansen-Totton & Catling, 2020). The role of other greenhouse gases during the Precambrian is unclear, but there is some evidence for strongly elevated methane levels during the Archean, which may also have accounted for some of the warming needed to offset the climate impacts of the dimmer young Sun (Catling & Zahnle, 2020). Probabilistic models of ocean pH through geologic time that account for the wide uncertainties in relevant proxy data produce a corresponding history with pH increasing from an initial slightly acidic-to-neutral range of 6.5-7 in the Archean to a slightly basic range of 7.5 to 9 during the Phanerozoic (Halevy & Bachan, 2017; Krissansen-Totton et al., 2018; Krissansen-Totton & Catling, 2020).

High values of pCO_2 and low values of ocean pH in Earth's past would suggest that the planet may have exhibited the stability to CO_2 perturbations described in this paper during the Archean and part of the Proterozoic. Much of the Precambrian seems to have displayed notable climatic stability and warmth, particularly after the major period of global glaciation leading from the Archean into the Proterozoic, which may have marked the transition from an oxygen-poor atmosphere with strong greenhouse warming from both CO_2 and CH_4 to an oxidized atmosphere with limited CH_4 warming (Daines & Lenton, 2016; Olson et al., 2016; Catling & Zahnle, 2020). With $p$$CO_2$ held at high levels (perhaps 0.01-0.1 bar) by the silicate weathering feedback (Krissansen-Totton et al., 2018) and, potentially, CO_2-generating authigenic clay formation ("reverse weathering") (Isson & Planavsky, 2018; Krissansen-Totton & Catling, 2020), the mid-Proterozoic atmosphere would have been quite stable to transient CO_2 release and/or consumption from the many LIPs recorded during this period (Ernst & Youbi, 2017). This may partially explain the apparent lack of transient climate extremes during the "Boring Billion" period (Buick et al., 1995) between approximately 1.7 to 0.75 Ga, though underlying geologic causes are still necessary to explain the long-lasting warm, steady background climate (Cawood & Hawkesworth, 2014). The stability to CO_2 perturbations would have decreased over time as increasing solar luminosity caused CO_2 to be drawn down, which may have been a necessary precondition that allowed for transient enhanced weathering events to trigger one or both of the Neoproterozoic snowball episodes (Goddéris et al., 2003; Donnadieu et al., 2004). Even in the Phanerozoic, the issue of background $p$$CO_2$ and its influence on the sensitivity of climate to a given increase/decrease in CO_2 plays an important role in the debate over the interpretation of the evidence for events like the Paleocene-Eocene Thermal Maximum (Pagani et al., 2006; Higgins & Schrag, 2006).

The remaining lifespan of the complex biosphere is estimated to be $\sim$1 Ga based on the modeled timing of the drawdown of atmospheric CO_2 to a level below the lower limits of tolerance for C4 plants as the Sun continues to brighten (Caldeira & Kasting, 1992). However, a severe LIP eruption could conceivably end complex life much earlier, similar to the suggestion that a LIP eruption ended habitable conditions on Venus (Ernst et al., 2017; Way & Del Genio, 2020). The low CO_2 conditions of Earth's future should make environmental conditions even more sensitive to CO_2 perturbations than they were during past LIPs. However, the evolution of pelagic calcifiers over the past 200 million years may have strongly increased environmental resilience to CO_2 perturbations (Henehan et al., 2016), suggesting a potential counter to the effects of reduced CO_2. A biogeochemical model that includes the effects of pelagic calcifiers on ocean chemistry could be used to examine the impact of future LIP eruptions under low $p$$CO_2$, high insolation conditions.

2.5 Summary and Conclusions

In this article, we used idealized climate and ocean chemistry models to demonstrate that high pCO_2 atmospheres on planets in the middle and outer regions of the HZ confer robust temperature- and pH-stability in the face of CO_2 perturbations that would cause severe environmental change in the low-pCO_2 context of Phanerozoic Earth. Both temperature- and pH-stability arise because of the rapid growth in pCO_2 necessary to maintain a temperate climate as instellation decreases with distance from the host star on planets with N_2-CO_2-H_2O atmospheres in the HZ. The pCO_2 necessary for above-freezing temperatures at the outer edge of the HZ can be more than a million times greater than that required near the inner edge, assuming constant pN_2, so CO_2's logarithmic radiative forcing response means that a given mass of CO_2 added to or subtracted from the atmosphere of a temperate planet near the inner edge has a vastly larger effect on surface temperature than the same change in atmospheric CO_2 mass near the outer edge. Similarly, as pCO_2 increases, there is a reduction in the fraction of CO_2 that partitions into the ocean as dissolved inorganic carbon for a given mass of carbon injected into the atmosphere-ocean system, meaning the marginal impact of a given CO_2 change on ocean pH decreases as background levels go up.

The CO_2 perturbations imposed in the experiments in this study are equivalent to 5000 GtC and 50,000 GtC added to the atmosphere, which are, respectively, an estimate of the amount of carbon that would be released if all accessible fossil fuels were burnt (Ramirez et al., 2014) and a high estimate of the amount of carbon released due to LIP volcanism during the most severe mass extinction in Earth history (Kump, 2018). The temperature response to the 5000 GtC perturbation falls below 4 K at S_{eff} =0.8, where the initial pCO_2=1.5 $\times 10^{-3}$ bar, corresponding to an orbital distance of d = 1.12 au in the Solar System. The temperature response to the 50,000 GtC perturbation reaches the same 4 K threshold at Seff=0.7 and pCO_2=5.4$\times 10^{-2}$ bar, corresponding to d=1.2 au. Those values of d can serve as inner boundaries for "stability zones" where N_2-CO_2-H_2O atmospheres are relatively invulnerable to temperature effects of CO_2 changes at or below a given magnitude (see Fig. 2.5). Analogously, the magnitude of pH reduction falls below 0.5 units at S_{eff} = 0.82 (d =1.1 au) and S_{eff}=0.78 (d=1.13 au) for 5000 GtC and 50,000 GtC perturbations respectively.

These results suggest that many Earth-like planets throughout the mid-to-outer habitable zone may be safe from extreme environmental change from transient CO_2

perturbations of sizes that have caused catastrophes in Earth's past, particularly planets in the 50,000 GtC stability zone (Figs. 2.4 and 2.5). Similarly, climate change and ocean acidification from CO_2 emitted by the burning of fossil fuels may be a less serious issue for civilizations on planets receiving less instellation than Earth (see 5000 GtC stability zone in Fig. 2.5). This represents a significant habitability advantage for temperate planets in the mid-to-outer reaches of the HZ compared to those near the inner edge. The large climate swings that have punctuated the Phanerozoic Eon are in part a result of Earth's low $p\mathrm{CO}_2$ and relative proximity to the inner edge of the habitable zone during this period.

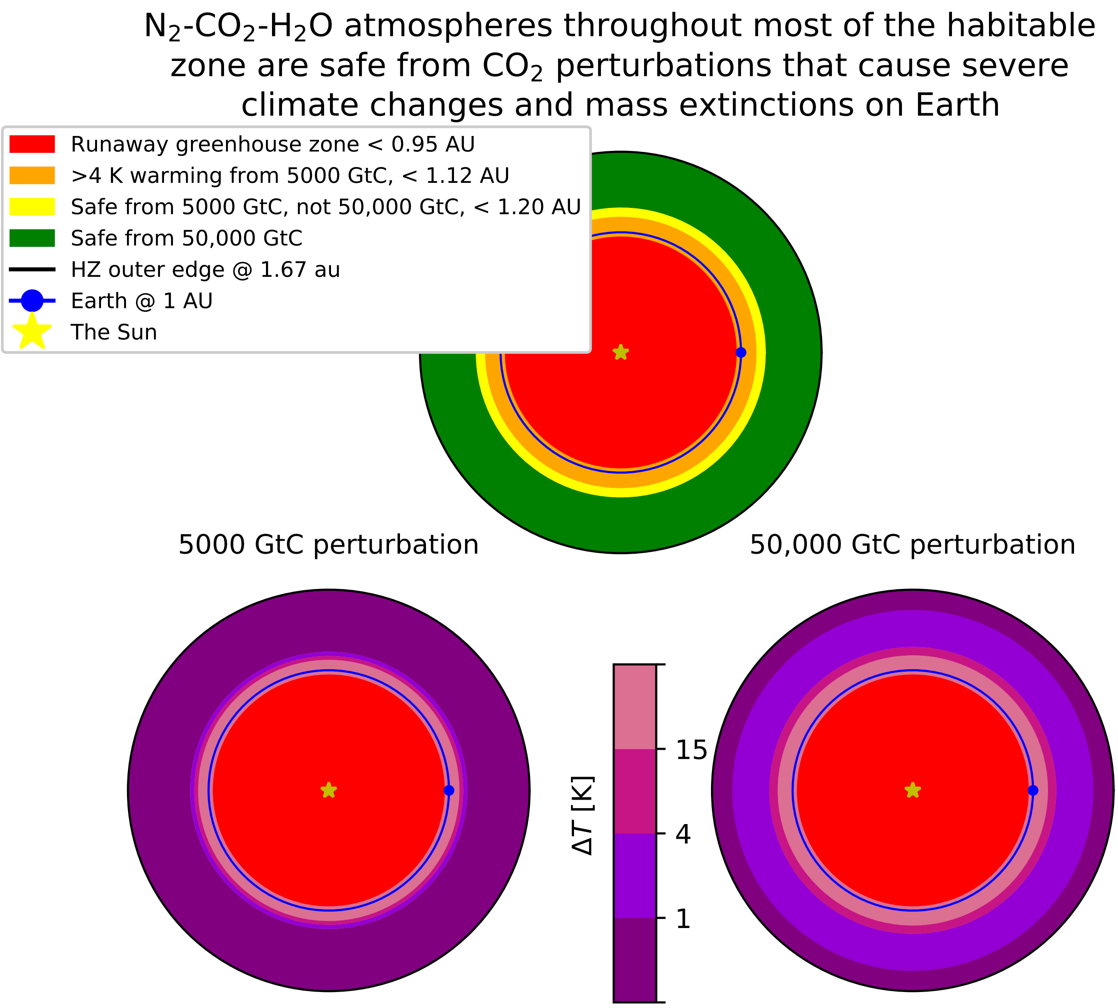

Figure 2.5: **Illustrations of climate stability as a function of orbital radius within the HZ in a solar system with a star identical to the Sun.** The yellow stars represent G-type stars. The red zone in each panel is the region where Earth-like planets are likely to be in the uninhabitable runaway greenhouse state, extending to 0.95 au. The blue dots and rings each represent the Earth's 1 au orbit. In the top panel, the orange zone is within the HZ but outside of either stability zone, meaning that Earth-like planets in this region would warm by more than 4 K under a 5000 GtC CO_2 perturbation, based on the temperature response of simulations initialized at T = 273.15 K. The orange zone extends from the inner edge of the HZ at 0.95 to 1.12 au. In the yellow zone, planets experience <4 K of warming from a 5000 GtC perturbation but more than 4 K of warming from a 50,000 GtC perturbation, and it extends from 1.12 to 1.20 au. In the green zone, planets would experience <4 K of warming from either a 5000 GtC perturbation or a 50,000 GtC perturbation, extending from 1.20 to 1.67 au. The black region is beyond the outer edge of the HZ, beginning at 1.67 au. The bottom panels show the temperature change as a function of orbital radius for the 5000 GtC perturbation (left) and the 50,000 GtC perturbation (right).

Chapter 3

Thermodynamic and energetic limits on continental silicate weathering strongly impact the climate and habitability of wet, rocky worlds

I am awed by how things weather: an oak mantel
in the house in Spain, fingered to a sheen,
the marks of hands leaned into the lintel,
the tokens in the drawer I sometimes touch –
a crystal lived-in on a trip, the watch
my father's wrist wore to a thin gold sandwich.
It is an equilibrium
which breasts the cresting seasons but still stays
calm
and keeps warm. It deserves a good name.
Weathering. Patina, gloss and whorl.
The trunk of the almond tree, gnarled but still
fruitful.
Weathering is what I would like to do well.

Excerpt from *Weathering*
Alastair Reid

Abstract

Note: This chapter was published as Graham & Pierrehumbert (2020). The "liquid water habitable zone" (HZ) concept is predicated on the ability of the silicate weathering feedback to stabilize climate across a wide range of instellations. However, representations of silicate weathering used in current estimates of the effective outer edge of the HZ do not account for the thermodynamic limit on concentration of weathering products in runoff set by clay precipitation, nor for the energetic limit on precipitation set by planetary instellation. We find that when the thermodynamic limit is included in an idealized coupled climate/weathering model, steady-state planetary climate loses sensitivity to silicate dissolution kinetics, becoming sensitive to temperature primarily through the effect of temperature on runoff and to pCO_2 through an effect on solute concentration mediated by pH. This increases sensitivity to land fraction, CO_2 outgassing, and geological factors such as soil age and lithology, all of which are found to have a profound effect on the position of the effective outer edge of the HZ. The interplay between runoff sensitivity and the energetic limit on precipitation leads to novel warm states in the outer reaches of the HZ, owing to the decoupling of temperature and precipitation. We discuss strategies for detecting the signature of silicate weathering feedback through exoplanet observations in light of insights derived from the revised picture of weathering.

3.1 Introduction

The classical "liquid water habitable zone" (HZ) is the orbital region around stars where rocky planets with N_2-H_2O-CO_2 atmospheres can potentially support stable liquid water on their surfaces (Huang, 1959; Hart, 1979; Kasting et al., 1993; Kopparapu et al., 2013; Ramirez, 2018). The inner edge of the HZ is the instellation at which a planet's oceans are likely to undergo rapid escape to space, either due to enhanced loss of water from a warm, wet stratosphere (the "moist greenhouse state") or due to full ocean evaporation and subsequent escape (the "runaway greenhouse state") (e.g. Kasting, 1988b; Kasting et al., 1993; Kopparapu et al., 2013). The outer edge of the HZ is the instellation at which a planet cannot maintain a temperature above the freezing point of water anywhere on its surface with an atmosphere of N_2, H_2O, and CO_2 alone (e.g. Kadoya & Tajika, 2019). Depending on conditions like the spectrum of the host star, the outer edge may be defined by the "maximum greenhouse limit", where an increase to the CO_2 partial pressure on a hypothetical planet would increase the Rayleigh scattering albedo enough to outweigh the greenhouse effect and cause the planet to freeze, or it may be defined by the "CO_2 condensation limit", where CO_2 can no longer accumulate to higher levels in the atmosphere because it is forced to condense or deposit at the planet's surface (e.g. Kasting et al., 1993; Kopparapu, 2013b).

The HZ concept as currently understood relies on the existence of a negative feedback mechanism on ocean-bearing rocky planets to control the concentration of atmospheric CO_2 and maintain surface liquid water at a variety of instellations. Without some kind of long-term negative feedback on climate, the question of whether a given planet's atmospheric CO_2 level is consistent with the presence of surface liquid H_2O at that planet's particular instellation is largely a matter of luck, and the lifetime of habitability for those planets lucky enough to start off temperate will be relatively short, due to the gradual brightening of stars. Walker et al. (1981) (WHAK) suggested that temperature-, runoff-, and pCO_2-dependent weathering of silicate minerals (a process which produces cations that react with oceanic carbonate ions to form carbonate minerals that are sequestered in Earth's crust and subsequently recycled through the mantle) has served the role of stabilizing feedback on Earth, drawing down CO_2 as the sun has brightened from $\sim$70% of its current luminosity over the past 4 billion years (Ga) (Sagan & Mullen, 1972; Bahcall et al., 2001). Kasting et al. (1988) hypothesized that this silicate weathering feedback also operates on rocky ocean- and land-bearing exoplanets, and this idea underpins much subsequent work regarding the HZ (though see e.g. Pierrehumbert & Gaidos (2011); Kite & Ford (2018); Ramirez & Levi (2018) for non-standard habitability scenarios that do not involve the silicate weathering feedback). Recently, studies modeling planetary weathering behavior have suggested that enhanced weathering due to high pCO_2 in the outer reaches of the habitable zone may act to draw CO_2 down to levels that force a planet into the snowball state at instellations greater than the "maximum greenhouse limit" or "CO_2 condensation limit", effectively decreasing the width of the HZ, but the magnitude (and even the existence) of this effect is strongly dependent on the details of the silicate weathering feedback (Menou, 2015; Haqq-Misra et al., 2016; Abbot, 2016; Kadoya & Tajika, 2019). Accurately representing silicate weathering in models is therefore necessary for predicting the extent of the HZ and the behavior of planets within it. These issues will become increasingly crucial as observation and analysis of temperate rocky planets and their atmospheres by future telescopes becomes commonplace. Here, we focus on continental weathering, though a full evaluation of habitability would, among other things, require a treatment of seafloor weathering as well (see Section 3.5.1 for discussion of this issue).

In this study, we use a simple 0-dimensional climate model and the weathering framework developed in Maher & Chamberlain (2014) (MAC) to re-examine planetary weathering behavior and the outer edge of the habitable zone. The MAC model of weathering is the first to include a thermodynamic limit on cation concentration in runoff due to equilibration between dissolving silicates and precipitating clays. We also include an energetic limit on precipitation and runoff that accounts for the fact that evaporation (and therefore precipitation) is ultimately driven by instellation, which implies the existence of a maximum precipitation rate for a planet, defined as the rate at which all incoming stellar radiation must be used for latent heat of evaporation (Pierrehumbert, 2002; O'Gorman & Schneider, 2008). We find that including these limits in global weathering models strongly impacts the climate and weathering behavior of wet, rocky exoplanets in the HZ. In particular, including the thermodynamic limit on solute concentration increases the importance of hydrology and surface properties like land fraction and soil age for global weathering fluxes, alternately expanding or contracting the effective width of the habitable zone depending on choice of parameters. With the energetic limit on precipitation, global precipitation ceases to be a function of temperature under some circumstances, leading to fundamental changes in the functioning of the silicate weathering feedback.

In the remainder of this paper, we will more thoroughly introduce the silicate weathering feedback, along with its thermodynamic and energetic limits, which have not been included in previous studies of exoplanet habitability (Section 3.2); describe the simple models we used to examine the impact of these limits on the behavior of planets within the HZ (Section 3.3); present the results of our calculations (Section 3.4); and discuss implications of these results (Section 3.5).

3.2 The Continental Silicate Weathering Feedback

The continental silicate weathering feedback is a mechanism proposed by WHAK to explain how Earth has maintained a relatively stable, temperate climate over geologic time despite volcanic outgassing of CO_2 and the long-term brightening of the Sun. In Earth's carbonate-silicate cycle (e.g. Siever, 1968; Walker et al., 1981), volcanic CO_2 is released into the atmosphere/ocean system by the metamorphism of carbonate minerals in the planet's interior. The CO_2 acts as an acid in aqueous silicate weathering reactions that speed up the release of Ca^{2+} and Mg^{2+} cations which are then carried by rivers to the oceans, where they react with carbonate ions and precipitate as carbonate minerals. These minerals sink to the ocean floor, where they are subducted into the Earth, completing the cycle. This complex process can be represented schematically as:

$$\mathrm{CaSiO_3} + \mathrm{CO_2} \leftrightarrow \mathrm{CaCO_3} + \mathrm{SiO_2} \tag{3.1}$$

where the rightward direction represents a silicate mineral reacting with (and consuming) a CO_2 molecule to form a carbonate mineral and silica (SiO_2), and the leftward direction represents an overall reaction where a carbonate mineral is metamorphosed with silica in Earth's mantle to form a silicate and CO_2. In actuality, a variety of silicate minerals can take the place of $CaSiO_3$ in the above equation, and secondary minerals, e.g. clays, precipitate in regions being weathered and play vital roles in controlling the rates of the weathering reactions (Alekseyev et al., 1997; Maher et al., 2009; Maher & Chamberlain, 2014), with important implications to be discussed in Section 3.2.2.

3.2.1 The WHAK Model

To understand where a negative feedback enters into this process in the WHAK model, we can isolate the step where the silicate mineral is dissolved:

$$\begin{gathered}\mathrm{CaSiO_3}(s) + 2\mathrm{CO_2}(g) + \mathrm{H_2O}(l) \rightarrow \\ \mathrm{Ca}^{2+}(aq) + 2\mathrm{HCO_3^-}(aq) + \mathrm{SiO_2}(aq)\end{gathered} \tag{3.2}$$

Laboratory studies demonstrate that the kinetics of silicate dissolution depend directly on temperature and pH for a variety of silicate minerals (e.g. Schott & Berner, 1985; Brady, 1991; Knauss et al., 1993; Oxburgh et al., 1994; Welch & Ullman, 1996; Chen & Brantley, 1998; Weissbart & Rimstidt, 2000; Oelkers & Schott, 2001; Palandri & Kharaka, 2004; Carroll & Knauss, 2005; Golubev et al., 2005; Bandstra & Brantley, 2008; Brantley et al., 2008). Atmospheric pCO_2 influences temperature through its greenhouse effect and pH through its action as a weak acid in aqueous solution and its fertilizing effect on plants, which in turn produce organic acids in soils (Brady, 1991; Brady & Carroll, 1994). In the remainder of this study, we ignore the impacts of life on weathering and focus on the ability of abiotic planets to achieve stable, temperate climates, since the impact of organisms on weathering may vary immensely from planet to planet, depending on specifics of metabolism and biogeochemical pathways. Increasing the CO_2 partial pressure of the atmosphere warms the planet and reduces the pH of rainwater, both of which should accelerate silicate dissolution under conditions where the kinetics of dissolution is relevant. This increases the delivery of Ca^{2+} (or Mg^{2+}) cations to the ocean, which accelerates consumption of CO_2 and decreases pCO_2 until the rate of CO_2 consumption by silicate weathering is again equal to the rate of CO_2 production by outgassing. The opposite takes place in the case of a CO_2 reduction, so silicate weathering can act as a negative feedback on changes to the climate.

The temperature-dependence of silicate dissolution rates is usually represented as a simplified Arrhenius law:

$$r \propto \exp\left(\frac{T - T_{ref}}{T_e}\right) \tag{3.3}$$

where r is the silicate dissolution rate, T is the temperature at which dissolution is taking place, and T_{ref} is a reference temperature. $T_e = \frac{T_{ref}^2 R}{E_{act}}$ is the temperature change required to increase or decrease the dissolution rate by a factor of e, where R is the ideal gas constant and E_{act} is the activation energy of the dissolution reaction. Under kinetically limited conditions, higher temperatures accelerate the dissolution of silicate minerals.

The pH-sensitivity of silicate dissolution is more complicated, as the magnitude and sign of the dependence often depends on the pH itself (e.g. Brantley et al., 2008). Under alkaline conditions, reduced pH often inhibits dissolution rates; near neutral conditions, the effect of pH is weak or non-existent; and in acidic conditions, reduced pH often accelerates dissolution. Under neutral-to-acid conditions, the silicate dissolution rate varies with pH as (e.g. Kump et al., 2000):

$$r \propto [\mathrm{H}^+]^{n_H} \tag{3.4}$$

$$\log_{10}(r) \propto -n_H \times \mathrm{pH} \tag{3.5}$$

where $[\mathrm{H}^+]$ is the activity or concentration of H^+ ions and n_H is the reaction order with respect to H^+ ion activity.

Following Berner (1992), in the limit where there are no influences on the water's pH but CO_2 concentration, the concentration of H^+ ions is determined by the reaction:

$$\mathrm{CO_2} + \mathrm{H_2O} \leftrightarrow \mathrm{H}^+ + \mathrm{HCO_3^-} \tag{3.6}$$

with an equilibrium constant of:

$$K_{eq} = \frac{[\mathrm{H}^+][\mathrm{HCO_3^-}]}{[\mathrm{CO_2}]} \tag{3.7}$$

$$= \frac{[\mathrm{H}^+]^2}{[\mathrm{CO_2}]} \tag{3.8}$$

which implies:

$$[\mathrm{H}^+] \propto [\mathrm{CO_2}]^{0.5} \tag{3.9}$$

$$\propto \mathrm{pCO_2^{0.5}} \tag{3.10}$$

where $\mathrm{pCO_2}$ is the partial pressure of gaseous CO_2 in equilibrium with the silicate/water system, the last step following from Henry's Law. Combined with equation 3.4, this produces an expression for the $\mathrm{pCO_2}$-dependence of silicate dissolution, assuming a water/rock system in equilibrium with gaseous CO_2 and without any other influences on pH:

$$r \propto \mathrm{pCO_2}^{0.5\times n_H} \tag{3.11}$$

$$\propto \mathrm{pCO_2}^{\beta} \tag{3.12}$$

where β is simply $0.5\times n_H$. It is important to recognize that the apparently direct dependence of dissolution rate on CO_2 is actually mediated by the impact of CO_2 on pH, and does not reflect a response to the abundance of CO_2 as a reactant, implying that other substances that influence pH in weathering systems could have just as much impact on weathering rates.

Combining the $\mathrm{pCO_2}$-dependence and temperature-dependence presented above, the kinetically-limited dissolution rate of silicate minerals can be represented as:

$$\frac{r}{r_{ref}} = \exp\left(\frac{T - T_{ref}}{T_e}\right)\left(\frac{\mathrm{pCO_2}}{\mathrm{pCO_{2,\mathit{ref}}}}\right)^{\beta} \tag{3.13}$$

where the "ref" subscript refers to a reference value for a given variable. The values of T_e and β, which determine the sensitivity of the reaction rate to changes in pCO_2 and temperature, vary considerably for different silicate minerals. We choose the default values listed in Table 3.1 based on results from laboratory silicate dissolution experiments like those cited after equation 3.2.

Parameter	**Units**	**Definition**	**Default Value**
γ	–	Land fraction	0.3
a_g	–	Surface albedo	0.2
a	–	Planetary albedo	0.3
R_{planet}	meters (m)	Planetary radius	6.37×10^6
γ_{ref}	–	Modern land fraction	0.3
T_{ref}	Kelvin (K)	Modern global-avg. temperature	288
$pCO_{2,ref}$	bar	Pre-industrial CO_2 partial pressure	280×10^{-6}
p_{ref}	m yr^{-1}	Modern global-avg. precipitation	0.99 (Xie & Arkin, 1997)
q_{ref}	m yr^{-1}	Modern global-avg. runoff	0.20 (Oki et al., 2001)
Γ	–	Fraction of precip. that becomes runoff	$\frac{q_{ref}}{p_{ref}}$ =0.2
ϵ	1/K	Fractional change in precip. per K change in temp.	0.03
V_{ref}	mol yr^{-1}	Modern global CO_2 outgassing	7.5×10^{12} (Gerlach, 2011; Haqq-Misra et al., 2016)
v	mol m^{-2} yr^{-1}	Modern CO_2 outgassing per m^2 planetary area	$\frac{V_{ref}}{4\pi R^2_{planet}} =$ 0.0147
$w_{w,ref}$	mol m^{-2} yr^{-1}	Modern weathering per m^2 planetary area	$v = 0.0147$

Λ	variable	Thermodynamic coefficient for C_{eq}	1.4×10^{-3}
n	–	Thermodynamic pCO_2 dependence	0.316
α*	–	$L\phi\rho_{sf}AX_r\mu$ (see Section 3.2.2 and below)	3.39×10^{5}
L*	m	Flow path length	1
ϕ*	–	Porosity	0.1
ρ_{sf}*	kg m^{-3}	Mineral mass to fluid volume ratio	12728
A*	m^2 kg^{-1}	Specific surface area	100
X_r*	–	Reactive mineral conc. in fresh rock	0.36
μ*	–	Scaling constant	e^2
t_s*	years	Soil age	10^5
m*	kg mol^{-1}	Mineral molar mass	0.27
$k_{eff,ref}$*	mol m^{-2} yr^{-1}	Reference rate constant	8.7×10^{-6}
β	–	Kinetic weathering pCO_2 dependence	0.2 (e.g. Rimstidt et al., 2012)
T_e	Kelvin	Kinetic weathering temperature dependence	11.1 (Berner, 1994)

Table 3.1: **List of parameters used in this study.** This table lists parameters used in our calculations, their units, their definitions, and the default values they take. A single asterisk (*) means the default parameter value was drawn from Table S1 of the supplement to Maher & Chamberlain (2014). For default parameters drawn from other sources, the citation is given in the "**Value(s)**" column.

WHAK assumes that the global weathering rate is kinetically-limited, which would imply that increasing temperature or pCO_2 should always increase the flux of cations delivered to the ocean at a given runoff rate. This produces an equation of the form:

$$\frac{W}{W_{ref}} = \frac{Q}{Q_{ref}} \exp\left(\frac{T - T_{ref}}{T_e}\right)\left(\frac{pCO_2}{pCO_{2,ref}}\right)^{\beta} \tag{3.14}$$

where W is the global silicate weathering rate, Q is the global runoff, and the ref subscript refers to a reference value for a given variable. This formulation of global weathering adds another temperature dependence on top of the kinetic dependence, since runoff increases with precipitation, which increases with global temperature (e.g. Held & Soden, 2006; O'Gorman & Schneider, 2008). Some formulations of the weathering feedback (e.g. Berner, 1994; Pierrehumbert, 2010a; Abbot et al., 2012) use $(\frac{Q}{Q_{ref}})^a$ where $a = 0.65$ based on Dunne (1978); Peters (1984), but Abbot et al. (2012) demonstrated that weathering behavior in the WHAK model is not sensitive to the choice of a for values between 0 and 2, so we will use $a = 1$ for simplicity.

Rocky exoplanet climate and habitability studies that include silicate weathering invariably use the WHAK model (e.g. Kite et al., 2011; Abbot et al., 2012; Edson et al., 2012; Kadoya et al., 2012; Watanabe et al., 2012; Kadoya & Tajika, 2014; Menou, 2015; Foley, 2015; Abbot, 2016; Batalha et al., 2016; Haqq-Misra et al., 2016; Paradise & Menou, 2017; Ramirez, 2018; Rushby et al., 2018; Kadoya & Tajika, 2019; Paradise et al., 2019; Checlair et al., 2019a). However, there are orders-of-magnitude discrepancies between the weathering rates predicted by laboratory silicate dissolution experiments and the weathering rates observed in field studies of silicate weathering (Velbel, 1993; Malmström et al., 2000; White & Brantley, 2003; Maher et al., 2006). Further, despite a fairly stable climate over the past 3-4 Ga given the long-term trend in solar forcing, Earth has varied between "hothouse", "icehouse", and even snowball states, which could be explained partially by variations in the strength of the negative feedback on Earth's climate (Kump & Arthur, 1997; West et al., 2005; Maher & Chamberlain, 2014).

3.2.2 The MAC Model

The "solute transport model" presented in Maher & Chamberlain (2014) (MAC) attempts to provide a mechanistic explanation for variations in the strength of the silicate weathering feedback on Earth through time and in different river catchments. The solute transport model is the first model of the silicate weathering feedback to explicitly include a "thermodynamic limit", C_{eq}, on cation concentration in runoff, which emerges due to the control on silicate mineral dissolution by precipitation of secondary minerals like clays (Alekseyev et al., 1997; Maher et al., 2006, 2009; Winnick & Maher, 2018). When silicate dissolution and clay precipitation reach thermodynamic equilibrium, the maximum solute concentration of silicate dissolution products is achieved, maximizing weathering flux for a given runoff. In the MAC framework, for river catchments draining silicate mineral assemblages, the flux of cations delivered to the ocean (and therefore the CO_2 sequestration potential) depends on the ratio between the mean fluid travel time through a reactive assemblage ($t_f \approx L\phi/q$) and the time required for the system to reach C_{eq}, its maximum concentration ($t_{eq} \approx C_{eq}/r_n$); L is the reactive flow path length (which may vary with soil thickness (Ferrier & Kirchner, 2008; Gabet & Mudd, 2009), although this depends on the setting where the bulk of weathering takes place (West, 2012; Carretier et al., 2018); see also Section S.1 in the supplement to Maher & Chamberlain (2014)), ϕ is the effective porosity of the minerals the water is flowing through, r_n is the mineral reaction rate, and q is the runoff. $r_n = \rho_{sf} k_{eff} A X_r f_w$, where ρ_{sf} is the ratio of the mass of solid mineral to volume of fluid, k_{eff} is the dissolution rate constant, A is the specific surface area for the minerals in the assemblage, X_r is the fraction of reactive minerals in fresh, unweathered soil/rock, and f_w is the fraction of fresh, unweathered soil/rock in the assemblage. $f_w = \frac{1}{1+mk_{eff}At_s}$, where m is the molar mass of the minerals and t_s is the age of the soil. Note that the fraction of unweathered minerals decreases with soil age, and that a higher weathering constant (k_{eff}) will lead to a smaller fraction at a given soil age, depleting the soil/rock of reactive minerals. The ratio of mean fluid travel time through an assemblage and mean time to reach thermodynamic equilibrium (t_f/t_e) is known as the Damköhler number (Da) (Boucher & Alves, 1963); MAC factor out runoff to introduce the "Damköhler coefficient" (D_w):

$$D_w = \frac{L\phi\rho_{sf}k_{eff}AX_r}{C_{eq}(1 + mk_{eff}t_s)} \tag{3.15}$$

The weathering rate constant k_{eff} can be described by an equation with the same functional form as our equation 3.13, e.g. $\frac{k_{eff}}{k_{eff,ref}} = \exp\left(\frac{T-T_{ref}}{T_e}\right)\left(\frac{pCO_2}{pCO_{2,ref}}\right)^{\beta}$. D_w is central to the MAC formulation of weathering; the higher the value of D_w for a mineral assemblage being drained by a given flux of runoff, the higher the concentration of cations in the runoff, up to the thermodynamic limit on concentration, C_{eq}. Further, a higher D_w value means that an increase in runoff leads to less dilution of solute, allowing for larger changes to weathering rates in response to climate perturbations.

Winnick & Maher (2018) showed that C_{eq} should be dependent on pCO_2. As discussed in Section 3.2.1, pCO_2 can be an important control on the pH of water at Earth's surface; this provides a mechanism for changes in pCO_2 to change the equilibrium concentrations of reactants and products in mineral dissolution/precipitation reactions. Following Winnick & Maher (2018), this can be illustrated with a theoretical silicate dissolution / clay precipitation reaction:

$$dD + 2CO_2(g) + H_2O \leftrightarrow sS + 2HCO_3^- + aA + bB + cSiO_2(aq) \tag{3.16}$$

where D is the dissolving mineral (e.g. plagioclase feldspar), A and B respectively are the divalent and monovalent weathering products (e.g. Ca^{2+} and Na^{+}), S is the precipitating secondary mineral (e.g. halloysite), and lower-case letters are stoichiometric coefficients. We can then write the equilibrium constant for the reaction as:

$$K = \frac{[HCO_3^-]^2[A]^a[B]^b[C]^c}{(pCO_2)^2} \tag{3.17}$$

$$= \frac{z[A]^{2+a+b+c}}{(pCO_2)^2} \tag{3.18}$$

where $z = (\frac{2}{a})^2(\frac{b}{a})^b(\frac{c}{a})^c$ captures the relative stoichiometric coefficients and the second step assumes that no other reactions influence the concentrations of the reactants. Now we can write C_{eq} in terms of pCO_2, z, K, and the stoichiometric coefficients:

$$[A] = C_{eq} = (\frac{K}{z})^{\frac{1}{2+a+b+c}}(pCO_2)^{\frac{2}{2+a+b+c}} \tag{3.19}$$

$$= \Lambda(pCO_2)^n \tag{3.20}$$

where $[A]$, the divalent cation concentration, is chosen for C_{eq} since the delivery of Ca^{2+} to the oceans by silicate weathering is thought to be the dominant sink for CO_2 on geologic timescales through $CaCO_3$ formation and burial (France-Lanord & Derry, 1997; Sun et al., 2016). The temperature-dependence of C_{eq} is weak (see below and Winnick & Maher (2018)), so we will ignore it in this study. This is a powerful formulation because it allows the pCO_2 feedback strength to be derived directly from equilibrium chemistry. However, it is also a simplification, since the concentrations of reactants in mineral dissolution and precipitation reactions will be influenced by other, coupled reactions and particularly by the presence of other sources of acidity and alkalinity. We also note that we have only modeled "open-system" weathering in this study, meaning we have assumed that the weathering system is always in equilibrium with the ambient air and is thus continually recharged with CO_2 as weathering takes place. In the limit of "closed-system" weathering, weathering takes place in a system that is not recharged with CO_2. These two formulations of weathering display different behavior at low pCO_2, with C_{eq} varying linearly with CO_2 in the closed system case. However, Winnick & Maher (2018) demonstrate that their behavior generally converges at $pCO_2 \leq 10^{-1}$ bar, and a slightly different functional form of the relationship between pCO_2 and C_{eq} at low pCO_2 would not impact the qualitative results of this study.

Still following Winnick & Maher (2018), we will use the dissolution of plagioclase feldspar (An20) and precipitation of halloysite as the example reaction to derive default values for the coefficient and exponent in equation 3.20:

$$\begin{aligned} &1.66\mathrm{Ca_{0.2}Na_{0.8}Al_{1.2}Si_{2.8}O_8} + 2\mathrm{CO_2}(g) + 3\mathrm{H_2O} \\ &\leftrightarrow \mathrm{Al_2Si_2O_5(OH)_4} + 0.33\mathrm{Ca^{2+}} + 1.33\mathrm{Na^+} + 2\mathrm{HCO_3^-} \\ &+ 2.66\mathrm{SiO_2}(aq) \end{aligned} \tag{3.21}$$

which gives $n = 0.316$ and an equilibrium constant of $K = 10^{-13.3}$ at 288 K, implying $\Lambda = 0.0014$. As noted above, K is weakly temperature-dependent, producing variations in Λ with temperature: for the above reaction, $\Lambda(273\text{ K}) = 0.0011$ and $\Lambda(373\text{ K}) = 0.0033$. This effect provides a weak negative feedback on climate by increasing C_{eq} with temperature, but simulations we carried out that included this temperature-dependence (not shown) differed insignificantly from those that excluded it, so for simplicity we did not include this effect in the simulations shown in this study. It is also important to note that different mineral assemblages can have a large range of values for n, and Λ can span orders of magnitude for different lithologies (Winnick & Maher, 2018), so we vary these parameters widely in our calculations.

Using equations 3.15 and 3.20 for D_w and C_{eq} and the weathering and solute concentration equations given in MAC, we can derive a version of MAC's weathering equation that includes the impact of temperature and $\mathrm{pCO_2}$ on dissolution kinetics and the impact of $\mathrm{pCO_2}$ on thermodynamic equilibrium solute concentration (see the supplement to Maher & Chamberlain (2014) for a full derivation of equation 3.22):

$$C = C_{eq}\frac{\mu D_w/q}{1+\mu D_w/q} \tag{3.22}$$

$$w = qC_{eq}\frac{\mu D_w/q}{1+\mu D_w/q} \tag{3.23}$$

$$= \frac{\alpha}{[k_{eff,ref}\exp\left(\frac{T-T_{ref}}{T_e}\right)\left(\frac{\mathrm{pCO_2}}{\mathrm{pCO_{2,ref}}}\right)^{\beta}]^{-1} + mAt_s + \alpha[(qC_{eq})]^{-1}} \tag{3.24}$$

where C is the solute concentration in runoff, w is weathering per unit surface area, $\alpha = L\phi\rho_{sf}AX_r\mu$ for compactness of notation, and $\mu = e^2$ (see supplement to MAC, where μ is instead called τ). Through its thermodynamic impact on C_{eq} (equation 3.20), $\mathrm{pCO_2}$ has a strong effect on the concentration of solute in runoff, and thus on the weathering flux and $\mathrm{CO_2}$ sink at a given runoff. Figure 3.1 shows the solute concentrations and weathering fluxes for the weathering assemblage described in the previous paragraph across a wide range of runoff and $\mathrm{pCO_2}$. In the limit where q is very large, the concentration C falls linearly with q and the weathering flux w tops

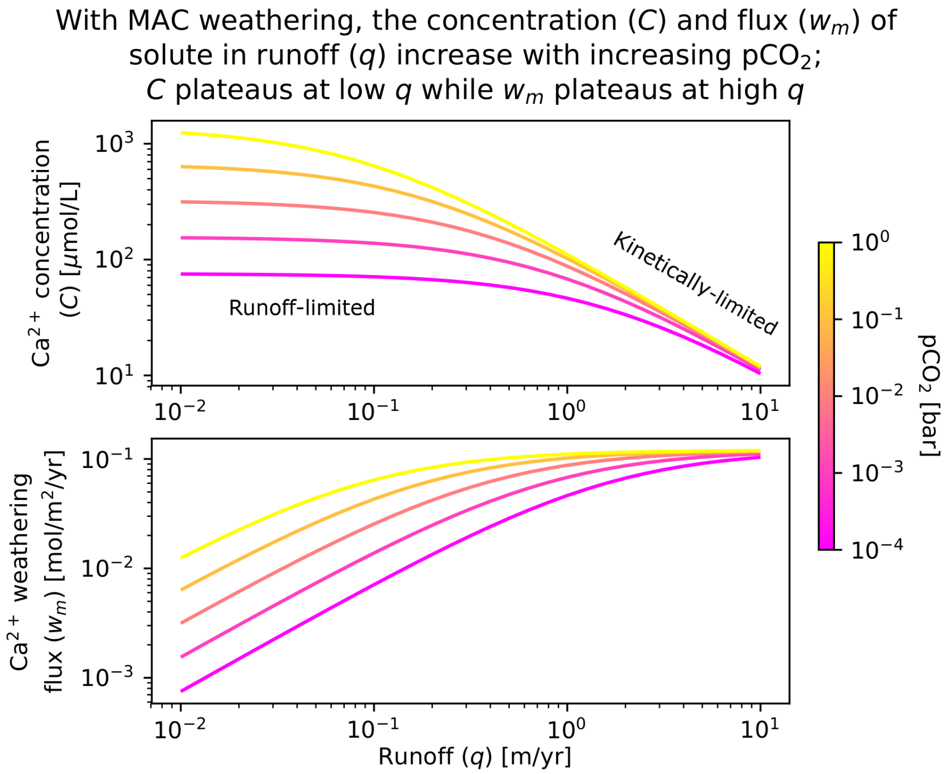

Figure 3.1: **Solute concentrations and weathering fluxes as functions of runoff and pCO$_2$ with our default parameter choices (see Table 3.1)**. The top plot shows Ca^{2+} concentrations (equation 3.22) and the bottom plot shows Ca^{2+} fluxes to the ocean (equation 3.23). The pinkest curves have a C_{eq} calculated with pCO$_2$ = 10^{-4} bar (see equation 3.20), and the color of the curves shifts from pink to yellow as pCO$_2$ increases from 10^{-4} to 10^{-3} to 10^{-2} to 10^{-1} to 10^{0} bar CO$_2$. The regions with runoff limitation and kinetic limitation are labeled as such.

out at a value of μD_w, equal to $\frac{\alpha}{k_{eff}^{-1}+mAt_s}$. This is "kinetically-limited" weathering behavior similar to that assumed in the WHAK model. This happens when t_s is small and q or C_{eq} is large – when relatively fresh, unweathered soil is being flushed out by large enough volumes of runoff to maintain very dilute solute concentrations. When mAt_s is large enough relative to other terms not to neglect, $\alpha/(qC_{eq}) \sim 0$, and $[k_{eff}]^{-1} \sim 0$, e.g. when runoff and the weathering rate constant are both large but t_s is non-negligible so the soil being flushed out by the runoff is already partially weathered, equation 3.24 limits to a constant value of $\frac{\alpha}{mAt_s}$, which goes to zero as t_s grows very large. Weathering in this limit is "supply-limited," since the weathering rate is dictated by the rate of supply of fresh material to the weathering zone, with a lower t_s implying a higher rate of delivery and a less stringent supply limit. When $qC_{eq} \ll$

$\alpha/(mAt_s)$ and $qC_{eq} \ll \alpha k_{eff}$, e.g. when runoff flushes the system out slowly enough relative to other factors that the solute can approach its thermodynamic limit on concentration C_{eq}, the weathering rate varies linearly with runoff. In this regime, the system displays "runoff-limited" (also referred to as "chemostatic") weathering, where the kinetics of silicate dissolution do not influence weathering rate, and weathering flux is controlled entirely by runoff at a given pCO_2.

For context, we will briefly discuss where Earth lies in terms of kinetic vs. runoff controls on global weathering flux, using results from studies that apply the MAC framework to interpret proxies and direct weathering measurements. By averaging the annual-mean silica concentrations and fluxes from a dataset of large rivers draining granitic lithologies (Gaillardet et al., 1999), Maher & Chamberlain (2014) estimate that Earth as a whole lies in the transition zone between fully runoff-limited and kinetically-limited behavior, with a high degree of variation between individual rivers (see their Figures 2 and 3). Von Blanckenburg et al. (2015) combine general circulation model simulations and a beryllium weathering proxy to derive a similar result for Earth's weathering regime since the Last Glacial Maximum. Additionally, using non-averaged solute concentration vs. runoff measurements paired with individual estimates of C_{eq} for rivers draining both granitic and basaltic lithologies, Ibarra et al. (2016) showed that the median concentration-runoff pairs for many individual rivers also lie in the transition regime, though they are on average closer to the runoff limit than the global average estimate by Maher & Chamberlain (2014). Finally, we note that most of the cases examined in this paper lie in the runoff-limited regime or near the transition to kinetic limitation, like Earth.

3.3 Model Description & Methods

Here we describe the models we used to evaluate the consequences of thermodynamic and energetic limits on silicate weathering for the climate stability of rocky land- and ocean-bearing planets in the habitable zone. We coupled a zero-dimensional energy balance model to a zero-dimensional CO_2 balance model to simulate the first-order behavior of planets under a variety of conditions. This clearly requires extreme simplification of planetary processes, but this is justified given the lack of observational information about habitable zone worlds at present.

The energy balance model equates the global average of absorbed instellation with outgoing longwave radiation (OLR):

$$S_{avg} = \frac{1}{4}(1-a)S \tag{3.25}$$
$$= OLR \tag{3.26}$$

where S_{avg} is the globally-averaged absorbed instellation, S is the top-of-atmosphere instellation at the substellar point, a is the planetary albedo, and 1/4 is a geometric factor accounting for the fact that a planet's surface area is 4× the area of its cross-section.

By default, our simulations assume a constant planetary albedo $a = 0.3$, approximately corresponding to Earth's present-day value (Stephens et al., 2015). We note that a major uncertainty in our study is the exclusion of interactive cloud effects, which strongly impact planetary albedo and energy balance (see Section 3.5.1 for discussion of this point). We also include a set of simulations with planetary albedo that is a function of surface albedo as well as atmospheric albedo due to Rayleigh scattering by pCO_2. This allows us to approximate the impact of atmospheric scattering on the climates of planets orbiting G2-stars like the Sun; the planetary albedos of worlds orbiting K- and M-dwarfs are less affected by Rayleigh scattering, since those classes of stars emit light at longer wavelengths where atmospheres are more strongly absorbing and display weaker scattering (e.g. Kopparapu et al., 2013). The equations for calculating Rayleigh scattering planetary albedo under a two-stream Eddington approximation are (Pierrehumbert, 2010a):

$$\tau_{ray} = 0.19513 \frac{\mathrm{pCO_2}}{1\ \mathrm{bar\ CO_2}} \tag{3.27}$$
$$a_a = \frac{(0.5 - 0.75\cos\zeta)(1 - \exp(-\tau_{ray}/\cos\zeta)) + 0.75\tau_{ray}}{1 + 0.75\tau_{ray}} \tag{3.28}$$
$$a_a' = \frac{0.75\tau_{ray}}{1 + 0.75\tau_{ray}} \tag{3.29}$$
$$a = 1 - \frac{(1 - a_g)(1 - a_a)}{(1 - a_g)a_a' + (1 - a_a')} \tag{3.30}$$

where τ_{ray} is the Rayleigh scattering optical depth as a function of pCO_2 on a planet with surface gravity equal to Earth's at wavelength 0.5 micron, which is near the peak of the solar spectrum (drawn from Table 5.2 in Pierrehumbert (2010a)), a_a is the atmospheric albedo due to Rayleigh scattering of incoming solar radiation, $\cos\zeta$ is the cosine of the zenith angle of the star (taken to be 2/3 in this study, based on Cronin (2014)), a_a' is the atmospheric albedo for upward-directed diffuse radiation from the surface, a_g is the surface albedo, and the equation for a combines a_a, a_a', and a_g to get total planetary albedo. In the subset of experiments that include this representation of Rayleigh scattering, we vary a_g from 0.1 to 0.3, covering a range of plausible surface albedos that Earth may have displayed throughout its history as cloud and continental coverage evolved (Rosing et al., 2010).

OLR is calculated using a polynomial fit presented in Kadoya & Tajika (2019) that approximates the output of the 1-D radiative-convective model used in Kopparapu et al. (2013) with 1 bar N_2 and saturated H_2O for temperatures between 150 K and 350 K and pCO_2 between 10^{-5} bar and 10 bar:

$$OLR(T, \mathrm{pCO_2}) = I_0 + \mathbf{T}\mathbf{B}\Upsilon^t \tag{3.31}$$

$$\mathbf{T} = (1\ \xi\ \xi^2\ \xi^3\ \xi^4\ \xi^5\ \xi^6) \tag{3.32}$$

$$\Upsilon = (1\ \upsilon\ \upsilon^2\ \upsilon^3\ \upsilon^4) \tag{3.33}$$

where T is the surface temperature in K, pCO_2 is the partial pressure of CO_2 in bars, $I_0 = -3.1$ W m^{-2}, and $\xi = 0.01 \times (T - 250)$. For $pCO_2 < 1$ bar:

$$\upsilon = 0.2 \times \log_{10}(\mathrm{pCO_2}) \tag{3.34}$$

$$\boldsymbol{B} = \begin{bmatrix} 87.8373 & -311.289 & -504.408 & -422.929 & -134.611 \\ 54.9102 & -677.741 & -1440.63 & -1467.04 & -543.371 \\ 24.7875 & 31.3614 & -364.617 & -747.352 & -395.401 \\ 75.8917 & 816.426 & 1565.03 & 1453.73 & 476.475 \\ 43.0076 & 339.957 & 996.723 & 1361.41 & 612.967 \\ -31.4994 & -261.362 & -395.106 & -261.600 & -36.6589 \\ -28.8846 & -174.942 & -378.436 & -445.878 & -178.948 \end{bmatrix} \tag{3.35}$$

For 10 bar $> pCO_2 >$ 1 bar:

$$\upsilon = \log_{10}(\mathrm{pCO_2}) \tag{3.36}$$

$$\boldsymbol{B} = \begin{bmatrix} 87.8373 & -52.1056 & 35.2800 & -1.64935 & -3.43858 \\ 54.9102 & -49.6404 & -93.8576 & 130.671 & -41.1725 \\ 24.7875 & 94.7348 & -252.996 & 171.685 & -34.7665 \\ 75.8917 & -180.679 & 385.989 & -344.020 & 101.455 \\ 43.0076 & -327.589 & 523.212 & -351.086 & 81.0478 \\ -31.4994 & 235.321 & -462.453 & 346.483 & -90.0657 \\ -28.8846 & 284.233 & -469.600 & 311.854 & -72.4874 \end{bmatrix} \tag{3.37}$$

This simple parameterization of OLR allows us to perform rapid simulations across a wide range of parameters, with a maximum absolute error of 3.3 W m^{-2} and an average absolute error of 0.6 W m^{-2} in the range of temperatures and pCO_2 mentioned above (Kadoya & Tajika, 2019). The main drawback in using this parameterization is that we cannot evaluate climates at pCO_2 above 10 bar or with varying N_2 abundance.

The CO_2 balance model sets CO_2 outgassing from volcanism equal to CO_2 consumption from weathering:

$$v = w \tag{3.38}$$

where $v = V/(4\pi R^2_{planet})$ is the total volcanic outgassing of CO_2 (V) divided by the planetary surface area, R_{planet} is the radius of the planet, and w is the CO_2 consumption by weathering per unit planetary surface area. To compare the behavior of planets with the WHAK and MAC weathering models, we run simulations with each formulation:

$$w_w = w_{w,ref} \frac{\gamma p}{\gamma_{ref} p_{ref}} \exp\left(\frac{T - T_{ref}}{T_e}\right)\left(\frac{\mathrm{pCO_2}}{\mathrm{pCO}_{2,ref}}\right)^{\beta} \tag{3.39}$$

$$w_m = \gamma \frac{\alpha}{[k_{eff,ref} \exp\left(\frac{T-T_{ref}}{T_e}\right)\left(\frac{\mathrm{pCO_2}}{\mathrm{pCO}_{2,ref}}\right)^{\beta}]^{-1} + mAt_s + \alpha[q\Lambda(\mathrm{pCO_2})^n]^{-1}} \tag{3.40}$$

where w_w is the weathering per unit planetary area using the WHAK model; γ is the global land fraction, which is included to account for the fact that continental silicate weathering only happens on continents; p is the global average precipitation per unit area; and w_m is the weathering per unit planetary area using the MAC model. Crucially, the impact of the kinetic dissolution rate and its dependence on temperature and pCO_2 is greatly weakened in equation 3.40. This is because increased dissolution of silicates also depletes soils and rocks of their reactive components more completely for a given soil age, reducing the reactivity of the assemblage and counteracting the increase in dissolution rate. However, pCO_2 still has a powerful impact on silicate weathering through its control of the thermodynamic equilibrium concentration of solute in runoff (equation 3.20).

We take the runoff q to be a linear function of precipitation p, which is itself taken to be a linear function of temperature T (e.g. Held & Soden, 2006; O'Gorman & Schneider, 2008):

$$q = \Gamma \times p \tag{3.41}$$

$$p = p_{ref}(1 + \epsilon(T - T_{ref})) \tag{3.42}$$

where Γ is the proportionality constant between precipitation and runoff and ϵ is the fractional change in global precipitation per Kelvin deviation from a reference surface temperature.

We also include the upper limit on precipitation noted by Pierrehumbert (2002); O'Gorman & Schneider (2008). In steady-state, global precipitation is equal to global evaporation. Global evaporation is ultimately driven by instellation, which provides the energy required for water to transition from liquid to gas (the latent heat of vaporization). If there is not enough instellation to make up for the cooling caused by a given amount of evaporation, then a planet cannot sustain that level of precipitation. This implies a maximum global precipitation given by:

$$p_{lim} = \frac{S_{avg}}{L(T)} \tag{3.43}$$

$$L(T) = 1.918 \times 10^9 (\frac{T}{T - 33.91})^2 \tag{3.44}$$

where p_{lim} is the maximum precipitation sustainable on a planet at a given instellation and $L(T)$ is the latent heat of vaporization for water in J m^{-3}, converted from L in J kg^{-1} given by the Henderson-Sellers equation (Henderson-Sellers, 1984) with multiplication by water's density 1000 kg m^{-3}.

More speculatively, we propose that the actual value of p_{lim} at a given instellation may be lower than that given by equation 3.43 for planets with land, since stellar energy absorbed by continents can only recycle water that ultimately evaporated from the ocean (note that the validity of equation 3.43 was only demonstrated in the case of a fully ocean-covered planet by O'Gorman & Schneider (2008)). Although the influence of a given amount of land area on the energetic precipitation limit should depend on the latitude of the land mass (e.g. a continent will intercept many more photons if it straddles the equator or substellar point than if it sits on a pole or at the terminator) and the efficiency of the atmosphere at moving energy from the land surface to the ocean surface, we suggest an approximate, first-order scaling of p_{lim} with global ocean fraction (1-γ), such that equation 3.43 represents p_{lim} in the 100% ocean coverage limit:

$$p_{lim,land} = (1 - \gamma) \frac{S_{avg}}{L(T)} \tag{3.45}$$

where $p_{lim,land}$ is the energetic limit on precipitation for planets with a non-zero surface land fraction. Since we have not yet demonstrated the validity of equation 3.45 explicitly with GCM simulations (a subject for future work), we use equation 3.43 for the energetic limit in most calculations, but we also carry out a set of experiments with equation 3.45 to examine the impact of the proposed scaling.

We search for equilibrium pCO_2 and T for planets at S from 1400 W m^{-2} to 473 W m^{-2}, the outer edge of the classical habitable zone for an Earth-sized planet orbiting a G-star according to Kopparapu et al. (2013), defined by the "maximum greenhouse" limit where Rayleigh scattering from CO_2 accumulation begins to outweigh CO_2's warming effect. Note that we do *not* have a representation of Rayleigh scattering in our default model, so we take the value of the outer edge given in Kopparapu et al. (2013), though we also explore the impact of a Rayleigh scattering parameterization in a separate set of simulations. To find equilibrium values, we solve for pCO_2 and T where $v = w$ and $S_{avg} = OLR$ simultaneously. Using this procedure to find steady-state climates, we compare the behavior of planets with weathering described by the MAC formulation against that of planets under the WHAK formulation and vary parameters across a range of values to examine the sensitivity of our models. In particular, we examine the pCO_2 and temperatures of our simulations as a function of instellation, and we calculate the "effective outer edge of the habitable zone" as the instellation at which the temperature of a simulation with a given set of parameters drops below freezing (while acknowledging that planets may be able to reach global average temperatures somewhat below freezing before entering a "hard snowball state" (e.g. Abbot et al., 2011; Yang et al., 2012)). In the next section we present the results of these calculations.

3.4 Results

We begin by comparing the simulations with the WHAK formulation against the simulations with the MAC formulation. The different weathering models lead to qualitative differences in weathering behavior, planetary climate, and the effective outer edge of the HZ. Then, we examine the impact of varying the parameters that represent hydrology, weathering thermodynamics, surface properties, and albedo in our model of the MAC formulation of weathering. The effective outer edge of the habitable zone is quite sensitive to all of these sets of parameters. This makes it difficult to predict what fraction of rocky, ocean-bearing planets in the HZ we should expect to find in a temperate state instead of a snowball or a moist greenhouse, even if we ignore the strong possibility that other greenhouse gases or CO_2 cycling mechanisms will be present on putatively Earth-like planets. Finally, we examine the impact of the energetic limit on precipitation set by planetary instellation (see equations 3.43 and 3.45), which we find fundamentally changes the functioning of the silicate weathering feedback under some circumstances by decoupling planetary temperature and global runoff.

3.4.1 WHAK vs. MAC

Sensitivity to land fraction and CO_2 outgassing rate

As demonstrated in Abbot et al. (2012); Foley (2015), weathering behavior with the WHAK model is fairly insensitive to planetary land fraction; in contrast, MAC planet climates are considerably more sensitive to land fraction, particularly at $\gamma < 0.3$ (see Fig. 3.2 and the leftmost column in Fig. 3.3). The MAC simulation with $\gamma = 0.15$ is 30-40 K warmer than the simulation with $\gamma = 0.3$ at all instellations, and with $\gamma < 0.15$, we failed to find stable solutions within the the temperature and pCO_2 range of the OLR parameterization we are using, though stable climates conceivably exist with $pCO_2 > 10$ bar and/or $T > 350$ K. Also, other combinations of parameters would lead to different values in either direction for the minimum γ, so $\gamma = 0.15$ is not a hard minimum on the land fraction a planet needs to stabilize its climate via silicate weathering. Interestingly, Fig. 3.2 shows that the temperature of the $\gamma = 0.15$ case stops decreasing with instellation when S/S_0 falls below ~ 0.4 (see red curve in top panel of Fig. 3.2). This is because that set of simulations hits the energetic limit on precipitation at that instellation (see Section 3.4.3 for further analysis of this phenomenon). Since $v = w$, and γ is a multiplicative factor on the front of the equations for w_w and w_m (equations 3.39 and 3.40), a fractional change in γ at constant v has the same effect as multiplying v by the reciprocal of that fraction while holding γ constant. So, planets under the MAC formulation are also sensitive to increases in CO_2 outgassing rates, as reducing γ by a factor of 2 from 0.3 to 0.15 is equivalent to multiplying volcanic outgassing by 2 while holding land fraction constant.

The difference in land fraction and outgassing sensitivity between MAC and WHAK planets is due to the lack of weathering sensitivity to dissolution kinetics in the MAC planets. Under decreased land fraction (or increased outgassing), more weathering must happen per unit land area to balance outgassing. Without temperature-dependent changes in solute concentration via changes in dissolution kinetics, MAC planets are forced to compensate for changes in land fraction or outgassing through changes to precipitation rate (which responds to temperature) and maximum solute concentration C_{eq} (which responds to pCO_2). On WHAK planets, the solute concentration can increase or decrease without limit in response to both temperature and pCO_2 due to changes in the kinetic silicate dissolution rate. This allows for greater changes in concentration to bolster changes in runoff in response to altered land area or outgassing rate on WHAK planets. This means smaller changes in precipitation are

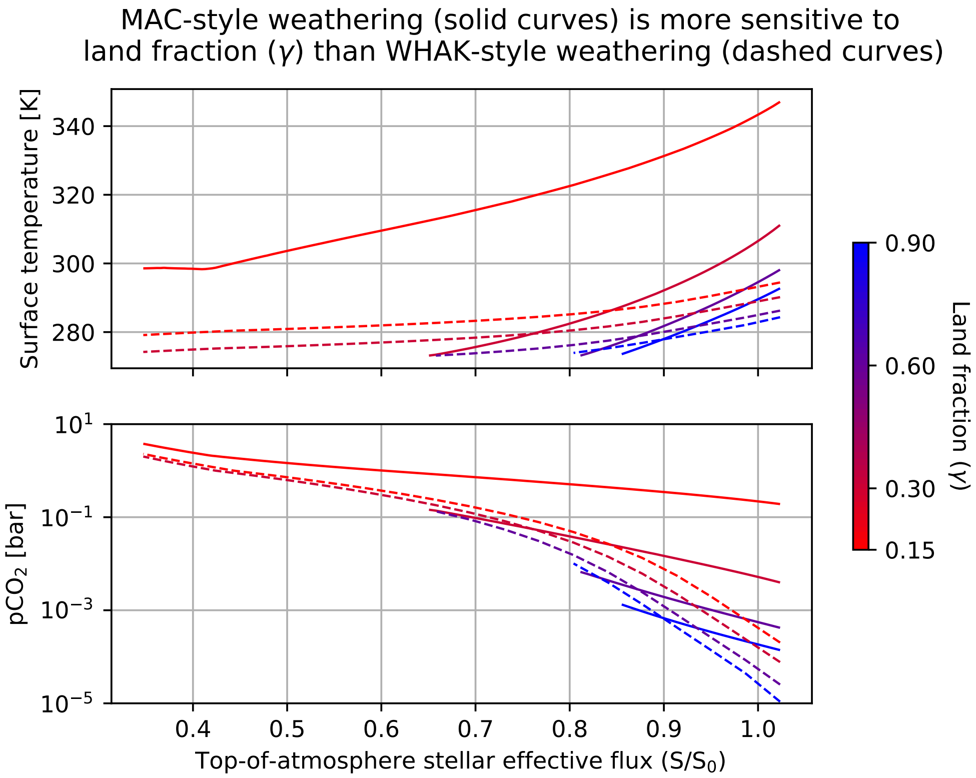

Figure 3.2: **A comparison of instellation vs. temperature and pCO_2 for WHAK and MAC simulations at varying land fraction.** The top plot shows top-of-atmosphere stellar effective flux (S/S_0, where $S_0 = 1368$ W m^{-2}) vs. temperature. The bottom plot shows TOA stellar effective flux vs. pCO_2. Solid curves use the MAC formulation of weathering, and dashed curves use the WHAK formulation. The reddest curves have land fraction (γ)=0.15. γ=0.3 curves are red-purple, $\gamma = 0.6$ curves are blue-purple, and $\gamma = 0.9$ curves are blue.

necessary to alter weathering fluxes to balance land fraction and outgassing changes. Smaller precipitation changes imply smaller temperature changes.

Sensitivity to Parameters Controlling Silicate Dissolution Kinetics

In agreement with Abbot (2016), the climates of WHAK planets as a function of instellation in our models are sensitive to the kinetic pCO_2-dependence (β; dashed curves in middle column in Fig. 3.3) and temperature-dependence (T_e; dashed curves in rightmost column in Fig. 3.3) in equation 3.39. For high values of β, weathering is greatly accelerated by high pCO_2, which increases CO_2 drawdown and induces cooling at low instellations where high pCO_2 is required for habitability. This means that lower β values translate to a better climate control as a function of instellation in the

WHAK formulation, with the limit of a perfect thermostat at $\beta = 0$, other things being equal (Pierrehumbert, 2010a; Ramirez, 2017). Lower T_e values also translate to more effective climate control, since weathering rates respond more strongly to a given change in temperature. In contrast to the results for the WHAK formulation,

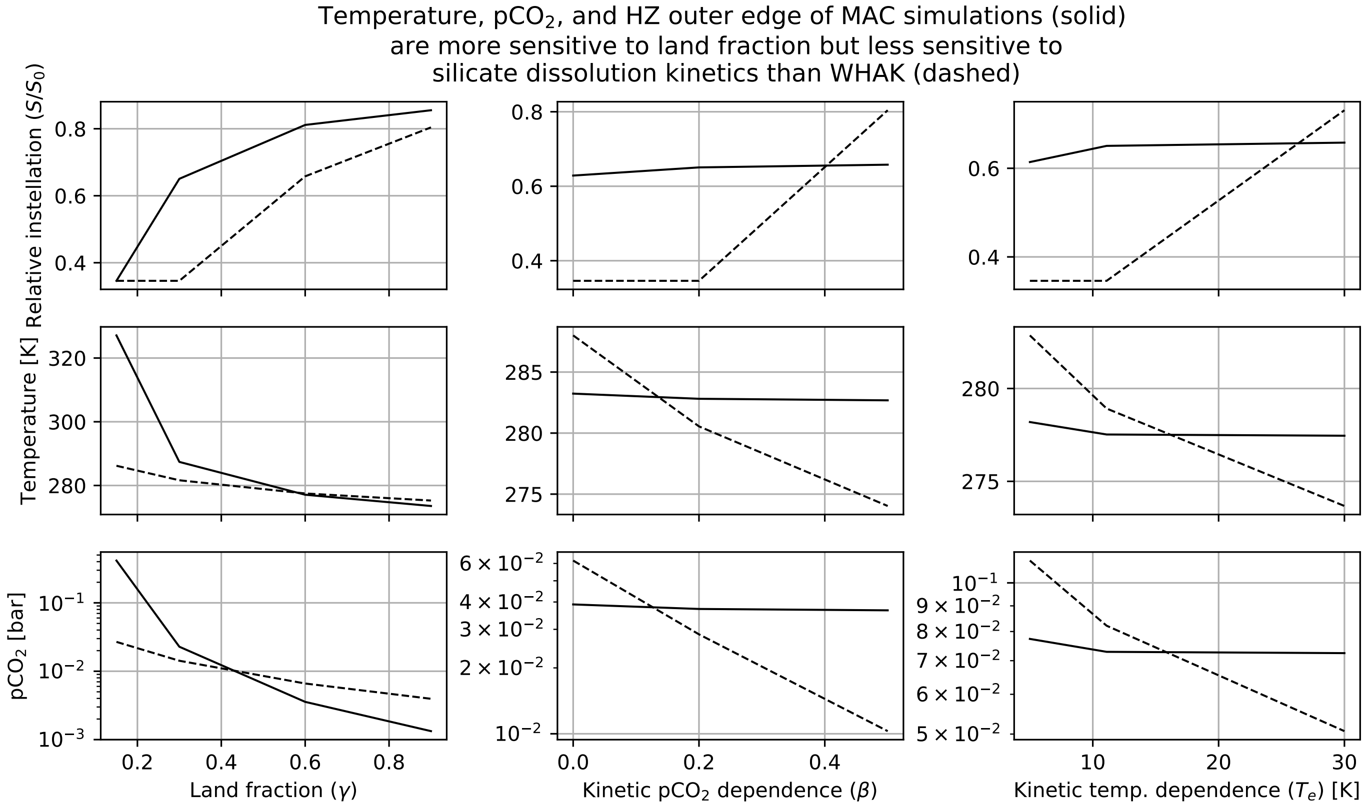

Figure 3.3: **A comparison of the sensitivity to land fraction and silicate dissolution kinetics of WHAK simulations and MAC simulations.** Dashed curves show results for WHAK simulations, solid curve show results for MAC simulations. The top row shows the relative instellation (S/S_0, where $S_0 = 1368$ W m^{-2}) of the outer edge of the habitable zone, defined as the instellation where planetary temperature drops below freezing with a given set of weathering parameters. If the calculated outer edge is below the classical outer edge for Earth as defined in Kopparapu et al. (2013), the outer edge is set to the classical outer edge ($S/S_0 = 1/1.7^2 = 0.346$). The middle row shows the temperature for each simulation at the highest HZ outer edge instellation of the group of simulations in that column. The bottom row shows the pCO_2 for each simulation at the highest HZ outer edge instellation of the group of simulations in that column. The leftmost column shows simulations under varying land fraction (γ), the center column shows simulations under varying kinetic pCO_2 dependence (β), and the right column shows simulations under varying kinetic temperature dependence (T_e). Any parameters not being varied take their default value.

the climates of MAC planets with our default parameter choices show almost no sensitivity to β and T_e (solid curves in middle and rightmost columns of Fig. 3.3). This is because increased kinetic dissolution rates (e.g. increased k_{eff}) tend to deplete mineral assemblages of reactive components, reducing the impact of kinetics on steady state weathering intensity. Kinetics only influences the steady state weathering flux when the dissolution rate is very slow relative to the rate at which the weathering system is flushed out by runoff. Our MAC simulations are far from the condition where the kinetic dissolution rate determines weathering flux (see final paragraph in Section 3.2.2). Instead, weathering flux is determined by the interplay between runoff, cation concentration, and pCO_2 governed by the thermodynamics of silicate dissolution and clay precipitation (see Figure 3.1 and Section 3.2.2).

3.4.2 Sensitivity to Hydrology, Thermodynamic pCO_2-dependence, Surface Properties, and Rayleigh Scattering Albedo

The climates of planets under the MAC formulation are very sensitive to hydrology, the thermodynamics of silicate dissolution and clay precipitation, and surface properties in weathering assemblages because these factors combine to control the concentration and flux of cations to the ocean. Rayleigh scattering albedo can also have a strong effect on the behavior of planets near the outer edges of the habitable zones of G-stars, because of both its direct radiative effects and its effects on weathering arising from energetic limits on precipitation and runoff.

Hydrology

The hydrologic cycle is parameterized roughly in our model by making runoff linearly dependent on precipitation and precipitation linearly dependent on temperature.

Increasing Γ, the fraction of precipitation converted to runoff, reduces temperature and pCO_2 and moves the effective outer edge of the HZ closer to the star (see the leftmost column of Fig. 3.4). This is because a greater quantity of runoff per unit precipitation leads to a larger weathering flux at a given temperature and pCO_2, allowing for a given outgassing rate to be balanced with less rain at colder temperatures. This effect is also illustrated in the bottom panel of Fig. 3.1: a given weathering flux can be achieved at successively lower pCO_2 by increasing runoff (moving rightward in the plot). Increasing ϵ, the fractional change in precipitation per unit K, moves the effective outer edge of the HZ away from the star quite strongly, but doesn't have as much impact on temperature and pCO_2 (see second column in Fig. 3.4). ϵ governs

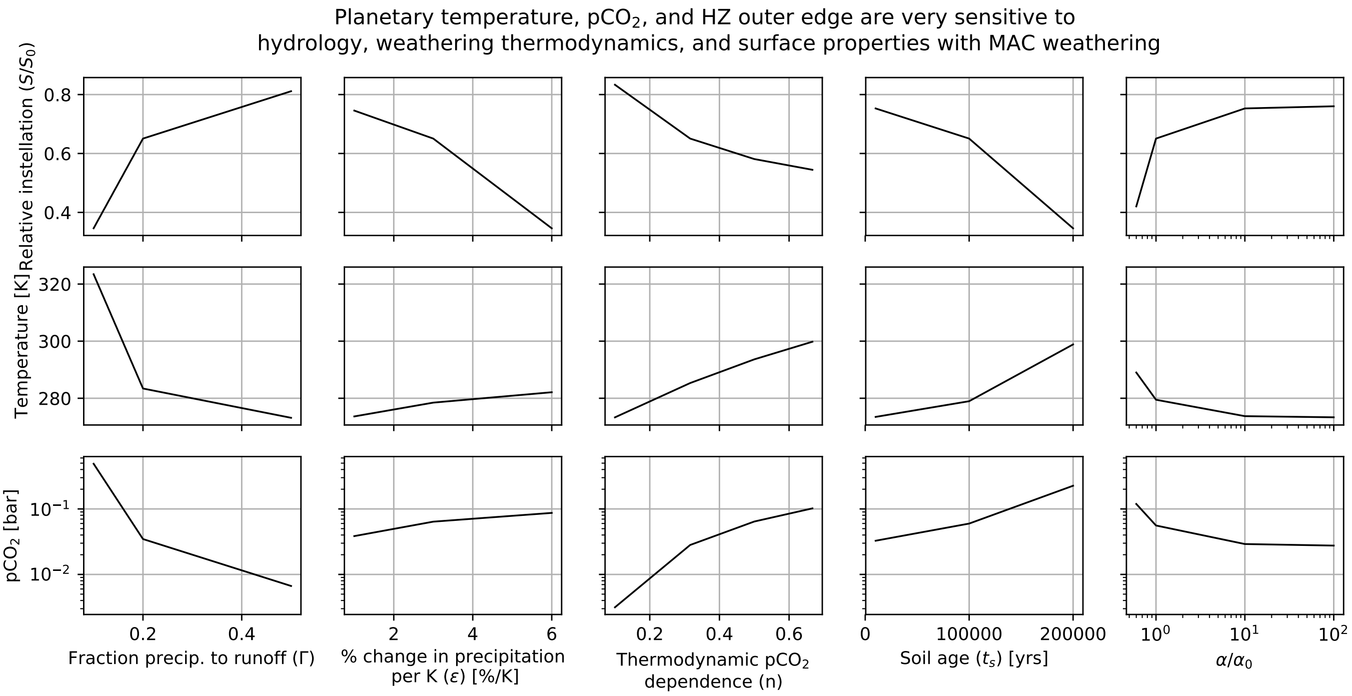

Figure 3.4: **The sensitivity of MAC weathering simulations to variations in hydrological properties, thermodynamic pCO_2 dependence of C_{eq}, and surface properties.** The top row shows the relative instellation (S/S_0, where $S_0 = 1368$ W m^{-2}) of the outer edge of the habitable zone, defined as the instellation where planetary temperature drops below freezing with a given set of weathering parameters. If the calculated outer edge is below the classical outer edge for Earth as defined in Kopparapu et al. (2013), the outer edge is set to the classical outer edge ($S/S_0 = 1/1.7^2 = 0.346$). The middle row shows the temperature for each simulation at the highest HZ outer edge instellation of the group of simulations in that column. The bottom row shows the pCO_2 for each simulation at the highest HZ outer edge instellation of the group of simulations in that column. The leftmost column shows simulations varying the fraction of precipitation that ends up as runoff to the ocean (Γ), the second column shows simulations varying the % change in precipitation per Kelvin temperature change (ϵ), the third column shows simulations varying the exponent in the thermodynamic dependence of C_{eq} on pCO_2 (n), the fourth column shows simulations varying the soil age (t_s), and the fifth and final column shows simulations varying the ratio of $L\phi\rho_{sf}AX_r\mu$ to its default value (α/α_0), which can be thought of as the baseline weathering potential for a given mineral assemblage. Any parameters not being varied take their default value.

the strength of the temperature-dependence of the silicate weathering feedback in the MAC model, since it controls how much the global weathering flux changes in response to temperature changes. Increasing ϵ makes the weathering flux more sensitive to temperature, which allows a planet with a given set of parameters to maintain balance against CO_2 outgassing out to lower instellations before hitting the freezing point.

Thermodynamic Control of C_{eq}

Increasing the thermodynamic pCO_2 dependence of C_{eq} in isolation (n in equations 3.20 and 3.40) at a given pCO_2 below 1 bar tends to reduce C_{eq}, which reduces weathering flux, necessitating larger pCO_2 to balance outgassing. So, increasing n tends to move the outer edge of the HZ farther from the star and increase temperatures and pCO_2 (see middle column of Fig. 3.4).

Increasing the thermodynamic coefficient Λ tends to increase C_{eq}, which allows the concentration of solute in runoff to reach higher levels and therefore allows for a larger maximum weathering flux at a given runoff rate. This means increases to Λ cool planets, moving the effective outer edge of the habitable zone closer to the star (Fig. 3.5).

Surface Properties

The physical properties of the surface of a planet have important impacts on its weathering behavior which have not been considered in previous studies of exoplanet weathering.

Increasing soil age (t_s) tends to move the effective outer edge of the HZ farther from the star and increase planetary temperature and pCO_2 (see the second-from-right column in Fig. 3.4). This is because older soils are more depleted of weatherable minerals. This increases the time necessary for water moving through a mineral assemblage to reach thermodynamic equilibrium between silicate dissolution and clay precipitation (t_{eq}, see Section 3.2.2), which decreases solute concentration and increases the quantity of runoff necessary to generate a large enough weathering flux to balance outgassing. At high enough t_s, reactive minerals are so depleted that the negative feedback between weathering and climate is lost, as weathering rates are dictated by the supply of reactive minerals to the assemblage ("supply-limited" weathering (West et al., 2005; Foley, 2015)–not shown, since no equilibrium climate is possible in this regime with our models). The t_s where supply limitation sets in varies depending on the values taken by other parameters.

α is the product of several different parameters: reactive flow path length (L), porosity of the mineral assemblage being weathered (ρ), the ratio of mineral mass to fluid volume (ρ_{sf}), the specific surface area of minerals being weathered (A), the

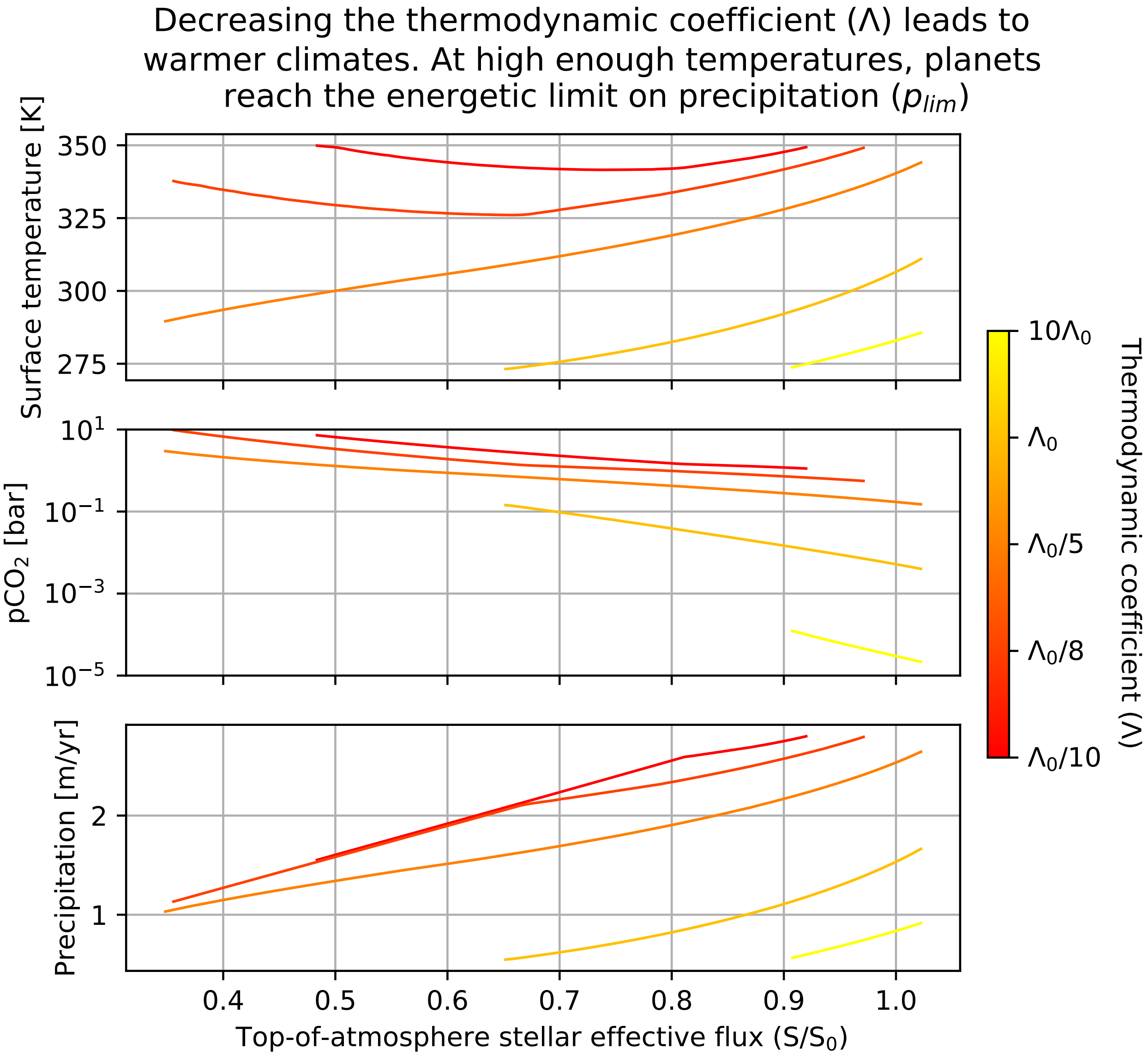

Figure 3.5: **A comparison of temperature, pCO$_2$, and precipitation vs. instellation for simulations varying thermodynamic coefficient for C_{eq}'s dependence on pCO$_2$ (Λ).** The top plot shows instellation vs. temperature (T), the center plot shows instellation vs. pCO$_2$, and the bottom plot shows instellation vs. precipitation. The reddest curves use $\Lambda = \Lambda_0/10$ (where $\Lambda_0 = 1.4 \times 10^{-3}$), and the curves become more yellow as Λ is increased through $\Lambda_0/8$,$\Lambda_0/5$, Λ_0, and $10\Lambda_0$. Parameters not being varied take their default values.

concentration of reactive minerals in fresh, unweathered bedrock (X_r), and a scaling constant that brings the theoretical scaling of solute concentration in line with reactive transport modeling (μ; see the supplement to Maher & Chamberlain (2014)).

Increasing any of these parameters brings water flowing through a mineral assemblage closer to thermodynamic equilibrium at a given runoff flux, so α might be thought of as a set of physical properties that determines the baseline weathering potential for a mineral assemblage (an aspect of "weatherability", e.g. Kump & Arthur (1997)). Moving the solute concentration closer to its thermodynamic limit C_{eq} at constant runoff increases the weathering flux (see Fig. 3.1), drawing down CO_2, reducing temperature, and moving the effective outer edge of the habitable zone closer to the star (see rightmost column in Fig. 3.4).

Rayleigh Scattering Albedo

We use equation 3.30 to estimate the effect on climate of planetary albedo (a) variations due to Rayleigh scattering at 0.5 micron by CO_2 for Earth-mass planets with a range of surface albedos orbiting Sun-like stars, and we compare the simulations with interactive albedo to simulations with a constant planetary albedo equal to the reflectivity of the surface/clouds (see Fig. 3.6). Our approach to estimating Rayleigh scattering albedo likely overestimates its importance to planetary energy balance, as atmospheric near-infrared absorption should also increase with pCO_2, so these simple calculations represent a conservative upper bound on the strength of Rayleigh scattering. We used a reduced thermodynamic coefficient of $\Lambda = \Lambda_0/5$ to decrease C_{eq} and force the simulations to accumulate large pCO_2 so that the CO_2-induced Rayleigh scattering effect would be clearer. We should also note that any change to a parameter that increases pCO_2 (e.g. an increase in soil age) would have the same effect on Rayleigh scattering as the reduction in Λ that we use; there is no specific relationship between Λ and Rayleigh scattering. At low pCO_2, the impact of CO_2-induced Rayleigh scattering is negligible, leading to changes in albedo of order 1 percent; under these circumstances, planetary albedo is dominated by the prescribed albedo of the surface (which represents the combined surface albedo, cloud albedo, and albedo of the non-CO_2 part of the atmosphere). But, as expected, as pCO_2 grows with decreasing instellation (middle panel in Fig. 3.6), elevated Rayleigh scattering leads to increased albedo (solid curves in bottom panel of Fig. 3.6), which in turn cools a simulation relative to the corresponding simulation without Rayleigh scattering (compare solid and dashed curves in top panel of Fig. 3.6). This cooling effect moves the effective outer edge of the habitable zone closer to the star.

3.4.3 Impact of an Energetic Limit on Precipitation

In steady-state, precipitation is in equilibrium with evaporation, which is ultimately driven by instellation. This implies a maximum planetary precipitation rate constrained by planetary instellation (equation 3.43), a prediction which is borne out by both 1-dimensional (Pierrehumbert, 2002) and 3-dimensional (O'Gorman & Schneider, 2008; Le Hir et al., 2009) climate models.

Energetic Limit Without Land Fraction Dependence

The impact of the energetic limit on precipitation is illustrated in Figure 3.5. Reducing Λ (the thermodynamic coefficient in equation 3.20) reduces C_{eq} for a given pCO_2, which increases the temperature, pCO_2, and precipitation necessary to achieve a runoff high enough to balance outgassing. Simulations with $\Lambda = \Lambda_0/5$ and above (where Λ_0 is the default value for Λ listed in Table 3.1) have temperature slopes identical to those of their precipitation curves because precipitation is linear with respect to temperature. However, for the simulations with $\Lambda_0/8$ and $\Lambda_0/10$, temperature eventually becomes decoupled from precipitation and begins to increase instead of decrease as instellation falls. This is because the temperatures in these simulations are forced so high by the restriction of C_{eq} that they each achieve the maximum precipitation at a given instellation somewhere in the HZ. For simulations that reach their maximum precipitation rate at some instellation, precipitation then follows p_{lim} and decreases linearly with instellation beyond that (note that the red and red-orange precipitation curves converge onto the same line in the bottom panel of Fig. 3.5, since they both follow equation 3.43). Since precipitation (and therefore runoff) decreases faster with instellation when governed by equation 3.43, this forces pCO_2 to grow at a higher rate with decreasing instellation in order to increase C_{eq} and allow solute to accumulate to high enough concentrations to maintain a weathering flux balanced with outgassing despite reduced runoff (see the bottom panel of Fig. 3.1 to see the relationship between pCO_2, runoff, and weathering flux for a given set of parameters). This increased CO_2 accumulation per unit instellation reduction is what leads to the counter-intuitive temperature increase at low instellations in the red and red-orange curves in the top panel of Fig. 3.5.

Energetic Limit With Land Fraction Dependence

We also ran a set of simulations with $p_{lim,land}$ (equation 3.45) instead of p_{lim} (equation 3.43) to examine the impact of scaling the energetic limit on global precipitation by surface ocean fraction (1-γ). This leads to several changes in the weathering behavior of planets in the energetically limited regime as a function of land fraction γ. This is demonstrated in Figure 3.7, which compares the temperature, pCO_2, and precipitation for simulations with thermodynamic coefficient $\Lambda = \Lambda_0/5$ at $S/S_0 = 0.346$ (the classical outer edge of the habitable zone for an Earth-mass planet around a G2-star according to Kopparapu et al. (2013)) with and without the new scaling law for the energetic limit.

The first point to note is that scaling the energetic limit with ocean fraction lowers the temperature at which a planet's precipitation becomes energetically limited for a given instellation, since a reduced fraction of the instellation is available to drive precipitation. For the simulations that use p_{lim}, a thermodynamic coefficient of $\Lambda_0/5$ (with other parameters set to default values) leads to a surface temperature that is not high enough to enter the energetically-limited regime at any instellation (see Fig. 3.5 and the dashed curves in Fig. 3.7) regardless of land fraction; in contrast, simulations that use $p_{lim,land}$ instead of p_{lim} enter the energetically limited regime for all γ when $\Lambda = \Lambda_0/5$ (see solid curves in Fig. 3.7).

Another difference between these sets of simulations is that energetically-limited simulations that use $p_{lim,land}$ tend to display warmer temperatures and higher pCO_2 than those using p_{lim} (see top and middle panels of Fig. 3.7). This is because simulations with $p_{lim,land}$ are restricted to a lower maximum precipitation rate (see bottom panel in Fig. 3.7). A lower precipitation rate implies a lower rate of runoff in our models, which forces pCO_2 to build to higher levels in order to increase the thermodynamic limit C_{eq} enough for the low runoff to deliver sufficient cations to the ocean to balance outgassing of CO_2.

Finally, there is a qualitative difference in the dependence of planetary climate and weathering behavior on land fraction (γ) for energetically-limited planets with $p_{lim,land}$. In our simulations, under non-energetically-limited conditions (and under energetically-limited conditions governed by p_{lim} instead of $p_{lim,land}$), increased land fraction leads to cooling (e.g. Fig. 3.2 or the leftmost column of Fig. 3.3). This is because a larger land area allows a given outgassing rate to be balanced with a smaller weathering flux per unit land surface, necessitating lower precipitation rates and temperatures. In contrast, energetically-limited simulations with $p_{lim,land}$ may warm or cool with increased γ (see top panel of Fig. 3.7). When cooling dominates, it is because of the effect just discussed. When warming occurs with increased land fraction, it is because $p_{lim,land}$ (and therefore runoff) becomes very small at high γ since the ocean surface fraction becomes small, which forces pCO_2 to increase greatly so that C_{eq} becomes large enough that the tiny rates of runoff can still deliver enough cations to the ocean to balance outgassing.

3.5 Discussion & Conclusions

3.5.1 Discussion

The Influence of Tectonic Mode on Silicate Weathering

In this study, we did not address the tectonic regime of the planets we modeled, but weathering is probably strongly impacted by tectonic mode. Planets with plate tectonics have a robust mechanism for removing weathered material and delivering fresh weatherable material to the planetary surface, potentially improving their ability to avoid a "supply-limited" weathering regime where the negative feedback between climate and weathering is lost due to depletion of weatherable minerals (West et al., 2005; Foley, 2015). Simulations of plate tectonic planets display efficient CO_2 degassing under most conditions (Noack et al., 2014). Simulations of stagnant lid planets suggest that they may also be able to avoid the supply limit over geologic timescales (Foley & Smye, 2018; Foley, 2019) and display efficient degassing and volcanism under a range of conditions, though their volcanic activity may become limited at high core-mass fraction or high planetary mass (Noack et al., 2014, 2017; Dorn et al., 2018). Between these endmembers, there are intermediate states like the "episodic" mode, with long periods of stagnant lid behavior punctuated by periods of relatively rapid resurfacing and outgassing (Lenardic et al., 2016).

The MAC formulation suggests some natural ways to explicitly incorporate tectonic mode into simulations of planetary weathering behavior. Through its impact on the Damköhler coefficient (D_w), the average soil age of material being weathered in our simulations (t_s) has a powerful impact on the weathering behavior of rocky planets. Young soils lead to large values of D_w, allowing for a robust weathering feedback. Ancient soils that are depleted in reactive minerals can enter a supply-limited weathering regime. We would expect that planets with more rapid resurfacing will, on average, have younger soils and therefore greater values of D_w. They should also have higher volcanic outgassing rates. Younger soils lead to more efficient weathering and therefore lower equilibrium pCO_2 and temperatures. Higher outgassing rates lead to higher equilibrium pCO_2 and temperature. Since greater volcanic activity may lead to both faster resurfacing and higher rates of outgassing, the effects tend to offset one another and it is difficult to predict what the net impact on planetary weathering behavior would be.

Tectonic mode should also influence the lithology of the material being weathered on a given planet. For example, the relative abundances of granitic and basaltic weatherable material may be determined by the relative rates of continental generation vs. production of flood basalts, which will in turn be controlled by the primary mode of resurfacing on a planet. Ibarra et al. (2016) showed that granitic and basaltic river catchments on Earth display divergent weathering behavior: rivers draining basaltic catchments tend to have higher values of C_{eq} and cation concentration. Winnick & Maher (2018) argued that the weathering of basaltic minerals should display greater sensitivity to pCO_2 because basalts have a higher proportion of divalent cations, which leads to a larger value for the thermodynamic pCO_2 sensitivity (n; see equations 3.19 and 3.20). Those results imply that planetary weathering dominated by granites vs. basalts could lead to quite different equilibrium climate states for planets with otherwise similar properties.

We also note the importance of mountain building processes for the silicate weathering feedback. Much of the chemical weathering on Earth takes place in mountainous regions where fresh minerals are exposed to the Earth's surface and soil is produced and eroded at high rates (Larsen et al., 2014a,b). Since orogeny is heterogeneous in space and time on Earth, the build-up and grind-down of mountains, as well as the climatic conditions at the locations on Earth where these processes take place, may have a profound impact on the carbon cycle and global climate of a planet through time. Periods of active mountain-building (particularly in areas with appreciable runoff) may lead to global cooling by increasing the fraction of fresh minerals (f_w; equivalent to reducing soil age) in the region being weathered, whereas periods of slow uplift may allow CO_2 to accumulate to high levels in the atmosphere (Raymo & Ruddiman, 1992; Jagoutz et al., 2016; Kump, 2018; Macdonald et al., 2019)

Relation to Previous Rocky Exoplanet Weathering Results

To our knowledge, all previous rocky exoplanet weathering studies have used some variant of the WHAK formulation to represent weathering. Simulations with the MAC formulation display some important differences in behavior compared to those with the WHAK formulation. So, if we assume that the MAC formulation is an accurate representation of planetary silicate weathering, some conclusions of these previous studies should be revisited. We survey a few points of interest below.

As we noted in Section 3.4, Abbot et al. (2012) and Foley (2015) found that planetary weathering behavior is relatively insensitive to land fraction with the WHAK model. We found the opposite with the MAC model: land fraction strongly impacts the planetary temperature, particularly at low land fraction. This suggests that understanding the processes that control oceanic volume (e.g. Kasting & Holm, 1992; Cowan & Abbot, 2014; Schaefer & Sasselov, 2015; Komacek & Abbot, 2016) and the development of continents (e.g. Rosing et al., 2006; Höning et al., 2014; Höning & Spohn, 2016; Höning et al., 2019) on exoplanets is extremely important for predicting the frequency of occurrence of truly habitable planets.

Snowball limit cycling is a hypothetical phenomenon on terrestrial planets where silicate weathering draws down CO_2 faster than outgassing supplies it, even at temperatures cold enough to freeze a planet, plunging a planet into the snowball state. In the snowball state, silicate weathering is expected to slow down or cease, allowing CO_2 to outgas and build up until a planet has warmed enough to deglaciate, at which point rapid silicate weathering freezes it again (Tajika, 2007; Menou, 2015; Batalha et al., 2016; Haqq-Misra et al., 2016; Abbot, 2016; Paradise & Menou, 2017; Ramirez, 2017) (although CO_2 condensation in the extreme cold of the snowballs or continued weathering at the seafloor during the snowball may make deglaciation difficult under some conditions (Turbet et al., 2017; Kadoya & Tajika, 2019)). In simulations with the WHAK formulation, limit cycling is driven by the kinetic dependence of weathering on pCO_2 (β) increasing weathering rates at low instellations where pCO_2 is very high. In the MAC formulation, kinetic pCO_2-dependence has essentially no impact on planetary weathering rates (see the middle column of Fig. 3.3), but the thermodynamic dependence of C_{eq} on pCO_2 leads to a similar result. Many parameter configurations lead to planets with equilibrium temperatures below freezing at instellations within the habitable zone, so planets with these parameter sets at low enough instellations would either be locked into a permanent snowball state or go through limit cycling. The fact that factors like hydrology and soil age and lithology impact the effective outer edge of the habitable zone so strongly (see top row in Fig. 3.4) implies that a planet's susceptibility to limit cycling (and therefore its habitability) is determined by a complex interplay of factors that are not easily constrained a priori. Arguing that a given planet (e.g. Mars (Batalha et al., 2016)) experienced limit cycling thus requires making many implicit and potentially unfounded assumptions about the properties that controlled its weathering (see Ramirez (2017); Hayworth et al. (2020) for further discussion of the early Martian limit cycling hypothesis).

Kite et al. (2011) use the WHAK formulation of weathering to argue that there may be conditions where silicate weathering acts as a destabilizing feedback on the climates of rocky tidally-locked planets. The "enhanced substellar weathering instability" (ESWI) is proposed to take place on tidally locked planets with relatively thin atmospheres composed largely of CO_2. Because heat transport in thin atmospheres decreases with reductions in density, a decrease in atmospheric mass can lead to net warming at the substellar point on a tidally locked planet despite the reduction in greenhouse effect, due to decreased ability of the atmosphere to export solar energy away from the substellar point. Because of the exponential dependence of weathering rates on temperature in the WHAK formulation, the vast majority of weathering on a tidally locked planet occurs near the substellar point, so an increase in temperature at the substellar point through a reduction in atmospheric pressure can enhance global weathering significantly. The enhanced weathering would in turn draw down more CO_2, again reducing atmospheric pressure, warming the substellar point, and enhancing weathering. This is a positive feedback leading to atmospheric collapse, since weathering begets more weathering, and the reverse scenario of runaway CO_2 accumulation also occurs in the case of an initial increase in atmospheric mass (or an initial cooling). However, the ESWI depends intimately on the strength of the temperature-dependence of the silicate weathering feedback. The non-exponential temperature-dependence in the MAC formulation might lead to global weathering that is less concentrated at the substellar point, implying that tidally locked planets with thin CO_2-dominated atmospheres may be less vulnerable to the ESWI than suggested by Kite et al. (2011).

Implications for Early Earth Climate Evolution

During Earth's Archean eon (4 to 2.5 Ga), the Sun was likely 20-30% fainter than today (e.g. Sagan & Mullen, 1972; Bahcall et al., 2001). Sparse proxy estimates from this period seem to imply a temperate world with ocean temperatures $< 40°C$ and occasional partial glaciations (e.g. Hren et al., 2009; Blake et al., 2010; Ojakangas et al., 2014; de Wit & Furnes, 2016; Catling & Zahnle, 2020), suggesting the climate was effectively buffered against reduced luminosity. The question of how the Earth maintained habitability despite this large change in luminosity is sometimes referred to as the "Faint Young Sun problem," a particularly famous component of the more general problem of constraining the evolution of the climate during Earth's deep prehistory. As we noted in the introduction, the silicate weathering feedback is often invoked as a source of the climatic buffering in Earth's past, and this interpretation is consistent with carbon cycle models of the Archean period that use WHAK-style kinetic representations of continental and seafloor weathering to estimate Archean Earth's equilibrium climate state (e.g. Charnay et al., 2017). In fact, the proxy record of ancient climate has been combined with WHAK-based inverse geologic carbon cycle modeling in attempts to simultaneously provide tighter constraints on Earth's temperature-CO_2 history, key globally-averaged parameters like T_e and β in the WHAK formulation, and the relative importance of processes like seafloor weathering and reverse weathering compared to continental weathering in the past (Krissansen-Totton & Catling, 2017; Krissansen-Totton et al., 2018; Krissansen-Totton & Catling, 2020). These examples illustrate how the WHAK framework, as a central component of most models of the carbon cycle of the ancient Earth, contributes to current understanding of the Archean Earth system and the Faint Young Sun problem.

As shown in Section 3.4.1, the MAC and WHAK formulations of weathering lead to different atmospheric responses to changes in boundary conditions. MAC is much more sensitive to changes in land fraction (γ) and volcanic outgassing (v), displaying a 30-40 K temperature increase in response to a factor-of-2 reduction in γ/v, compared to a ~ 5 K increase for WHAK (see Fig. 3.2 and the leftmost column of Fig. 3.3, noting that reductions in v are equivalent to proportional increases in γ). On the other hand, depending on parameter choices like n and β, either formulation of weathering can be more sensitive to changes in luminosity. On Earth, all of these boundary conditions have changed substantially since the Archean, with a general secular decrease in outgassing by as much as a factor of 10 or more (Dasgupta, 2013) and an increase in dry land by a factor of 10 or more (Flament et al., 2008; Johnson & Wing, 2020) accompanying the increase in solar luminosity already mentioned. This suggests an increase in γ/v by perhaps a factor of ~ 100 (!) since the Archean, which is enormous compared to the factor of 2 reduction that causes 30-40 K of warming in our default MAC model. Of course, other parameters in the MAC model have certainly changed since the Archean—we specifically discuss these boundary conditions because the magnitude of change over time and the divergence in response by WHAK and MAC help illustrate the point that replacing the WHAK formulation in carbon cycle models with a MAC-style parameterization could lead to substantially different conclusions about the evolution of the Earth system since the Archean.

Since the change in luminosity sensitivity between the two formulations can go in either direction, we will also ignore that potential difference between WHAK and

MAC and focus on sensitivity to land fraction and outgassing. Because MAC weathering requires larger increases in temperature than WHAK to maintain equilibrium in response to reduced γ/v, and because γ/v may have been a factor of 100 smaller during the Archean, replacing the WHAK model with the MAC formulation would lead to a much hotter inferred Archean climate, other things being equal. However, as noted in the beginning of this section, the (very limited) climate proxy estimates from the Archean suggest a world with a temperate climate not much warmer than our own. Assuming those estimates are trustworthy, the behavior of the MAC model may make it necessary to invoke other changes to the carbon cycle, e.g. a greater seafloor weathering flux, to generate enough weathering to balance outgassing at temperatures consistent with the mild climate implied by proxies. Other differences, particularly the lack of vascular land plants, may imply further weakening of Archean continental weathering (e.g. Rafiei & Kennedy, 2019), though the influence of plants is still poorly understood. These suggestions can be tested quantitatively. The implications of the MAC formulation for our interpretation of the proxy record of the evolution of the Earth system should be addressed rigorously with a statistical methodology that accounts for the huge uncertainties in most parameters when modeling the ancient carbon cycle (see the approach taken in Krissansen-Totton & Catling (2017); Krissansen-Totton et al. (2018); Krissansen-Totton & Catling (2020)).

Observability of the Silicate Weathering Feedback

Bean et al. (2017); Checlair et al. (2019b) suggest the use of "statistical comparative planetology" to detect the operation of the silicate weathering feedback on rocky planets in the HZ. Specifically, Bean et al. (2017); Checlair et al. (2019b) propose using a relatively large number of low cost, low precision CO_2-abundance measurements of rocky planets throughout the habitable zone with a future telescope to show that pCO_2 tends to decrease with increases in instellation, which would provide evidence for a stabilizing feedback on planetary climate. With the assumption that the silicate weathering feedback would adjust pCO_2 to hold planetary temperatures at 280 K, and with very optimistic assumptions for observational noise, Checlair et al. (2019b) conclude that ~ 10 planets with functioning silicate weathering feedbacks in the habitable zone would need to have their CO_2 partial pressures characterized to give an 80% chance of detecting a trend in pCO_2 vs. instellation. Under pessimistic instrumental noise assumptions, Checlair et al. (2019b) calculate that the number of necessary characterizations increases to ~ 50. These numbers bracket the range of estimated yields for "exo-Earth" planets from proposed next-generation telescopes

HabEx (Gaudi et al., 2020) and LUVOIR (Team et al., 2019). However, it is worth noting that recent studies suggest that the occurrence rate of Earth-like planets may be up to an order of magnitude lower than the numbers used to calculate those estimates (Pascucci et al., 2019; Neil & Rogers, 2019), which would lead to a proportional reduction in yield.

Our study suggests a larger number of observations may be required to establish a trend of pCO_2 vs. instellation and confirm the operation of the silicate weathering feedback, due to the huge variations in pCO_2 and temperature at a given instellation for planets with different different outgassing rates or combinations of hydrological, thermodynamic, and surface mineralogical parameters. As an example, see the middle panel in Fig. 3.5: at $S/S_0 \sim 0.9$, equilibrium pCO_2 varies by 4 orders of magnitude between the simulations with $\Lambda = \Lambda_0/10$ and $10\Lambda_0$. Both of those values of Λ are within the range expected from diversity of silicate mineral assemblage lithologies (Winnick & Maher, 2018). Varying other parameters produces a similar spread in pCO_2. Effectively, the potential diversity in weathering behavior among terrestrial planets adds a form of intrinsic "noise" to the statistical estimates in Checlair et al. (2019b). To add to the complication, variations in seafloor weathering or reverse weathering (discussed below in section 3.5.1) could also add to the variety of climates encountered in the HZ.

The diversity in equilibrium climates permitted by variations in hydrological, thermodynamic, and surface parameters, coupled with the potentially low occurrence rate of Earth-like planets noted above, suggests that the method outlined in Bean et al. (2017); Checlair et al. (2019b) may not be adequate to detect the silicate weathering feedback with upcoming telescope missions. Because of this, we suggest that a complementary method first suggested in Turbet (2019) to identify the breakdown of the silicate weathering feedback at the inner edge of the habitable zone may be able to successfully demonstrate the existence of the feedback with a smaller number of observations. We do not statistically quantify the number of characterizations necessary to identify the operation of the silicate weathering feedback with this method, as that is beyond the scope of the current study. The method from Turbet (2019) that we will discuss makes use of the potential for a large discontinuity in CO_2 concentration between planets on opposite sides of the inner edge of the habitable zone, defined here as the instellation above which a planet enters the runaway greenhouse state and loses its water to space (Kasting et al., 1993). There is not a unique instellation where the runaway greenhouse occurs, as the critical irradiation level depends on planetary rotation rate (Yang et al., 2014), planetary radius (Yang et al., 2019a), surface gravity (Yang et al., 2019a), stellar temperature (Kopparapu et al., 2013), background gas partial pressure (Ramirez, 2020a), surface water distribution (Kodama et al., 2018, 2019), and cloud properties (Leconte et al., 2013a), but for the purposes of this discussion, we will use a conservative estimate for an Earth-mass, rapidly-rotating planet around a Sun-like star given in Kopparapu et al. (2013). In that study, the critical instellation for a planet with those properties is found to be $S_{eff} = 1.05$ (where S_{eff}=S/S_{earth} is the ratio of flux received by the planet to the flux received by modern Earth).

For planets just beyond the inner edge (e.g. planets just within the HZ) with a functional silicate weathering feedback, CO_2 will be drawn down to low levels due to the high instellation. To give a conservative maximum estimate of pCO_2 at the inner edge of the habitable zone, we use eqn. 3.31 to find the pCO_2 necessary to equilibrate a planet with an albedo of 0.3 and $S_{eff} = 1.05$ at a surface temperature of 340 K. This yields a pCO_2 of 0.05 bar. In actuality, the pCO_2 could be considerably lower, depending on the various parameters that control the weathering rate, but with a higher pCO_2, a planet would be hot enough to enter a moist greenhouse regime and lose its water to space efficiently (Kasting et al., 1988).

In contrast, Earth-like planets within the inner edge of the HZ that undergo a runaway greenhouse and lose their oceans to space may end up in a "Venus-like" state with ~ 100 bars of CO_2 in their atmosphere due to the catastrophic decarbonation of their mineral inventories under extreme temperatures (though this prediction depends on the magnitude of carbon delivery to a planet during its accretion phase). Even in the absence of catastrophic decarbonation, if a planet loses its water due to the runaway but still has even a little bit of CO_2 outgassing (and an Earth-like inventory of carbon), a Venus-like CO_2-rich atmosphere will accumulate, since a fully dry planet cannot maintain a silicate weathering feedback. This suggests that there could be a 2-3 order of magnitude discontinuity in pCO_2 for Earth-like planets straddling opposite sides of the inner edge of the habitable zone, assuming an operative silicate weathering feedback within the HZ.

If present, the multiple-orders-of-magnitude change in pCO_2 across the inner edge of the HZ (see Fig. 3.8 for a schematic illustration of this concept) may be observable with next-gen telescopes like OST, HabEx, or LUVOIR without the need for a large number of atmospheric characterizations. However, it may be difficult to demonstrate that a planet has CO_2 partial pressures greater than a bar or two via infrared emission, since CO_2 becomes optically thick throughout the IR region at high column abundances; for example, remote observations of the night-side of Venus look similar to the day-side of Mars in the IR despite a factor of $\sim$ 16000 difference in CO_2 partial pressure, since IR only escapes from the top $\sim$bar of Venus's atmosphere (see Fig. 3 in Pierrehumbert (2011)).

In the absence of direct measurements of atmospheric pCO_2 at the surface of Venus-like planets, we propose that the contrast in albedo across the inner edge of the HZ at visible wavelengths due to Rayleigh scattering by CO_2 should be substantial and likely observable: low pCO_2 planets near the inner edge of the habitable zone would have albedos approximately equal to that of their surface + clouds, suggesting a maximum of around 0.3 (based on Earth's albedo in the visible (Tinetti et al., 2006)), whereas Venus-like planets would have visible-wavelength albedos > 0.9 due to efficient Rayleigh scattering by $\sim$100 bar of CO_2, even in the absence of shiny sulfuric acid clouds like those hosted by Venus (calculated at 0.5 micron with equation 3.30; see also Table 5.4 in Pierrehumbert (2010a)). Note that we are specifically discussing albedo in the visible region of the spectrum: albedo integrated across the spectrum would include near-IR absorption effects, which would reduce the albedo contrast across the inner edge of the HZ and introduce a dependence on stellar type since lower-temperature stars emit preferentially at longer wavelengths. By restricting the discussion to visible-wavelength albedo, we avoid those complications.

In summary, observations of large differences in pCO_2 and/or visible-wavelength albedo between planets on opposite sides of the inner edge of the habitable zone may allow for a demonstration that the silicate weathering feedback stabilizes planetary climate within the HZ and fails to stabilize climate outside of the HZ. In particular, because of the abrupt and large change in pCO_2 and albedo across the inner edge of the HZ, the existence of the silicate weathering feedback may be demonstrable with a smaller number of observations than a method that depends on the potentially noisy trend of pCO_2 vs. irradiation due to silicate weathering within the habitable zone.

Relating Planetary Characteristics to Weathering Controls

The potential diversity in climate outcomes we discuss above partially might partially from our ignorance of the constraints on parameters controlling weathering in the MAC formulation. A better understanding of the likely distributions of important variables like soil thickness and age, particularly as functions of bulk parameters like planetary mass, might serve to narrow the range of climate states we expect Earth-like planets with MAC-style weathering to exhibit. Without monumental advances in observational techniques (e.g. Turyshev et al., 2020), direct observation of these parameters on exoplanets is not feasible. Even on Earth, where observations are many orders of magnitude more dense and sensitive than they ever could be for an exoplanet, quantitative understanding of the factors controlling weathering is in its early stages. However, progress is still possible through a combination of theory, modeling, generalization from Earth observations where appropriate, and, eventually, "statistical comparative planetology" of the sort described by Bean et al. (2017); Checlair et al. (2019b).

Theory and modeling can be used to deepen understanding of the relationships between the parameters controlling weathering. In this study, we ignored a variety of potentially important feedbacks between variables in the MAC model. For example, a greater erosion rate decreases soil thickness ($\sim L$), increasing the production rate of soil (Heimsath et al., 2000), leading to a higher fraction of fresh, weatherable minerals in the soil column (f_w). The reduction in soil thickness tends to reduce D_w and solute concentration, while the increase in f_w has the opposite effect, and these opposing responses produce a "humped" functional dependence of weathering on erosion, where weathering rates increase with increasing erosion up to a point, beyond which weathering decreases (see Fig. S5 in the supplement to Maher & Chamberlain (2014) for calculations showing this effect). In turn, erosion rates depend on precipitation (Perron, 2017), topographic relief (Montgomery & Brandon, 2002), and vegetation cover (Collins et al., 2004), among other things. Accounting for the feedback between precipitation and erosion would lead to a stronger coupling between weathering and temperature under circumstances where increased erosion increases weathering rates, as seems to be the case on Earth, where erosion and weathering rates are positively correlated (e.g. Gaillardet et al., 1999). This may make extremely warm climates less likely to occur than a random sampling of parameter combinations in the MAC model would suggest, placing tighter constraints on likely pCO_2 values for planets with operative weathering feedbacks. Similarly, since tectonic uplift generates topographic relief which accelerates erosion, we would expect planets with greater globally-averaged uplift rates and/or more extreme topography to tend to be cooler, all else equal. Topography and uplift are determined by the tectonic state of a planet, which is probably strongly tied to variables like the mass and age (thermal history) of a planetary system. This suggests that continued development of theory surrounding the tectonics of Earth-like planets (see e.g. O'Neill, 2012, for discussion) could point toward observable correlations between HZ climate and bulk parameters like planetary mass or age. Depending on the expected size of the effects, such trends may be observable with OST/HabEx/LUVOIR-generation telescopes, a variant of the weathering feedback detection method discussed in Checlair et al. (2019b).

Limitations of This Study

An important limitation of this study is the exclusion of seafloor weathering. Oceanic crust alteration is an important sink of CO_2 on Earth, and it is possible that this form of weathering is temperature- or pCO_2-dependent, which implies that it may act as a negative feedback on Earth's climate in addition to continental silicate weathering (e.g. Brady & Gislason, 1997; Coogan & Gillis, 2013; Coogan & Dosso, 2015). For example, Krissansen-Totton et al. (2018) found that the inclusion of temperature- and pH-dependent seafloor weathering significantly moderated climate variations in a geological carbon cycle model of Earth's deep past. If seafloor weathering really does act as a negative feedback on climate, then the sensitivity of climate to land fraction, outgassing, and continental surface properties that we found with the MAC formulation of continental weathering should be less extreme. Our results are intended to highlight the different effects of MAC vs. WHAK continental weathering, and correspond to an extreme limit in which seafloor weathering does not act as a stabilizing or destabilizing feedback. Habitability calculations would be improved by an accurate model of seafloor weathering, but this presents a considerable challenge, as there is no clear consensus as to the nature of the seafloor weathering feedback (e.g. Caldeira, 1995), so we did not attempt to model this process. We do, however, suggest that the thermodynamic limit on solute concentration may also be relevant for seafloor weathering: ocean bottom water percolating through hydrothermal systems may reach a maximum concentration of solute analogous to C_{eq} for continental weathering, limiting the importance of kinetic controls on dissolution. In that case, unless the flow rate of water through hydrothermal systems is temperature dependent (analogous to the temperature dependence of runoff on continents), there might be limited scope for seafloor weathering to act as a thermostat. This idea could be explored with reactive transport modeling of seafloor hydrothermal systems. Regardless, the potential for alteration of oceanic crust to stabilize planetary climate is an important subject for further study, and it could have a strong impact on the effective outer edge of the habitable zone.

Another seafloor process left out of our habitability assessment is "reverse weathering", a process by which authigenic clay formation on the seafloor absorbs some fraction of the cations delivered to the ocean by silicate weathering, preventing the absorbed cations from forming carbonates to sequester CO_2 from the atmosphere-ocean system (e.g. Mackenzie & Garrels, 1966a; Dunlea et al., 2017; Isson & Planavsky, 2018; Trower & Fischer, 2019). At greater global rates of reverse weathering, fewer moles of CO_2 are sequestered per unit silicate weathering, forcing a planet to warm up compared to the no-reverse-weathering case so that enough cations are delivered to the ocean to form carbonates and balance a given amount of outgassing. Isson & Planavsky (2018) recently proposed that reverse weathering may provide a stabilizing climate feedback, operating as a complement to the silicate weathering feedback throughout the Precambrian on Earth. If reverse weathering accelerates under high pH (low pCO_2) conditions, then its warming effect should become more pronounced when CO_2 decreases and less pronounced when CO_2 increases, increasing the stability of climate to changes in outgassing (and land fraction) (Isson & Planavsky, 2018). However, the exact functional form of the pH-dependence of reverse weathering reactions is not currently well-constrained, and the significance of the process as a player in Earth's past climate may well have been moderate (Krissansen-Totton & Catling, 2020).

Another shortcoming of our study is the abstraction of inherently three-dimensional processes like precipitation and runoff on continents into zero-dimensional parameterizations. This was appropriate for a first attempt at understanding the implications of the MAC formulation for planetary weathering behavior, but examination of our conclusions with higher dimensional models would be worthwhile. Previous three-dimensional general circulation model (GCM) global weathering studies have used the WHAK formulation (e.g. Donnadieu et al., 2006; Edson et al., 2012; Paradise & Menou, 2017; Paradise et al., 2019). Expanding beyond our zero dimensional models would allow us to quantify the importance of things like continental configuration (e.g. Lewis et al., 2018), atmospheric circulation (e.g. Komacek & Abbot, 2019), clouds (Komacek & Abbot, 2019), and rotation rate (e.g. Yang et al., 2014; Jansen et al., 2019) for planetary precipitation, runoff, and weathering behavior. Importantly, a full GCM study would naturally provide self-consistent treatments of the scalings of runoff and the energetic limit on precipitation with land fraction.

Related to the previous point, this study ignored the crucial and poorly-constrained impacts of clouds on rocky planet climate. Clouds can have a profound impact on planetary albedo: water clouds on Earth reflect away approximately 47.5 W m^{-2} of insolation (Stephens et al., 2012), and simulations of tidally locked planets have found that thick cloud decks at the substellar point can reflect away enough starlight to double the instellation of the inner edge of the HZ for these planets (Yang et al., 2013). We implicitly included a cloud albedo effect by setting the surface albedo of our simulations to $a = 0.3$, approximately equal to Earth's present-day albedo with clouds, but cloud albedo is intimately linked to atmospheric circulation, so a constant cloud albedo is a grave simplification. Clouds can also have a strong greenhouse effect:

water clouds on Earth reduce OLR by approximately 26.4 W m^{-2} (Stephens et al., 2012). However, the particle size distribution for water clouds on exoplanets is completely unconstrained and has a strong impact on their net radiative effect (Komacek & Abbot, 2019). In addition to water clouds, CO_2 ice clouds might be present in the atmospheres of planets with thick CO_2 atmospheres (e.g. Forget & Pierrehumbert, 1997). CO_2 ice clouds have been found to have strong impacts on albedo and outgoing longwave radiation through their scattering properties in the visible and and near-infrared (Forget & Pierrehumbert, 1997; Pierrehumbert & Erlick, 1998), although the magnitude of their effect may have been overestimated (Kitzmann, 2016).

3.5.2 Conclusions

In this study, we applied the weathering framework developed by Maher & Chamberlain (2014) and extended by Winnick & Maher (2018) to evaluate rocky planet climate stability across a range of instellations and parameter choices. The MAC weathering framework includes a thermodynamic limit on weathering product concentration in runoff (C_{eq}) that previous formulations based on WHAK have not considered. C_{eq} is controlled by pCO_2 through the thermodynamics of coupled silicate dissolution and clay precipitation. We also included an energetic limit on global precipitation because instellation drives precipitation through generation of evaporation, meaning the total latent heat flux from global precipitation should not exceed globally averaged instellation (though precipitation may locally exceed absorbed surface instellation slightly due to turbulent heat fluxes from atmosphere to surface, an effect we ignored; see e.g. Pierrehumbert (2002); O'Gorman & Schneider (2008)).

We found that the MAC formulation leads to runoff- and pCO_2-controlled weathering on rocky planets, which leads to interesting changes in planetary weathering behavior compared to simulations with the WHAK formulation that are governed by the kinetics of silicate dissolution. Simulations using the MAC formulation have climates that are more sensitive to CO_2 outgassing rate and land fraction, but they are much less sensitive to the details of silicate dissolution kinetics like temperature- and pCO_2-dependence. These differences are due to the control of weathering rates in the MAC formulation by the thermodynamic balance between silicate dissolution and clay precipitation instead of the kinetics of silicate dissolution. In the WHAK formulation, increasing temperature increases both runoff and silicate dissolution rate, which increases the ability of WHAK planets to modulate their weathering flux with changes in temperature. In the MAC formulation, temperature only has an impact on weathering through changes in runoff (as well as a mild dependence of C_{eq} on temperature, which we excluded from our calculations), which leads to a weaker temperature-dependence of weathering compared to the exponential dependence displayed by WHAK. This means that decreases in land fraction or increases in volcanic outgassing require larger compensatory temperature changes for planets governed by MAC weathering than for WHAK planets.

We also found that planets governed by MAC-style weathering have climates sensitive to the parameterization of hydrology and surface properties like soil age and soil porosity. Changes to these parameters that make global weathering more effective at delivering cations to the ocean at a given temperature and pCO_2 lead to cooler equilibrium climates and move the effective outer edge of the habitable zone closer to the star. The apparent sensitivity of equilibrium rocky planet climate to these parameters suggests that "Earth-like" planets may be sensitive to the shifts in surface properties that are likely on a tectonically active surface, e.g. changes in uplift or outgassing rate. There may be significant risk of catastrophic transitions to moist greenhouse or snowball states through stochastic changes to the parameters that control weathering.

Lastly, we showed that the energetic limit on precipitation set by planetary instellation can unintuitively lead to increases in planetary temperature with decreases in instellation. This is because planets that have reached their maximum precipitation at a given instellation lose the feedback on climate provided by modulation of weathering flux in response to temperature through changes in planetary precipitation. Simulations beyond the instellation where the energetic limit kicks in experience a linear decrease in runoff with reduced instellation, which forces pCO_2 to increase to higher levels so that C_{eq} can increase to levels that allow runoff to carry enough solute for weathering to balance outgassing. This larger increase in pCO_2 with decrease in instellation in the energetically-limited regime leads to the increase in temperature with reduced instellation in some regions of parameter space, though at sufficiently high partial pressures the increase in pCO_2 can also lead to cooling as the increased Rayleigh scattering of a thicker atmosphere begins to outweigh the increased greenhouse effect.

In summary, the inclusion of energetic and thermodynamic limits in our simulations of continental silicate weathering on rocky, ocean-bearing exoplanets leads to a diversity of stable climates throughout the habitable zone, ranging from >350 K to freezing, depending on a complex interplay of poorly-understood factors. This diversity has important implications for the potential of future telescope missions to infer the operation of the silicate weathering feedback in the habitable zone with population statistics (see Section 3.5.1). The use of the MAC formulation allows for the explicit incorporation of variables like lithology, hydrology, and soil properties into models of terrestrial planet weathering, which allows for the investigation of a wealth of interesting questions about planetary habitability and the coupling of atmospheres and crusts. Future studies of rocky planet climate and weathering should consider applying the MAC framework instead of, or in addition to, the WHAK framework.

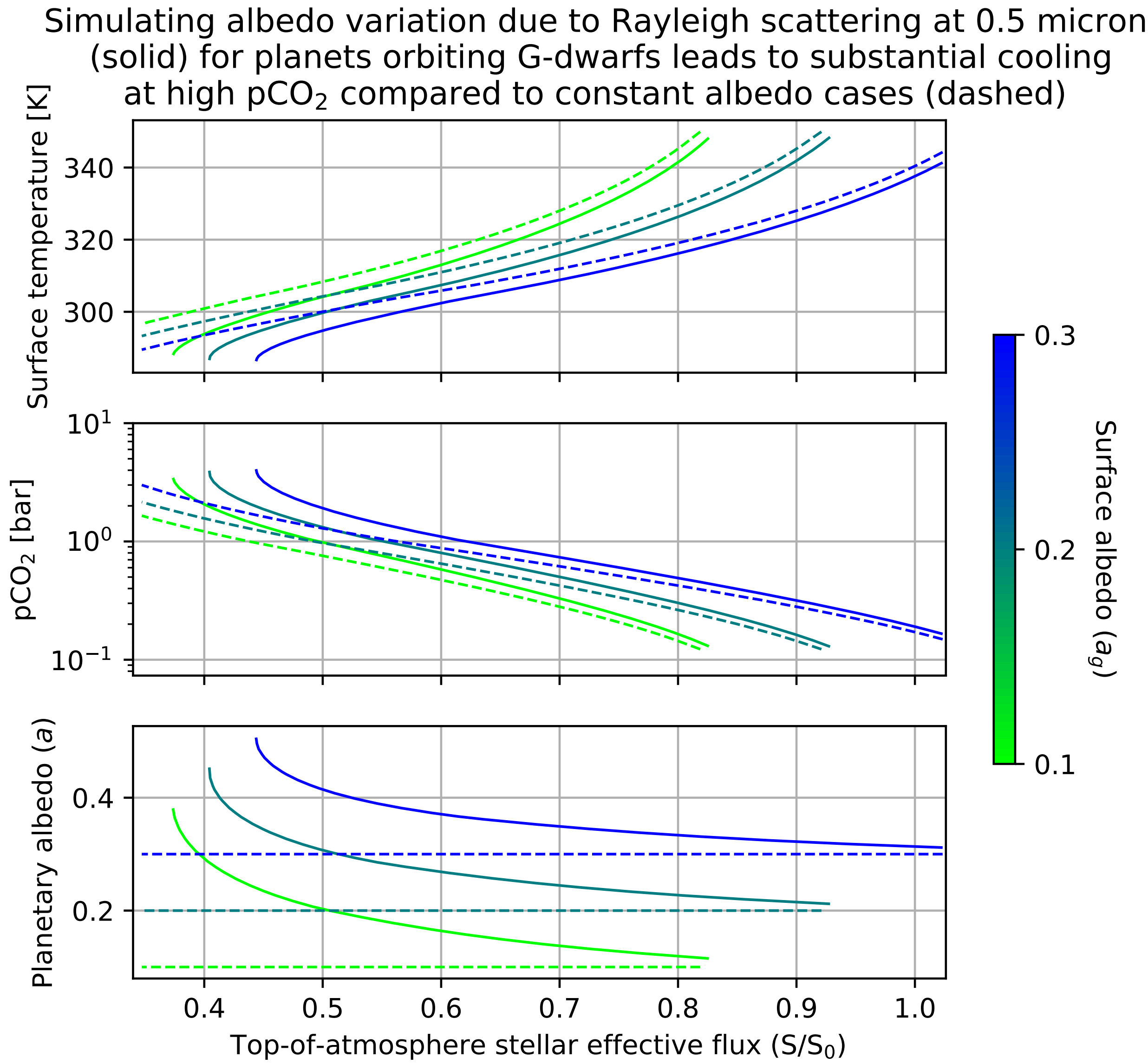

Figure 3.6: **Comparison of temperature, pCO_2, and planetary albedo vs. instellation in MAC simulations with (solid curves) and without (dashed curves) planetary albedo that varies as a function of pCO_2 and surface albedo.** The top plot shows relative instellation – the ratio of top-of-atmosphere instellation to modern day Earth instellation (S/S_0, where $S_0 = 1368$ W m^{-2})– vs. temperature (T). The middle plot shows relative instellation vs. pCO_2. The bottom plot shows relative instellation vs. planetary albedo. The bluest curves in each plot have a surface albedo $a_g = 0.3$, the blue-green curves have $a_g = 0.2$, and the green curves have $a_g = 0.1$. The thermodynamic coefficient $\Lambda = \Lambda_0/5$ in these simulations so that climates would reach high enough pCO_2 for Rayleigh scattering to become important. Other parameters take their default values.

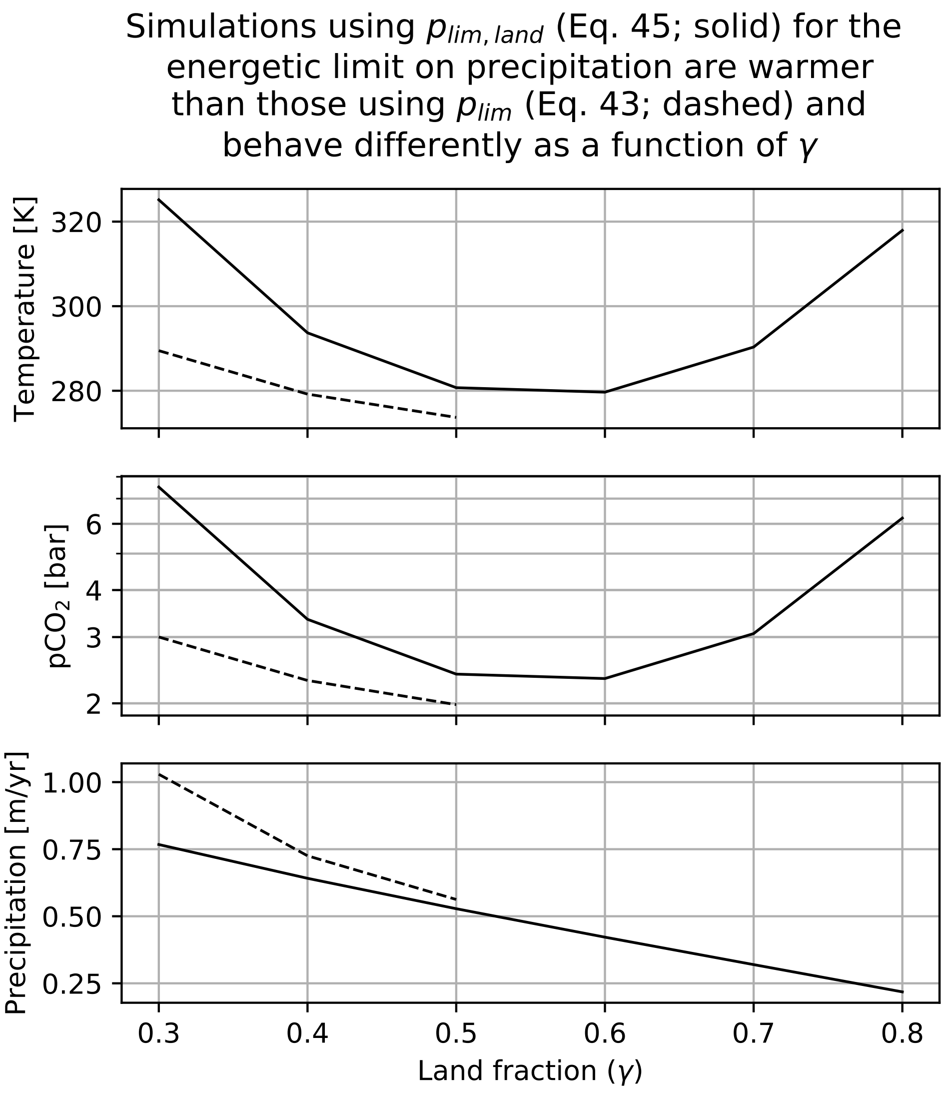

Figure 3.7: **A comparison of temperature, pCO_2, and precipitation at the classical outer edge of Earth's habitable zone ($S/S_0 = 0.346$ (Kopparapu et al., 2013)) as a function of land fraction (γ) for planets with an energetic limit on precipitation that either scales with ocean surface fraction (solid curves; equation 3.45) or is independent of ocean surface fraction (dashed curves; equation 3.43).** The top panel shows γ vs. temperature (T), the middle panel shows γ vs. pCO_2, and the bottom panel shows γ vs. precipitation (p). The simulations have thermodynamic coefficient $\Lambda = \Lambda_0/5$, but other parameters take their default values.

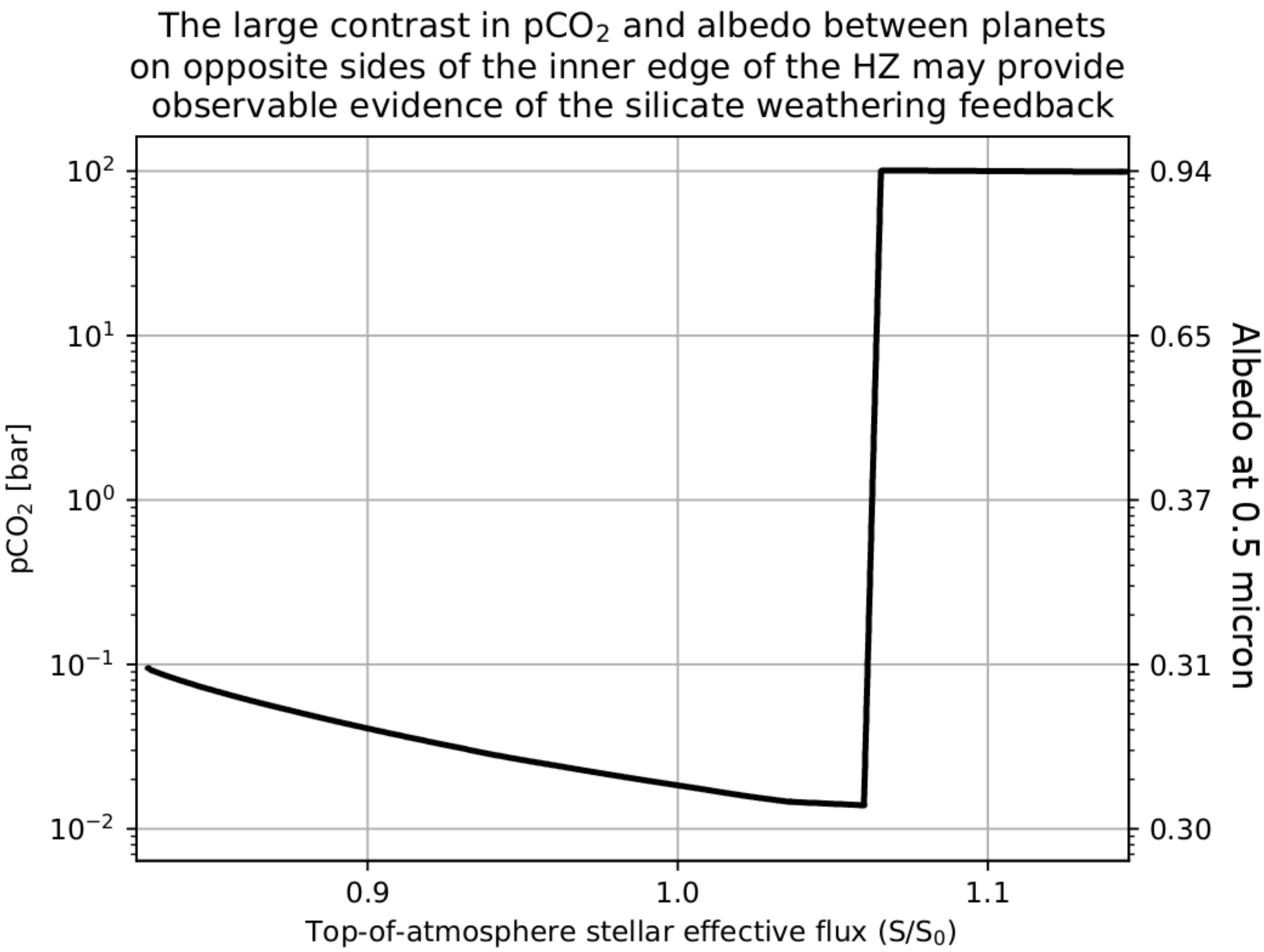

Figure 3.8: **A schematic plot showing variation of pCO_2 (left y-axis) and albedo (right y-axis) with instellation across the inner edge of the habitable zone (defined as the instellation at which a planet enters a runaway greenhouse and loses its oceans to space).** This curve is an illustration of what we expect to see based on the contrast between Earth and Venus in our solar system, and does not represent calculations we carried out. Planets with functional silicate weathering feedbacks within the habitable zone but near its inner edge will have low pCO_2 due to high instellation, while planets closer to the star than the inner edge of the habitable zone may experience catastrophic decarbonation of their carbonate minerals due to extreme heating by a post-runaway greenhouse steam atmosphere. The orders-of-magnitude difference in the pCO_2 and large contrast in albedo on opposite sides of the inner edge of the HZ may allow a statistically robust observation of the "pCO_2 cliff" with a small number of characterizations of planets' CO_2 abundances and/or albedos, confirming the operation of the silicate weathering feedback and helping to better constrain the location of the inner edge. The dependence between pCO_2 and albedo we used to generate the albedo axis in this plot assumes a surface albedo of 0.3; with a lower surface albedo, the contrast in albedos across the inner edge of the HZ would be even larger.

Chapter 4

CO_2 ocean bistability on terrestrial exoplanets

Mountains, a moment's earth-waves rising and
hollowing; the earth too's an ephemerid; the stars—
Short-lived as grass the stars quicken in the nebula
and dry in their summer, they spiral
Blind up space, scattered black seeds of a future;
nothing lives long, the whole sky's
Recurrences tick the seconds of the hours of the ages
of the gulf before birth, and the gulf
After death is like dated: to labor eighty years in a
notch of eternity is nothing too tiresome,
Enormous repose after, enormous repose before, the
flash of activity.
Surely you never have dreamed the incredible depths
were prologue and epilogue merely
To the surface play in the sun, the instant of life,
what is called life? I fancy
That silence is the thing, this noise a found word for
it; interjection, a jump of the breath at that silence;
Stars burn, grass grows, men breathe: as a man
finding treasure says "Ah!" but the treasure's the
essence;
Before the man spoke it was there, and after he has
spoken he gathers it, inexhaustible treasure.

The Treasure
Robinson Jeffers

Abstract

Note: This chapter was published as Graham et al. (2022b). Cycling of carbon dioxide between the atmosphere and interior of rocky planets can stabilize global climate and enable planetary surface temperatures above freezing over geologic time. However, variations in global carbon budget and unstable feedback cycles between planetary sub-systems may destabilize the climate of rocky exoplanets toward regimes unknown in the Solar System. Here, we perform clear-sky atmospheric radiative transfer and surface weathering simulations to probe the stability of climate equilibria for rocky, ocean-bearing exoplanets at instellations relevant for planetary systems in the outer regions of the circumstellar habitable zone. Our simulations suggest that planets orbiting G- and F-type stars (but not M-type stars) may display bistability between an Earth-like climate state with efficient carbon sequestration and an alternative stable climate equilibrium where CO_2 condenses at the surface and forms a blanket of either clathrate hydrate or liquid CO_2. At increasing instellation and with ineffective weathering, the latter state oscillates between cool, surface CO_2-condensing and hot, non-condensing climates. CO_2 bistable climates may emerge early in planetary history and remain stable for billions of years. The carbon dioxide-condensing climates follow an opposite trend in $p\mathrm{CO}_2$ versus instellation compared to the weathering-stabilized planet population, suggesting the possibility of observational discrimination between these distinct climate categories.

4.1 Introduction

Earth's surface is dominated by a liquid water ocean in direct contact with the lithosphere. This state of affairs seems to be crucial for Earth's long-term climate stability and habitability, with the carbonate-silicate cycle modulating and stabilizing the planet's atmospheric CO_2 inventory through a set of water-rock chemical reactions taking place on the continents and seafloor (Walker et al., 1981; Berner et al., 1983; Coogan & Gillis, 2013; Penman et al., 2020). The carbonate-silicate cycle acts as a thermostat when CO_2 is a net greenhouse gas; however, when CO_2 builds to high enough levels, it increases planetary Rayleigh scattering and behaves as a coolant, which can convert the carbonate-silicate cycle into a destabilizing positive feedback. This suggests that otherwise Earth-like planets with large enough carbon inventories might be able to support climate configurations with high enough $p\mathrm{CO}_2$ for either a hot, supercritical, Venus-like atmosphere at high instellations or an exotic, subcritical atmosphere with surface liquid CO_2 condensation coexisting with a liquid water ocean at low instellations. Planets of the latter variety might be difficult to remotely distinguish from more traditionally "Earth-like" planets lacking surface CO_2 condensation at equivalent orbits, but the geochemistry and potential habitability of these worlds would be radically different, even with a temperate surface climate. Most previous examinations of surface CO_2 condensation on terrestrial (exo)planets have focused on cold, glaciated climates where CO_2 would only condense as a solid (Turbet et al., 2017; Kadoya & Tajika, 2019; Bonati & Ramirez, 2021); waterworlds with high pressure ice mantles (Ramirez & Levi, 2018; Marounina & Rogers, 2020); or the potential for CO_2 condensation on Mars in the deep past (Kasting, 1991; Forget et al., 2013; Soto et al., 2015). In this study, we focus on surface CO_2 condensation on rocky exoplanets with temperate climates in different end-member weathering regimes that inform the anticipated diversity of potentially habitable planets (Kasting et al., 1993; Wordsworth et al., 2010b; von Paris et al., 2013).

From an astronomical perspective, carbon compounds are strongly depleted on the terrestrial planets of the Solar System relative to the nominal values in the Sun or the interstellar medium (Öberg & Bergin, 2021) as a result of processes operating in the protoplanetary disk (Krijt et al., 2020; Li et al., 2021) and on planetesimals (Hirschmann et al., 2021; Lichtenberg & Krijt, 2021). In addition, volatile partitioning into metal and melt phases can redistribute major carbon and hydrogen carriers between core, mantle, and atmospheric reservoirs and partly decouple the initially accreted volatile reservoir (Grewal et al., 2020; Fischer et al., 2020) from the atmospheric composition of rocky exoplanets. A recent example is provided by the outer TRAPPIST-1 planets, for which mass-radius contraints suggest volatile mass fractions on the order of several weight per cent (Agol et al., 2021). On a statistical level, the larger sub-Neptune cluster of the Kepler radius valley suggests that at least a fraction of systems accrete substantial volatile mass budgets during their formation (Zeng et al., 2019; Venturini et al., 2020). The anticipated variation in carbon abundance suggests that the majority of rocky exoplanets may exhibit diverse climate regimes, for which the thermodynamic limits to maintain clement surface states are poorly understood (Lichtenberg et al., 2022). Future exoplanet surveys that will aim to probe the atmospheres of temperate exoplanets to test the range of climate diversity (Gaudi et al., 2020; Quanz et al., 2021; Checlair et al., 2021) will rely on physically motivated theories to interpret their findings.

Here, we study the interplay between silicate weathering and CO_2 pressure variations to probe the limits of clement climates on terrestrial exoplanets. We use 1-D, two-stream radiative transfer and carbon cycle simulations to investigate the behavior of climates with high partial pressure of CO_2 ($p$$CO_2$) and low irradiation from the central star ($S_{\rm eff}$) without (sections 4.3.1, 4.3.2) and with (section 4.3.3) weathering feedbacks. Our simulations suggest that terrestrial planets at low instellations in the classical circumstellar habitable zone (HZ; Kasting et al., 1993) may emerge from their accretionary period directly into stable climate states with long-lasting periods of liquid CO_2 surface condensation, even in cases where they are not initially globally glaciated.

4.2 Methods

In this study we combine global-mean, clear-sky climate and silicate weathering calculations to examine the interplay between radiative and geochemical feedbacks on ocean-bearing, high-$p$$CO_2$ planets in the outer reaches of the classical habitable zone. Here we briefly outline the procedure we follow and the models we use for the radiative calculations and the weathering calculations.

4.2.1 Radiative transfer

We carry out radiative transfer calculations using the SOCRATES code (Edwards & Slingo, 1996), solving the plane-parallel, two-stream approximated radiative transfer equation with scattering (see the extensive description in Lichtenberg et al., 2021, though note that the implementation in that paper does not include scattering). Opacity coefficients are tabulated and derived from the HITRAN database, making use of the line-by-line and collision-induced absorption coefficients for H_2O (Gordon et al., 2017), CO_2 (Gordon et al., 2017; Gruszka & Borysow, 1997), N_2 (Gordon et al., 2017; Karman et al., 2015), and the H_2O continuum (Mlawer et al., 2012). We note that the CO_2 continuum spectrum is uncertain at high temperatures and pressures, which introduces a potentially significant source of error into our calculations (e.g. Halevy et al., 2009; Wordsworth et al., 2010a).

Molecule	A [units of 10^{-6}]	B [units of 10^{-3}]	Δ	σ_0 [10^{-7} m^2 kg^{-1}]
CO_2	4.39	6.4	0.0805	–
N_2	2.906	7.7	0.0305	–
H_2O	–	–	–	9.32

Table 4.1: Tabulation of Rayleigh scattering data used in this study. A and B values come from Cox (2015). σ_0 for H_2O is drawn from Pierrehumbert (2010a). Δ values come from Vardavas & Carver (1984).

Rayleigh scattering cross-sections for CO_2 and N_2 are calculated following Vardavas & Carver (1984)

$$\sigma_{R,i} = \frac{0.2756}{\mu_i} \times \frac{6+3\Delta}{\lambda^4(6-7\Delta)}[A(1+\frac{B}{\lambda^2})]^2, \tag{4.1}$$

where the subscript i iterates over the species present, $\sigma_{R,i}$ [m^2 kg^{-1}] is the Rayleigh scattering cross-section, μ_i is the molar mass of species i [kg mol^{-1}], λ [μm] is wavelength, coefficients A and B are taken from Cox (2015), Δ is the depolarization factor, and the numerical values we use are given in Table 4.1. For H_2O, as far as we are aware, values for the coefficients A and B have not been published at the relevant wavelengths. For this reason, and because H_2O is a minor constituent in the atmospheres we simulate, we use a simple λ^{-4} scaling to calculate H_2O's Rayleigh scattering cross-section,

$$\sigma_{R,H_2O} = \sigma_{R,0}\frac{\lambda_0^4}{\lambda^4}, \tag{4.2}$$

where $\sigma_{R,0} = 9.32 \times 10^{-7}$ m^2 kg^{-1} (Pierrehumbert, 2010a) and $\lambda_0 = 1$ μm. Here we take the opportunity to note that some previous papers (Kopparapu et al., 2013; Pluriel et al., 2019), have erroneously used H_2O Rayleigh scattering coefficients calculated using a depolarization ratio that was drawn from a study (Marshall & Smith,

1990) of the scattering properties of *liquid* H_2O, not water vapor. The total Rayleigh scattering cross-section is calculated by summing the cross-sections of the individual species, weighted by volumetric mixing ratio,

$$\sigma_{R,\mathrm{tot}} = \sum_i x_i \sigma_{R,i}, \tag{4.3}$$

where x_i represents the volumetric mixing ratio of a given species ($\sum_i x_i = 1$). SOCRATES does not allow vertically-varying Rayleigh scattering coefficients, so we take the mixing ratios at the surface to calculate the total scattering cross-sections.

The primary stellar spectrum we use in the presented calculations is based on measurements of the Sun's spectral irradiance (Kurucz, 1995), and thus represents irradiation from a G2V star. To show how the climate behaviors we identify depend on stellar type and age, we also present sets of simulations using spectra from AD Leonis, an M3.5V star (Segura et al., 2005), and Sigma Boötis, an F2V star (Segura et al., 2003). The different spectra result in different planetary albedo values for a given atmospheric composition and climate. We also tested the effects of a change in the solar spectrum with time: at 4.5 and 3.8 Ga before present (Claire et al., 2012) our simulations produced results that differed negligibly from the fiducial, modern case.

We apply a generalized pseudoadiabat formula (Graham et al., 2021) to calculate atmospheric temperature-pressure profiles with a variety of compositions and surface boundary conditions. This pseudoadiabat formula incorporates the fraction of retained condensate as a freely tunable parameter which can significantly impact the specific heat capacity and lapse rate in atmospheres with non-dilute condensable species. In our calculations, we assume that all condensate is instantaneously rained out upon condensation. We also assume H_2O saturation in the main set of simulations discussed in this paper. This formula is useful because it allows us to self-consistently calculate atmospheric profiles with any combination of condensable (e.g. H_2O, CO_2) and non-condensable (e.g. N_2) gases, though the atmospheres we focus on in this paper are simply CO_2+H_2O (sensitivity tests with up to 10 bar of N_2 produced qualitatively identical results, as expected). Throughout this paper, unless otherwise noted, atmospheres are taken to have isothermal stratospheres with $T_{\mathrm{strat}} = 150$ K. This is comparable to the stratospheric temperatures hypothesized for high-CO_2 planets in the outer reaches of the classical circumstellar habitable zone (Kopparapu et al., 2013), and time-stepped radiative-convective calculations in high-pCO_2 atmospheres have recovered a stratospheric temperature of 150 K (Wordsworth & Pierrehumbert, 2013). Condensation of H_2O and CO_2 is assumed to cease within the stratosphere, so the mixing ratios remain constant at pressure levels below the highest pressure level (lowest altitude level) with a temperature of 150 K. Assuming a constant stratospheric temperature considerably simplifies our climate calculations (described further below), at the expense of neglecting the feedback between instellation and stratospheric temperature, which can change a planet's outgoing longwave radiation and thus its surface temperature. Sensitivity tests carried out with an increased stratospheric temperature of up to 200 K demonstrate that the effect on climate is minor, with no qualitative changes to our results.

For rapid simulation of a wide range of surface conditions, we take an "inverse climate modeling" approach (Kasting, 1991). This entails choosing a $p\mathrm{CO_2}$ and a surface temperature (which in turn specifies $p\mathrm{H_2O}$ by the Clausius-Clapeyron relation), using those values as boundary conditions to integrate the pseudoadiabat from the surface up to the 150 K isothermal stratosphere, and running the radiative transfer code to get the OLR and albedo for that specific atmospheric temperature/pressure/composition combination. With those values, we can calculate the instellation necessary to maintain global-mean energetic balance between incoming and outgoing radiation,

$$(1-\alpha(T,\mathrm{pCO_2}))\frac{S}{4} = F_{\mathrm{out}}(T,\mathrm{pCO_2}), \tag{4.4}$$

$$S_{\mathrm{eff}}(T,\mathrm{pCO_2}) = \frac{S}{S_{\mathrm{Earth}}} = \frac{4F_{\mathrm{out}}(T,\mathrm{pCO_2})}{S_{\mathrm{Earth}}(1-\alpha(T,\mathrm{pCO_2}))}, \tag{4.5}$$

where S is top-of-atmosphere instellation, $S_{\mathrm{Earth}} = 1368$ W m^{-2} is Earth's present-day instellation, S_{eff} is the fraction of present-day Earth's instellation (e.g. $S_{\mathrm{eff}} = 0.3$ is equivalent to 30% of present-day Earth instellation), F_{out} is the OLR, and α is the global-mean planetary albedo, with the cosine of the stellar zenith angle assumed to be the instellation-weighted global mean of $\frac{2}{3}$ in all calculations (Cronin, 2014). We also set the surface albedo to 0.0, similar to the albedo of a cloudless sea surface, which would be 2–4% at the chosen stellar zenith angle (Li et al., 2006). Low-lying marine stratocumulus clouds that would increase the near-surface albedo to levels above that of the sea surface are expected to dissipate at $\mathrm{CO_2}$ levels far lower than 1 bar, the lowest $p\mathrm{CO_2}$ evaluated in this study, due to the inhibition of cloud-top radiative cooling and subsequent shutdown of cloud-sustaining lower-tropospheric convection (e.g. Schneider et al., 2019), though of course other processes could still cause low-lying clouds or hazes that would affect near-surface albedo on these planets.

We carried out a grid of these inverse climate calculations for $p\mathrm{CO_2}$ levels ranging from 1 bar to 73 bar with increments of 1 bar and for T_{surf} from 250 K to 365 K with increments of 5 K. Fig. 4.1 shows equilibrium S_{eff} (panel A), OLR (panel B), and albedo (panel C), all as functions of $T_{\rm surf}$ and pCO$_2$. Linear interpolation of OLR and albedo to temperatures and pCO$_2$ levels between the climate grid points allows for fast climate calculations to examine a wide variety of scenarios.

4.2.2 Carbon cycling

To examine how the carbon cycle might operate on abiotic terrestrial planets under very high pCO$_2$ conditions, we apply an idealized global-mean weathering formulation (Graham & Pierrehumbert, 2020) based on work that accounts for the impact of clay precipitation on weathering solute concentrations (Maher & Chamberlain, 2014) on the global-mean weathering flux,

$$W = \gamma \frac{\alpha}{[k_{\rm eff}]^{-1} + mAt_{\rm s} + \alpha[qC_{\rm eq}]^{-1}}, \tag{4.6}$$

where W [mol m^{-2} yr^{-1}] is the global-mean weathering flux, i.e. the total number of divalent cations (which react with oceanic carbon to form carbonate minerals, ultimately removing CO_2 from the atmosphere) delivered to the ocean from the land and/or seafloor in a year, divided by the surface area of the planet; γ is the fraction of planetary surface that is weatherable; α is a parameter that captures the effects of various weathering zone properties like characteristic water flow length scale, porosity, ratio of mineral mass to fluid volume, and the mass fraction of minerals in the weathering zone that are weatherable; $k_{\rm eff} = k_{\rm eff,ref} \exp\left(\frac{T_{\rm surf} - T_{\rm surf,ref}}{T_e}\right)\left(\frac{p{\rm CO}_2}{p{\rm CO}_{2,\rm ref}}\right)^{\beta}$ [mol m^{-2} yr^{-1}] is the effective kinetic weathering rate, i.e. the weathering rate in the absence of chemical equilibration with clay precipitation (Walker et al., 1981); m [kg mol^{-1}] is the average molar mass of minerals being weathered; A [m^2 kg^{-1}] is the average specific surface area of the minerals being weathered; t_s [yr] is the mean age of the material being weathered; $q = q_{\rm ref}(1 + \epsilon(T_{\rm surf} - T_{\rm surf,ref}))$ [m yr^{-1}] is the volume-weighted global-mean flux of water through the planet's weathering zones (in this study we apply a linear temperature dependence to runoff, based on the behavior of surface H_2O precipitation on Earth, but we note that the functional form for q could be very different when modeling seafloor weathering); and $C_{\rm eq} = \Lambda({\rm pCO_2})^n$ [mol m^{-3}] is the maximum concentration of divalent cations in the water passing through weathering zones, as determined by chemical equilibrium between silicate dissolution and clay precipitation. The values of all constants are given in Table 4.2. A more thorough set of weathering calculations would carefully account for the lithology of minerals being weathered (Hakim et al., 2021) and the differences between continental and seafloor weathering (Hayworth & Foley, 2020; Hakim et al., 2021), but our calculations are meant to be illustrative of the qualitative behavior of the carbon cycle under non-terrestrial conditions, so we restrict our simulations to the simplified approach in our equation 4.6.

Parameter	**Units**	**Definition**	**Fiducial Value**
γ	–	Land fraction	0.3
a_g	–	Surface albedo	0.0
R_{planet}	meters (m)	Planetary radius	6.37×10^6
T_{ref}	Kelvin (K)	Reference global-avg. temperature	288
$p\text{CO}_{2,\text{ref}}$	bar	Reference CO_2 partial pressure	280×10^{-6}
q_{ref}	m yr^{-1}	Modern global-avg. runoff	0.20 (Oki et al., 2001)
ϵ	1/K	Fractional change in precip. per K change in temp.	0.03
V_{ref}	mol yr^{-1}	Modern global CO_2 outgassing	7.5×10^{12} (Gerlach, 2011; Haqq-Misra et al., 2016)
v	mol m^{-2} yr^{-1}	Modern CO_2 outgassing per m^2 planetary area	0.0147
Λ	variable	Thermodynamic coefficient for C_{eq}	1.4×10^{-3}
n	–	Thermodynamic $p\text{CO}_2$ dependence	0.316
α*	–	$L\phi\rho_{sf}AX_r\mu$ (see Section 4.2.2 and below)	3.39×10^5
$k_{\text{eff,ref}}$*	mol m^{-2} yr^{-1}	Reference rate constant	8.7×10^{-6}
β	–	Kinetic weathering $p\text{CO}_2$ dependence	0.2 (Rimstidt et al., 2012)
T_{e}	Kelvin	Kinetic weathering temperature dependence	11.1 (Berner, 1994)

Table 4.2: Model parameters used in this study. This table lists parameters used in our calculations, their units, their definitions, and the default values they take. A single asterisk (*) means the default parameter value was drawn from Table S1 of the supplement to Maher & Chamberlain (2014). For default parameters drawn from other sources, the citation is given in the "Value" column.

Assuming the presence of weatherable silicates on a planetary surface, the global weathering flux of divalent cations into the ocean, which is equal to the global CO_2 consumption flux at equilibrium and in the absence of CO_2 surface condensation, is dependent on both background CO_2 and $T_{\rm surf}$. An increase to $p\rm CO_2$ or $T_{\rm surf}$ leads to an increase in the weathering rate, with the change mediated by either changes to the kinetics of silicate dissolution or changes to global runoff flux, depending on which term in equation 4.6 is dominant. This climate-dependence of CO_2 consumption means that silicate weathering can act as a stabilizing negative feedback on planetary climate (Walker et al., 1981). If the CO_2 outgassing flux from volcanoes and other sources (V) is greater than the CO_2 consumption flux from weathering, i.e. if $V > W$, and if there is no CO_2 surface condensation, CO_2 will accumulate in the atmosphere, which, under Earth-like circumstances, tends to warm the planet. Higher $p\rm CO_2$ and higher $T_{\rm surf}$ both lead to larger W, driving the CO_2 consumption rate closer and closer to V until CO_2 consumption is equal to CO_2 production and the atmospheric CO_2 inventory stabilizes. The same process in reverse acts to cool the planet and equilibrate the carbon cycle in cases where $W > V$. So, at least in the cases just discussed, climate on planets with silicate weathering will tend to find an equilibrium $T_{\rm surf}$ and $p\rm CO_2$ determined by the balance between silicate weathering and CO_2 outgassing, which can be stated simply as

$$V = W, \tag{4.7}$$

where V [mol m^{-2} yr^{-1}] is an assumed CO_2 outgassing flux and W is the weathering flux as defined in equation 4.6. The intersection points in $T_{\rm surf}$–$p\rm CO_2$ space of the nullclines given by equations 4.4 and 4.7 are climate states in equilibrium with respect to both energy and carbon fluxes.

The weathering parameterization represented by equations 4.6 and 4.7 implies the assumption of an Earth-like tectonic regime where the resurfacing of fresh silicates occurs rapidly enough to maintain a weathering flux in balance with CO_2 outgassing. This need not be the case: for example, if a planet is in a "sluggish lid", "episodic lid", or "stagnant lid" tectonic regime (e.g. Valencia & O'Connell, 2007; Korenaga, 2010; Kite et al., 2009; Foley, 2015; Lenardic, 2018; Lichtenberg et al., 2022), resurfacing may not be fast enough for weathering to keep up with the outgassing rate, leading to a global depletion of weatherable materials called "supply limitation" (West et al., 2005) or "transport limitation" (Kump et al., 2000), which in turn allows for volcanic CO_2 accumulation. Further, even with rapid tectonic resurfacing, the particular climate and/or arrangement of land on a given planet may not allow for high enough weathering fluxes to match outgassing rates, as we will go on to demonstrate. For these cases, it is important to note that surface CO_2 condensation can act as another major sink of atmospheric CO_2 (Kasting, 1991; Wordsworth et al., 2010b; von Paris et al., 2013; Turbet et al., 2017; Kadoya & Tajika, 2019; Bonati & Ramirez, 2021). As a result, under CO_2-condensing conditions, it is possible for the carbon cycle to reach equilibrium even when outgassing does not equal weathering, as condensation can make up the difference,

$$F_{\mathrm{cond}} = V - W, \tag{4.8}$$

where F_{cond} [mol m^{-2} yr^{-1}] is the flux of CO_2 condensing out onto the surface from the atmosphere.

4.3 Results

4.3.1 Climate hysteresis from temperature-dependent instellation absorption of H_2O

In climate simulations with high $p\mathrm{CO}_2$, cooling by Rayleigh scattering begins to outweigh greenhouse warming, such that temperature eventually begins to decrease while CO_2 increases (Fig. 4.1): in panel A, starting from the lowest $p\mathrm{CO}_2 = 1$ bar, each contour of S_{eff} moves to higher temperatures as CO_2 increases, until a peak T_{surf} is reached at a threshold $p\mathrm{CO}_2$, beyond which T_{surf} for a given S_{eff} begins to decrease as CO_2 increases. For instance, for $S_{\mathrm{eff}} = 0.4$ this peak is at $\approx$280 K and $p\mathrm{CO}_2 = 10$ bar. This occurs because, at high $p\mathrm{CO}_2$, the albedo (panel C) increases more rapidly with $p\mathrm{CO}_2$ than the OLR (panel B) decreases, since the atmosphere has become optically thick at almost all IR wavelengths. In other words, for any given S_{eff} and background gas composition, there is a maximum temperature that cannot be exceeded by adding

CO_2 to the atmosphere. This effect has been used to define the outer edge of the classical liquid water habitable zone as the lowest instellation at which atmospheres with 1 bar N_2, saturated H_2O, and variable CO_2 can maintain an Earth-like planet's global-mean surface temperature above freezing (Kasting et al., 1993; Kopparapu et al., 2013), i.e. the S_{eff} where the peak temperature is $T_{\text{surf}} = 273.15$ K. Using this "maximum greenhouse limit," the outer edge of the liquid water habitable zone has been placed at 1.67 astronomical units (au) (Kopparapu et al., 2013) , implying $S_{\text{eff}} = \frac{1}{1.67^2} = 0.359$, with $p\text{CO}_2 \approx$6-7 bar. Our fiducial simulations lack N_2, but, in comparison with Kopparapu et al. (2013), produce a similar value of $S_{\text{eff}} = 0.373$ for the lowest instellation where T_{surf} can be maintained above freezing, with $p\text{CO}_2 \approx$5-6 bars, demonstrating our climate model produces comparable results to previous efforts.

At low values of S_{eff} (e.g. along the white-dotted $S_{\text{eff}} = 0.40$ contour in Fig. 4.1A), we find that the climate responds smoothly to increases in $p\text{CO}_2$, with T_{surf} first increasing and then decreasing until reaching a $p\text{CO}_2$–T_{surf} combination that allows the CO_2 to condense at the surface. This is the point where a given S_{eff} contour intersects the black line that bounds the bottom-right grey area in Fig. 4.1A. At this point CO_2 is saturated and our simulations assume that any CO_2 added to the atmosphere simply condenses out onto the surface.

As S_{eff} increases, the maximum temperature climates can reach becomes higher and higher. H_2O is saturated in our simulations and, as such, $p\text{H}_2\text{O}$ increases exponentially with temperature. Therefore, as S_{eff} increases, water's impact on the climate also becomes more and more prominent. In addition to its well-known greenhouse effect, water can impact planetary albedo via several mechanisms, for instance via cloud and sea ice formation. Less obvious impacts of water on planetary albedo come from its contribution to Rayleigh scattering and its competing contribution to shortwave and near-IR absorption. At low $p\text{CO}_2$ ($\lesssim$ 3 bar) and high temperatures where $p\text{H}_2\text{O}$ is comparable to $p\text{CO}_2$, our simulations indicate that the Rayleigh scattering effect of water starts to become important, which is why the albedo contours bend leftward in the upper-left corner of Fig. 4.1C, indicating an increase in albedo from enhanced H_2O Rayleigh scattering as temperature increases. However, at high enough CO_2 ($\gtrsim$ 1.5 bar), $p\text{CO}_2$ remains much larger than $p\text{H}_2\text{O}$ even at the highest temperatures we simulated, and hence the Rayleigh scattering effect of H_2O is outweighed by that of CO_2. This suggests that increases to surface temperature up to 360 K stop significantly increasing a planet's Rayleigh scattering albedo via H_2O accumulation at $p\text{CO}_2$ above a few bar.

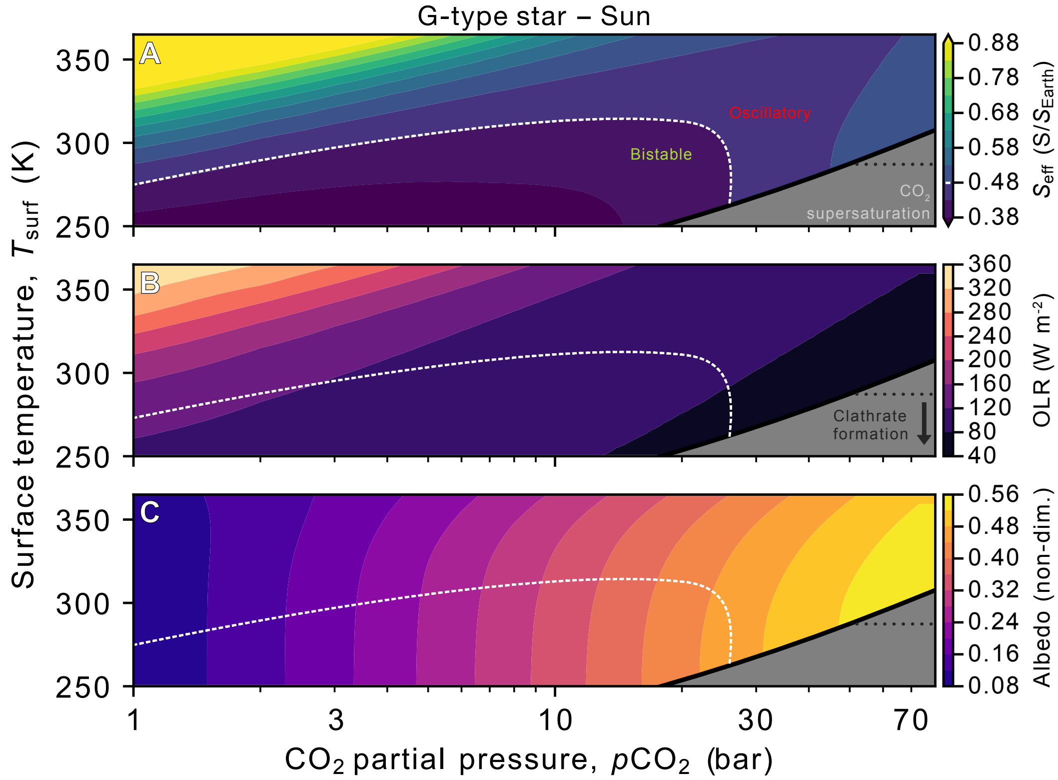

Figure 4.1: **Energetic properties of terrestrial planetary climates at low instellation as a function of surface temperature $T_{\rm surf}$ (y-axes) and CO_2 partial pressure (x-axes).** In each panel, the black line represents the CO_2 saturation vapor pressure curve; climates with CO_2 greater than that of the vapor pressure curve at a given temperature are super-saturated at their surface (grey region in all three panels). The white dotted line in each panel represents the approximate contour location of the $S_{\rm eff}$ value separating climates that can support CO_2 bistability vs. those that may limit cycle between condensing and non-condensing states (see Sections 4.3.2 and 4.3.3 for discussion of those climate types). The black dotted line in each panel marks the temperature below which CO_2 clathrate hydrates may be stable. In panel A, the contours represent the top-of-atmosphere stellar irradiation required to maintain a climate with a given surface temperature and pCO_2, normalized by the instellation received at Earth's orbit, i.e. $S/S_{\rm Earth} = S_{\rm eff}$. Panel B shows the global-mean outgoing longwave radiation (OLR). Panel C shows the global-mean planetary albedo.

Although H_2O's Rayleigh scattering ceases to be important at high pCO_2, H_2O's shortwave and near-IR absorption remain important, such that the elevated water content caused by increased temperature leads to increased absorption of instellation: albedo and equilibrium $S_{\rm eff}$ decrease with increased temperature at high pCO_2, as indicated by the rightward tilt of $S_{\rm eff}$ and albedo contours in the upper-right quadrants of Fig. 4.1 A and C. In other words, at high pCO_2, H_2O saturation leads to temperature-dependent planetary albedo similar to that caused by the ice-albedo feedback, though occurring at temperatures higher than those where the ice-albedo feedback is relevant. This temperature-dependent instellation absorption by H_2O introduces a form of hysteresis into the climate system that is analogous to the hysteresis caused by the ice-albedo feedback (Abbot et al., 2018), the consequences of which we explore here.

4.3.2 CO_2 ocean oscillations on temperate exoplanets

Climate limit cycling usually refers to the potential for climates to oscillate back and forth between snowball and temperate states (Menou, 2015; Haqq-Misra et al., 2016; Abbot, 2016; Paradise & Menou, 2017). That occurs when a temperate planet on which weathering dominates outgassing has its CO_2 drawn down until the ice-albedo feedback triggers global glaciation. At this point weathering slows below the rate of outgassing and allows CO_2 to accumulate and eventual deglaciate the planet, which restarts the cycle. Our simulations indicate the existence of a distinct limit cycle that can emerge when outgassing dominates weathering: the oscillation between a CO_2 surface-condensing state and a non-CO_2-condensing state on planets with CO_2-H_2O atmospheres. This variety of limit cycling is a consequence of the temperature-dependent planetary albedo that arises from H_2O's shortwave and near-IR absorption, in combination with CO_2's Rayleigh scattering effect.

In equation 4.4, energetic equilibrium between global-mean absorbed instellation and OLR is assumed, and each S_{eff} contour in Fig. 4.1A is a set of T_{surf}-pCO_2 pairs where equation 4.4 holds for that particular S_{eff} value. However, at high pCO_2, when S_{eff} is large enough to permit the high temperatures that raise water's vapor pressure enough to lower the planet's albedo substantially, the right-hand branches of the S_{eff} contours become energetically unstable to perturbations in temperature and pCO_2. The consequences of this phenomenon for planetary climate evolution are illustrated in Fig. 4.2. In this figure, we plot the right-hand branch of the set of T_{surf} and pCO_2 values that produce energetic equilibrium with $S_{\text{eff}} = 0.46$. Any combination of T_{surf} and pCO_2 not falling on the dark red line in Fig. 4.2 leads to energetic disequilibrium under an instellation of $S_{\text{eff}} = 0.46$. This results in either cooling in the case where the planetary outgoing longwave radiation (OLR) is higher than the absorbed stellar radiation (OLR $>$ ASR $= (1-\alpha)S/4$) in the light blue region, or warming in the light red region, where ASR $>$ OLR. When the climate resides on the upper, solid portion of the red curve, the temperature responds to energetic disequilibrium as follows:

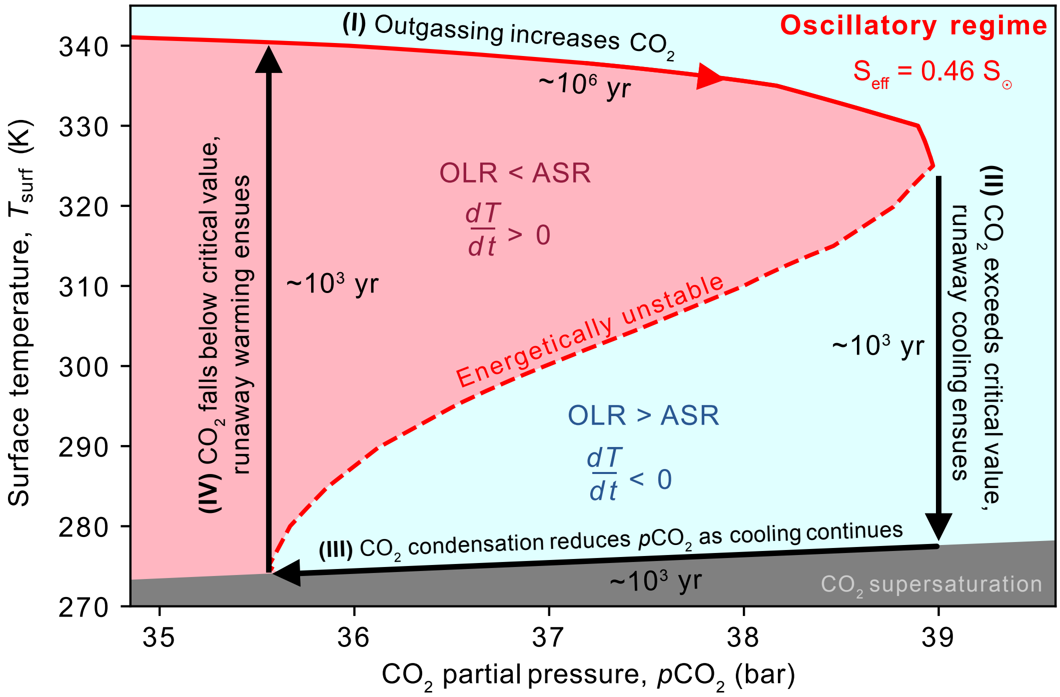

Figure 4.2: **Climatic limit cycling driven by CO_2 outgassing, Rayleigh scattering, temperature-dependent near-IR stellar absorption by H_2O, and surface CO_2 condensation.** In step (I), outgassing allows CO_2 to accumulate. In step (II), pCO_2 exceeds the value that triggers a positive feedback loop between cooling surface temperature and increasing planetary albedo. In step (III), the planetary surface temperature becomes low enough to trigger surface CO_2 condensation, so continued cooling now also decreases atmospheric pCO_2. In step (IV), a positive feedback loop between warming and albedo reduction from H_2O accumulation leads to runaway warming.

at a given pCO_2, a perturbation in temperature upward from equilibrium is met with a cooling response and a perturbation in temperature downward is met with a warming response, until energetic equilibrium is re-established. Similarly, an increase in CO_2 from equilibrium increases albedo, which causes the planet to cool to maintain equilibrium. Thus small changes to T_{surf} or pCO_2 in this region of parameter space near the solid red curve are met with a negative feedback that tends to maintain energetic equilibrium and move the climate back to the red curve. Starting from somewhere on the red curve near the area labeled (I), if CO_2 in the atmosphere is increased by outgassing, moving rightward along the equilibrium curve, the climate will eventually reach the curve's rightmost point.

If pCO_2 is increased beyond the value at the rightmost point of the red curve, the increase in albedo is enough to push the climate system into a state of energetic disequilibrium where OLR > ASR (the light blue region in Fig. 4.2), and the planet begins to cool. In this region, OLR responds only weakly to changes in temperature because pCO_2 is so high that the atmosphere is mostly opaque in the IR (see Fig. 4.1B), but the albedo responds substantially, increasing as temperature decreases, since H_2O in the atmosphere falls exponentially with temperature, reducing the atmosphere's ability to absorb instellation. This produces a positive feedback with runaway cooling (stage (II) in Fig. 4.2), where a reduction in temperature dries the atmosphere, which decreases ASR and thus pushes the system even further out of energetic equilibrium. This accelerates the cooling and reduces the ASR further. Any plausible rate of cooling vastly exceeds plausible rates of CO_2 accumulation from outgassing (compare thermal equilibration timescale of 1000 years (Pierrehumbert, 2010a) to a carbon cycle timescale of 10^6 years or more (Colbourn et al., 2015)), so the cooling trajectory is effectively straight down in T_{surf}-pCO_2 space.

After a temperature reduction of approximately 50 K, the conditions at the surface have cooled enough for CO_2 to begin to condense out onto the planetary surface, which is in this case covered by a liquid H_2O ocean. In stage (III) of the climate cycle, pCO_2 is directly dictated by surface temperature via CO_2's Clausius Clapeyron relation. Since the climate is still in the light blue region where OLR>ASR, continued cooling drives a rapid decrease in CO_2 partial pressure, resulting in decreasing planetary albedo and increasing ASR.

Eventually, the reduction in CO_2 partial pressure increases ASR enough to re-equilibrate with the OLR at the point where arrow (III) meets arrow (IV) in Fig. 4.2. However, this equilibrium point is unstable to further reductions in CO_2 or increases to temperature, which would shift the climate into the light red region of Fig. 4.2, where OLR<ASR and warming is self-reinforcing due to the accumulation of atmospheric water vapor and resultant reduction in planetary albedo. As a result, any internal climate variability that acted to transiently warm the climate away from this unstable equilibrium would trigger the positive warming feedback loop represented by arrow (IV) in Fig. 4.2, analogous to the cooling feedback loop represented by arrow (II). This warming feedback loop would finally carry the climate back to its initial energetically-stable state, at about 35.6 bar of CO_2 and $T_{\mathrm{surf}} \approx 340$ K. From here, assuming outgassing continues, the planet would begin another iteration of this cycle of atmospheric CO_2 accumulation, runaway cooling, CO_2 rain-out, and runaway warming.

For this example of a CO_2 ocean cycle, we chose an instellation that kept the surface temperature at each pCO_2 within the range of temperatures we simulated ($\leq$ 365 K). With higher S_{eff}, the maximum attainable temperature increases, and the unstable righthand branches of the S_{eff} contours shift rightward to higher pCO_2 (see Fig. 4.1). Both of those responses to higher S_{eff} would increase the size of temperature jumps over the course of a limit cycle. Therefore, planets that start off in a limit cycling state at low S_{eff} will undergo cycles of greater and greater amplitude as their star brightens and incident instellation increases.

Up to this point, we have discussed the evolution of climates with CO_2 outgassing but without a complementary weathering feedback. This can correspond to a scenario in which weathering is "supply-limited," i.e. the supply of weatherable minerals to the planetary surface is too low for weathering to keep up with the rate of CO_2 outgassing, or a scenario where liquid CO_2 or CO_2 clathrate hydrate blankets the ocean floor, suppressing weathering reactions in seafloor basalts (a scenario discussed further in Section 4.4). In the next subsection, we present calculations that include a simple weathering feedback.

4.3.3 Bistability from the interaction of Rayleigh scattering, weathering, and CO_2 condensation

With weathering included (Eq. 4.6) and assuming an outgassing rate of 15.8×10^{12} mol yr^{-1} ($2.1\times$ an Earth-like rate of 7.5×10^{12} mol yr^{-1} drawn from Haqq-Misra et al. (2016)), our model produces a set of weathering-outgassing equilibria corresponding to the solid purple line in Fig. 4.3. The curve has a negative slope because of the pCO_2-dependence of weathering, with lower T_{surf} required for weathering/outgassing equilibrium at higher values of pCO_2. A larger outgassing rate would result in the purple line residing at higher temperatures for a given pCO_2, changing the locations of stable and unstable equilibria, and a smaller outgassing rate would have the opposite effect. With a large enough increase in outgassing (just an increase to $2.2\times$ the Earth-like rate, in this case), the low-CO_2 solution becomes inaccessible, and with a large enough decrease in outgassing (a reduction to below $1.0\times$ the Earth-like rate, in this case), the high-CO_2 solution similarly disappears. Changes to the parameters in the weathering model (for example, changing the assumed global-mean soil thickness) would have analogous effects on the locations and presence of the equilibria. With the formulation of weathering applied here (from Maher & Chamberlain, 2014; Winnick & Maher, 2018; Graham & Pierrehumbert, 2020), the behavior of the system is quite sensitive to changes in outgassing, land fraction, or weathering parameters, while the more traditional kinetically-limited formulation introduced in Walker et al. (1981) would result in less sensitivity, as demonstrated in Graham & Pierrehumbert (2020).

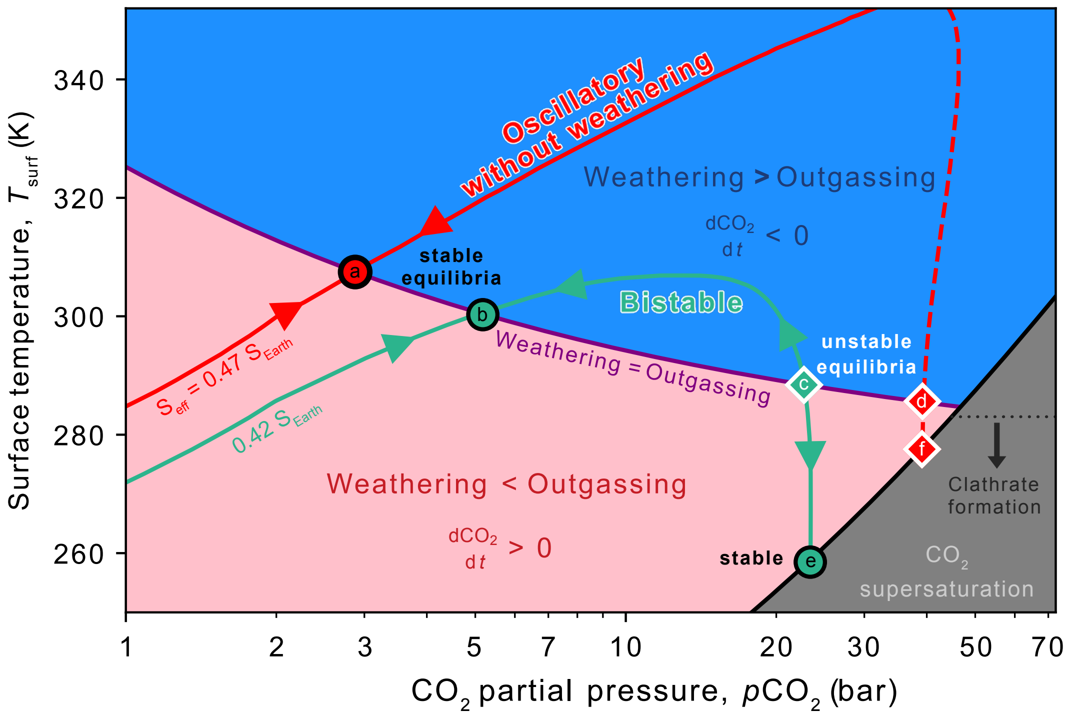

Figure 4.3: **Comparison of stable (circles with black outline: a, b, e) and unstable (diamonds with white outline: c, d, f) climate equilibria at different instellations.** The red line represents climate states with $S_{\text{eff}} = 0.47\ S_{\text{Earth}}$, with the solid part of the red line representing energetically stable climates and the dashed part of the red line representing energetically unstable climates. The green line represents climates with $S_{\text{eff}} = 0.42\ S_{\text{Earth}}$, with the possibility of bistability between an Earth-like scenario and a CO_2 condensing state. The purple line shows where weathering is equal to outgassing; the light red region below is where outgassing outpaces weathering, and the light blue region above is where weathering outpaces outgassing.

Fig. 4.3 indicates the existence of two equilibrium points where outgassing (V) is balanced by weathering (W), $V = W$, and OLR = ASR for planets at a given S_{eff}, with one equilibrium climate having a higher T_{surf} and a lower pCO_2 (red and green circles a and b in Fig. 4.3) than the other (red and green diamonds c and d). The physical reason for pairs of equilibria at each S_{eff} is CO_2's cooling effect at high partial pressures. For both S_{eff} values (0.42 and 0.47 S_{Earth}, green line and red line) plotted in Fig. 4.3, the warmer, lower-pCO_2 climate equilibrium (a and b) is stable with respect to both its energy fluxes and its carbon fluxes, meaning a planet will return to that climate equilibrium if perturbed away from it. These stable climates are the equilibria that are typically explored in studies of silicate weathering on terrestrial planets.

Unlike its counterpart, the second equilibrium climate state where $V = W$ on each S_{eff} curve (c and d) is unstable to climatic perturbations. This is best illustrated by examining unstable equilibrium c with $S_{\text{eff}} = 0.42\ S_{\text{Earth}}$ in Fig. 4.3. As noted earlier, compared to the timescale of carbon cycle response, the thermal equilibration timescale is instantaneous, so for this discussion we can assume that the climate is constrained to move along the green curve at all times. If a planet begins with a climate at point c, and its $p\text{CO}_2$ is perturbed downward (leftward on the plot), it warms up because of a reduction in CO_2 Rayleigh scattering and moves upward along the green S_{eff} isoline. This moves the planet into the blue zone of Fig. 4.3 where $W > V$, which means that CO_2 is now being consumed by weathering faster than it can be supplied by outgassing. This imbalance in carbon fluxes leads to further reduction in $p\text{CO}_2$, enhancing the initial perturbation and pushing the climate deeper and deeper into the blue region. Eventually the planet reaches the peak temperature for that S_{eff}, at which point the continued reduction in CO_2 begins to cool the climate, slowing weathering until finally the planet reaches the stable equilibrium point b.

Conversely, if a planet begins on the unstable equilibrium c and $p\text{CO}_2$ is perturbed upward (to the right on the plot), the planet's surface will cool and the climate will move into the light red area of Fig. 4.3, where outgassing is greater than weathering ($V > W$). With outgassing now outpacing weathering, $p\text{CO}_2$ will continue to grow, enhancing the initial climate perturbation until the T_{surf}–$p\text{CO}_2$ combination allows for CO_2 condensation at the planetary surface, at which point the carbon cycle has reached a new, stable equilibrium e governed by equation 4.8, with the imbalance between outgassing and weathering being balanced by surface condensation of CO_2. This suggests that rocky planets at low instellation can display carbon cycle bistability, where the same geologic boundary conditions (as represented by the parameters in equation 4.6) and same stellar environment can drive two very different stable equilibrium climates with $p\text{CO}_2$ differing by an order of magnitude, one of which displays surface CO_2 condensation and one of which does not.

The carbon cycling behavior of a planet irradiated by relative instellation of $S_{\text{eff}} = 0.47\ S_{\text{Earth}}$ (the green curve in Fig. 4.3) is considerably different than that of the previous example because of the H_2O absorption-based radiative feedbacks that cause the CO_2 ocean limit cycling discussed in Section 4.3.2. In this case, even though the intersection point f (red-white diamond) between the $S_{\text{eff}} = 0.47\ S_{\text{Earth}}$ curve (red, dashed curve) and the CO_2 saturation vapor pressure curve (black) is stable with respect to the carbon cycle, it is unstable with respect to energy fluxes: a small perturbation in temperature upward or CO_2 downward from that point would trigger self-reinforcing warming like that exemplified by arrow (IV) in Fig. 4.2. This would warm the planet to $T_{\mathrm{surf}} \approx 350$ K. This is in the blue region of Fig. 4.3, where weathering outpaces outgassing, so CO_2 would subsequently be consumed by weathering until the carbon cycle reached the stable equilibrium a, where $V = W$ for $S_{\mathrm{eff}} = 0.47\ S_{\mathrm{Earth}}$.

In summary, within the modeling framework applied in this article, a climate transition occurs between $S_{\mathrm{eff}} = 0.42\ S_{\mathrm{Earth}}$ and $S_{\mathrm{eff}} = 0.47\ S_{\mathrm{Earth}}$ where the climate configurations that allow for surface CO_2 condensation become energetically unstable by the same mechanism that allows for the CO_2 ocean limit cycles described in Section 4.3.2. However, in this case, the addition of a weathering feedback terminates the cycle before its CO_2 accumulation phase (analogous to step (I) in Fig. 4.2) can be initiated.

4.3.4 Variations in stellar type

As noted in Section 4.2.1, the fiducial case studied in this article is irradiated by a solar (G2V type) spectrum drawn from Kurucz (1995). Irradiation by spectra corresponding to different stellar types can result in different climate behavior compared to what we have examined so far. Here we examine the impact of an F-type (F2V) spectrum and an M-type (M3.5V) spectrum on our basic results. In all cases, the OLR remains the same, but the planetary albedo is altered by changes to the stellar spectrum impinging on the planet. The general trend is simple to state: planets orbiting hotter, bluer stars can support the bistability between climates with and without CO_2 oceans at higher instellations than cooler, redder stars.

F-type stars

To examine the behavior of climates irradiated by F-type stars, we apply the spectrum of Sigma Boötis, an F2V star, drawn from Segura et al. (2003), in Fig. 4.4. Because F-type stars display spectra that are shifted toward higher (bluer) frequencies than G- or M-type stars, the Rayleigh scattering effect of CO_2 is stronger for planets orbiting these stars, as Rayleigh scattering increases greatly in efficacy at shorter wavelengths. Thus, a given increase in pCO_2 leads to a larger increase in albedo for these planets, as demonstrated in Fig. 4.4C, where the planetary albedo reaches nearly 0.68 at the highest pCO_2 shown (compared to a maximum albedo of 0.56 in simulations irradiated by a solar spectrum shown in Fig. 4.1C). This higher sensitivity of albedo to pCO_2 leads to climate configurations where the bistability between climates with and without CO_2 oceans can persist to a higher instellation, reaching ≈ 54% of that of modern-day Earth (Fig. 4.4A), compared to ≈ 45% for climates irradiated by the solar spectrum (Fig. 4.1).

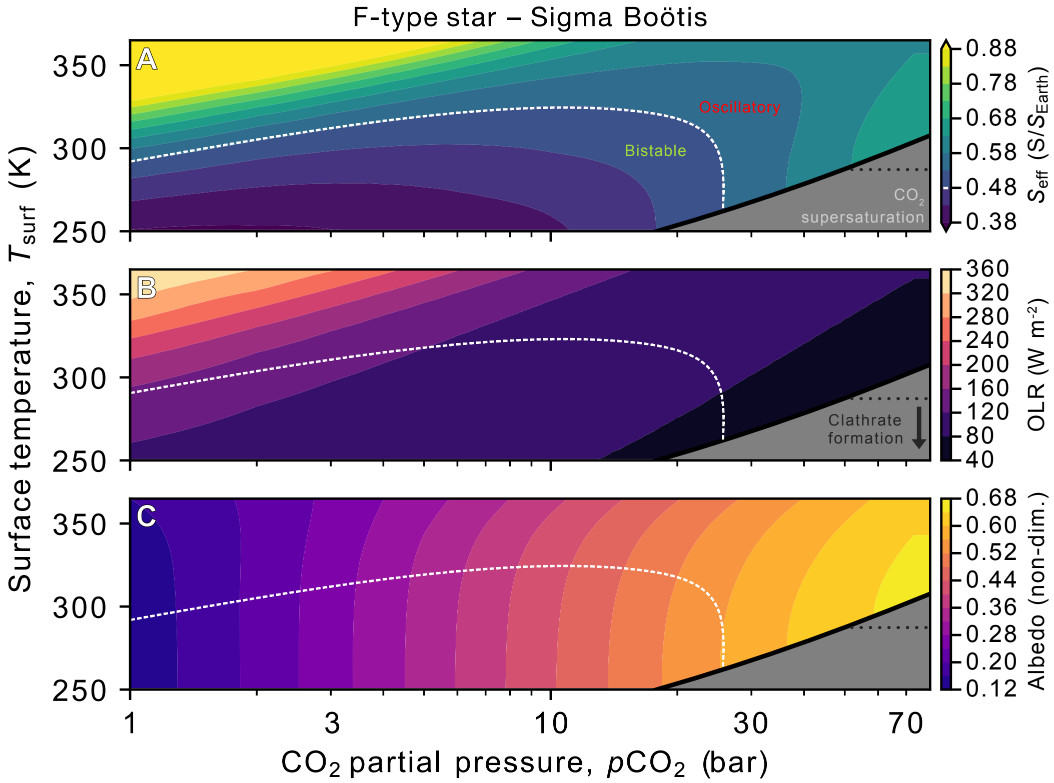

Figure 4.4: **Energetic properties of terrestrial planetary climates irradiated by Sigma Boötis, an F2V star, at low instellation as a function of surface temperature T_{surf} (y-axes) and CO_2 partial pressure (x-axes).** Panels and color coding are the same as in Fig. 4.1.

M-type stars

To examine the behavior of planets orbiting M-type stars, we apply the spectrum of AD Leonis, an M3.5V star (Segura et al., 2005), in Fig. 4.5. For planets orbiting M-type stars, which emit a larger proportion of their energy at lower (redder) frequencies than G- or F-type stars, the Rayleigh scattering impact of atmospheric pCO_2 is weaker. Even at the highest pCO_2 simulated in this paper (72 bar), albedo does not exceed 0.18 (Fig. 4.5C) for planets orbiting AD Leonis, compared to maximum simulated albedo values of 0.56 and 0.68 for planets orbiting G- and F-type stars, respectively. Interestingly, this weak dependence of planetary albedo upon CO_2

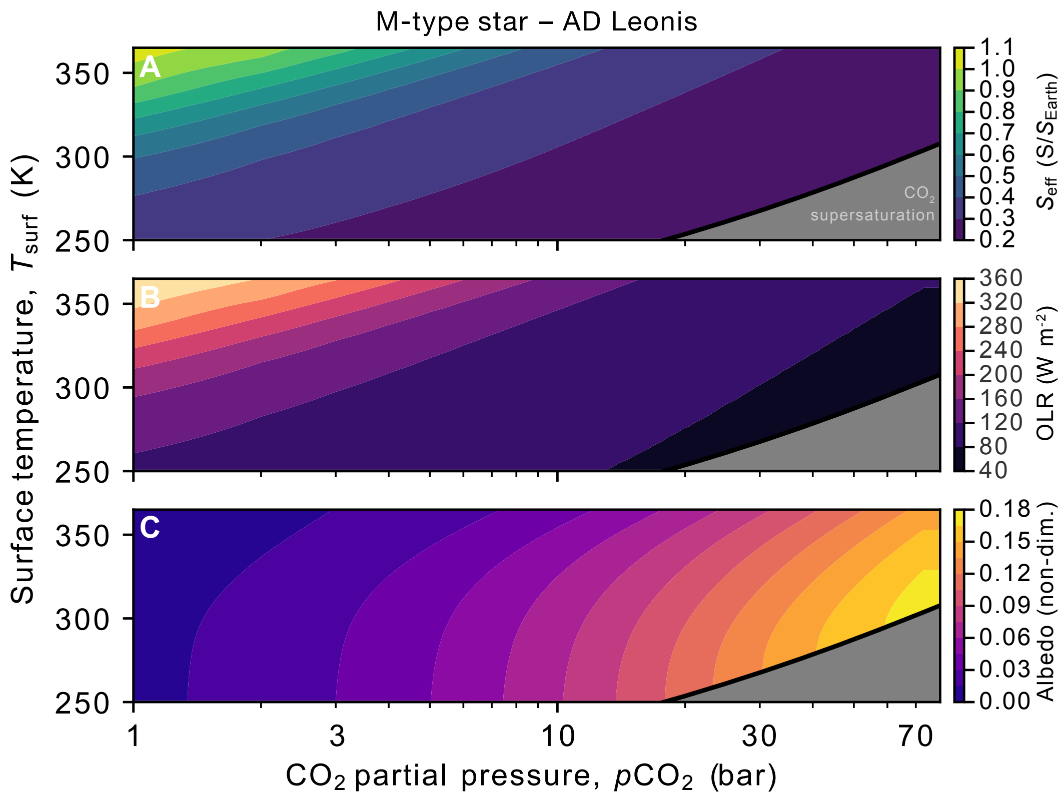

Figure 4.5: **Energetic properties of terrestrial planetary climates irradiated by AD Leonis, an M3.5V star, at low instellation as a function of surface temperature T_{surf} (y-axes) and CO_2 partial pressure (x-axes).** Panels and color coding are the same as in Fig. 4.1.

leads to a complete lack of bistable climate states in our M-star simulations. Without a substantial increase in albedo with pCO_2, CO_2's reduction of OLR dominates its radiative impact, allowing the molecule to remain a net greenhouse gas across the entirety of the parameter space we studied. Thus, for planets with functional weathering feedbacks that orbit M-type stars, we expect there to be only one stable climate state, corresponding to an Earth-like equilibrium that lacks condensed CO_2 at the surface. Correspondingly, we do not expect planets orbiting M-stars to display limit cycling between CO_2-condensing and non-condensing states, regardless of outgassing rate or TOA instellation.

4.4 Discussion

The interaction of liquid CO_2 and liquid H_2O at the planetary surface is fundamental to evaluating the climate state and surface geochemistry of planets with large inventories of both condensed phases. The range of temperatures over which liquid CO_2 would be stable in the presence of a liquid water ocean is relatively narrow (Marounina & Rogers, 2020). At temperatures above 304.5 K CO_2 becomes supercritical and does not condense. At temperatures below 282.91 K and pressures below 4.46 MPa (44.6 bar), mixtures of condensed CO_2, condensed H_2O, and CO_2-rich vapor are metastable, with an equilibrium state of CO_2 hydrate, a crystalline phase where water molecules encase CO_2 molecules (Wendland et al., 1999).

Experiments in Earth's ocean demonstrate that hydrate forms rapidly upon contact between liquid CO_2 and liquid H_2O, with visible masses forming over the course of just a few hours (Brewer et al., 1999). This suggests that with surface temperatures below the 282.91 K quadruple point of CO_2 hydrates mentioned in the previous paragraph, precipitation of condensed CO_2 from the atmosphere into a liquid water-rich ocean would result in immediate formation of solid hydrates that would then sink through the water and settle on the seafloor. This may result in large-scale hydrate build-up on the ocean floor, which would suppress or halt seafloor silicate weathering, similar to high-pressure ice phases on waterworlds with extremely deep oceans (Kite & Ford, 2018), removing a potentially important CO_2 sink and making it even more difficult for a planet to exit a stable CO_2 condensing state. Other forms of low-temperature seafloor alteration would also be dramatically altered, with likely major consequences for ocean chemistry (Coogan & Gillis, 2018b). Similar layered structures of hydrate and water have also been proposed for icy moons and dwarf planets (Boström et al., 2021), suggesting exploration of such bodies in the solar system may also provide insight into the structure of low-instellation terrestrial planets. Further, assuming a slow rate of subduction, the formation of large seafloor hydrate reservoirs could consume large fractions of the water in planets with Earth-like volatile inventories, since each CO_2 molecule in a hydrate is accompanied by 5.75 H_2O molecules in the most common hydrate structure (Brewer et al., 1999). Thus, under the conditions where CO_2 hydrates are stable (at temperatures below 282.91 K), a planet's subduction rate could exert a powerful direct control on ocean depth and salinity, both of which are first-order parameters in determining planetary climate and surface geochemistry (Olson et al., 2020). Finally, the coexistence of liquid CO_2 and H_2O in the air may lead to the formation of aerial CO_2 hydrates, altering the atmospheric lapse rate through latent heat release (Kasting, 1991), but it is unclear whether this would be an efficient process given the factor-of-a-thousand difference in vapor pressure between CO_2 and H_2O at relevant temperatures.

At temperatures above the hydrate quadruple point (282.9 K) and below CO_2's triple point (304.5 K), liquid CO_2 and liquid H_2O can coexist. Under pressures like those at the sea surface, liquid CO_2 is less dense than liquid H_2O, so CO_2 that rains into the ocean from the atmosphere would float and form a layer on top of the water (House et al., 2006; Marounina & Rogers, 2020). However, liquid CO_2 is also more compressible than liquid water, such that CO_2 can become denser than water at high enough pressures (House et al., 2006; Marounina & Rogers, 2020). This means that if liquid CO_2 enters the water ocean at a deep enough point, then instead of floating on top of the water, it will sink to the seafloor. Therefore, submarine CO_2 degassing in such conditions would result in the formation of a liquid CO_2 layer at the lithosphere/ocean interface. It is unclear whether silicate weathering by liquid CO_2 is possible, so the impact of this seafloor layer on carbon sequestration is an open question. All in all, the coexistence of liquid CO_2 and liquid H_2O suggests the possibility of "layer cake" oceans at the surfaces of some rocky, low-instellation planets, with an H_2O layer nestled between two CO_2 layers. This analysis remains speculative without detailed thermodynamic modeling, which is beyond the scope of this article but would make for insightful work on the surface conditions of rocky exoplanets under low instellation.

The properties of the atmosphere and ocean under CO_2 condensing conditions also have implications for the viability of origin of life scenarios on prebiotic planets akin to the Hadean Earth. In one popular school of thought regarding the origin of life, surface UV fluxes are held to be important drivers of prebiotic chemistry (Sasselov et al., 2020; Liu et al., 2021). The surface UV flux has been quantified in a variety of models approximating early Earth and early Mars atmospheres (Rugheimer et al., 2015; Ranjan & Sasselov, 2016; Ranjan et al., 2017), and atmospheres with multibar CO_2 pressures demonstrated significant UV attenuation from scattering and absorption (Ranjan et al., 2017). This suggests that atmospheres with 10s of bar of CO_2 like those expected for the CO_2 condensing cases examined in this paper would not receive enough UV light at their surfaces to drive the relevant prebiotic chemistry. With respect to submarine origin of life scenarios, the seafloor being covered in liquid CO_2 or CO_2 hydrate in conditions with surface CO_2 condensation would preclude water-rock reactions like serpentinization (Sleep et al., 2011) or aqueous organo-metal chemistry near hot vents (Sobotta et al., 2020). It seems that several major models for the origin of life require processes that would be difficult on planets displaying the CO_2 condensing conditions explored here, even with temperate and otherwise habitable surface climates.

Given the likely reduced potential for life to emerge on CO_2 condensing planets, an observational discriminant between these worlds and their non-condensing counterparts would be useful for prioritizing targets in the search for life beyond the solar system. Here, we propose a potential method for distinguishing between CO_2 condensing and non-condensing worlds and, more generally, constraining the $p\mathrm{CO_2}$ of a given exoplanet. This proposal is based on the tendency of CO_2 to dimerize and form molecular complexes at high pressures and low temperatures like those that occur in the CO_2 condensing atmospheres explored in this paper (Leckenby & Robbins, 1966; Slanina et al., 1992; Tsintsarska & Huber, 2007; Asfin et al., 2015). Similar to a method proposed for constraining O_2 partial pressure using spectroscopic O_2 dimer features in exoplanet observations (Misra et al., 2014), we suggest that high resolution spectroscopy from astronomical surveys may be able to detect CO_2 dimer features on high-$p\mathrm{CO_2}$ exoplanets. Using a quadratic fit to estimate the CO_2 dimerization equilibrium constant as a function of temperature based on data from molecular dynamics simulations (Tsintsarska & Huber, 2007), we find that CO_2 dimers would make up ≈5% of the atmosphere by molar fraction at the surface on planets with surface CO_2 condensation and surface temperatures between 273.15 K (H_2O's freezing point temperature) and 304 K (CO_2's critical temperature). Planets in the same temperature range but with lower, non-condensing $p\mathrm{CO_2}$ levels have much smaller levels of dimerization; for example, an atmosphere with 6 bar of CO_2 and a surface temperature of 288 K would have a dimer fraction of less than a percent at the surface. Consequently, it may be possible to discriminate between CO_2-condensing and non-CO_2-condensing atmospheres using the presence or absence of CO_2 dimer features. These features have been detected in the near- and mid-infrared around 3700 cm^{-1} (2.7 μm) (Jucks et al., 1987, 1988; Moazzen-Ahmadi & McKellar, 2013), 2350 cm^{-1} (4.3 μm) (Walsh et al., 1987; Dehghany et al., 2010), and 1250-1400 cm^{-1} (7.1–8.0 μm) (Baranov et al., 2004; Asfin et al., 2015), placing the features within the proposed wavelength range of future telescope architectures like the Large Interferometer For Exoplanets (Quanz et al., 2021). Fox & Kim (1988) note the possibility of detection of CO_2 dimers in the atmospheres of Mars and Venus, where they are suggested to exist at parts-per-thousand mole fractions, much lower than the expected dimer abundance in CO_2 condensing atmospheres due to the low pressure and high temperatures on Mars and Venus respectively.

If the proposed method for constraining $p\mathrm{CO_2}$ by dimer feature detection is borne out under more comprehensive examination, it may allow identification of statistical trends in $p\mathrm{CO_2}$ versus instellation. Such a trend is expected if there is a population of Earth-like planets in the habitable zones of stars with CO_2 levels controlled by silicate weathering, which would introduce a trend of CO_2 decrease with increasing instellation (Bean et al., 2017; Checlair et al., 2019b; Lehmer et al., 2020b). Conversely, for the population of planets where CO_2 levels are controlled by condensation, the opposite trend would emerge: $p\mathrm{CO_2}$ would increase with increasing instellation. For instance, this trend can be observed in Fig. 4.1A, where CO_2's saturation vapor pressure curve intersects increasingly large S_{eff} contours as $p\mathrm{CO_2}$ increases. Statistical comparative planetology may thus be able to distinguish populations of terrestrial exoplanets with CO_2 levels controlled by different physical and chemical processes, even if the individual measurements are too low in precision to unambiguously place a given planet into either population. A more detailed analysis of spectral response for the different climate scenarios we outline will be beneficial to analyse the optimal observational architecture (Team et al., 2019; Apai et al., 2019; Quanz et al., 2021).

4.4.1 Caveats

Any proposal to analyze the atmospheres of exoplanets is hindered by the potential presence of clouds, and the above is no different: high altitude cloud decks consisting of liquid or solid CO_2 or H_2O may obscure parts of the atmosphere on these CO_2 condensing planets. Clouds might also impact the OLR and albedo of these planets, potentially changing the patterns of climate behavior as a function of $p\mathrm{CO_2}$ and instellation. Thus, the inclusion of clouds may alter the conclusions of this clear-sky study. In particular, if it turns out that thick, global, high-altitude cloud decks obscure the bulk of the planetary atmosphere in most high-$p\mathrm{CO_2}$ climates, the bistability we identify might be muted or eliminated due to the reduced importance of CO_2 Rayleigh scattering of visible light under such conditions. Planetary albedo would instead be determined by cloud properties, with little dependence on $p\mathrm{CO_2}$. We do not include clouds in our simulations for a variety of reasons. Most importantly, it is simply not possible to self-consistently calculate realistic cloud distributions in a one-dimensional model, or even to theoretically estimate cloud deck locations or cloud condensation nuclei density, so any attempt at cloud inclusion would either require arbitrary choices of all of these fundamental parameters for four distinct cloud varieties (solid H_2O, liquid H_2O, solid CO_2, liquid CO_2) or a many-dimensional parameter space sweep. Further, to our knowledge, the physical and optical properties of liquid CO_2 droplets have not been measured, making it difficult to estimate their impact without making unsupported guesses about their physical properties. The radiative impacts of CO_2 ice clouds have been examined in some detail (Forget & Pierrehumbert, 1997; Forget et al., 2013; Kitzmann, 2016, 2017), and most recent work has found that their net effect on climate is likely to be small under most parameter assumptions, though further work is warranted on this problem. The behavior of water clouds (either solid or liquid) in thick CO_2 atmospheres is relatively under-explored, though some 3D GCM studies of early Mars (Wordsworth et al., 2013; Kite et al., 2021) have examined this regime. Wordsworth et al. (2013) found a small radiative impact from water clouds in the cool, arid climates they simulated. Kite et al. (2021) found a significant climate effect from high-altitude water clouds in arid simulations and a minimal effect in simulations with a global ocean. Our simulations assumed an Earth-like global ocean. Thus, although clouds are a significant source of uncertainty in climate modeling, excluding their effects for a principal examination (similar to studies on the runaway greenhouse effect, e.g. Kopparapu et al., 2013) of the phenomena we are studying is justified.

We also neglected the ice-albedo feedback in our simulations because the vast majority of climates we examined had surface temperatures above freezing. Previous studies (e.g. Turbet et al., 2017; Kadoya & Tajika, 2019) have found that planets that fall into globally glaciated states at low instellation may experience surface CO_2 condensation at drastically lower $p\mathrm{CO_2}$ values than the planets we have examined, since the surface temperatures of glaciated planets are tens of Kelvin colder than surface temperatures on temperate planets, though a functional seafloor weathering feedback might be enough to draw down CO_2 to low levels and prevent CO_2 condensation even in a snowball state at low instellations (e.g. Chambers, 2020). The potential for a climate transition from a snowball state with surface CO_2 condensation to a temperate state with continued surface CO_2 condensation is an interesting target for further modeling, and may provide an alternative route to a bistable CO_2-ocean-bearing climates on Earth-like planets with low instellation. In some regions of parameter space (especially low instellation and high $p\mathrm{CO_2}$), the accumulation of CO_2 and resultant cooling from Rayleigh scattering could itself drive a planet into a snowball state as well, providing another intriguing and counter-intuitive climate scenario for follow-up.

Finally, we note that meridional surface temperature gradients on these planets could lead to CO_2 condensation at somewhat lower surface pressures for a given temperature than calculated here, as the poles tend to be cooler than the global mean surface temperature on planets with Earth-like obliquities and rotation rates, allowing CO_2 surface condensation with less atmospheric CO_2 accumulation. However, meridional surface temperature gradients are greatly reduced at high surface pressures (Chemke & Kaspi, 2017) and atmospheres that are made up mostly of condensable species also tend to have very small meridional temperature gradients due to the powerful winds that develop in response to the large pressure gradients that would be caused by temperature gradients in condensable-rich atmospheres. For example, the equator-to-pole temperature gradient for a pure H_2O atmosphere is calculated to be on the order of ~ 1 K (Ding & Pierrehumbert, 2018).

4.4.2 Conclusion

In summary, our simulations suggest that the interplay of the radiative properties of CO_2-rich atmospheres and the weathering of silicates leads to super-saturated and cyclic climates for planets under low irradiation for G-type and more massive stars. A qualitative sketch of the distinct climate regimes suggested by our study is shown in Fig. 4.6. The cooling impact of Rayleigh scattering at very high CO_2 levels introduces bistability between a climate state where silicate weathering maintains CO_2 at relatively low levels and a state where CO_2 outgassing outpaces silicate weathering, maintaining CO_2 at such high levels that it condenses at the surface. At intermediate instellation, planetary temperatures can become large enough for water vapor in the atmosphere to significantly impact planetary albedo through absorption of incoming light, destabilizing surface CO_2 condensing climate states and giving rise to limit cycles between CO_2 condensing and non-condensing states. The dynamic interplay between radiation and carbon cycling profoundly impacts the climate state and surface geochemistry of otherwise Earth-like planets in the outer reaches of the liquid water habitable zone. These CO_2-condensing climate states are potentially distinguishable by observational characterization of CO_2 dimer features and a trend in pCO_2 versus instellation opposite to that anticipated from the nominal carbonate-silicate cycle feedback.

4.5 Open Research

We have archived the data necessary to reproduce the plots in this article at Graham et al. (2022a).

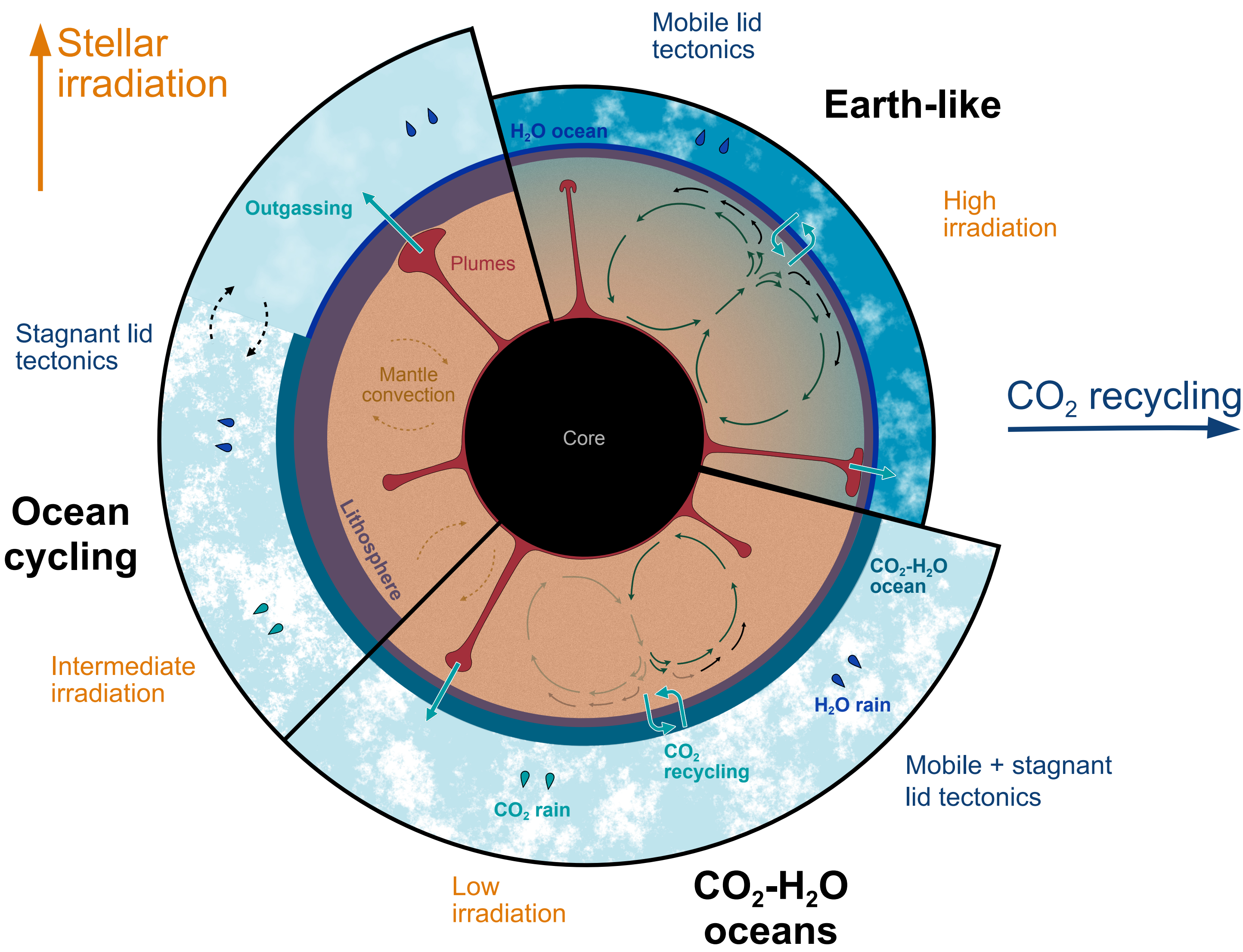

Figure 4.6: **A schematic illustrating the climate states examined in this chapter.** Planets with high (Earth-like) CO_2 recycling driven by efficient weathering and mobile lid tectonics that receive high stellar irradiation are likely to occupy Earth-like climate states with H_2O oceans and relatively thin atmospheres. Planets with CO_2 recycling that may range from low to high, with either mobile lid or stagnant lid tectonics, and which receive low stellar irradiation, may occupy climate states with thick CO_2 atmospheres and surface CO_2 condensation, producing oceans with both liquid CO_2 and liquid H_2O. Planets with low CO_2 recycling at intermediate instellations may oscillate between a CO_2-H_2O ocean state and a state with only H_2O oceans. Credit for this illustration goes to Tim Lichtenberg, co-author of the published version of this chapter (Graham et al., 2022b).

Chapter 5

Sluggish hydrology under dim suns: energetically-limited precipitation and silicate weathering

Light leaves overhead danced in the fire's breath,
tree-trunks were seen: it was the rock wall
That fascinated my eyes and mind. Nothing strange;
light-gray diorite with two or three slanting seams in
it,
Smooth-polished by the endless attrition of slides
and floods; no fern nor lichen, pure naked rock . . .
as if I were
Seeing rock for the first time. As if I were seeing
through the flame-lit surface into the real and bodily
And living rock. Nothing strange . . . I cannot
Tell you how strange: the silent passion, the deep
nobility and childlike loveliness: this fate going on
Outside our fates. It is here in the mountain like a
grave smiling child. I shall die, and my boys
Will live and die, our world will go on through its
rapid agonies of change and discovery; this age will
die,
And wolves have howled in the snow around a new
Bethlehem: this rock will be here, grave, earnest,
not passive: the energies
That are its atoms will still be bearing the whole
mountain above: and I, many packed centuries ago,
Felt its intense reality with love and wonder, this
lonely rock.

Oh Lovely Rock
Robinson Jeffers

Abstract

Note: This chapter will be submitted as a letter soon.

Implicit in the definition of the classical circumstellar habitable zone (HZ) is the hypothesis that the carbonate-silicate cycle can maintain clement climates on exoplanets with land and surface water across a range of instellations by homeostatically adjusting atmospheric CO_2 partial pressure (pCO_2). This hypothesis is made by analogy to the functioning of the Earth system, but it is an open question whether silicate weathering can stabilize climate on planets in the outer reaches of the HZ, where instellations are lower than those received by even the Archean Earth and CO_2 is thought likely to dominate atmospheres. Since weathering products from the land are produced and carried to the ocean by the action of water, silicate weathering rates are intimately coupled to the hydrologic cycle, which intensifies with hotter surface temperatures under Earth-like conditions. Here, we use idealized global climate model (GCM) simulations with correlated-k real gas radiation to demonstrate that the bulk hydrologic cycle responds counterintuitively to changes in surface climate on planets with CO_2-H_2O atmospheres at low instellations, with global evaporation and precipitation rates decreasing as CO_2 partial pressures and surface temperatures increase at a given instellation. Depending on the methodology used to estimate weathering rates, this may mean silicate weathering acts as a destabilizing positive feedback on climate for many planets with high pCO_2 at lower instellations within the HZ. Thus the weathering thermostat may break down and lead to uncontrolled CO_2 accumulation that plunges otherwise Earth-like worlds into climates sporting either inhospitably hot temperatures or widespread condensation of CO_2 onto the surface, depending on instellation. Lasting planetary habitability in the outer reaches of the nominal HZ may be geochemically implausible.

5.1 Introduction

Intensification of the hydrologic cycle with surface temperature is one of the most robust features to emerge from studies modeling Earth's warmer future climate under the influence of higher CO_2 (Held & Soden, 2006; O'Gorman & Schneider, 2008; Kundzewicz, 2008; O'Gorman et al., 2012; Allan et al., 2020), and the same basic behavior emerges under diverse simulated exoplanetary climate conditions (Xiong et al., 2022). Earth's global-mean precipitation rate is consistently predicted to increase approximately linearly with global-mean surface temperature at $\approx$2% per Kelvin (e.g. Held & Soden, 2006; O'Gorman & Schneider, 2008; O'Gorman et al., 2012), lagging well behind the 7% that would be expected from a naive application of the Clausius-Clapeyron relation because of simultaneous slowdown in atmospheric circulation under warming conditions (Vecchi et al., 2006). This coupling between hydrologic cycling and surface temperature is a fundamental component of some formulations of the silicate weathering feedback (Walker et al., 1981), particularly the model described in Maher & Chamberlain (2014) (MAC), where it becomes the primary mechanism by which silicate weathering is sensitive to global surface temperature, suggesting precipitation's temperature sensitivity may play a crucial role in the long-term regulation of the climates of Earth and exoplanets with carbonate-silicate cycles like Earth's (Graham & Pierrehumbert, 2020).

In fact, the concept of the classical circumstellar habitable zone (HZ; defined as the range of instellations around a given star where an N_2-CO_2-H_2O atmosphere can sustain surface temperatures above freezing on an Earth-like, ocean-bearing planet Kasting et al., 1993; Kopparapu et al., 2013) is predicated on silicate weathering's hypothesized ability to regulate CO_2 content in the atmosphere to maintain a temperate surface (Kasting et al., 1988). Thus the outer edge of the HZ is defined as the instellation beyond which the addition of CO_2 to the atmosphere can no longer maintain planetary surface temperatures above freezing due to CO_2 condensation and/or Rayleigh scattering at extremely high (multi-bar) CO_2 partial pressures (Kasting et al., 1993; Kopparapu et al., 2013; Kadoya & Tajika, 2019). This outer limit only makes sense under the assumption of a negative feedback controlling CO_2 in the atmospheres of Earth-like terrestrial planets, adjusting the greenhouse gas to levels appropriate for liquid water at a given instellation. The estimated width of the HZ is an important input in the design of the next generation of space telescopes, some of which hope to observe and characterize the atmospheres of a handful of "Earth analogues" (Guimond & Cowan, 2018; Team et al., 2019; Gaudi et al., 2020; Quanz et al., 2021). In particular, a narrower HZ requires a larger telescope to find a given number of these planets (e.g. Kasting & Harman, 2013), so, in addition to potentially determining the fate of untold numbers of extraterrestrial worlds, the degree of coupling between planetary precipitation rates and background surface temperature may even have practical implications for funding allocation by space agencies.

Given the potential importance of precipitation-climate coupling for climate stability and long-term planetary habitability, it is an underappreciated fact that the energetic cost of evaporating water into the atmosphere places a serious constraint on the maximum rate of global-mean precipitation a planet at a given instellation can sustain (Pierrehumbert, 1999, 2002; O'Gorman & Schneider, 2008; Le Hir et al., 2009; Pierrehumbert, 2010a; O'Gorman et al., 2012). This is readily apparent from a bulk representation of the steady-state surface energy budget:

$$S_{\text{abs}} = H_{\text{sens,rad}} + L \tag{5.1}$$

where S_{abs} is the absorbed instellation at the surface, $H_{\text{rad,sens}}$ is the combined flux from longwave (infrared) and sensible (dry turbulent) heating/cooling of the surface, and L is the latent heat flux from the surface. If we raise the concentration of CO_2 enough for a large amount of water vapor to accumulate in the boundary layer, longwave cooling of the surface will be suppressed and boundary layer stability will increase as the temperature contrast between the ground and the overlying air is reduced (Pierrehumbert, 2002, 2010a; O'Gorman & Schneider, 2008). Each of those effects acts to reduce the magnitude of term $H_{\text{rad,sens}}$, while the evaporative flux (and therefore L) increases, which, at steady-state, is equivalent to the statement that the mean precipitation increases (Pierrehumbert, 1999). Eventually, at high enough temperatures, the latent heat flux dominates the right side of the equation and approaches the value of the absorbed instellation, such that nearly all incoming radiation goes into driving evaporation. Beyond this point, the only way to drive evaporation higher is to form an inversion layer at the surface, such that a sensible heat flux can be directed downward into the surface (i.e. turning $H_{\text{sens,rad}}$ negative so that L can exceed S_{abs}) (Pierrehumbert, 2002; O'Gorman et al., 2012), but the magnitude of this possible overshoot is limited (O'Gorman & Schneider, 2008; Pierrehumbert, 2010a). Thus the instellation absorbed at the surface of a planet places a fairly robust upper cap on global rates of precipitation. GCM simulations have suggested that this phenomenon may have throttled weathering rates during the hot, high-CO_2 aftermath of Earth's snowball events (Le Hir et al., 2009) and low-dimensional exoplanet weathering and climate models have recently included a crude parameterization of the effect (Graham & Pierrehumbert, 2020; Coy, 2022), but the implications of a maximum global precipitation rate for the stability of exoplanetary climate are still largely unexplored.

Here, we combine global climate model (GCM) simulations with the weathering model introduced in (Maher & Chamberlain, 2014, MAC) and elaborated in Winnick & Maher (2018); Graham & Pierrehumbert (2020); Hakim et al. (2021) to investigate carbon cycle stability in the outer reaches of the HZ. The MAC weathering model accounts for the fact that formation of secondary minerals (i.e. clays) in the weathering zone leads to chemical equilibration that caps the concentration of weathering products in runoff, shifting the main temperature feedback in the carbonate-silicate cycle from the kinetics of silicate dissolution (e.g. Walker et al., 1981, WHAK) to the temperature sensitivity of hydrologic cycling. The combination of reduced top-of-atmosphere (TOA) instellation and elevated albedo from high CO_2 partial pressures (pCO_2) places strong upper bounds on the amount of global precipitation planets in low-instellation regimes can generate. This led us to suggest based on global-mean simulations in Graham & Pierrehumbert (2020) that the energetic limit on precipitation might lead to warmer climates than previously expected in the outer reaches of the HZ. Here, we find that when weathering is calculated according to the MAC formulation, the carbonate-silicate cycle transitions from a negative, stabilizing feedback for planets at high instellation and low pCO_2 to a positive, destabilizing feedback for planets with energetically-limited hydrology due to low instellation and high pCO_2. In the unstable, low-instellation regime, CO_2 accumulation can slow weathering, accelerating further CO_2 accumulation. This mechanism may force planets into geologically stable high-pCO_2 climate states, resulting in either dense, supercritical CO_2/H_2O atmospheres with extremely hot surface temperatures or, at lower instellations within the HZ, relatively temperate CO_2 oceans (e.g. Graham et al., 2022b). Thus energetically-limited precipitation may induce a novel form of climate hysteresis driven by an un-noticed positive feedback in the carbonate-silicate cycle, with important implications for our understanding of planetary climate within the HZ. In Section 5.2 we describe the models and methods we applied, in Section 5.3 we describe the results of our simulations,in Section 5.4 we discuss the implications of these results as well as some potential caveats, and in Section 5.5 we conclude.

5.2 Methods

5.2.1 Climate model

To simulate planetary climate, we use the open-source Isca general circulation model (GCM) framework (Vallis et al., 2018), which solves the hydrostatic pressure-coordinate primitive equations on a sphere using a pseudospectral dynamical core. The model has been used in a wide variety of planetary climate contexts (e.g. Penn & Vallis, 2018; Thomson & Vallis, 2019a,b; Yang et al., 2019b). We present fourteen GCM simulations, with eleven in high-$p\mathrm{CO_2}$, low-instellation model configurations and three with more Earth-like configurations (discussed further below; see also Table 5.1). All simulations have a T42 horizontal resolution (64 latitudes, 128 longitudes) and 40 vertical sigma-pressure layers. We employ built-in Isca features like a simple Betts-Miller convective relaxation scheme (Betts & Miller, 1993) and a bucket hydrology configuration governing evaporation (Vallis et al., 2018), modeled after the treatment of soil in Manabe (1969). Boundary layer fluxes are treated with Isca's default Monin-Obukov scheme (Vallis et al., 2018) as in Frierson et al. (2006). The land configuration in the simulations we present consists of a simplified, topography-free polygonal representation of modern-day continents, but qualitatively similar results emerged from a smaller set of simulations with a single large, equatorial continent (not shown), suggesting the basic physical phenomenon in play is insensitive to continental configuration. A full description of the Isca model can be found in (Vallis et al., 2018), and Python scripts for reproducing our specific simulations are available upon request. Planetary surfaces are given a uniform albedo of 0.05, comparable to that of Earth's seawater at the insolation-weighted global-mean zenith angle of $\approx$48.19° (Li et al., 2006; Cronin, 2014). We use Isca's slab ocean configuration with a reduced, 10-meter mixed layer depth to accelerate convergence of the simulations to energetic steady-state. Obliquity and eccentricity are set to zero, so there is no seasonal cycle. The day length in all simulations is 24 hours, so our results are specific to rapidly rotating planets like Earth. Isca's current implementation is cloud-free, a significant simplification, but this study is aimed at demonstrating a qualitative phenomenon rather than e.g. exactly emulating Earth's climate, so the trade-off between accuracy and flexibility was judged worthwhile. Further, under high $\mathrm{CO_2}$ conditions, low-lying high-albedo water clouds are predicted to decrease substantially in extent due to the inhibition of cloud-top radiative cooling in a highly opaque atmosphere (Schneider et al., 2019; Goldblatt et al., 2021), so the approximation may be less grave under those conditions. We only present simulations where $\mathrm{CO_2}$ is subsaturated throughout the atmosphere, so although CO_2 clouds may be relevant in similar climates with slightly higher pCO$_2$ or lower temperatures (e.g. Kitzmann, 2017), their neglect has no impact on our results. The model also excludes land or sea ice, so the ice-albedo feedback (e.g. Sellers, 1969) is not in play, but this is not a serious issue for the warm climates we are examining, all of which sport little or no surface area with temperatures below freezing (as described in Section 5.3.1). Further, the ice-albedo feedback is weakened significantly under thick CO_2 atmospheres, which reduce the impact of changes to the surface albedo on planetary energy budgets (Von Paris et al., 2013).

Radiative transfer calculations coupled to Isca's dynamics are carried out with the SOCRATES code (Edwards & Slingo, 1996), using the correlated-k method to solve the plane-parallel, two-stream approximated radiative transfer equation with scattering for atmospheres irradiated by a solar (G-star) spectrum. In high-instellation, low-pCO$_2$ simulations, we used the standard, validated spectral files used by the UK Met Office in the latest iteration of its Unified Model to simulate Earth's climate (Walters et al., 2019). For high pCO$_2$ model configurations, we used a spectral file from NASA GISS's ROCKE-3D (Way et al., 2017) database and created for GCM modeling of the Martian atmosphere, similar (though not identical) in construction to that used in Guzewich et al. (2021) (Eric T. Wolf, personal communication). The file is valid for atmospheres up to 10 bars with $> 90\%$ CO_2 and temperatures up to 400 K, with some loss of accuracy above 310 K (though we compared TOA fluxes from this model at high temperatures with those generated using a high resolution 318 band spectral file used in Graham et al. (2022b) and found the output from the GCM stayed within 5 W m^{-2} of the higher resolution calculations). Rayleigh scattering is interactively calculated with coefficients included in SOCRATES for the relevant gases. For CO_2, opacity coefficients were tabulated and derived from the HITRAN database, making use of line-by-line and collision-induced absorption coefficients, along with sub-Lorentzian line-broadening and self-broadening (Perrin & Hartmann, 1989; Baranov et al., 2004; Gordon et al., 2017), and similarly for H_2O, which included line-by-line and collision-induced absorption coefficients and the H_2O MT-CKD continuum, along with broadening coefficients that are unfortunately calculated with respect to Earth air (Mlawer et al., 2012; Gordon et al., 2017), which may somewhat underestimate water opacities at high temperatures (Pierrehumbert, 2010a). We note that the CO_2 continuum spectrum is uncertain at high temperatures and pressures, which introduces a potentially significant source of error into our calculations (e.g. Halevy et al., 2009; Wordsworth et al., 2010a).

	S [W m^{-2}]:				
	675	750	800	1000	1250
pCO$_2$ [bars]:					
2×10^{-4}					✓
3×10^{-4}					✓
4×10^{-4}					✓
1		✓	✓	✓	
2	✓	✓	✓	✓	
3	✓	✓	✓		
4	✓				

Table 5.1: Table with checkmarks indicating the combinations of substellar TOA instellation (S; columns) and CO_2 partial pressure (pCO_2; rows) used in the simulations presented in this study. The simulations with $pCO_2 < 1$ bar (marked green) are supplemented by 1 bar of N_2, while those with $pCO_2 > 1$ bar have no atmospheric N_2.

With one exception, each simulation was run until the TOA and surface energy fluxes were balanced to within <1% and then for at least a year further, with stated results coming from averages over the final year of data for each simulation. The three low pCO_2 simulations have N_2-dominated atmospheres, surface pressures of 1 bar, and CO_2 concentrations of 200, 300, and 400 parts per million by volume (ppmv), all irradiated by TOA instellation of S = 1250 W m^{-2}. The eleven high pCO_2 simulations have TOA substellar shortwave instellations of S = 675, 750, 800 or 1000 W m^{-2} and CO_2 partial pressures of one, two, three, or four bars (see Table 5.1). All simulations have atmospheric H_2O content determined by Isca's hydrologic cycle. The simulation with three bars of CO_2 irradiated by S = 800 W m^{-2} is the exception to the statement about equilibration of fluxes to within < 1%, as one of its grid cells exceeded the model's temperature limit of 350 K during spin-up while TOA fluxes were still 1.9% out of balance. Thus results from that simulation are averaged over a period during which the planetary surface was still gradually heating, with a 2% TOA flux imbalance, instead of < 1% like the others. Based on the behavior of the other simulations, the model would have warmed another Kelvin or two in the mean if it had been able to run to equilibrium, a small error unlikely to have any impact on the qualitative trends demonstrated here.

5.2.2 Weathering models

For both the MAC and the WHAK formulation, we calculate a weathering flux (F_{sil} [moles m^{-2} yr^{-1}]) in any grid cell that 1.) has land, 2.) has a surface temperature above the triple point of water, 273.15 K, and 3.) has a local precipitation flux greater

Parameter	**Units**	**Definition**	**Fiducial Value**
γ_{Earth}	–	Earth's land fraction	0.3
a_g	–	Surface albedo	0.05
R_{planet}	meters (m)	Planetary radius	6.37×10^{6}
W_{ref}	moles per year (mol yr^{-1})	Reference weathering rate equal to recent Earth outgassing estimate	3.4×10^{12} (Coogan & Gillis, 2020)
T_{ref}	Kelvin (K)	Reference global-avg. temperature	288
$p\text{CO}_{2,\text{ref}}$	bar	Reference CO_2 partial pressure	280×10^{-6}
Λ	variable	Thermodynamic coefficient for C_{eq}	1.4×10^{-3}
n	–	Thermodynamic $p\text{CO}_2$ dependence	0.316
α*	–	$L\phi\rho_{sf}AX_r\mu$ (see Section 5.2.2 and below)	3.39×10^{5}
$k_{\text{eff,ref}}$*	mol m^{-2} yr^{-1}	Reference rate constant	8.7×10^{-6}
β	–	Kinetic weathering $p\text{CO}_2$ dependence	0.2 (Rimstidt et al., 2012)
T_{e}	Kelvin	Kinetic weathering temperature dependence	11.1 (Berner, 1994)

Table 5.2: Weathering parameters used in this study. This table lists parameters used in our calculations, their units, their definitions, and the default values they take. A single asterisk (*) means the default parameter value was drawn from Table S1 of the supplement to Maher & Chamberlain (2014). For default parameters drawn from other sources, the citation is given in the "Value" column.

than zero. Here, we focus exclusively on continental silicate weathering, ignoring the potential contribution of analogous reactions on the seafloor (e.g. Coogan & Gillis, 2013) due to lack of clarity about the strength of this feedback, but we return to the issue of seafloor weathering in Section 5.4. A global weathering rate (W_{tot} [moles yr^{-1}]) is calculated by multiplying each cell's weathering flux by the surface area (dA) of the grid cell and then adding them all together i.e.

$$W_{\text{tot}} = \sum_{\text{lat,lon}} F_{\text{sil}} dA \tag{5.2}$$

rendering the CO_2 consumption rate for a planet with the assumed weathering properties and background climate.

For silicate weathering to serve as a stabilizing negative feedback on planetary climate, it must act to maintain the climate at a set-point determined by the properties of the silicates being weathered, the orbital and surface properties of the planet, and the planet's CO_2 outgassing rate. This requires global weathering to accelerate with increases to $p\mathrm{CO_2}$ and surface temperature. Under such conditions, if a planet has its climate perturbed in a way that makes its weathering rate fall below its CO_2 outgassing rate, CO_2 will be consumed more slowly than it is added to the atmosphere, leading to net CO_2 growth and surface warming until the global weathering rate has accelerated to the point that it is equal to outgassing, whence the atmospheric CO_2 content will stop evolving. In the opposite scenario, where global weathering decelerates in response to increases in $p\mathrm{CO_2}$ and surface temperature, the process becomes a destabilizing feedback. In this case, a perturbation that caused weathering rates to fall below outgassing rates would become self-reinforcing, with the resulting CO_2 accumulation decelerating global weathering rates (rather than accelerating them), further accelerating CO_2 accumulation, further slowing weathering rates, leading to a positive feedback loop that would end in catastrophic warming (or catastrophic cooling in the case where the initial perturbation forced weathering rates to be faster than outgassing rates).

Thus the stability of a carbon cycle at a given instellation can be determined by calculating how the weathering rate changes with $p\mathrm{CO_2}$ (the so-called "weathering curve" (Penman et al., 2020)): if weathering rate is positively correlated with $p\mathrm{CO_2}$, it acts as a stabilizing negative feedback, but if it is inversely correlated with $p\mathrm{CO_2}$ it acts as a destabilizing positive feedback. So, rather than carry out very long asynchronously-coupled simulations evolving atmospheric $p\mathrm{CO_2}$ according to the balance between an assumed outgassing flux and a calculated weathering flux, we take the much simpler approach of doing a handful of simulations at a variety of $p\mathrm{CO_2}$ and diagnosing the global weathering rates from these "snapshots." Simply determining the sign of the slope of the weathering curve at a given instellation is sufficient for determining the stability of the carbon cycle. Under stabilizing conditions, imposing an outgassing rate would inexorably drive the $p\mathrm{CO}_2$ to the level that generates a weathering rate equal to the assumed outgassing rate. Under destabilizing conditions, the final outcome would be determined by the initial conditions, i.e. whether the planet started off with outgassing greater than or smaller than its initial weathering rate.

In the next subsections, we describe how the two weathering models we deploy (MAC and WHAK) calculate F_{sil} as a function of local climate.

WHAK

The formulation of weathering developed in Walker et al. (1981) (WHAK) is the basis for the calculations in most previous exoplanet weathering/climate studies, including the few that have employed 3D GCMs (e.g. Edson et al., 2012; Paradise & Menou, 2017; Jansen et al., 2019; Paradise et al., 2019). We carry out calculations using the WHAK weathering formulation to compare with results from the more chemically realistic MAC formulation presented below. WHAK weathering assumes silicate weathering rates are limited by the kinetics of silicate dissolution, which produces an exponential dependence on temperature and a power-law dependence on CO_2 partial pressure ($p\mathrm{CO}_2$). We represent this as:

$$F_{\mathrm{sil}} = \frac{W_{\mathrm{ref}}}{\gamma_{\mathrm{Earth}} \times 4\pi R_{\mathrm{Earth}}^2} \exp\left(\frac{T - T_{\mathrm{ref}}}{T_{\mathrm{e}}}\right)\left(\frac{\mathrm{pCO}_2}{\mathrm{pCO}_{2,\mathrm{ref}}}\right)^{\beta} \tag{5.3}$$

where F_{sil} [mol m^{-2} yr $^{-1}$] is the weathering flux from a grid cell, i.e. the number of divalent cations (which react with oceanic carbon to form carbonate minerals, ultimately removing CO_2 from the atmosphere) delivered to the ocean per unit time per unit land area in a given grid cell; W_{ref} is a reference global weathering rate (assumed equal to an estimate of Earth's modern-day CO_2 outgassing, see Table 5.2); $\gamma_{\mathrm{Earth}} \times 4\pi R_{\mathrm{Earth}}^2$ is the approximate land area of the Earth, calculated by multiplying its land fraction (γ_{Earth}) by its surface area ($4\pi R_{\mathrm{Earth}}^2$), necessary for translating W_{ref} from a global weathering rate into a weathering flux per unit land area; T [K] is the local surface temperature in a grid box; T_{e} is the e-folding temperature for the weathering reaction; $p\mathrm{CO}_2$ [bar] is the CO_2 partial pressure; and β is the power-law dependence on $p\mathrm{CO}_2$. The values of T_e and β, which determine the sensitivity of the reaction rate to changes in temperature and $p\mathrm{CO}_2$, vary considerably for different silicate minerals. We choose the default values listed in Table 5.2 based on results from laboratory silicate dissolution experiments (e.g. Schott & Berner, 1985; Brady, 1991; Knauss et al., 1993; Oxburgh et al., 1994; Welch & Ullman, 1996; Chen & Brantley, 1998; Weissbart & Rimstidt, 2000; Oelkers & Schott, 2001; Palandri & Kharaka, 2004;

Carroll & Knauss, 2005; Golubev et al., 2005; Bandstra & Brantley, 2008; Brantley et al., 2008). In this formulation of WHAK, we ignore the runoff-dependence assumed in the original formulation (Walker et al., 1981), as it has been demonstrated not to substantially impact global weathering rates, which are dominated by the exponential temperature dependence and power-law CO_2 dependence (Abbot et al., 2012). Further, truly kinetically-limited weathering would not be impacted by changes to runoff, since the weathering rate would instead be determined by the rate of production of cations through silicate dissolution. Absent an accompanying change to temperature or $p\mathrm{CO}_2$, any change to runoff above zero would simply change the dilution of weathering products without ultimately altering their rate of production or delivery to the ocean.

MAC

The other weathering model we apply in our simulations is modified from (Graham & Pierrehumbert, 2020), which applied a global-mean version of the MAC weathering model (Maher & Chamberlain, 2014; Winnick & Maher, 2018) to calculate global weathering fluxes from models of Earth-like exoplanets. The MAC model accounts for the impact of clay formation in the weathering zone, which sets a maximum concentration on weathering products in runoff, drastically increasing the importance of hydrology for determining weathering fluxes when water moves through the weathering zone at a rate that allows for weathering products to reach the maximum chemically-equilibrated concentration. In this paper, rather than a global-mean formulation, we apply the weathering model from Graham & Pierrehumbert (2020) locally in each land grid cell, with the weathering flux in a given cell determined by the parameterized silicate properties, local H_2O precipitation flux, surface temperature, and $p\mathrm{CO}_2$:

$$F_{\mathrm{sil}} = \frac{\alpha}{[k_{\mathrm{eff}}]^{-1} + mAt_{\mathrm{s}} + \alpha[qC_{\mathrm{eq}}]^{-1}}, \tag{5.4}$$

where F_{sil} [mol m^{-2} yr^{-1}] is the weathering flux from a given cell as above; α is a parameter that captures the effects of various weathering zone properties like characteristic water flow length scale, porosity, ratio of mineral mass to fluid volume, and the mass fraction of minerals in the weathering zone that are weatherable (see Graham & Pierrehumbert (2020) for a full explanation); $k_{\mathrm{eff}} = k_{\mathrm{eff,ref}} \exp\left(\frac{T_{\mathrm{surf}} - T_{\mathrm{surf,ref}}}{T_{\mathrm{e}}}\right)\left(\frac{p\mathrm{CO}_2}{p\mathrm{CO}_{2,\mathrm{ref}}}\right)^{\beta}$ [mol m^{-2} yr^{-1}] is the effective kinetic weathering rate, i.e. the weathering rate in the absence of chemical equilibration with clay formation (Walker et al., 1981); m [kg mol^{-1}] is the average molar mass of minerals being weathered; A [m^2 kg^{-1}] is the average specific surface area of the minerals being weathered; t_s [yr] is the mean age of the material being weathered; q [m yr^{-1}] is the flux of water through the grid cell, given by the precipitation in that grid cell output by the GCM; and $C_{\mathrm{eq}} = \Lambda(p\mathrm{CO}_2)^n$ [mol m^{-3}] is the maximum concentration of divalent cations in the water passing through weathering zones, as determined by chemical equilibrium between dissolving silicates and the secondary minerals (clays) that form from their products. The default values of all constants are given in Table 5.2.

By equating local precipitation and q, we are assuming that any rain that falls on land drives weathering that delivers solutes to the ocean, i.e. that all precipitation is converted to runoff. Thus these calculations provide an upper limit on weathering fluxes and the efficiency of MAC weathering as a climate feedback with a given set of parameters, as smaller rates of runoff to the ocean would reduce weathering rates. On modern Earth, 20-26% of precipitation falling on land may be converted to runoff (Ghiggi et al., 2019; Graham & Pierrehumbert, 2020; Coy, 2022), but this value is likely to be heavily dependent on factors like topography, surface temperature, and background atmosphere. As long as runoff is largely monotonic with precipitation, as seems likely (Le Hir et al., 2009; Ghiggi et al., 2019) (though it is unclear whether this must be the case (O'Gorman et al., 2012)), the qualitative behavior we describe should hold. Smaller rates of conversion from rain to runoff exacerbate the severity of the mechanism explored here by allowing the energetically-limited regime to be accessed under smaller background CO_2 outgassing rates.

5.3 Results

5.3.1 Surface temperature

The mean climate states and CO_2 equilibrium climate sensitivities (ECS) of the simulations are in line with previously published estimates.

The ECS is the steady-state change in global-mean surface temperature from a doubling of atmospheric CO_2, commonly used in studies of Earth's climate (Knutti et al., 2017; Romps, 2020; Goodwin, 2021). The modern Earth's ECS is generally estimated to fall between 1.5 K and 4.5 K per doubling (e.g. Knutti et al., 2017). This is consistent with the global-mean temperature behavior of our low-$p\mathrm{CO}_2$ simulations, which warmed from 298.1 to 301.5 K as CO_2 was doubled from 200 ppmv to 400 ppmv (see green line and dots in Fig. 5.1), indicating a reasonable ECS of 3.4 K. These simulations are substantially hotter than the modern Earth despite receiving 8% less

TOA instellation because they lack clouds and the surface has a uniform, dark albedo of 0.05, resulting in planetary albedo of 0.1 due to N_2's modest Rayleigh scattering effect, in contrast to Earth's cloud- and ice-maintained albedo of 0.29 (Stephens et al., 2015). None of the low-pCO$_2$ simulations displays temperatures below freezing on any landmass, and in each case the fraction of planetary surface area below freezing at the poles is small (4.2%, 2.5%, and 1.7% for the 200 ppmv, 300 ppmv, and 400 ppmv simulations respectively).

In climate simulations with very high CO_2, ECS is known to increase as a function of pCO$_2$ due to the increasing importance of self-broadening and activation of spectral regions that are minor at lower pressures (e.g. Halevy et al., 2009; Pierrehumbert, 2010a; Wolf et al., 2018; Graham, 2021). Our high pCO$_2$ simulations reflect this behavior, with all displaying an ECS of ≈15 K (see blue, cyan, magenta, and red lines with dots in Fig. 5.1). This is consistent with the behavior of GCM simulations of early Earth atmospheres with instellations slightly larger and pCO$_2$ levels slightly lower than those presented here (Wolf et al., 2018), as well as with ECS values calculated using a polynomial fit (Kadoya & Tajika, 2019) to radiative-convective column model output (Kopparapu et al., 2013) with 1 bar N_2, saturated H_2O, and up to 10 bars CO_2 (Graham, 2021). None of the presented high-pCO$_2$ simulations has temperatures below freezing on any landmass, and only the 1 bar, S = 750 W m^{-2} has any planetary surface area below freezing (5.2%, at the poles). Finally, as expected, with a given pCO$_2$, increased instellation leads to higher surface temperatures.

5.3.2 Energy budgets and precipitation

Low pCO$_2$, high instellation

The behavior of the low-pCO$_2$ simulations is largely consistent with expectations from simulations of Earth climate. They approximately reproduce the expected positive trend in global-mean surface latent heat flux (green line with circle markers in Fig. 5.2), the expected negative trend in global-mean upward longwave from the surface (green line with x markers in Fig. 5.3), and the expected positive trend in precipitation (green lines in Figs. 5.4 and 5.5). Averaged across the three low-pCO$_2$ simulations, global-mean latent heat flux and global-mean precipitation both increased by 1.1 % K^{-1}, a bit less than the median value of 1.7% K^{-1} found in Earth climate simulations Held & Soden (2006). Despite increasing somewhat with surface temperature, for all three low-pCO$_2$ simulations the latent heat flux remained far below the limit set by S_{abs} (green line with star markers in Fig. 5.2), which decreased slightly in

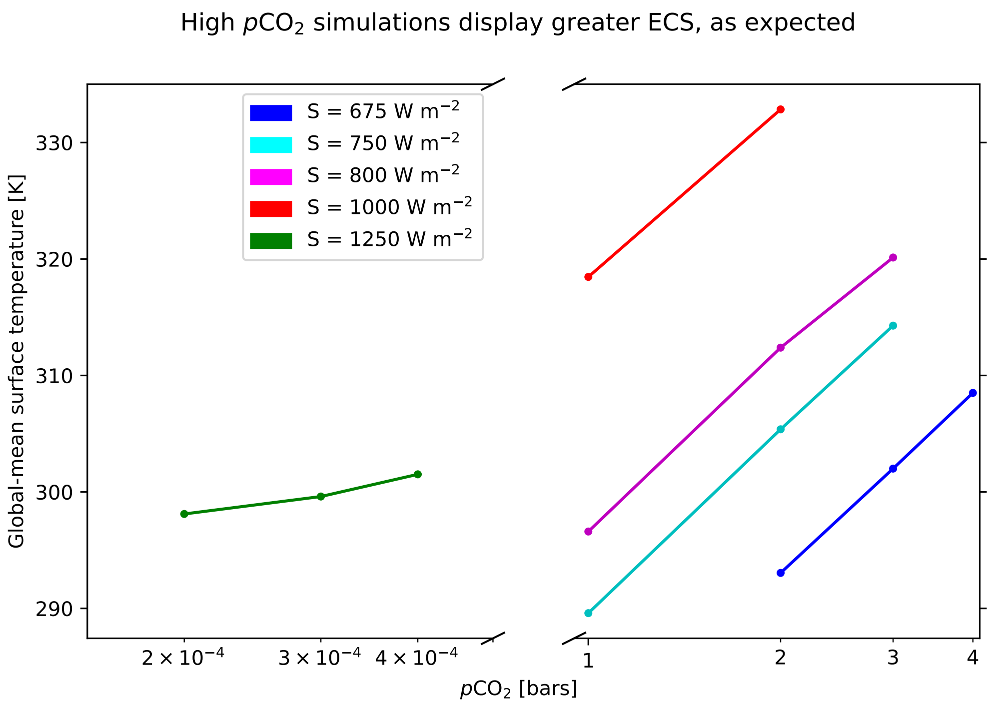

Figure 5.1: **Global-mean surface temperature as a function of $p\mathrm{CO_2}$ at various instellations S.** The low-$p\mathrm{CO_2}$, high-instellation simulations display an ECS of 3.4 K, close to estimates of the modern Earth's (1.5 to 4.5 K). The high-$p\mathrm{CO_2}$, low-instellation simulations all display ECS values of around 15 K due to CO_2's self-broadening effect. Blue corresponds to $S = 675$ W m^{-2}, cyan to 750 W m^{-2}, magenta to 800 W m^{-2}, red to 1000 W m^{-2}, and green to 1250 W m^{-2}.

response to CO_2's growth because of increased atmospheric absorption of instellation by H_2O as specific humidity rose. The total global-mean net upward longwave flux decreased by 8.7 W m^{-2} from the 200 ppmv simulation to the 400 ppmv simulation, a somewhat greater reduction than the 4-5 W m^{-2} per CO_2 doubling in Earth GCM simulations (e.g. Gutowski Jr et al., 1991; Boer, 1993), but this is to be expected since our low $p\mathrm{CO_2}$ simulations have a warmer background climate than Earth, meaning they should experience larger increases in highly opaque lower-tropospheric water vapor for a given change in temperature than cooler Earth simulations because of the exponential dependence of H_2O partial pressure on temperature. The sensible heat flux of the low-$p\mathrm{CO_2}$ simulations changes very little as a function of CO_2, with a reduction of $\approx$1 W m^{-2} between the 200 ppmv and 300 ppmv simulations, and an increase of $\approx$1 W m^{-2} between the 300 ppmv and 400 ppmv simulations (green line with plus-shaped markers in Fig. 5.3). This contrasts somewhat with simulations of

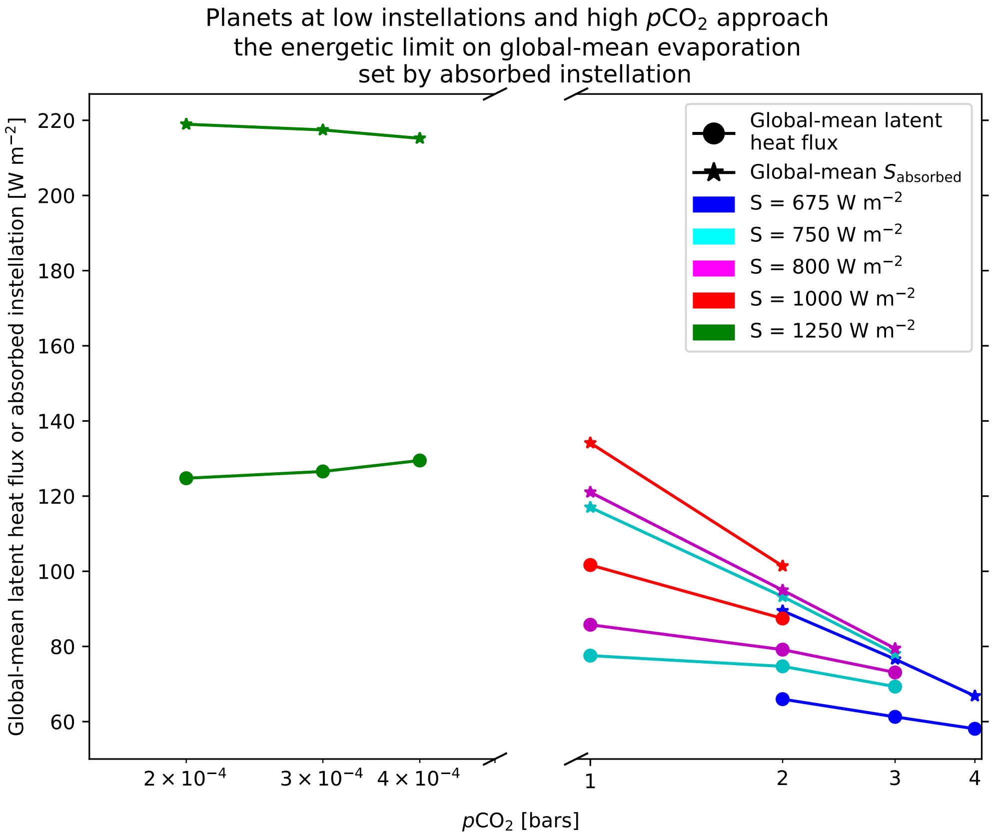

Figure 5.2: **Global-mean absorbed instellation and global-mean upward latent heat flux as functions of pCO$_2$ at various S** For low-pCO$_2$, high-instellation simulations, latent heat flux (circle markers) increases with pCO$_2$, but remains far below absorbed instellation (star markers). For high-pCO$_2$, low-instellation simulations, a large majority of their absorbed instellation goes into the latent heat of evaporation. Colors are as in Fig. 5.1.

Earth, where the surface's upward sensible heat flux consistently decreases by 1-3 W m^{-2} (Gutowski Jr et al., 1991; Boer, 1993) under a doubling of CO$_2$. This difference may be due to our neglect of topography. Nonetheless the changes in sensible heat flux are small in magnitude and the flux itself is already a small enough term in the surface budget that it has no impact on our qualitative results.

High pCO$_2$, low instellation

The high pCO$_2$, low-instellation simulations display markedly different behavior from that described above and are clearly operating in a regime where the energetic limit set by absorbed instellation exerts substantial influence. For all sets of high-pCO$_2$

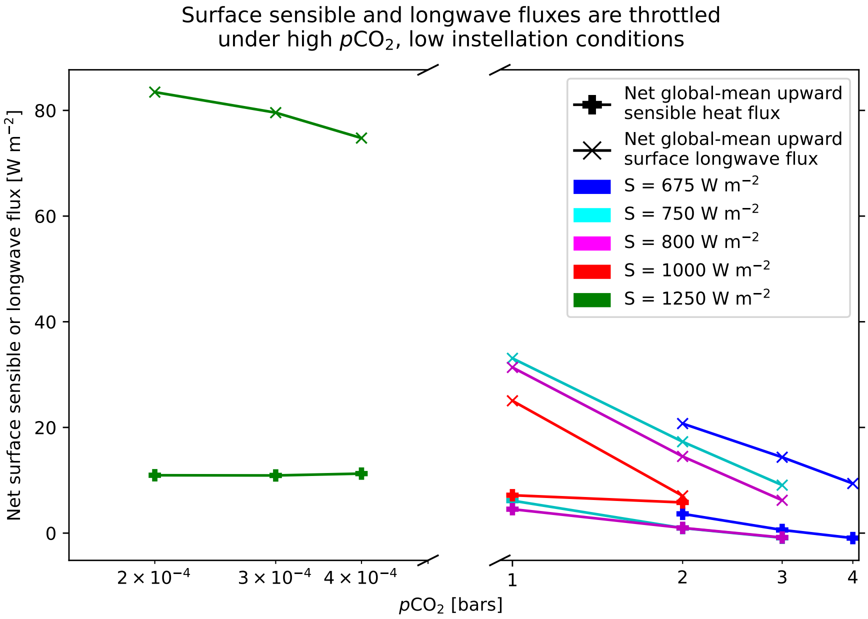

Figure 5.3: **Net upward sensible or longwave heat flux [W m^{-2}] as a function of pCO$_2$ for simulations at various S.** For low-pCO$_2$ simulations, the sensible heat flux (x-shaped markers) changes little with pCO$_2$, while for high-pCO$_2$ simulations it drops substantially, even becoming negative in some cases. For both low- and high-pCO$-$2 simulations, the longwave flux (plus-shaped markers) decreases with increasing CO$_2$, as expected. Colors are as in Fig. 5.1.

simulations irradiated by a given S, global-mean upward latent heat flux at the surface decreases with increasing pCO$_2$, despite the fact that surface temperature increases substantially (see blue, cyan, magenta, and red lines with circles in Fig. 5.2). These reductions in latent heat flux are accompanied (and driven) by large reductions in absorbed instellation at the surface (see blue, cyan, magenta, and red lines with stars in Fig. 5.2) due mostly to increases in albedo from CO$_2$'s Rayleigh scattering, from values of 0.16-0.17 for the pCO$_2$=1 bar cases, to 0.26-0.27 in the pCO$_2$=3 bars simulations, to 0.30 in the pCO$_2$=4 bars case. As pCO$_2$ is increased in these simulations, even though the absolute latent heat flux goes down, an increasing proportion of the absorbed instellation at the surface goes into evaporation, with values ranging from 66% to 92% for the high-pCO$_2$ cases, compared with a range of 57% to 60% for the low-pCO$_2$ simulations (see Table 5.3). Correspondingly, the sensible and longwave heat flux contributions to the surface energy budgets in the high-pCO$_2$ simulations are substantially reduced in both absolute and relative terms (see blue, cyan, magenta, and red plus-shaped markers and x-shaped markers in Fig. 5.3). Interestingly, the global-mean sensible heat flux becomes negative (directed into the surface) in the

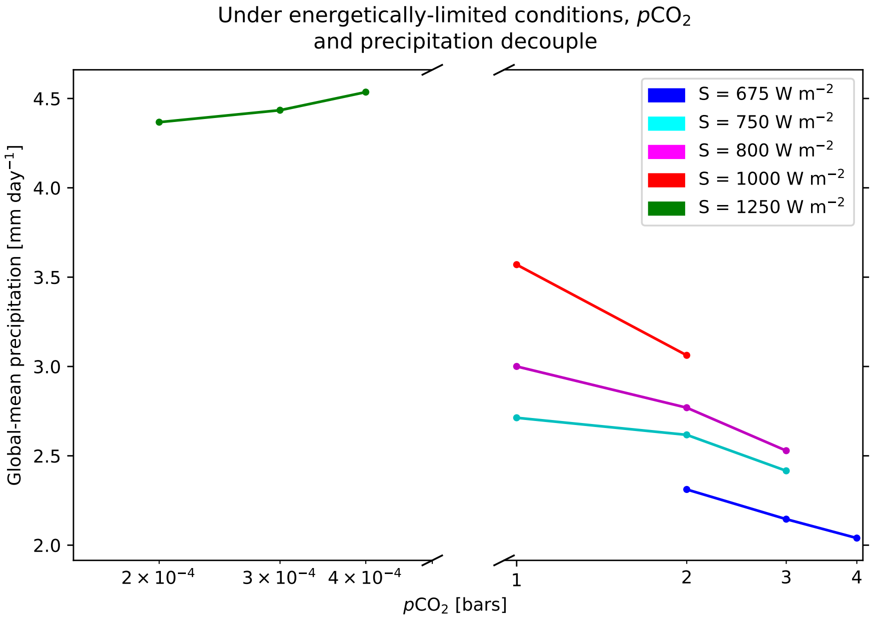

Figure 5.4: **pCO$_2$ vs. global-mean precipitation.** For low-pCO$_2$, high-instellation simulations, precipitation increases with pCO$_2$. For high-pCO$_2$, low-instellation simulations in the regime where a large majority of their absorbed instellation goes into driving evaporation, precipitation falls with pCO$_2$. Colors are as in Fig. 5.1.

pCO$_2$=3 bars simulations irradiated by S = 750 W m^{-2} and 800 W m^{-2} and in the pCO$_2$=4 bars, S = 675 W m^{-2} simulation, but in each case the net sensible heating of the surface is less than 1 W m^{-2}.

As implied by the trends in latent heat flux vs pCO$_2$ displayed in Fig. 5.2, global-mean precipitation rates in the high-pCO$_2$ simulations fall with increasing CO$_2$ (see blue, cyan, magenta, and red lines in Fig. 5.4). This results in counterintuitive behavior, driving precipitation rates that decrease with increasing surface temperature (see blue, cyan, magenta, and red lines in Fig. 5.5). Despite some high-pCO$_2$ simulations having surface temperatures much larger than the low-pCO$_2$ simulations, the low-pCO$_2$ simulations all have global-mean precipitation rates larger than any of the high-pCO$_2$ simulations, consistent with the fact that the low-pCO$_2$ precipitation rates are sustained by latent heat fluxes larger than the S_{abs} received by any of the high-pCO$_2$ simulations except the pCO$_2$=1 bar, S = 1000 W m^{-2} case (compare green line with circles to blue, cyan, magenta, and red lines with stars in Fig. 5.2). In the next section we explore the implications of this energetically-limited precipitation behavior for the functioning of the carbon cycle.

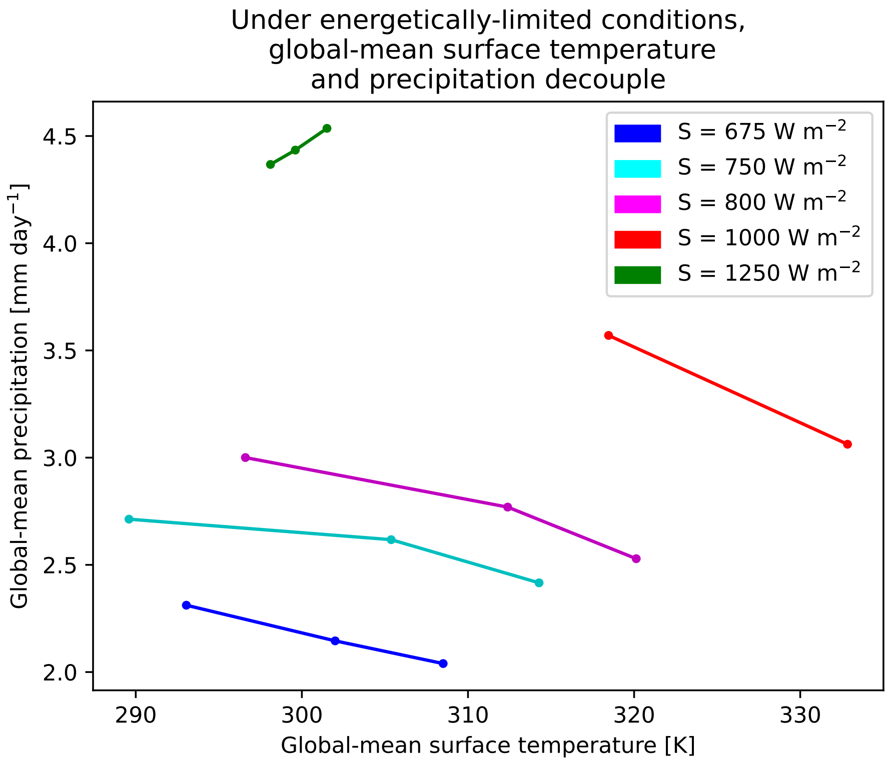

Figure 5.5: **Global-mean surface temperature vs. global-mean precipitation.** For low-$p\mathrm{CO_2}$, high-instellation simulations, precipitation increases with surface temperature. For high-$p\mathrm{CO_2}$, low-instellation simulations in the regime where a large majority of their absorbed instellation goes into driving evaporation, precipitation falls with temperature. Colors are as in Fig. 5.1.

$p\mathrm{CO_2}$ [bars]:	**S [W m^{-2}]:** 675	750	800	1000	1250
2×10^{-4}					0.57
3×10^{-4}					0.58
4×10^{-4}					0.60
1		0.66	0.71	0.76	
2	0.74	0.80	0.83	0.86	
3	0.80	0.89	0.92		
4	0.87				

Table 5.3: **Fraction of absorbed instellation going into evaporation** ($\frac{L}{S_{\mathrm{abs}}}$). Table layout identical to Table 5.1 except $\frac{L}{S_{\mathrm{abs}}}$ values replace checkmarks.

5.3.3 Weathering rates

In this Section we will present estimates of weathering rates based on output fields from the GCM simulations described above, with weathering fluxes calculated according to both the WHAK and MAC formulations. Sensitivity tests varying the parameters in the weathering models within plausible ranges generated fairly large changes in absolute fluxes but did not affect the qualitative picture presented here.

WHAK weathering

When weathering is calculated according to the WHAK formulation (equation 5.3), the weathering rate increases strongly in response to increases in $p\mathrm{CO_2}$ and S for all simulations, regardless of initial $p\mathrm{CO_2}$ or instellation (see Fig. 5.6). This makes sense, given the WHAK formulation's exponential temperature-dependence and power-law $p\mathrm{CO_2}$ dependence, both of which naturally produce big increases in weathering fluxes for modest changes in temperature and/or $p\mathrm{CO_2}$. The increases produced by this model are unrealistically large even if we take the WHAK formulation at face value, as the global rate of rock uplift sets a "supply limit" on the rate of silicate weathering of $\mathcal{O}(100)$ trillion moles of $\mathrm{CO_2}$ per year on Earth [Tmol yr^{-1}] (e.g. Kump, 2018), but the positive slope of the curves in Fig. 5.6 confirms in principle the continued operation of WHAK weathering as a negative feedback even under high-$p\mathrm{CO_2}$, low-instellation conditions where energetically-limited precipitation is relevant. Earth's outgassing rate is generally estimated to lie somewhere between 3 and 15 Tmol yr^{-1} (Coogan & Gillis, 2020), substantially smaller than even the smallest weathering rate produced by the these simulations, but this is due to our mostly arbitrary choice of weathering constant W_{ref} in equation 5.3. A smaller W_{ref} would produce proportionally smaller weathering rates without changing the qualitative trends in weathering vs. $p\mathrm{CO_2}$.

MAC weathering

With MAC weathering, the low $p\mathrm{CO_2}$ simulations respond essentially as expected (Fig. 5.7). Although the strength of the weathering response to the changes in the surface climate is much weaker than in the WHAK case, the weathering rate in the low $p\mathrm{CO_2}$ simulations still increases with increasing $p\mathrm{CO_2}$, producing a stabilizing negative feedback. This provides tentative evidence that MAC-style continental weathering may be able to stabilize the climates of planets under Earth-like conditions of high instellation and low $p\mathrm{CO_2}$.

In contrast, the high $p\mathrm{CO_2}$, low instellation simulations in the energetically-limited regime produce a drastically different carbon cycle than the WHAK calculations or the low-$p\mathrm{CO_2}$ MAC calculations would suggest. While they do display somewhat higher weathering rates than the low $p\mathrm{CO_2}$ simulations due to the thermodynamic $p\mathrm{CO_2}$-dependence of the maximum concentration of weathering products in runoff

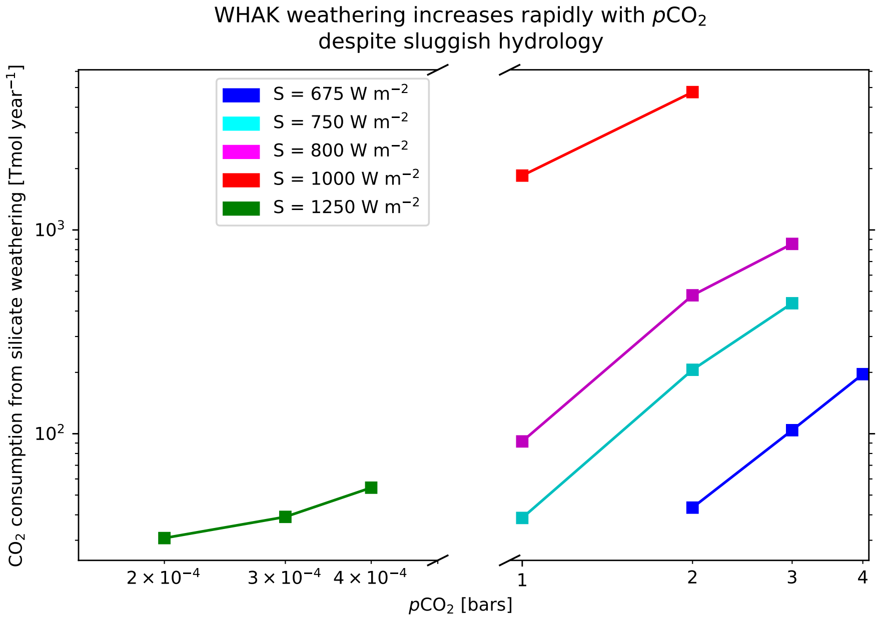

Figure 5.6: **Global WHAK weathering rates [Tmol yr^{-1}] vs. pCO$_2$ for a variety of instellations**. Weathering fluxes are calculated according to the WHAK formulation (equation 5.3). For all simulations, the weathering rate increases with CO_2. Colors are as in Fig. 5.1.

(C_{eq} in equation 5.4, a much weaker effect than that the kinetic pCO$_2$-dependence of WHAK weathering represented by β in equation 5.3), all of the high-pCO$_2$ simulations display the opposite response to further increases in CO_2: at a given S, as pCO$_2$ increases (along with surface temperature), the global weathering rate goes down (see blue, cyan, magenta, and red lines in Fig. 5.7). As described in Section 5.2.2, anti-correlation between global weathering rates and pCO$_2$ destabilizes the carbon cycle, so the high-pCO$_2$ simulations are all displaying a defective climate thermostat with a positive feedback that would likely induce runaway climate heating or cooling. Although this result runs counter to Earth-based intuitions, the unusual trends in pCO$_2$ vs. weathering make sense given the increased importance of hydrologic cycling in the MAC weathering framework and the reduction in global-mean precipitation triggered by reduced S_{abs}.

Another unexpected weathering trend appears in the set of high pCO$_2$ simulations: holding CO_2 constant, the global weathering rate goes down even as instellation rises and drives both surface temperature (Fig. 5.1) and global-mean precipitation (Fig. 5.4) upward with it. This trend obviously cannot be explained by a global-mean argument, since all of the variables that directly control weathering are, in bulk, either increasing (i.e. q and surface temperature) or staying the same (i.e. pCO$_2$)

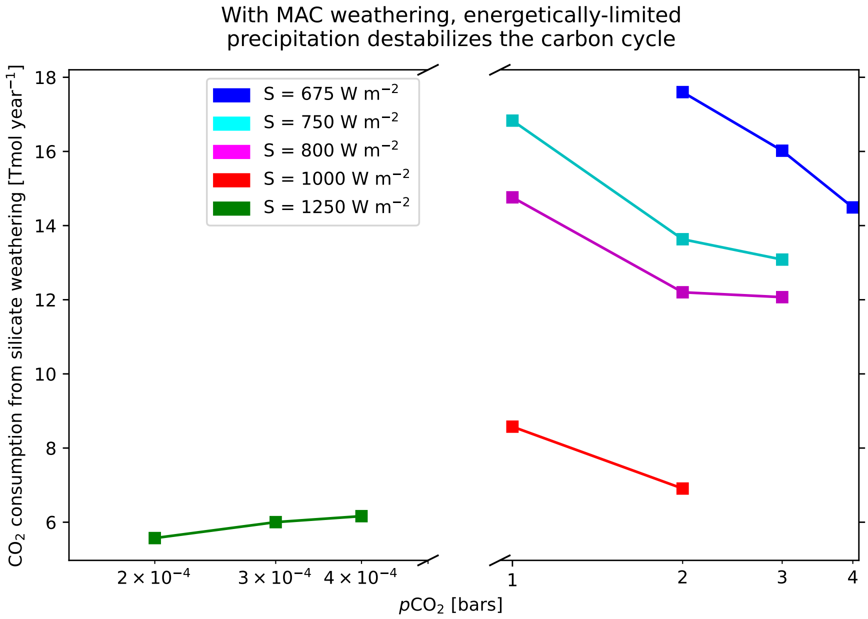

Figure 5.7: **Global MAC weathering rates with fiducial parameter values [Tmol yr^{-1}] vs. pCO$_2$ for a variety of instellations**. Weathering fluxes are calculated according to the MAC formulation (equation 5.4). For low-pCO$_2$ simulations, the weathering rate increases with CO_2, while for high-pCO$_2$ simulations weathering decreases with increasing CO_2. Colors are as in Fig. 5.1.

as S is increased. Instead, the explanation lies in the intensification of moisture extremes expected in warming climates from simple thermodynamic considerations (Held & Soden, 2006; Allan et al., 2020), often referred to by the phrase "wet gets wetter, dry gets drier" (WGWDGD) in discussions of Earth climate (Allan et al., 2020) though over the past several years it has become clear that this basic picture does not hold as well over land in Earth simulations as it does over the ocean (Byrne & O'Gorman, 2015; Feng & Zhang, 2015; Allan et al., 2020). Although WGWDGD does not perfectly describe the moisture response over land in Earth simulations under the (comparatively) small climate perturbations projected for this century, it quite accurately describes the behavior of the precipitation in our high-pCO$_2$ simulations as S is increased.

In other words, although the total global precipitation flux increases with S in our high-pCO$_2$ simulations, it also becomes concentrated onto a smaller area, meaning deserts expand as S goes up. For example, in the S = 675 W m^{-2}, pCO$_2$=2 bars case, over half of the planet's land area receives more than 1 mm day^{-1} precipitation, whereas only about a quarter of the land area in S = 1000 W m^{-2} receives that much water (see right side of Fig. 5.8). This is compensated by an increasing fraction

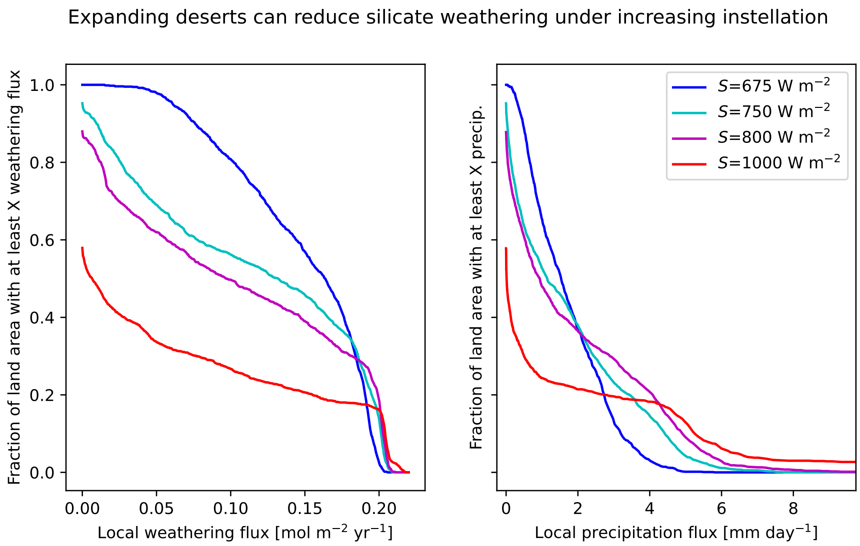

Figure 5.8: **The change in spatial distribution of weathering (left) and precipitation (right) that accompanies increasing TOA instellation** Results shown are for simulations with $p\mathrm{CO_2} = 2$ bars and $S = 675$ W m^{-2} (blue), $S = 750$ W m^{-2} (cyan), $S = 800$ W m^{-2} (magenta), and $S = 1000$ W m^{-2} (red). The y-value of a curve represents the fraction of land with at least as much weathering flux (left) or precipitation (right) as the corresponding x-axis value. Even though the total global precipitation increases as S increases, the total global weathering rate decreases because less land is receiving substantial precipitation. See Section 5.3.3. Colors are as in Fig. 5.1.

of landmass with high precipitation fluxes, i.e. only ≈5% of the landmass in the aforementioned $S = 675$ W m^{-2} simulation exceeds 4 mm day^{-1} of rain, but about 20% of the landmass in the 1000 W m^{-2} simulation meets that criterion, and higher S generally leads to a longer "tail" of landmass with large local precipitation fluxes. As can be seen by comparing the weathering flux curves on the left side of Fig. 5.8 with the precipitation flux curves on the right, local weathering tracks local precipitation quite directly, so it might seem that the long tail of high precipitation over land should more than make up for the expansion in dry areas. However, past a point determined by balance between the kinetics of silicate dissolution and the timescale and surface area of contact between water and dissolving silicates, extremely high precipitation has diminishing returns in terms of weathering rates (Maher & Chamberlain, 2014). If water flushes out a weathering zone rapidly enough, the system becomes kinetically limited and any further increases to the water's flow rate will simply change the degree of dilution of weathering products rather than increasing their flux. We can see this effect in Fig. 5.8 where all of the local weathering fluxes drop off abruptly around

0.2 mol m^{-2} yr even though a direct scaling of weathering flux with water flux would suggest a long tail of much larger local fluxes for the $S = 1000$ W m^{-2} simulation. Interestingly, although the precipitation rate and S_{abs} both increase as S goes up, simulations at a given pCO$_2$ still move progressively closer to the energetic limit on set by S_{abs} (see Table 5.3), which may play a role in constraining the areal extent of precipitation over land and forcing the growth of desert regions. The potential for reduction in weathering with increased S is another destabilizing influence in the carbon cycle, since even with a functional negative feedback at a given instellation (i.e. positive slope in weathering vs. pCO$_2$), this effect would force pCO$_2$ to higher equilibria at higher instellations, likely significantly reducing a planet's habitable lifetime under increasing parent star luminosity.

5.4 Discussion

Here we will discuss some implications, caveats, and directions for further investigation of the behaviors suggested by our simulations.

5.4.1 Limit cycling?

First, we note that our WHAK weathering results (Fig. 5.6) are qualitatively consistent with previous WHAK-based exoplanet weathering calculations driven by zero-dimensional (Menou, 2015; Abbot, 2016), one-dimensional (Haqq-Misra et al., 2016; Kadoya & Tajika, 2019), and three-dimensional (Paradise & Menou, 2017) climate models. In all of these cases, the direct power-law dependence of weathering fluxes on pCO$_2$ (the β term in eqn. 5.3) means that planets at lower instellations (where larger pCO$_2$ is necessary to maintain a given surface temperature) display much higher weathering rates under temperate conditions, necessitating colder surface climates to reduce weathering enough to equilibrate with an Earth-like outgassing rate. Under fairly broad combinations of instellation and weathering properties (e.g. Abbot, 2016), this direct pCO$_2$-dependence was suggested to draw CO$_2$ down to levels that would glaciate planets. This led to the prediction that terrestrial planets in the outer reaches of the HZ would spend most of their time in snowball states, punctuated by intermittent periods of temperate surface conditions when cold- and ice-induced slowdowns in weathering allowed CO$_2$ to build up to high enough levels to achieve deglaciation briefly, at which point weathering would accelerate again and re-glaciate the planet, a periodic process termed "limit cycling" (Menou, 2015; Haqq-Misra et al., 2016). The huge increases in WHAK weathering rates for our high-pCO$_2$ simulations

(Fig. 5.6) are consistent with this picture, though we did not carry out simulations at low enough pCO_2 values and surface temperatures to determine whether the WHAK weathering rates would remain extremely high even as the planets approached glaciation.

Compared to the results discussed above, our MAC weathering calculations (see Fig. 5.7) suggest completely different behavior for planets with CO_2 dominated atmospheres at reduced instellations within the HZ. Although they do display somewhat higher weathering rates than their low-pCO_2 counterparts because of the pCO_2-dependence of the equilibrium concentration of solutes (C_{eq} in equation 5.4), the high-pCO_2 MAC simulations do not display the orders-of-magnitude increase in weathering compared to cases with lower CO_2 that is seen with WHAK. From this it seems that MAC weathering imparts much less susceptibility to the limit cycling mechanism, which at first glance appears to be a point in favor of climate stability at low instellation. However, the anti-correlation between MAC weathering rates and pCO_2 that the energetic limit on precipitation engenders for the high-pCO_2, low-instellation simulations introduces a different variety of climate instability that may be just as deleterious as limit cycling for habitability in the outer reaches of the HZ, if not more so.

5.4.2 Catastrophic carbon cycle hysteresis

With MAC-style, hydrologically-regulated weathering, energetically-limited precipitation can cause a breakdown of the negative feedback on climate that emerges within the carbonate-silicate cycle. Our high-pCO_2, low-instellation simulations displayed reductions in weathering with CO_2 growth, opposite the trend required to stabilize climate by balancing CO_2 sequestration against CO_2 outgassing. This suggests that planets with combinations of temperature, pCO_2, and instellation that place them in the energetically-limited regime are in danger of catastrophe: runaway accumulation of atmospheric CO_2 due to progressive throttling of weathering rates.

The mechanism by which this CO_2 runaway might occur can be illustrated with direct reference to Fig. 5.7. The pCO_2=1 bar, S = 1000 W m^{-2} simulation (red squares in Fig. 5.7) displays a weathering rate of 8.6 Tmol yr^{-1}. If we take this as our initial climate state and impose a volcanic CO_2 degassing rate of 10 Tmol yr $^{-1}$, which is well within the range of estimates for Earth's outgassing rate (Catling & Kasting, 2017; Coogan & Gillis, 2020), the planet's pCO_2 will begin to grow because the flux into the atmosphere is greater than the flux out. Under Earth-like conditions, this would cause warming, an intensification of the hydrological cycle, and an acceleration in weathering (as we see in the low-pCO_2 cases, the green squares in Fig. 5.7), moving the carbon cycle closer to equilibrium, but in this case the opposite happens, with a progressive reduction in the weathering rate as CO_2 accumulates. By the time our hypothetical $S = 1000$ W m^{-2} planet had accumulated another bar of CO_2, its weathering rate would have fallen to only 6.9 Tmol yr^{-1} (see red square at pCO_2=2 bars in Fig. 5.7). Thus the planet would have a carbon cycle further out of balance with its 10 Tmol yr^{-1} outgassing rate than when it started, with no signs of slowing down. We did not carry the $S = 1000$ W m^{-2} simulations to higher pCO_2 because of the temperature constraints of our modeling framework, but even at pCO_2=2 bars the planet is verging on inhospitable conditions, with a global-mean surface temperature in excess of 330 K (red dot at pCO_2=2 bars in Fig. 5.1). Assuming the negative weathering trend holds out to even larger pCO_2, or at least that the weathering rate remains below the assumed 10 Tmol yr^{-1} outgassing rate, the planet would eventually be forced by the carbonate-silicate cycle into an uninhabitably hot state, likely continuing to warm until it degassed all of the available CO_2 from its interior, ending up with a dense, steamy, supercritical CO_2/H_2O atmosphere unless some unknown process was triggered along the way that allowed the weathering rate to accelerate back to parity with the outgassing rate. Simulations of water photolysis and hydrogen escape on CO_2-rich planets orbiting G-stars suggest that the upper-atmospheric cold trap generated by the low instellations and high CO_2 partial pressures under consideration would throttle water loss to insignicant levels, allowing these hot, steam-rich surface conditions to persist over geologic timescales (Wordsworth & Pierrehumbert, 2013).

At somewhat lower instellations than $S = 1000$ W m^{-2}, CO_2 condensation at the surface would become a possibility at high enough pCO_2, meaning the energetic limit on precipitation presents a pathway to reach the stable CO_2 ocean states proposed in Graham et al. (2022b). The mechanism of carbon cycle destabilization suggested in that study was based on the fact that CO_2 becomes a coolant at extremely high partial pressures, which also leads to a slowdown of weathering with pCO_2 accumulation but requires much higher CO_2 to initiate than the mechanism discussed here. This means that energetically-limited weathering may increase the probability that low-instellation planets within the HZ end up with CO_2 oceans, with uncertain implications for their habitability. Although CO_2 ocean worlds are restricted to relatively clement climates below 304 K (the critical temperature of CO_2), they would still sport extreme surface pressures (up to 72 bars), and in the process of accumulating that much CO_2 surface temperatures can peak at extreme levels (> 400 K) before Rayleigh scattering begins to outweigh CO_2's greenhouse effect and further accumulation begins to cool the planet (Graham et al., 2022b). Intriguingly, some work has suggested that liquid and supercritical CO_2 may be conducive to prebiotic chemistry (Shibuya & Takai, 2022), and supercritical CO_2 may drive rapid carbonate formation (see Section 5.4.3 and McGrail et al., 2017), suggesting these worlds may not be as hostile to life as they appear at first.

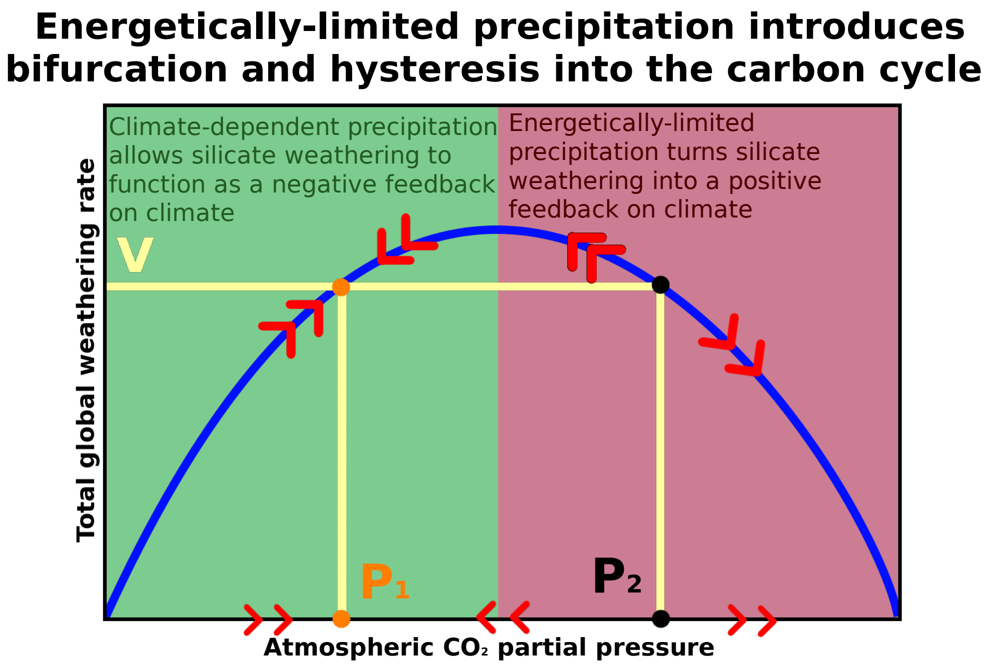

Figure 5.9: **A schematic of the saddle node bifurcation in the carbon cycle suggested by our simulations.** The blue curve represents the global weathering rate as a function of $p\mathrm{CO_2}$. Weathering increases with increasing $p\mathrm{CO_2}$ (and surface temperature) in the green zone, and it decreases with increasing $p\mathrm{CO_2}$ (and surface temperature) in the red zone. Weathering rates are equal to outgassing (V) at $p\mathrm{CO_2}$=P_1 (orange) and at $p\mathrm{CO_2}$=P_2 (black). The P_1 equilibrium is stable because weathering acts as a negative feedback in that regime, while the P_2 equilibrium is unstable due to silicate weathering's positive feedback behavior. The red arrows indicate the directions CO_2 and weathering would evolve for a climate intialized from various points relative to the two equilibria.

The climate behavior under discussion suggests that the reversal in the slope of the weathering curve induced by energetically-limited precipitation introduces a saddle node bifurcation (e.g. Strogatz, 1994) into the carbon cycle, similar to that introduced by the ice-albedo feedback into the global-mean energy budgets of rapidly rotating planets (Abbot et al., 2018). Saddle node bifurcations are associated with hysteresis, i.e. multiple equilibria in systems with the same forcings. For example, ice-albedo bifurcations mean that rapidly-rotating ocean-bearing planets can occupy a temperate, Earth-like state, a frigid, shiny snowball state, and potentially several other states of intermediate iciness with the same instellation and greenhouse gas concentrations (e.g. Abbot et al., 2011; Rose, 2015). If a planet's instellation or greenhouse gas concentration is lowered enough for it to fall into a snowball state, the same variable must be raised to a higher level than before in order to escape the snowball state; this is what is meant by hysteresis, and this is what allows multiple climatic equilibria for a given set of forcing parameters. The stabilizing action of the silicate weathering feedback is thought to be the main process that prevents long-term hysteresis associated with the ice-albedo feedback from dominating the evolution of the Earth system (e.g. Kukla et al., 2022), but when governed by energetically-limited precipitation, our simulations suggest that the carbon cycle can become the cause of bifurcation and associated climate catastrophe, rather than the remedy.

We provide a schematic of the presumed bifurcation in Fig. 5.9. We say "presumed" because constraints with our modeling framework prevented us from extending our high-$p\mathrm{CO}_2$ simulations to low enough $p\mathrm{CO}_2$ to see whether their weathering curves would arch back down into negative feedback territory as they moved further from the energetic limit on precipitation, but this seems plausible given the behavior of the low-$p\mathrm{CO}_2$ simulations. Further modeling work to confirm or refute these ideas is a fruitful topic for future investigations. Thus we suggest that planets at low instellations within the HZ (tentatively up to at least $S \approx 1000$ W m^{-2}, the highest instellation with energetically-limited behavior in this study) may display a maximum attainable global weathering rate for a given surface configuration, with weathering rates increasing with CO_2 up to a point, after which they begin to fall with further accumulation (represented by the bow shape of the schematic blue weathering curve in Fig. 5.9). When driven by an outgassing rate (V in Fig. 5.9) less than the maximum weathering rate, such a planet would have two carbon cycle equilibria in the region of the weathering curve we are considering. In the low-$p\mathrm{CO}_2$ regime where the weathering curve has a positive slope with respect to $p\mathrm{CO}_2$ (the green region in Fig. 5.9), the equilibrium $p\mathrm{CO}_2$ (P_1, colored orange) would be stable and attracting, while in the high-$p\mathrm{CO}_2$, energetically-limited regime (red region in Fig. 5.9), the equilibrium $p\mathrm{CO}_2$ (P_2, colored black) would be unstable and repulsive. A planet governed by the weathering curve in Fig. 5.9 and driven by an outgassing rate V, when initialized with $p\mathrm{CO}_2 < P_1$ or $P_1 < p\mathrm{CO}_2 < P_2$ would evolve toward P_1 and stabilize there, as in the traditional picture of the silicate weathering feedback. However, if it was initialized with $p\mathrm{CO}_2 > P_2$, it would instead begin to uncontrollably accumulate CO_2, with an unclear end-point likely defined by either re-activation of the silicate weathering feedback (discussed further in Section 5.4.3), depletion of the planet's degassable carbon into the atmosphere, or initiation of surface condensation of CO_2 as in Graham et al. (2022b).

At an outgassing rate equal to the energetically-capped maximum weathering rate (i.e. if V were shifted so the horizontal yellow line would be tangent to the blue weathering curve in Fig. 5.9), the two equilibria combine into a single equilibrium climate ($P_1 = P_2$) that is stable to downward perturbations in CO_2 but unstable to upward perturbations, since both changes reduce weathering and cause CO_2 accumulation. At outgassing rates above this, the two equilibria "annihilate" (a defining feature of saddle node bifurcations, e.g. Strogatz, 1994), eliminating balanced carbon cycle solutions and forcing the system into uncontrolled CO_2 accumulation regardless of its initial $p\mathrm{CO}_2$. Decreasing V back down to a point where equilibria re-appeared would not allow the planet to recover to temperate conditions, since its weathering rate would now be pinned below the original V in whatever new, high-$p\mathrm{CO}_2$ state it found itself in, somewhere low on the blue curve in the bottom right corner of Fig. 5.9. Thus a temporary increase in outgassing rates on an initially-habitable planet might permanently end its ability to maintain stable, temperate climates, a severe form of climate hysteresis.

Further, there are pathways into the energetically-limited regime that do not require any changes to outgassing. For example, if the $p\mathrm{CO}_2$ necessary to deglaciate a planet in a snowball state lies at $p\mathrm{CO}_2 > P_2$ (black markers in Fig. 5.9), then escape from global glaciation due to reduced weathering in icy conditions could counterintuitively propel a previously temperate planet into a death spiral of uncontrolled heating. Upon accumulating enough CO_2 to deglaciate, rather than weathering away the excess to return to a temperate climate, runaway CO_2 accumulation would ensue due to the processes described above for planets initialized from $p\mathrm{CO}_2 > P_2$. Similarly, if Earth-like planets outgas massive CO_2 atmospheres during their magma ocean phases like some models suggest (e.g. Solomatova & Caracas, 2021), some may become "locked in" to this early, hot, high-$p\mathrm{CO}_2$ phase by energetically-constrained weathering, never managing to develop habitable conditions at all. However, expectations that planets will also face a large flux of impacts producing highly weatherable ejecta in the early stages after planet formation (e.g. Kadoya et al., 2020) may help mitigate this danger. Further, at low instellations, deglaciation can be prevented by CO_2 condensation onto the icy planetary surface (Turbet et al., 2017; Kadoya & Tajika, 2019), which may restrict the parameter space that allows for a post-Snowball death spiral.

The behaviors identified above may even have relevance to Earth history. Simulations in a GCM of the CO_2-rich aftermath of Earth's Marinoan Snowball event 635 million years ago found that our planet may have approached the energetic limit on precipitation under those conditions, throttling growth in runoff and resulting in weathering rates substantially reduced compared to previous estimates (Le Hir et al., 2009). Weathering still showed robust growth with pCO_2, but the study used WHAK-style kinetically-limited fluxes, suggesting it may have substantially overestimated rates of CO_2 consumption. Based on our present existence, the Earth evidently did not exit the Neoproterozoic snowball into a phase of runaway CO_2 growth, but it would be worthwhile to revisit the calculations in Le Hir et al. (2009) to assess whether we might have gotten close to such a catastrophe, given the approach to energetically-limited precipitation. Similarly, although vigorous debate remains over proxy interpretation (Galili et al., 2019; Vérard & Veizer, 2019; Herwartz et al., 2021), some paleotemperature constraints suggest that the Archean Earth may have had surface temperatures in the vicinity of 340 K (e.g. Lowe et al., 2020; McGunnigle et al., 2022), again presenting the possibility that early Earth may at times have verged on the energetically-limited weathering behavior simulated here. Finally, we note that early Mars, which was irradiated by a lower instellation than any of the planets we modeled, is generally postulated to have had a CO_2-dominated atmosphere, and displays abundant evidence of active hydrologic cycling (e.g. Kite, 2019; Kite et al., 2019, 2021), may be another environment in which energetically-limited precipitation and weathering became relevant.

5.4.3 Caveats

In this study, we focused exclusively on modeling continental silicate weathering rates in a significantly simplified cloud-free GCM with a specific, idealized land configuration and an assumption of spatially uniform lithology and soil properties. There are a variety of possibilities that we did not model which could prevent the carbon cycle destabilization discussed above.

One important consideration is the potential contribution of low-temperature off-axis hydrothermal basalt alteration, frequently referred to as "seafloor weathering," which has been proposed as an alternative or complementary stabilizing, temperature-and $p\mathrm{CO_2}$-sensitive $\mathrm{CO_2}$ sequestration flux analogous to the continental weathering feedback (e.g. Francois & Walker, 1992; Brady & Gislason, 1997; Coogan & Gillis, 2013; Coogan & Dosso, 2015; Krissansen-Totton & Catling, 2017; Krissansen-Totton et al., 2018; Coogan & Gillis, 2018a; Hayworth & Foley, 2020). Some work has discounted its ability to act as a stabilizing feedback (Caldeira, 1995; Abbot et al., 2012), but these conclusions have been questioned due to laboratory (Brady & Gislason, 1997) and geochemical (Coogan & Gillis, 2013; Coogan & Dosso, 2015; Coogan & Gillis, 2018a) data that indicate an appreciable temperature-dependence of seafloor weathering reactions, potentially allowing the process to accelerate under warmer climates and operate as a negative feedback, with important implications for the history of Earth (Krissansen-Totton & Catling, 2017; Krissansen-Totton et al., 2018) and the habitability of exoplanets (Hayworth & Foley, 2020; Chambers, 2020). However, these modeling works generally ignore the throttling effect of clay formation which plays such a fundamental role in the weakening of the continental silicate weathering feedback in the MAC framework. If the waters flowing through seafloor basalts tend to reach their equilibrium concentration of weathering products before the formation of carbonates, then without a feedback between porewater flow rates and global surface temperatures there is limited scope for seafloor weathering to operate as a thermostat. Developing a complete MAC-style model of seafloor weathering that accounts for the major controls on porewater flow rates and the precipitation of relevant clay phases, as suggested in Graham & Pierrehumbert (2020), with first steps taken in Hakim et al. (2021), is a necessary next step toward evaluating the importance of seafloor weathering to the carbon cycle of Earth and other exoplanets. This is particularly crucial given the fact that clay formation on the seafloor was likely much more efficient in early Earth's oceans (and in the oceans of abiotic exoplanets) due to the lack of biosilicifying organisms, which maintain the modern Earth's ocean in a subsaturated state with respect to silica (Siever, 1992; Kalderon-Asael et al., 2021). Silica is one of the weathering products that drives the formation of many of the clays that consume weathering-derived cations and reduce carbonate precipitation, decreasing the effectiveness of weathering at driving carbon sequestration; thus, although seafloor clay precipitation ("reverse weathering") has been suggested to exert its own form of negative feedback (e.g. Isson & Planavsky, 2018; Krissansen-Totton & Catling, 2020), it may also prevent traditional seafloor weathering from operating efficiently. The net impact on the carbon cycle of weathering-related processes occurring on the seafloor remains unclear (Krissansen-Totton & Catling, 2020).

Another possible exit route from uncontrolled CO_2 accumulation could arise through the power-law dependence of C_{eq} in equation 5.4 (characterized by exponent n in Table 5.2), which allows for larger concentrations of weathering products in a given amount of water for planets with larger pCO$_2$, suggesting that further accumulation of CO_2 in the energetically-limited regime could eventually reverse the sign of the weathering curve back into negative feedback territory. This is the mechanism that allowed the subset of simulations that entered the parameterized energetically-limited precipitation regime in the global-mean study of Graham & Pierrehumbert (2020) to avoid runaway CO_2 accumulation, instead equilibrating at hot temperatures with high pCO$_2$. In this scenario, the slope of the blue weathering curve in Fig. 5.9 would eventually reverse and begin to increase again at high pCO$_2$, introducing a new, stable carbon cycle equilibrium at a $p\mathrm{CO}_2 > P_2$. However, we note that the chemical equilibrium constants governing C_{eq} are negatively temperature-dependent for many lithologies, such that the maximum concentration of weathering products decreases exponentially with increasing temperature, opposite the behavior of kinetic rate constants and offsetting the power-law increase of C_{eq} with pCO$_2$ (Hakim et al., 2021). A set of weathering calculations including this effect led to even larger drops in global weathering rates with pCO$_2$ in the high-CO_2 simulations, exacerbating the bifurcation and hysteresis identified above. Still, there remains a possibility that weathering rates could, under some circumstances, begin to climb again at extremely high pCO$_2$ when CO_2 begins to cool the planetary surface instead of warm it. Further, some field measurements suggest that supercritical CO_2 forms carbonates extremely rapidly upon being brought into contact with basalts (McGrail et al., 2017), suggesting the intriguing possibility that weathering would increase greatly under supercritical conditions, providing another possible mechanism for the weathering curve to regain its negative feedback at extremely high pCO$_2$.

More generally, the amount and spatial arrangement of land can have complex and difficult-to-predict impacts on continental weathering rates via changes to runoff and precipitation (Baum et al., 2022). It may be that certain continental configurations tend to produce positive feedback behavior, while others produce negative feedback behavior. Relatedly, topography heavily influences (and is influenced by) precipitation (Roe, 2005) and erosion (Montgomery & Brandon, 2002) rates, which in turn affect the thickness and age of soils (e.g. Heimsath et al., 2000; Owen et al., 2011), with direct impacts on silicate weathering rates (Ferrier & Kirchner, 2008; Hilley et al., 2010; West, 2012; Maher & Chamberlain, 2014). Surface evolution driven by plate movements (e.g. Coy, 2022) means that all of these factors may constantly co-evolve on an Earth-like planet with plate tectonics. Further, planets in the "stagnant lid" mode (no plate tectonics, e.g. Foley, 2019) may display systematic differences in topograpy (Guimond et al., 2022) and outgassing rates (Guimond et al., 2021), likely introducing further major variation into all of these factors controlling weathering rates and climate evolution. Correlations and feedbacks between the many variables controlling weathering fluxes could significantly change the picture we have presented, and a much broader parameter sweep and investigation of these issues is necessary.

Finally, we note that this study focused on rapidly-rotating planets orbiting Sun-like G stars. Carbon cycling on slowly-rotating and tidally-locked planets has received much less attention. Kite et al. (2011) found that WHAK-style silicate weathering can transform into a positive feedback for tidally-locked planets with thin, CO_2-dominated atmospheres through a mechanism completely different from that explored here. Weathering-induced climate hysteresis on tidally-locked planets with very limited water inventories has also been suggested (Ding & Wordsworth, 2020). Other WHAK-based calculations have suggested a significant dependence of weathering rates on planetary rotation rate (Jansen et al., 2019) and enormous changes to weathering rates as a function of continental position on fully synchronous rotators (Edson et al., 2012). These effects are especially important since slowly-rotating planets are expected to experience very efficient true polar wander, leading to continuous reorientation of their surfaces with respect to the substellar point on timescales comparable to that of the carbonate-silicate cycle as a result of mantle convection (Leconte, 2018). Hydrological cycling on tidally-locked planets displays subtle behavior with unclear implications for weathering rates (Labonté & Merlis, 2020). MAC weathering calculations have not yet been applied to tidally-locked climates, so it is unclear whether the mechanisms we have identified in this study will come into play in that context, but this is a crucial area for future research to evaluate the potential climate stability of planets orbiting M-dwarfs, the most plentiful stars in the universe (e.g. Catling & Kasting, 2017).

5.5 Conclusion

In this study, for the first time, we calculated estimates of continental silicate weathering fluxes for Earth-like exoplanets by applying the MAC weathering model to output from GCM simulations of planetary climate under a variety of $p\mathrm{CO}_2$ values and TOA instellations. Weathering rates and fluxes predicted according to MAC diverge profoundly from values calculated according to the more widely used but chemically simplistic WHAK model, particularly at lower instellations within the HZ. Importantly, because of the strong dependence of weathering fluxes on hydrologic cycling within the MAC framework, we found that planets near the energetically-limited precipitation regime (where most instellation that reaches the surface goes into driving evaporation of water) may lose the ability to stabilize their climates through the carbonate-silicate cycle. This introduces a previously-unrecognized form of hysteresis into the carbon cycle that may drive planets into phases of runaway CO_2 accumulation, resulting in either extremely hot surface temperatures or the condensation of CO_2 into an ocean at the planetary surface. Planets with high pCO$_2$ irradiated by low instellations are particularly susceptible to approaching this weathering regime because their surface energy budgets are more heavily constrained than those of low-pCO$_2$, high-instellation planets within the HZ like Earth. Although our modeling is preliminary and our conclusions are tentative, this work calls into question the geochemical plausibility of long-term surface habitability for planets in the outer reaches of the nominal "habitable zone."

Chapter 6

Summary and Conclusions

I.
Kick at the rock, Sam Johnson, break your bones:
But cloudy, cloudy is the stuff of stones.
II.
We milk the cow of the world, and as we do
We whisper in her ear, 'You are not true.'

Epistemology
Richard Wilbur

6.1 Summary

The carbonate-silicate cycle is thought to play a fundamental role in Earth's long-term habitability, regulating atmospheric CO_2 content through climate-dependent silicate weathering to maintain stable, temperate surface conditions across geologic timescales. By analogy with the functioning of the Earth system, the same process is hypothesized to operate on some rocky exoplanets, if they have water oceans and exposed landmasses. If true, this would allow exoplanets to adjust their CO_2 to levels that allow for habitable surface temperatures across a much wider range of orbits and for much longer periods of time than would be the case in the absence of such feedbacks. The range of orbits around a star where the silicate weathering feedback could in principle maintain CO_2 at levels that would prevent global glaciation is widely known as the "circumstellar habitable zone." This concept plays an important role in current thinking around the search for life in other stellar systems and increasingly in the design of the next generation of telescopes that are intended to begin scanning the skies for exoplanetary biosignatures in earnest. Given the recent launch of the James Webb Space Telescope and the continued rapid advance in the state of exoplanetary astronomy, it is a timely moment to revisit the silicate weathering feedback in the context of rocky exoplanets. That is what I attempted to achieve in this thesis through a hierarchy of models of terrestrial exoplanet climate and "exogeochemistry."

In Chapter 2, I used a zero-dimensional polynomial climate model and a simplified ocean carbonate chemistry model to examine the sensitivity of planetary climate and oceanic pH to CO_2 perturbations as a function of TOA instellation. Although I did not explicitly model silicate weathering, I assumed its presence by initializing the simulations at each instellation with enough CO_2 to maintain surface temperatures above freezing, leading to much larger atmospheric CO_2 in the outer reaches of the HZ than in the inner reaches. Although the CO_2 perturbations I imposed are enormous in the context of the Earth system, analogous in size to events that have repeatedly wiped out the majority of species on the planet, they had increasingly muted effects on climate and seawater pH for planets at increasingly distant orbits due to the larger CO_2 inventories on those planets. Assuming the carbonate-silicate cycle efficiently adjusts CO_2 across the HZ, most habitable planets will be invulnerable even to events like the large igneous province that annihilated $\approx$90% of life on Earth at the Permian-Triassic boundary, suggesting the Earth system may be unusually vulnerable to such shocks compared to most Earth-like planets (if other such planets exist). Industrial Revolutions are safer at lower instellations.

In Chapter 3, I coupled a zero-dimensional polynomial climate model to a pair of idealized weathering models to examine the implications of the assumed functioning of the silicate weathering feedback for exoplanetary climate at instellations across the HZ. The widely used model of Walker et al. (1981) (WHAK) presumes that silicate weathering rates are determined by the kinetics of silicate dissolution, imparting a powerful exponential dependence on temperature and power-law dependence on CO_2 and allowing weathering to act as an efficient climate feedback. The newer, more chemically detailed weathering model of Maher & Chamberlain (2014) (MAC) accounts for the chemical equilibration of dissolving silicates with clays that form in the weathering zone, and had never been applied to exoplanetary climates before this study. Silicate equilibration with clays sets an upper limit on the concentration of weathering products in runoff and moves the main temperature feedback in the weathering process from chemical kinetics to hydrology, which responds approximately linearly to increases in temperature, leading to a much weaker climate feedback than the WHAK formulation would suggest. Compared to WHAK, MAC weathering resulted in much larger sensitivity of climate to bulk planetary parameters like the land fraction and outgassing rate, significantly diverging from previous results.

Weathering rates also displayed strong dependencies on lithology and surface properties like the thickness and age of the soils being weathered in the MAC formulation, suggesting a multiplicity of impossible-to-constrain parameters have large impacts on steady-state climate for exoplanets with Earth-like carbon cycles. We can expect a diversity of climates within the HZ based on silicate weathering considerations alone.

In Chapter 4 I carried out a suite of radiative transfer calculations simulating planetary climates irradiated by F-, G-, and M-star spectra under extremely high CO_2 and applied the MAC weathering model to analyze their stability. I found that for F- and G-star planets, Rayleigh scattering can destabilize the carbon cycle by making CO_2 into a net anti-greenhouse gas, leading to reductions in surface temperature and silicate weathering with increases in $p\mathrm{CO}_2$. Thus, even in the presence of a functional carbonate-silicate cycle, CO_2 oceans may be geologically stable for exoplanets at low enough instellations, with their weathering rate pinned beneath their outgassing rate and the difference made up by surface condensation of outgassed CO_2. At somewhat larger instellations, and with inefficient weathering, these planets can warm significantly enough for the albedo effect of accumulating water vapor to begin to impact the planetary energy balance, which can destabilize the CO_2 ocean states and trigger exotic limit cycling behavior driven by CO_2 condensation and outgassing that sees a planet oscillate between hot states without surface CO_2 condensation and cooler states with surface CO_2 condensation. At high enough instellation, CO_2 condensing solutions disappear entirely, with F-stars allowing the states at higher instellations due to their bluer spectra and attendant enhanced Rayleigh scattering. The co-existence of low-CO_2 climate states and CO_2 ocean climate states for the same boundary conditions within the carbon cycle is a novel form of climate hysteresis for Earth-like exoplanets at low instellations orbiting F- and G-stars. M-planets, however, do not display the above effects because M-stars are cool and red, reducing the Rayleigh scattering efficiency of CO_2, driving a much weaker albedo increase that is not sufficient to change silicate weathering into a positive feedback.

In Chapter 5, I used a 3D GCM to simulate planetary climate and test the responses of the MAC and WHAK weathering formulations to increases in CO_2 under high-instellation, low-$p\mathrm{CO}_2$ conditions and low-instellation, high-$p\mathrm{CO}_2$ conditions. For the more Earth-like low-$p\mathrm{CO}_2$ simulations, both MAC and WHAK produced stabilizing negative feedbacks on climate, though with significantly different strengths of response, consistent with the global-mean results presented in Chapter 3. However, at high instellations, while the WHAK formulation still produced increases in weathering for increases in $p\mathrm{CO}_2$, the MAC formulation did not, instead producing reductions in weathering with growing CO_2, despite the fact that CO_2 was still operating efficiently as a greenhouse gas (distinguishing this from the mechanism identified in Chapter 4, which requires CO_2 to act as a coolant). This was explained with reference to the surface energy budgets of each simulation: instellation absorbed at the surface sets a hard upper bound on global evaporation and precipitation rates because of water's latent heat, so planets at low instellation with relatively high albedo like the high-$p$$CO_2$ simulations are constrained to lower precipitation rates than planets with low albedo and high instellations like the low-$p$$CO_2$ simulations. Since the high-$p$$CO_2$ planets were near their energetic limits on precipitation, they lost the feedback provided by intensification of the hydrologic cycle under hotter conditions, disrupting the ability of MAC weathering to respond to increases in surface temperature, preventing stabilization of the climate. In fact, because of the increase in albedo, the surface energy budget was progressively reduced by CO_2 accumulation in the high-CO_2 simulations, leading to reductions in global-mean precipitation and weathering rates in the MAC formulation. This mechanism may induce runaway CO_2 accumulation under easily-accessible conditions for Earth-like planets at low instellations, suggesting the potential for a severe form of carbon cycle hysteresis with bistability between temperate, Earth-like low-$p$$CO_2$ climates and a class of extremely high-$p$$CO_2$ climates with energetically-constricted weathering rates and either extremely hot temperatures at higher instellations or relatively mild temperatures with widespread surface CO_2 condensation at lower instellations.

6.2 Future directions

I hope to extend this work in a number of different directions in the near future, with the intertwined goals of improving predictions of exoplanetary climate and improving deep time Earth system modeling. Of relevance to both realms, it will be necessary to carry out a systematic intercomparison between weathering predictions produced by global-mean climate models and 3D climate models, given the 3D-specific behaviors that emerged in Chapter 5 but not Chapters 3 or 4. It may be that global-mean weathering models do a poor job of capturing even qualitative weathering behavior under certain circumstances, reducing their utility in addressing some questions about planetary climate evolution and necessitating the application of more complex 3D models that more faithfully resolve atmospheric dynamics and hydrological cycling.

In the exoplanetary realm, a natural extension of my thesis work will be to simulate weathering on planets with levels of CO_2 and instellation falling between the values examined in Chapter 5 to confirm or refute the suggestion that the weathering curve reverses slope at intermediate CO_2 levels due energetically-limited precipitation, introducing a saddle-node bifurcation into the carbon cycle. Another low-hanging fruit will be to carry out the first 3D simulations of MAC weathering on tidally-influenced planets orbiting M- and K-stars. The few works that have examined the interplay of rotation and weathering behavior (e.g. Kite et al., 2011; Edson et al., 2012; Jansen et al., 2019, all of which use WHAK weathering) have found that weathering rates are strongly affected by rotation. It will be a simple matter to swap an M- or K-star spectral file into Isca and adjust the planetary rotation rate to re-examine these issues with MAC weathering and compare against WHAK-based results. In addition, no work has yet accounted for the efficiency of true polar wander on slowly-rotating planets, which likely drives continuous planetary reorientation relative to their rotational/orbital axes in response to shifts in the planet's moment of inertia driven by mantle convection (Leconte, 2018). Depending on the characteristic convective mode within a planet's mantle and the relative timescales of true polar wander and carbonate-silicate cycling, this may lead to planets with climates doomed to vary chaotically on geologically short timescales (10-100 thousand years) from the continuous alteration of surface weatherability and weathering rates driven by continental rearrangement. This might have dramatic implications for the habitability of M-star planets, and it is a natural extension of the GCM weathering work carried out in Chapter 5.

With respect to Earth system modeling, there is a rich set of problems that require re-examination with the MAC model, both to infer Earth's broad-stroke gigayear-scale climate evolution and to interpret specific climate events and trends in the geologic record. I plan to carry out proxy-informed Bayesian inverse carbon cycle modeling with the techniques laid out in Krissansen-Totton & Catling (2017); Krissansen-Totton et al. (2018); Krissansen-Totton & Catling (2020) to examine the impact of incorporating MAC-based formulations of both continental and seafloor weathering on proxy interpretations and predictions of various Earth system parameters from the Archean Eon to the Phanerozoic. I also plan to carry out the first carbon cycle calculations incorporating temperature-dependent reverse weathering, based on the suggestion in Higgins & Schrag (2015) that such behavior would help explain the evolution of oceanic magnesium across the Cenozoic. As noted in Chapter 1, section 1.2.3, this temperature-dependence would act as a destabilizing positive feedback in the climate system and would likely be quite important in the silica-rich seas expected on Precambrian Earth and abiotic exoplanets.

6.3 Concluding remarks

It took billions of years of uninterrupted surface habitability for lumbering multicellular behemoths like ants, sponges, and people to emerge on Earth (Knoll et al., 2016; Dohrmann & Wörheide, 2017). This despite a dynamic planetary surface buffeted by innumerable environmental stressors such as: a steadily brightening sun (Sagan & Mullen, 1972); a taffy-like crust constantly being folded, crunched, bent, melted, chemically altered, frozen, buried, and produced anew (Korenaga, 2018); repeated collisions with remnants from planetary formation (Johnson et al., 2022); a seething interior that constantly excretes warming gases and periodically expels millions of cubic kilometers of magma laced with poisons and heavy metals (Ernst & Youbi, 2017); the list goes on. As described in Chapter 1, current dominant thinking holds that this delicate state of affairs was managed at least in part by stabilizing feedback(s?) within the carbonate-silicate cycle (Walker et al., 1981; Isson et al., 2020). The astro- and geophysical preconditions that were necessary for this climatic stabilization to emerge on the Earth are certainly not fully understood (e.g. Langmuir & Broecker, 2012), but many factors have been identified that might have prevented it. For example, had the Earth received significantly more water during its formation (a scenario which may actually be favored on a galactic scale, Lichtenberg et al., 2019), the enormous pressure on the seafloor would suppress outgassing and geochemical cycling (Kite et al., 2009; Krissansen-Totton et al., 2021). This would prevent the operation of negative feedbacks like the carbonate-silicate cycle that rely on atmosphere-interior exchange.[1] This is just one example among many processes or events that might have resulted in an Earth that was not amenable to climate stabilization by carbonate-silicate cycling.

The perceived chain of unlikely events required to produce and maintain a planet that could host complex multicellular life has led some workers to propose that true "Earth-twins" are extremely uncommon, a notion dubbed the "Rare Earth hypothesis" (Ward & Brownlee, 2003). Tentatively, the work I have presented in this thesis supports this idea. Although I found that *assuming* a functional silicate weathering feedback on Earth-like planets can produce environments more stable and placid than the Earth at lower instellations (Chapter 2, Graham, 2021), I also found that the efficient functioning of the feedback is heavily dependent on potentially-highly-variable surface properties like soil age (Chapter 3, Graham & Pierrehumbert, 2020),

[1]Though it has been hypothesized that a combination of luck and/or novel sea-ice-related stabilization mechanisms may enable long-term habitability on these these planets under narrow circumstances (Levi et al., 2017; Kite & Ford, 2018; Ramirez & Levi, 2018)

and that low instellations may severely compromise the mechanisms required for climate stabilization (Chapter 4, Graham et al., 2022b, Chapter 5). Of course, drawing any profound conclusions from the highly idealized models deployed in these studies would be a mistake, but the results suggest that even planets nearly indistinguishable from Earth have many paths to biospheric doom.

Further, certain readings of the geologic record support the idea that Earth's habitability may have been more precarious than its ≈4 billion years (e.g. Mojzsis et al., 1996; Bell et al., 2015; Hassenkam et al., 2017) of continuous inhabitance would suggest. For example, Earth has experienced low-latitude glaciations ("Snowball Earth") at least three times, with two at the end of the Proterozoic Eon during the Cryogenian period (720 to 635 Ma, Hoffman et al., 1998; Pierrehumbert et al., 2011; Hoffman et al., 2017; Pu et al., 2022) and one or more at the beginning of the Proterozoic (≈2.4 Ga, Kopp et al., 2005; Hoffman, 2013; Zakharov et al., 2017; Warke et al., 2020). In each case, the subsequent shutdown of silicate weathering allowed CO_2 to accumulate to high enough levels for deglaciation to occur, presumably resulting in brutally hot super-greenhouse conditions and extremely rapid sea level rise in the immediate aftermath (e.g. Myrow et al., 2018), followed by rapid drawdown of CO_2 by resumption of silicate weathering (Kasemann et al., 2014; Fang & Xu, 2022). The glaciations lasted millions of years, and if volcanic outgassing had been less intense, they could have lasted much longer (Hoffman et al., 2017; Lan et al., 2022). So, although the carbonate-silicate cycle eventually came to the rescue, it also failed repeatedly to prevent our planet from freezing to the equator, or nearly so.

Just as the silicate weathering feedback allowed our planet to freeze, it may have nearly allowed Earth to cook. The Permian-Triassic mass extinction (252 Ma), in which more than 90% of species on Earth may have gone extinct (Chen & Benton, 2012), was caused in part by lethally hot temperatures (a warming of ≈14-18 K resulting in equatorial ocean temperatures that may have exceeded 313 K, Sun et al., 2012; Benton, 2018) and ocean acidification (Clarkson et al., 2015; Jurikova et al., 2020), both of which were driven by a large increase in atmospheric $p\mathrm{CO_2}$ (perhaps up to six-fold (!), Wu et al., 2021). This event, Earth's worst known mass extinction, also demonstrated an anomalously long duration, with extreme temperatures persisting for five million years (e.g. Isson et al., 2022), an order of magnitude longer than would be predicted by the 200-400 thousand year response time of the silicate weathering feedback (Colbourn et al., 2015). This has led to the suggestion that the silicate weathering thermostat broke down during this period, perhaps due to a slowdown in rock uplift that allowed the CO_2 outgassing caused by the Siberian Traps large igneous province to overwhelm the "supply limit" of cations set by the exposure of fresh silicates (Kump, 2018). Evidently the thermostat's breakdown (if that's what happened) was not permanent, but a five million year bout of mass global death is enough to be worrisome. If it had lasted ten million years, would we be here?

My point is that Earth's geologic record can be taken to suggest that an operational carbonate-silicate cycle may not guarantee lasting habitability, and it may primarily be a matter of luck that our biosphere has attained such complexity and persisted for so long. Beyond the qualitative support from the Snowball events and the Permian-Triassic mass extinction, this notion may find quantitative support in the fact that on timescales beyond 400 thousand years (which is approximately the operational timescale of the weathering feedback, as noted above, Colbourn et al., 2015), Earth's surface temperature appears to exhibit random walk behavior (Arnscheidt & Rothman, 2022). This makes sense, given the fact that changes in surface properties can transiently alter weathering rates and force the climate to adjust to regain balance with outgassing, allowing weathering to act as both a climate feedback and a climate forcing (Penman et al., 2020). Thus random variations in global "weatherability" due to e.g. large-scale shifts in soil age or surface lithology (both of which which I showed to have large impacts on weathering fluxes and rates, Chapter 3, Graham & Pierrehumbert, 2020) could easily wander into uninhabitable territory on long timescales. Simple simulations exploring the impact of stochastic forcings on planets with widely-distributed climate stabilization parameters came to a similar conclusion, suggesting Earth's long-term habitability was by no means inevitable (Tyrrell, 2020).

This is all to say, based on the understanding of the carbonate-silicate cycle that I have developed over the course of this PhD, I do not expect environments that allow for complex, multicellular, Earth-like biospheres to be very common in the universe, even if we restrict our attention to the ostensible "habitable zone." Future telescopic surveys searching for biosignatures based on our understanding of Earth-life may come away very disappointed (though non-detections can provide useful information too, e.g. Checlair et al., 2020). From this perspective, it seems substantially more effort should be directed toward theorizing about viable extremophile metabolisms that might allow biospheres to persist on planets with failed carbon cycles, with a particular focus on whether these planets might produce their own classes of biosignatures distinct from those inferred from Earth's history. The (disputed) discovery (Greaves et al., 2021) of phosphine, a potential biosignature (Sousa-Silva et al., 2020), on Venus, a potential example of a planet with a failed carbon cycle (Way et al., 2022), provides a possible demonstration of the value of this approach. Some first steps in this direction for "Snowball" planets have also been taken recently, with analysis of the spectral signatures displayed by a variety of organisms growing on ice (Coelho et al., 2022). Development of "agnostic" biosignatures that assume nothing about the particulars of biosphere or environment (e.g. Walker et al., 2020; Marshall et al., 2021; Bartlett et al., 2022) may be another fruitful avenue for avoiding the pitfalls of over-generalizing based on Earth's potentially very unusual history. Worlds like ours could be arbitrarily rare, given the strong selection bias imposed by the fact that it takes a long time to evolve intelligent animals: anywhere intelligent animals find themselves must have been habitable for a long time, so our environment's long-term stability is not surprising. Paraphrasing Collins & Hawking (1973), the fact that we find ourselves on a planet that never burnt or froze itself to death would be simply a reflection of our own existence.

Bibliography

Abbot, D. S. 2016, The Astrophysical Journal, 827, 117

Abbot, D. S., Bloch-Johnson, J., Checlair, J., et al. 2018, The Astrophysical Journal, 854, 3

Abbot, D. S., Cowan, N. B., & Ciesla, F. J. 2012, Astrophysical Journal, 756, 178

Abbot, D. S., & Switzer, E. R. 2011, Astrophysical Journal, 735, L27

Abbot, D. S., Voigt, A., & Koll, D. 2011, Journal of Geophysical Research, 116

Abe, Y., Abe-Ouchi, A., Sleep, N. H., & Zahnle, K. J. 2011, Astrobiology, 11, 443

Agol, E., Dorn, C., Grimm, S. L., et al. 2021, The Planetary Science Journal, 2, 1, doi: `10.3847/PSJ/abd022`

Alekseyev, V. A., Medvedeva, L. S., Prisyagina, N. I., Meshalkin, S. S., & Balabin, A. I. 1997, Geochimica et Cosmochimica Acta, 61, 1125

Allan, R. P., Barlow, M., Byrne, M. P., et al. 2020, Annals of the New York Academy of Sciences, 1472, 49

Alt, J. C., & Teagle, D. A. 1999, Geochimica et Cosmochimica Acta, 63, 1527

Alvarez, L. W., Alvarez, W., Asaro, F., & Michel, H. V. 1980, Science, 208, 1095

Anglada-Escudé, G., Amado, P. J., Barnes, J., et al. 2016, Nature, 536, 437

Apai, D., Milster, T. D., Kim, D. W., et al. 2019, The Astronomical Journal, 158, 83

Archer, D. 2016, Climatic Change, 138, 1

Arnscheidt, C. W., & Rothman, D. H. 2020, Proceedings of the Royal Society A, 476, 20200303

—. 2022, Science Advances, 8, eadc9241

Asfin, R. E., Buldyreva, J. V., Sinyakova, T. N., Oparin, D. V., & Filippov, N. N. 2015, The Journal of chemical physics, 142, 051101

Bahcall, J. N., Pinsonneault, M., & Basu, S. 2001, The Astrophysical Journal, 555, 990

Bains, W. 2004, Astrobiology, 4, 137

Bandstra, J. Z., & Brantley, S. L. 2008, in Kinetics of Water-Rock Interaction (Springer), 211–257

Baranov, Y. I., Lafferty, W. J., & Fraser, G. T. 2004, Journal of molecular spectroscopy, 228, 432

Barstow, J. K., & Irwin, P. G. 2016, Monthly Notices of the Royal Astronomical Society: Letters, 461, L92

Bartlett, S., Li, J., Gu, L., et al. 2022, Nature Astronomy, 6, 387

Batalha, N. E., Kopparapu, R. K., Haqq-Misra, J., & Kasting, J. F. 2016, Earth and Planetary Science Letters, 455, 7

Batalha, N. M. 2014, Proceedings of the National Academy of Sciences, 111, 12647

Baum, M., Fu, M., & Bourguet, S. 2022, Geophysical Research Letters, e2022GL098843

Bean, J. L., Abbot, D. S., & Kempton, E. M.-R. 2017, The Astrophysical Journal, 841, L24

Beerling, D. J., Harfoot, M., Lomax, B., & Pyle, J. A. 2007, Philosophical Transactions of the Royal Society A: Mathematical, Physical and Engineering Sciences, 365, 1843

Bell, E. A., Boehnke, P., Harrison, T. M., & Mao, W. L. 2015, Proceedings of the National Academy of Sciences, 112, 14518

Benton, M. J. 2018, Philosophical Transactions of the Royal Society A: Mathematical, Physical and Engineering Sciences, 376, 20170076

Berner, R. 1994, Am J Sci, 294, 56

Berner, R. A. 1992, Geochimica et Cosmochimica Acta, 56, 3225

—. 2012, Comptes Rendus Geoscience, 344, 544

Berner, R. A., & Caldeira, K. 1997, Geology, 25, 955

Berner, R. A., Lasaga, A. C., & Garrels, R. M. 1983, American Journal of Science, 283, 641

Betts, A. K., & Miller, M. J. 1993, in The representation of cumulus convection in numerical models (Springer), 107–121

Bixel, A., & Apai, D. 2020, The Astrophysical Journal, 896, 131, doi: 10.3847/1538-4357/ab8fad

Blake, R. E., Chang, S. J., & Lepland, A. 2010, Nature, 464, 1029

Blättler, C. L., & Higgins, J. A. 2017, Earth and Planetary Science Letters, 479, 241

Boer, G. J. 1993, Climate Dynamics, 8, 225

Bonati, I., & Ramirez, R. 2021, Monthly Notices of the Royal Astronomical Society

Bond, D. P., & Grasby, S. E. 2017, Palaeogeography, Palaeoclimatology, Palaeoecology, 478, 3

—. 2020, Geology

Bond, D. P., & Wignall, P. B. 2014, Volcanism, impacts, and mass extinctions: causes and effects, 505, 29

Borucki, W., Koch, D., Batalha, N., et al. 2008, Proceedings of the International Astronomical Union, 4, 289

Borucki, W. J., Agol, E., Fressin, F., et al. 2013, Science, 340, 587

Boström, M., Esteso, V., Fiedler, J., et al. 2021, Astronomy & Astrophysics, 650, A54

Boucher, D. F., & Alves, G. E. 1963, Dimensionless Numbers: For Fluid Mechanics Heat Transfer, Mass Transfer and Chemical Reaction (American Institute of Chemical Engineers)

Boukrouche, R., Lichtenberg, T., & Pierrehumbert, R. T. 2021, Beyond runaway: initiation of the post-runaway greenhouse state on rocky exoplanets. https://arxiv.org/abs/2107.14150

Bounama, C., von Bloh, W., & Franck, S. 2007, Astrobiology, 7, 745

Brady, P., & Gislason, S. 1997, Geochim Cosmochim Ac, 61, 965

Brady, P. V. 1991, Journal of Geophysical Research: Solid Earth, 96, 18101

Brady, P. V., & Carroll, S. A. 1994, Geochimica et Cosmochimica Acta, 58, 1853

Brantley, S. L., Kubicki, J. D., & White, A. F. 2008

Brewer, P. G., Friederich, G., Peltzer, E. T., & Orr, F. M. 1999, Science, 284, 943

Broadley, M. W., Barry, P. H., Ballentine, C. J., Taylor, L. A., & Burgess, R. 2018, Nature Geoscience, 11, 682

Broecker, W. S., & Sanyal, A. 1998, Global Biogeochemical Cycles, 12, 403

Buick, R., Des Marais, D. J., & Knoll, A. H. 1995, Chemical Geology, 123, 153

Burke, C. J., Christiansen, J. L., Mullally, F., et al. 2015, The Astrophysical Journal, 809, 8

Byrne, M. P., & O'Gorman, P. A. 2015, Journal of Climate, 28, 8078

Caldeira, K. 1995, Am J Sci, 295, 1077

Caldeira, K., & Kasting, J. 1992, Nature, 360, 721

Carretier, S., Goddéris, Y., Martinez, J., Reich, M., & Martinod, P. 2018, Earth Surface Dynamics, 6, 217

Carroll, S. A., & Knauss, K. G. 2005, Chemical Geology, 217, 213

Catanzarite, J., & Shao, M. 2011, The Astrophysical Journal, 738, 151

Catling, D. C., & Kasting, J. F. 2017, Atmospheric evolution on inhabited and lifeless worlds (Cambridge University Press)

Catling, D. C., & Zahnle, K. J. 2020, Science Advances, 6, eaax1420

Caves, J. K., Jost, A. B., Lau, K. V., & Maher, K. 2016, Earth and Planetary Science Letters, 450, 152

Caves Rugenstein, J. K., Ibarra, D. E., & von Blanckenburg, F. 2019, Nature, 571, 99

Cawood, P. A., & Hawkesworth, C. J. 2014, Geology, 42, 503

Chambers, J. 2020, The Astrophysical Journal, 896, 96

Charnay, B., Le Hir, G., Fluteau, F., Forget, F., & Catling, D. C. 2017, Earth and Planetary Science Letters, 474, 97

Charnay, B., Wolf, E. T., Marty, B., & Forget, F. 2020, arXiv preprint arXiv:2006.06265

Chaverot, G., Bolmont, E., & Turbet, M. 2022, in European Planetary Science Congress, EPSC2022–883

Checlair, J. 2021, PhD thesis, The University of Chicago

Checlair, J., Menou, K., & Abbot, D. S. 2017, The Astrophysical Journal, 845, 132

Checlair, J. H., Hayworth, B. P., Olson, S. L., et al. 2020, arXiv preprint arXiv:2008.03952

Checlair, J. H., Salazar, A. M., Paradise, A., Menou, K., & Abbot, D. S. 2019a, The Astrophysical Journal Letters, 887, L3

Checlair, J. H., Abbot, D. S., Webber, R. J., et al. 2019b, arXiv preprint arXiv:1903.05211

Checlair, J. H., Villanueva, G. L., Hayworth, B. P. C., et al. 2021, Astronomical Journal, 161, 150, doi: 10.3847/1538-3881/abdb36

Chemke, R., & Kaspi, Y. 2017, The Astrophysical Journal, 845, 1

Chen, Y., & Brantley, S. L. 1998, Chemical geology, 147, 233

Chen, Z.-Q., & Benton, M. J. 2012, Nature Geoscience, 5, 375

Claire, M. W., Sheets, J., Cohen, M., et al. 2012, The Astrophysical Journal, 757, 95

Clarkson, M., Kasemann, S. A., Wood, R., et al. 2015, Science, 348, 229

Coelho, L. F., Madden, J., Kaltenegger, L., et al. 2022, Astrobiology, 22, 313

Cohen, A. S., Coe, A. L., Harding, S. M., & Schwark, L. 2004, Geology, 32, 157

Colbourn, G., Ridgwell, A., & Lenton, T. 2015, Global Biogeochemical Cycles, 29, 583

Collins, C. B., & Hawking, S. W. 1973, The Astrophysical Journal, 180, 317

Collins, D. B. G., Bras, R., & Tucker, G. E. 2004, Journal of Geophysical Research: Earth Surface, 109

Coogan, L., & Gillis, K. 2020, Earth and Planetary Science Letters, 536, 116151

Coogan, L. A., & Dosso, S. E. 2015, Earth and Planetary Science Letters, 415, 38

Coogan, L. A., & Gillis, K. 2018a, Geochimica et Cosmochimica Acta, 243, 24

Coogan, L. A., & Gillis, K. M. 2013, Geochemistry, Geophysics, Geosystems, 14, 1771

—. 2018b, Annual Review of Earth and Planetary Sciences, 46, 21

Cowan, N. B., & Abbot, D. S. 2014, The Astrophysical Journal, 781, 27

Cox, A. N. 2015, Allen's astrophysical quantities (Springer)

Cox, G. M., Halverson, G. P., Stevenson, R. K., et al. 2016, Earth and Planetary Science Letters, 446, 89

Coy, B. P. 2022, PhD thesis, UNIVERSITY OF CHICAGO

Cronin, T. W. 2014, Journal of the Atmospheric Sciences, 71, 2994

Daines, S. J., & Lenton, T. M. 2016, Earth and Planetary Science Letters, 434, 42

Dasgupta, R. 2013, Rev Mineral Geochem, 75, 183

de Wit, M. J., & Furnes, H. 2016, Science advances, 2, e1500368

Dehghany, M., McKellar, A., Afshari, M., & Moazzen-Ahmadi, N. 2010, Molecular Physics, 108, 2195

Deng, K., Yang, S., & Guo, Y. 2022, Nature communications, 13, 1

Ding, F., & Pierrehumbert, R. T. 2018, The Astrophysical Journal, 867, 54

Ding, F., & Wordsworth, R. D. 2020, The Astrophysical Journal Letters, 891, L18

Dohrmann, M., & Wörheide, G. 2017, Scientific reports, 7, 1

Domagal-Goldman, S. D., & Kopparapu, R. 2018, in AGU Fall Meeting Abstracts, Vol. 2018, P31C–3734

Donnadieu, Y., Goddéris, Y., Pierrehumbert, R., et al. 2006, Geochemistry, Geophysics, Geosystems, 7

Donnadieu, Y., Godderis, Y., Ramstein, G., Nedelec, A., & Meert, J. 2004, Nature, 428, 303

Dorn, C., Noack, L., & Rozel, A. 2018, Astronomy & Astrophysics, 614, A18

Dressing, C. D., & Charbonneau, D. 2013, The Astrophysical Journal, 767, 95

—. 2015, The Astrophysical Journal, 807, 45

Driese, S. G., Jirsa, M. A., Ren, M., et al. 2011, Precambrian Research, 189, 1

Dunlea, A. G., Murray, R. W., Ramos, D. P. S., & Higgins, J. A. 2017, Nature communications, 8, 844

Dunne, T. 1978, Nature, 274, 244

Early, T. J. T. E. C., Team, R. S., Ahrer, E.-M., et al. 2022, arXiv preprint arXiv:2208.11692

Ebelmen, J.-J. 1845in , 66

Edmond, J. M., & Huh, Y. 2003, Earth and Planetary Science Letters, 216, 125

Edson, A., Lee, S., Bannon, P., Kasting, J. F., & Pollard, D. 2011, Icarus, 212, 1

Edson, A. R., Kasting, J. F., Pollard, D., Lee, S., & Bannon, P. R. 2012, Astrobiology, 12, 562

Edwards, J., & Slingo, A. 1996, Quarterly Journal of the Royal Meteorological Society, 122, 689

Erbacher, J., Huber, B. T., Norris, R. D., & Markey, M. 2001, Nature, 409, 325

Ernst, R. E., Buchan, K. L., Jowitt, S. M., & Youbi, N. 2017

Ernst, R. E., & Youbi, N. 2017, Palaeogeography, palaeoclimatology, palaeoecology, 478, 30

Fang, Y., & Xu, H. 2022, Precambrian Research, 380, 106824

Feng, H., & Zhang, M. 2015, Scientific reports, 5, 1

Ferrier, K. L., & Kirchner, J. W. 2008, Earth and Planetary Science Letters, 272, 591

Fields, B. D., Melott, A. L., Ellis, J., et al. 2020, Proceedings of the National Academy of Sciences

Fischer, R. A., Cottrell, E., Hauri, E., Lee, K. K. M., & Le Voyer, M. 2020, Proc. Nat. Acad. Sci. USA, 117, 8743, doi: 10.1073/pnas.1919930117

Flament, N., Coltice, N., & Rey, P. F. 2008, Earth and Planetary Science Letters, 275, 326

Foley, B. J. 2015, The Astrophysical Journal, 812, 36

—. 2019, The Astrophysical Journal, 875, 72

Foley, B. J., & Smye, A. J. 2018, Astrobiology, 18, 873

Foreman-Mackey, D., Hogg, D. W., & Morton, T. D. 2014, The Astrophysical Journal, 795, 64

Forget, F., & Pierrehumbert, R. T. 1997, Science, 278, 1273

Forget, F., Wordsworth, R., Millour, E., et al. 2013, Icarus, 222, 81

Foster, G. L., Hull, P., Lunt, D. J., & Zachos, J. C. 2018, Placing our current 'hyperthermal'in the context of rapid climate change in our geological past, The Royal Society Publishing

Foster, G. L., Royer, D. L., & Lunt, D. J. 2017, Nature communications, 8, 1

Fox, K., & Kim, S. J. 1988, Journal of Quantitative Spectroscopy and Radiative Transfer, 40, 177

France-Lanord, C., & Derry, L. A. 1997, Nature, 390, 65

Francois, L. M., & Walker, J. 1992, American Journal of Science, 292, 81

Frank, A., Carroll-Nellenback, J., Alberti, M., & Kleidon, A. 2018, Astrobiology, 18, 503

Frierson, D. M. W., Held, I. M., & Zurita-Gotor, P. 2006, Journal of the Atmospheric Sciences, 63, 2548, doi: 10.1175/JAS3753.1

Gabet, E. J., & Mudd, S. M. 2009, Geology, 37, 151

Gaidos, E. 2013, The Astrophysical Journal, 770, 90

Gaidos, E., Mann, A., Kraus, A., & Ireland, M. 2016, Monthly Notices of the Royal Astronomical Society, 457, 2877

Gaillard, F., & Scaillet, B. 2014, Earth and Planetary Science Letters, 403, 307

Gaillardet, J., Dupré, B., Louvat, P., & Allegre, C. 1999, Chemical geology, 159, 3

Galili, N., Shemesh, A., Yam, R., et al. 2019, Science, 365, 469

Gardner, J. P., Mather, J. C., Clampin, M., et al. 2006, Space Science Reviews, 123, 485

Gaudi, B. S., Seager, S., Mennesson, B., et al. 2020, arXiv e-prints, arXiv:2001.06683. https://arxiv.org/abs/2001.06683

Gaudi, B. S., Seager, S., Mennesson, B., et al. 2020, The Habitable Exoplanet Observatory (HabEx) Mission Concept Study Final Report. https://arxiv.org/abs/2001.06683

Gerlach, T. 2011, Eos, Transactions American Geophysical Union, 92, 201

Ghiggi, G., Humphrey, V., Seneviratne, S. I., & Gudmundsson, L. 2019, Earth System Science Data, 11, 1655

Gilbert, E. A., Barclay, T., Schlieder, J. E., et al. 2020, The Astronomical Journal, 160, 116

Gillis, K., & Coogan, L. 2011, Earth and Planetary Science Letters, 302, 385

Gillon, M., Jehin, E., Lederer, S. M., et al. 2016, Nature, 533, 221

Gillon, M., Triaud, A. H., Demory, B.-O., et al. 2017, Nature, 542, 456

Godderis, Y., & Donnadieu, Y. 2019, Geological Magazine, 156, 355

Goddéris, Y., Donnadieu, Y., Nédélec, A., et al. 2003, Earth and planetary science letters, 211, 1

Goldblatt, C. 2015, Astrobiology, 15, 362

Goldblatt, C., McDonald, V. L., & McCusker, K. E. 2021, Nature Geoscience, 1

Goldblatt, C., Robinson, T. D., Zahnle, K. J., & Crisp, D. 2013, Nature Geoscience, 6, 661

Goldblatt, C., & Watson, A. J. 2012, Philosophical Transactions Of The Royal Society A-Mathematical Physical And Engineering Sciences, 370, 4197

Golubev, S. V., Pokrovsky, O. S., & Schott, J. 2005, Chemical Geology, 217, 227

Goodwin, P. 2021, Oxford Open Climate Change, 1, kgab007

Gordon, I. E., Rothman, L. S., Hill, C., et al. 2017, Journal of Quantitative Spectroscopy and Radiative Transfer, 203, 3, doi: 10.1016/j.jqsrt.2017.06.038

Graham, R., Lichtenberg, T., Boukrouche, R., & Pierrehumbert, R. 2021, Planetary Science Journal

Graham, R., Lichtenberg, T., & Pierrehumbert, R. 2022a, Data for "CO2 ocean bistability on terrestrial exoplanets", Zenodo, doi: https://doi.org/10.5281/zenodo.6546737

Graham, R., Lichtenberg, T., & Pierrehumbert, R. T. 2022b, Journal of Geophysical Research: Planets, e2022JE007456

Graham, R., & Pierrehumbert, R. 2020, Astrophysical Journal, 896

Graham, R. J. 2021, Astrobiology, 21, 1406

Greaves, J. S., Richards, A. M., Bains, W., et al. 2021, Nature Astronomy, 5, 655

Grewal, D. S., Dasgupta, R., & Farnell, A. 2020, Geochimica et Cosmochimica Acta, 280, 281

Gruszka, M., & Borysow, A. 1997, Icarus, 129, 172, doi: 10.1006/icar.1997.5773

Guimond, C. M., & Cowan, N. B. 2018, The Astronomical Journal, 155, 230

Guimond, C. M., Noack, L., Ortenzi, G., & Sohl, F. 2021, Physics of the Earth and Planetary Interiors, 320, 106788

Guimond, C. M., Rudge, J. F., & Shorttle, O. 2022, The Planetary Science Journal, 3, 66

Gutowski Jr, W. J., Gutzler, D. S., & Wang, W.-C. 1991, Journal of climate, 4, 121

Guzewich, S. D., Way, M. J., Aleinov, I., et al. 2021, Journal of Geophysical Research: Planets, 126, e2021JE006825

Hakim, K., Bower, D. J., Tian, M., et al. 2021, The Planetary Science Journal, 2, 49

Halevy, I., & Bachan, A. 2017, Science, 355, 1069

Halevy, I., Pierrehumbert, R. T., & Schrag, D. P. 2009, Journal of Geophysical Research-atmospheres, 114

Haqq-Misra, J., Kopparapu, R. K., Batalha, N. E., Harman, C. E., & Kasting, J. F. 2016, The Astrophysical Journal, 827, 120

Hart, M. H. 1978, Icarus, 33, 23

—. 1979, Icarus, 37, 351

Hassenkam, T., Andersson, M., Dalby, K., Mackenzie, D., & Rosing, M. 2017, Nature, 548, 78

Hayworth, B. P., & Foley, B. J. 2020, The Astrophysical Journal Letters, 902, L10

Hayworth, B. P., Kopparapu, R. K., Haqq-Misra, J., et al. 2020, Icarus, 113770

Heimsath, A. M., Chappell, J., Dietrich, W. E., Nishiizumi, K., & Finkel, R. C. 2000, Geology, 28, 787

Held, I. M., & Soden, B. J. 2006, Journal of climate, 19, 5686

Heller, R., & Armstrong, J. 2014, Astrobiology, 14, 50

Henderson-Sellers, B. 1984, Quarterly Journal of the Royal Meteorological Society, 110, 1186

Henehan, M. J., Hull, P. M., Penman, D. E., Rae, J. W., & Schmidt, D. N. 2016, Philosophical Transactions of the Royal Society B: Biological Sciences, 371, 20150510

Herwartz, D., Pack, A., & Nagel, T. J. 2021, Proceedings of the National Academy of Sciences, 118, e2023617118

Hessler, A. M., Lowe, D. R., Jones, R. L., & Bird, D. K. 2004, Nature, 428, 736

Higgins, J. A., & Schrag, D. P. 2006, Earth and Planetary Science Letters, 245, 523

—. 2015, Earth and Planetary Science Letters, 416, 73

Hilley, G., Chamberlain, C., Moon, S., Porder, S., & Willett, S. 2010, Earth and Planetary Science Letters, 293, 191

Hirschmann, M. M., Bergin, E. A., Blake, G. A., Ciesla, F., & Li, J. 2021, Proceedings of the National Academy of Sciences, 118, e2026779118, doi: 10.1073/pnas.2026779118

Hoffman, P. F. 2013, Chemical Geology, 362, 143

Hoffman, P. F., Kaufman, A. J., Halverson, G. P., & Schrag, D. P. 1998, Science, 281, 1342

Hoffman, P. F., Abbot, D. S., Ashkenazy, Y., et al. 2017, Science Advances, 3, e1600983

Höning, D., Hansen-Goos, H., Airo, A., & Spohn, T. 2014, Planetary and Space Science, 98, 5

Höning, D., & Spohn, T. 2016, Physics of the Earth and Planetary Interiors, 255, 27

Höning, D., Tosi, N., Hansen-Goos, H., & Spohn, T. 2019, Physics of the Earth and Planetary Interiors, 287, 37

House, K. Z., Schrag, D. P., Harvey, C. F., & Lackner, K. S. 2006, Proceedings of the National Academy of Sciences, 103, 12291

Howell, J. E. 2019, Research Notes of the AAS, 3, 85

Hren, M., Tice, M., & Chamberlain, C. 2009, Nature, 462, 205

Huang, G., Eager, J., Mayne, N., et al. 2021, Precambrian Research, 366, 106423

Huang, S.-S. 1959, American scientist, 47, 397

Huang, Y., & Bani Shahabadi, M. 2014, Journal of Geophysical Research: Atmospheres, 119, 13

Hull, P. 2015, Current Biology, 25, R941

Hull, P. M., Bornemann, A., Penman, D. E., et al. 2020, science, 367, 266

Ibarra, D. E., Caves, J. K., Moon, S., et al. 2016, Geochimica et Cosmochimica Acta, 190, 265

Ingersoll, A. 1969, J. Atmos. Sci., 26, 1191 – 1198

Isson, T., Planavsky, N., Coogan, L., et al. 2020, Global Biogeochemical Cycles, 34, e2018GB006061

Isson, T. T., & Planavsky, N. J. 2018, Nature, 560, 471

Isson, T. T., Zhang, S., Lau, K. V., et al. 2022, Nature communications, 13, 1

Jacobson, M. Z. 2005, Journal of Geophysical Research: Atmospheres, 110

Jagoutz, O., Macdonald, F. A., & Royden, L. 2016, Proceedings of the National Academy of Sciences, 113, 4935

Jansen, T., Scharf, C., Way, M., & Del Genio, A. 2019, The Astrophysical Journal, 875, 79

Johnson, B. W., & Wing, B. A. 2020, Nature Geoscience, 13, 243

Johnson, T. E., Kirkland, C. L., Lu, Y., et al. 2022, Nature, 608, 330

Jucks, K., Huang, Z., Dayton, D., Miller, R., & Lafferty, W. 1987, The Journal of chemical physics, 86, 4341

Jucks, K., Huang, Z., Miller, R., et al. 1988, The Journal of chemical physics, 88, 2185

Jurikova, H., Gutjahr, M., Wallmann, K., et al. 2020, Nature Geoscience, 13, 745

Kadoya, S., Krissansen-Totton, J., & Catling, D. C. 2020, Geochemistry, Geophysics, Geosystems, 21, e2019GC008734

Kadoya, S., & Tajika, E. 2014, The Astrophysical Journal, 790, 107

—. 2019, The Astrophysical Journal, 875, 7

Kadoya, S., Tajika, E., & Watanabe, Y. 2012, Proceedings of the International Astronomical Union, 8, 319

Kah, L. C., & Riding, R. 2007, Geology, 35, 799

Kalderon-Asael, B., Katchinoff, J. A., Planavsky, N. J., et al. 2021, Nature, 595, 394

Kanzaki, Y., & Murakami, T. 2015, Geochimica et Cosmochimica Acta, 159, 190

Karman, T., Miliordos, E., Hunt, K. L. C., Groenenboom, G. C., & van der Avoird, A. 2015, Journal of Chemical Physics, 142, 084306, doi: 10.1063/1.4907917

Kasemann, S. A., von Strandmann, P. A. P., Prave, A. R., et al. 2014, Earth and Planetary Science Letters, 396, 66

Kasting, J. F. 1988a, Icarus, 74, 472

—. 1988b, Icarus, 74, 472

—. 1991, icarus, 94, 1

—. 2019, Elements: An International Magazine of Mineralogy, Geochemistry, and Petrology, 15, 235

Kasting, J. F., Chen, H., & Kopparapu, R. K. 2015, The Astrophysical Journal Letters, 813, L3

Kasting, J. F., & Harman, C. E. 2013, Nature, 504, 221

Kasting, J. F., & Holm, N. G. 1992, Earth and Planetary Science Letters, 109, 507

Kasting, J. F., Kopparapu, R., Ramirez, R. M., & Harman, C. E. 2014, Proceedings of the National Academy of Sciences, 111, 12641

Kasting, J. F., Pollack, J. B., & Ackerman, T. P. 1984a, Icarus, 57, 335

—. 1984b, Icarus, 57, 335

Kasting, J. F., Toon, O. B., & Pollack, J. B. 1988, Scientific American, 258, 90

Kasting, J. F., Whitmire, D. P., & Reynolds, R. T. 1993, Icarus, 101, 108

Kawashima, Y., & Rugheimer, S. 2019, The Astronomical Journal, 157, 213

Kidder, D. L., & Worsley, T. R. 2010, Palaeogeography, Palaeoclimatology, Palaeoecology, 295, 162

Kite, E., Gaidos, E., & Manga, M. 2011, Astrophys Journal, 743

Kite, E. S. 2019, Space Science Reviews, 215, 10

Kite, E. S., & Ford, E. B. 2018, The Astrophysical Journal, 864, 75

Kite, E. S., Manga, M., & Gaidos, E. 2009, The Astrophysical Journal, 700, 1732

Kite, E. S., Mayer, D. P., Wilson, S. A., et al. 2019, Science Advances, 5, eaav7710

Kite, E. S., Steele, L. J., Mischna, M. A., & Richardson, M. I. 2021, Proceedings of the National Academy of Sciences, 118

Kitzmann, D. 2016, The Astrophysical Journal Letters, 817, L18

—. 2017, Astronomy & Astrophysics, 600, A111

Knauss, K. G., Nguyen, S. N., & Weed, H. C. 1993, Geochimica et Cosmochimica Acta, 57, 285

Knoll, A. H., Bergmann, K. D., & Strauss, J. V. 2016, Philosophical Transactions of the Royal Society B: Biological Sciences, 371, 20150493

Knutti, R., Rugenstein, M. A., & Hegerl, G. C. 2017, Nature Geoscience, 10, 727

Kodama, T., Genda, H., O'ishi, R., Abe-Ouchi, A., & Abe, Y. 2019, Journal of Geophysical Research: Planets

Kodama, T., Nitta, A., Genda, H., et al. 2018, Journal of Geophysical Research: Planets, 123, 559

Komacek, T. D., & Abbot, D. S. 2016, The Astrophysical Journal, 832, 54

—. 2019, The Astrophysical Journal, 871, 245

Komacek, T. D., Fauchez, T. J., Wolf, E. T., & Abbot, D. S. 2020, The Astrophysical Journal Letters, 888, L20

Kopp, R., Kirschvink, J., Hilburn, I., & Nash, C. 2005, P Natl Acad Sci Usa, 102, 11131

Kopparapu, R., Wolf, E. T., Arney, G., et al. 2017, The Astrophysical Journal, 845, 5

Kopparapu, R. K. 2013a, The Astrophysical Journal Letters, 767, L8

—. 2013b, Astrophysical Journal Letters, 767, L8

Kopparapu, R. K., Ramirez, R. M., SchottelKotte, J., et al. 2014, The Astrophysical Journal Letters, 787, L29

Kopparapu, R. K., Wolf, E. T., Haqq-Misra, J., et al. 2016, The Astrophysical Journal, 819, 84

Kopparapu, R. K., Ramirez, R., Kasting, J. F., et al. 2013, The Astrophysical Journal, 765, 131

Korenaga, J. 2010, The Astrophysical Journal Letters, 725, L43

—. 2018, Philosophical Transactions of the Royal Society A: Mathematical, Physical and Engineering Sciences, 376, 20170408

Korte, C., Kozur, H. W., Bruckschen, P., & Veizer, J. 2003, Geochimica et Cosmochimica Acta, 67, 47

Krijt, S., Bosman, A. D., Zhang, K., et al. 2020, Astrophysical Journal, 899, 134, doi: 10.3847/1538-4357/aba75d

Krissansen-Totton, J., Arney, G. N., & Catling, D. C. 2018, Proceedings of the National Academy of Sciences, 115, 4105

Krissansen-Totton, J., & Catling, D. C. 2017, Nature communications, 8, 1

—. 2020, Earth and Planetary Science Letters, 537, 116181

Krissansen-Totton, J., Galloway, M. L., Wogan, N., Dhaliwal, J. K., & Fortney, J. J. 2021, The Astrophysical Journal, 913, 107

Kukla, T., Lau, K. V., Ibarra, D. E., & Rugenstein, J. K. 2022

Kump, L. R. 2018, Philosophical Transactions of the Royal Society A: Mathematical, Physical and Engineering Sciences, 376, 20170078

Kump, L. R., & Arthur, M. A. 1997, in Tectonic uplift and climate change (Springer), 399–426

Kump, L. R., Brantley, S. L., & Arthur, M. A. 2000, Annual Review of Earth and Planetary Sciences, 28, 611

Kundzewicz, Z. W. 2008, Ecohydrology & Hydrobiology, 8, 195

Kurucz, R. 1995, in Laboratory and Astronomical High Resolution Spectra, Vol. 81, 17

Labonté, M.-P., & Merlis, T. M. 2020, The Astrophysical Journal, 896, 31

Lacis, A. A., Schmidt, G. A., Rind, D., & Ruedy, R. A. 2010, Science, 330, 356

Lan, Z., Huyskens, M. H., Le Hir, G., et al. 2022, Geophysical Research Letters, 49, e2021GL097156

Langmuir, C. H., & Broecker, W. 2012, How to build a habitable planet (Princeton University Press), 718

Larsen, I. J., Almond, P. C., Eger, A., et al. 2014a, Science, 343, 637

Larsen, I. J., Montgomery, D. R., & Greenberg, H. M. 2014b, Geology, 42, 527

Le Hir, G., Donnadieu, Y., Godderis, Y., et al. 2009, Earth Planet Sc Lett, 277, 453

Leckenby, R., & Robbins, E. 1966, Proceedings of the Royal Society of London. Series A. Mathematical and Physical Sciences, 291, 389

Leconte, J. 2018, Nature geoscience, 11, 168

Leconte, J., Forget, F., Charnay, B., Wordsworth, R., & Pottier, A. 2013a, Nature, 504, 268

Leconte, J., Forget, F., Charnay, B., et al. 2013b, Astronomy & Astrophysics, 554, A69

Leconte, J., Wu, H., Menou, K., & Murray, N. 2015, Science, 347, 632

Lefèvre, M., Turbet, M., & Pierrehumbert, R. 2021, The Astrophysical Journal, 913, 101

Léger, A., Defrère, D., Malbet, F., Labadie, L., & Absil, O. 2015, The Astrophysical Journal, 808, 194

Lehmer, O., Catling, D., Buick, R., Brownlee, D., & Newport, S. 2020a, Science advances, 6, eaay4644

Lehmer, O. R., Catling, D. C., & Krissansen-Totton, J. 2020b, Nature communications, 11, 1

Lenardic, A. 2018, Philosophical Transactions of the Royal Society A: Mathematical, Physical and Engineering Sciences, 376, 20170416

Lenardic, A., Jellinek, A., Foley, B., O'Neill, C., & Moore, W. 2016, Journal of Geophysical Research: Planets, 121, 1831

Levi, A., Sasselov, D., & Podolak, M. 2017, The Astrophysical Journal, 838, 24

Lewis, N. T., Lambert, F. H., Boutle, I. A., et al. 2018, The Astrophysical Journal, 854, 171

Li, F., Penman, D., Planavsky, N., et al. 2021, Precambrian Research, 364, 106279

Li, G., & Elderfield, H. 2013, Geochimica et Cosmochimica Acta, 103, 11

Li, J., Bergin, E. A., Blake, G. A., Ciesla, F. J., & Hirschmann, M. M. 2021, Sci. Adv., 7, eabd3632, doi: 10.1126/sciadv.abd3632

Li, J., Scinocca, J., Lazare, M., et al. 2006, Journal of climate, 19, 6314

Lichtenberg, T., Bower, D. J., Hammond, M., et al. 2021, Journal of Geophysical Research: Planets, 126, e2020JE006711

Lichtenberg, T., Golabek, G. J., Burn, R., et al. 2019, Nature Astronomy, 3, 307

Lichtenberg, T., & Krijt, S. 2021, Astrophysical Journal Letters, 913, L20, doi: 10.3847/2041-8213/abfdce

Lichtenberg, T., Schaefer, L. K., Nakajima, M., & Fischer, R. A. 2022, arXiv e-prints, arXiv:2203.10023. https://arxiv.org/abs/2203.10023

Lin, H. W., Abad, G. G., & Loeb, A. 2014, The Astrophysical Journal Letters, 792, L7

Lindström, S., van de Schootbrugge, B., Hansen, K. H., et al. 2017, Palaeogeography, Palaeoclimatology, Palaeoecology, 478, 80

Lindström, S., Sanei, H., Van De Schootbrugge, B., et al. 2019, Science advances, 5, eaaw4018

Lingam, M., & Loeb, A. 2017, The Astrophysical Journal, 848, 41

—. 2019, International Journal of Astrobiology, 18, 112

Liu, Z., Wu, L.-F., Kufner, C. L., et al. 2021, Nature Chemistry, 13, 1126, doi: 10.1038/s41557-021-00789-w

Lopez, E. D., & Rice, K. 2018, Monthly Notices of the Royal Astronomical Society, 479, 5303

Lowe, D. R., Ibarra, D. E., Drabon, N., & Chamberlain, C. P. 2020, American Journal of Science, 320, 790

Macdonald, F. A., Swanson-Hysell, N. L., Park, Y., Lisiecki, L., & Jagoutz, O. 2019, Science, 364, 181

Macdonald, F. A., & Wordsworth, R. 2017, Geophysical Research Letters, 44, 1938

Mackenzie, F. T., & Garrels, R. M. 1966a, American Journal of Science, 264, 507

—. 1966b, Journal of Sedimentary Research, 36, 1075

Maher, K., & Chamberlain, C. 2014, science, 343, 1502

Maher, K., Steefel, C. I., DePaolo, D. J., & Viani, B. E. 2006, Geochimica et Cosmochimica Acta, 70, 337

Maher, K., Steefel, C. I., White, A. F., & Stonestrom, D. A. 2009, Geochimica et Cosmochimica Acta, 73, 2804

Maliva, R. G., Knoll, A. H., & Siever, R. 1989, Palaios, 519

Maliva, R. G., Knoll, A. H., & Simonson, B. M. 2005, Geological Society of America Bulletin, 117, 835

Malmström, M. E., Destouni, G., Banwart, S. A., & Strömberg, B. H. 2000, Environmental science & technology, 34, 1375

Manabe, S. 1969, Monthly Weather Review, 97, 739

Marounina, N., & Rogers, L. A. 2020, The Astrophysical Journal, 890, 107

Marshall, B. R., & Smith, R. C. 1990, Applied Optics, 29, 71

Marshall, J. E., Lakin, J., Troth, I., & Wallace-Johnson, S. M. 2020, Science Advances, 6, eaba0768

Marshall, S. M., Mathis, C., Carrick, E., et al. 2021, Nature communications, 12, 1

McGrail, B. P., Schaef, H. T., Spane, F. A., et al. 2017, Environmental Science & Technology Letters, 4, 6

McGunnigle, J., Cano, E., Sharp, Z., et al. 2022, Geology

McInerney, F. A., & Wing, S. L. 2011, Annual Review of Earth and Planetary Sciences, 39, 489

Menou, K. 2015, Earth and Planetary Science Letters, 429, 20, doi: 10.1016/j.epsl.2015.07.046

Mills, B., Daines, S. J., & Lenton, T. M. 2014, Geochemistry, Geophysics, Geosystems, 15, 4866

Mills, B., Watson, A. J., Goldblatt, C., Boyle, R., & Lenton, T. M. 2011, Nature Geosciences, 4, 861

Misra, A., Meadows, V., Claire, M., & Crisp, D. 2014, Astrobiology, 14, 67

Mlawer, E. J., Payne, V. H., Moncet, J. L., et al. 2012, Philos. Trans. Royal Soc. A, 370, 2520, doi: 10.1098/rsta.2011.0295

Moazzen-Ahmadi, N., & McKellar, A. 2013, International Reviews in Physical Chemistry, 32, 611

Mojzsis, S. J., Arrhenius, G., McKeegan, K., et al. 1996, Nature, 384, 55

Mol Lous, M., Helled, R., & Mordasini, C. 2022, Nature astronomy, 6, 819

Montgomery, D. R., & Brandon, M. T. 2002, Earth and Planetary Science Letters, 201, 481

Moore, K., & Cowan, N. B. 2020, Monthly Notices of the Royal Astronomical Society, 496, 3786

Moore, W. B., Lenardic, A., Jellinek, A., et al. 2017, Nature Astronomy, 1, 1

Moore, W. B., & Webb, A. A. G. 2013, Nature, 501, 501

Mulders, G. D., Pascucci, I., Apai, D., & Ciesla, F. J. 2018, The Astronomical Journal, 156, 24

Müller, R. D., Mather, B., Dutkiewicz, A., et al. 2022, Nature, 605, 629

Myrow, P. M., Lamb, M., & Ewing, R. 2018, Science, 360, 649

Nakajima, S., Hayashi, Y. Y., & Abe, Y. 1992, Journal of the Atmospheric Sciences, 49, 2256

Nakamura, K., & Kato, Y. 2004, Geochimica et Cosmochimica Acta, 68, 4595

Neil, A. R., & Rogers, L. A. 2019, arXiv preprint arXiv:1911.03582

—. 2020, The Astrophysical Journal, 891, 12

New, M., Liverman, D., Schroder, H., & Anderson, K. 2011, Philosophical Transactions of the Royal Society A, 369, 6

Noack, L., Godolt, M., von Paris, P., et al. 2014, Planetary and Space Science, 98, 14

Noack, L., Rivoldini, A., & Van Hoolst, T. 2017, Physics of the Earth and Planetary Interiors, 269, 40

Öberg, K. I., & Bergin, E. A. 2021, Phys. Rep., 893, 1, doi: 10.1016/j.physrep.2020.09.004

Oelkers, E. H., & Schott, J. 2001, Geochimica et Cosmochimica Acta, 65, 1219

Ojakangas, R. W., Srinivasan, R., Hegde, V., Chandrakant, S., & Srikantia, S. 2014, Current Science, 387

Oki, T., Agata, Y., Kanae, S., et al. 2001, Hydrological Sciences Journal, 46, 983

Olson, S. L., Jansen, M., & Abbot, D. S. 2020, The Astrophysical Journal, 895, 19

Olson, S. L., Reinhard, C. T., & Lyons, T. W. 2016, Proceedings of the National Academy of Sciences, 113, 11447

O'Neill, C. 2012, Australian Journal of Earth Sciences, 59, 189

Owen, J. J., Amundson, R., Dietrich, W. E., et al. 2011, Earth Surface Processes and Landforms, 36, 117

Oxburgh, R., Drever, J. I., & Sun, Y.-T. 1994, Geochimica et Cosmochimica Acta, 58, 661

O'Gorman, P. A., Allan, R. P., Byrne, M. P., & Previdi, M. 2012, Surveys in geophysics, 33, 585

O'Gorman, P. A., & Schneider, T. 2008, Journal of Climate, 21, 3815

Pagani, M., Caldeira, K., Archer, D., & Zachos, J. C. 2006, SCIENCE-NEW YORK THEN WASHINGTON-, 314, 1556

Palandri, J. L., & Kharaka, Y. K. 2004, A compilation of rate parameters of water-mineral interaction kinetics for application to geochemical modeling, Tech. rep., Geological Survey Menlo Park CA

Paradise, A., & Menou, K. 2017, The Astrophysical Journal, 848, 1

Paradise, A., Menou, K., Valencia, D., & Lee, C. 2019, Journal of Geophysical Research: Planets

Pascucci, I., Mulders, G. D., & Lopez, E. 2019, The Astrophysical Journal Letters, 883, L15

Payne, R. C., Brownlee, D., & Kasting, J. F. 2020, Proceedings of the National Academy of Sciences, 117, 1360

Pearce, M., & Raftery, A. E. 2021, Demographic Research, 44, 1271

Penman, D. E., Rugenstein, J. K. C., Ibarra, D. E., & Winnick, M. J. 2020, Earth-Science Reviews, 103298

Penn, J., & Vallis, G. K. 2018, The Astrophysical Journal, 868, 147

Perrin, M., & Hartmann, J. 1989, Journal of Quantitative Spectroscopy and Radiative Transfer, 42, 311

Perron, J. T. 2017, Annual Review of Earth and Planetary Sciences, 45, 561

Peters, N. 1984, U.S. Geological Survey Water Supply Paper 2228, 39

Petigura, E. A., Howard, A. W., & Marcy, G. W. 2013, Proceedings of the National Academy of Sciences, 110, 19273

Pierrehumbert, R., & Erlick, C. 1998, Journal of the atmospheric sciences, 55, 1897

Pierrehumbert, R., & Gaidos, E. 2011, The Astrophysical Journal Letters, 734, L13

Pierrehumbert, R. T. 1995, Journal of the Atmospheric Sciences, 52, 1784

—. 1999, GEOPHYSICAL MONOGRAPH-AMERICAN GEOPHYSICAL UNION, 112, 339

—. 2002, Nature, 419, 191

—. 2010a, Principles of Planetary Climate (Cambridge University Press)

—. 2010b, The Astrophysical Journal Letters, 726, L8

—. 2011, Physics Today, 64, 33

Pierrehumbert, R. T., Abbot, D. S., Voigt, A., & Koll, D. 2011, Annual Review Of Earth And Planetary Sciences, 39, 417

Pluriel, W., Marcq, E., & Turbet, M. 2019, Icarus, 317, 583

Pogge von Strandmann, P. A., Desrochers, A., Murphy, M., et al. 2017, Geochemical Perspectives Letters, 3

Pogge von Strandmann, P. A., Jenkyns, H. C., & Woodfine, R. G. 2013, Nature Geoscience, 6, 668

Pollard, W. G. 1979, American Scientist, 67, 653

Popp, M., Schmidt, H., & Marotzke, J. 2016, Nature Communications, 7, 10627

Pu, J. P., Macdonald, F. A., Schmitz, M. D., et al. 2022, Science Advances, 8, eadc9430

Quanz, S. P., Ottiger, M., Fontanet, E., et al. 2021, arXiv e-prints, arXiv:2101.07500. https://arxiv.org/abs/2101.07500

Quanz, S. P., Absil, O., Benz, W., et al. 2021, Experimental Astronomy, 1

Quintana, E. V., Barclay, T., Raymond, S. N., et al. 2014, Science, 344, 277

Racki, G., Rakociński, M., Marynowski, L., & Wignall, P. B. 2018, Geology, 46, 543

Rafiei, M., & Kennedy, M. 2019, Nature communications, 10, 1

Ramirez, R. 2018, Geosciences, 8, 280

Ramirez, R. M. 2017, Icarus, 297, 71

—. 2020a, Monthly Notices of the Royal Astronomical Society, 494, 259

—. 2020b, Scientific Reports, 10, 1

Ramirez, R. M., Kopparapu, R. K., Lindner, V., & Kasting, J. F. 2014, Astrobiology, 14, 714

Ramirez, R. M., & Levi, A. 2018, Monthly Notices of the Royal Astronomical Society, 477, 4627

Ranjan, S., & Sasselov, D. D. 2016, Astrobiology, 16, 68

Ranjan, S., Wordsworth, R., & Sasselov, D. D. 2017, Astrobiology, 17, 687

Raymo, M. E. 1992, in NATO ASI Series I, Vol. 3, Start of a Glacial, ed. G. Kukla & E. Went, Proceedings of the Mallorca NATO ARW (Springer-Verlag, Heidelberg), 207–223

Raymo, M. E., & Ruddiman, W. F. 1992, Nature, 359, 117

Reid, G., McAfee, J., & Crutzen, P. 1978, Nature, 275, 489

Rimstidt, J. D., Brantley, S. L., & Olsen, A. A. 2012, Geochimica et Cosmochimica Acta, 99, 159

Roe, G. H. 2005, Annual Review of earth and planetary sciences, 33, 645

Rogner, H.-H. 1997, Annual review of energy and the environment, 22, 217

Romps, D. M. 2020, Journal of Climate, 33, 3413

Rose, B. E. 2015, Journal of Geophysical Research: Atmospheres, 120, 1404

Rosing, M. T., Bird, D. K., Sleep, N. H., & Bjerrum, C. J. 2010, Nature, 464, 744

Rosing, M. T., Bird, D. K., Sleep, N. H., Glassley, W., & Albarede, F. 2006, Palaeogeography, Palaeoclimatology, Palaeoecology, 232, 99

Rothman, D. H. 2017, Science Advances, 3, e1700906

Rugheimer, S., Segura, A., Kaltenegger, L., & Sasselov, D. 2015, The Astrophysical Journal, 806, 137

Rushby, A. J., Johnson, M., Mills, B. J., Watson, A. J., & Claire, M. W. 2018, Astrobiology, 18, 469

Rye, R., Kuo, P., & Holland, H. 1995, Nature, 378, 603

Sagan, C., & Mullen, G. 1972, Science, 177, 52

Sasselov, D. D., Grotzinger, J. P., & Sutherland, J. D. 2020, Science Advances, 6, eaax3419

Schaefer, L., & Sasselov, D. 2015, The Astrophysical Journal, 801, 40

Schneider, T., Kaul, C. M., & Pressel, K. G. 2019, Nature Geoscience, 12, 163

Schoene, B., Eddy, M. P., Samperton, K. M., et al. 2019, Science, 363, 862

Schott, J., & Berner, R. A. 1985, in The chemistry of weathering (Springer), 35–53

Schwieterman, E. W., Reinhard, C. T., Olson, S. L., Harman, C. E., & Lyons, T. W. 2019, The Astrophysical Journal, 878, 19

Schwieterman, E. W., Kiang, N. Y., Parenteau, M. N., et al. 2018, Astrobiology, 18, 663

Seeley, J. T., & Jeevanjee, N. 2021, Geophysical Research Letters, 48, e2020GL089609, doi: `https://doi.org/10.1029/2020GL089609`

Segura, A., Kasting, J., Meadows, V., et al. 2005, Astrobiology, 5, 706

Segura, A., Krelove, K., Kastings, J. F., et al. 2003, Astrobiology, 3, 689

Segura, A., Walkowicz, L. M., Meadows, V., Kasting, J., & Hawley, S. 2010, Astrobiology, 10, 751

Sellers, W. D. 1969, J. Appl. Meteor., 8, 392

Sheldon, N. D. 2006, Precambrian Research, 147, 148

Shibuya, T., & Takai, K. 2022, Progress in Earth and Planetary Science, 9, 1

Siever, R. 1968, Sedimentology, 11, 5

—. 1992, Geochimica et Cosmochimica Acta, 56, 3265

Simpson, C. 2019, AGUFM, 2019, PP54A

—. 2021, The American Naturalist, 198, 590

Slanina, Z., Fox, K., & Kim, S. J. 1992, Thermochimica acta, 200, 33

Sleep, N. H., Bird, D. K., & Pope, E. C. 2011, Philosophical Transactions of the Royal Society B: Biological Sciences, 366, 2857

Sleep, N. H., & Zahnle, K. 2001, Journal of Geophysical Research: Planets, 106, 1373

Sobolev, S. V., Sobolev, A. V., Kuzmin, D. V., et al. 2011, Nature, 477, 312

Sobotta, J., Geisberger, T., Moosmann, C., et al. 2020, Life, 10, 35

Solé, R. V., Montoya, J. M., & Erwin, D. H. 2002, Philosophical Transactions of the Royal Society of London. Series B: Biological Sciences, 357, 697

Solomatova, N. V., & Caracas, R. 2021, Science advances, 7, eabj0406

Somelar, P., Soomer, S., Driese, S. G., et al. 2020, Chemical Geology, 119678

Soto, A., Mischna, M., Schneider, T., Lee, C., & Richardson, M. 2015, Icarus, 250, 553

Sousa-Silva, C., Seager, S., Ranjan, S., et al. 2020, Astrobiology, 20, 235

Stark, C. C., Roberge, A., Mandell, A., et al. 2015, The Astrophysical Journal, 808, 149

Stephens, G. L., O'Brien, D., Webster, P. J., et al. 2015, Reviews of geophysics, 53, 141

Stephens, G. L., Li, J., Wild, M., et al. 2012, Nature Geoscience, 5, 691

Stevenson, D. J. 1999, Nature, 400, 32

Stevenson, D. J. 2018, Physics Today, 71, 10

Stewart, E., Ague, J. J., Ferry, J. M., et al. 2019, American Mineralogist: Journal of Earth and Planetary Materials, 104, 1369

Strauss, J. V., & Tosca, N. J. 2020, Geology, 48, 599

Strogatz, S. 1994, Nonlinear dynamics and chaos (Westview Press)

Suissa, G., Mandell, A. M., Wolf, E. T., et al. 2020, The Astrophysical Journal, 891, 58

Sun, X., Higgins, J., & Turchyn, A. V. 2016, Marine Geology, 373, 64

Sun, Y., Joachimski, M. M., Wignall, P. B., et al. 2012, Science, 338, 366

Svensen, H., Planke, S., Polozov, A. G., et al. 2009, Earth and Planetary Science Letters, 277, 490

Tajika, E. 2007, Earth, 59, 293

Tasker, E., Tan, J., Heng, K., Kane, S., & Spiegel, D. 2017, Nature astronomy, 1, 1

Team, L., et al. 2019, arXiv preprint arXiv:1912.06219

Thomson, S. I., & Vallis, G. K. 2019a, Quarterly Journal of the Royal Meteorological Society, 145, 2627

—. 2019b, Atmosphere, 10, 803

Tilley, M. A., Segura, A., Meadows, V., Hawley, S., & Davenport, J. 2019, Astrobiology, 19, 64

Tinetti, G., Meadows, V. S., Crisp, D., et al. 2006, Astrobiology, 6, 881

Tolley, A. 2018, Centauri Dreams. `https://www.centauri-dreams.org/2018/12/14/climate-change-and-mass-extinctions-implications-for-exoplanet-life/`

Trower, E. J., & Fischer, W. W. 2019, Sedimentary geology, 384, 1

Tsintsarska, S., & Huber, H. 2007, Molecular Physics, 105, 25

Tsumura, K. 2020, Scientific Reports, 10, 1

Turbet, M. 2019, sf2a, Di

Turbet, M., Bolmont, E., Ehrenreich, D., et al. 2020, Astronomy & Astrophysics, 638, A41

Turbet, M., Ehrenreich, D., Lovis, C., Bolmont, E., & Fauchez, T. 2019, Astronomy & Astrophysics, 628, A12

Turbet, M., Forget, F., Leconte, J., Charnay, B., & Tobie, G. 2017, Earth and Planetary Science Letters, 11, 11

Turyshev, S. G., Shao, M., Toth, V. T., et al. 2020, arXiv preprint arXiv:2002.11871

Tyrrell, T. 2020, Communications Earth & Environment, 1, 1

Urey, H. C. 1952, Mrs. Hepsa Ely Silliman Memorial Lectures

Valencia, D., & O'Connell, R. 2007, The Astrophysical Journal, 670, L45

Vallis, G. K., Colyer, G., Geen, R., et al. 2018, Geoscientific Model Development

van der Ploeg, R., Selby, D., Cramwinckel, M. J., et al. 2018, Nature communications, 9, 1

Vardavas, I., & Carver, J. H. 1984, Planetary and space science, 32, 1307

Vecchi, G. A., Soden, B. J., Wittenberg, A. T., et al. 2006, Nature, 441, 73

Velbel, M. A. 1993, Chemical Geology, 105, 89

Venturini, J., Guilera, O. M., Haldemann, J., Ronco, M. P., & Mordasini, C. 2020, Astronomy & Astrophysics, 643, L1, doi: 10.1051/0004-6361/202039141

Vérard, C., & Veizer, J. 2019, Geology, 47, 881

Von Blanckenburg, F., Bouchez, J., Ibarra, D. E., & Maher, K. 2015, Nature Geoscience, 8, 538

von Blanckenburg, F., Bouchez, J., Willenbring, J. K., Ibarra, D. E., & Rugenstein, J. K. C. 2022, Proceedings of the National Academy of Sciences, 119, e2202387119

von Paris, P., Grenfell, J. L., Hedelt, P., et al. 2013, Astronomy & Astrophysics, 549, A94

Von Paris, P., Selsis, F., Kitzmann, D., & Rauer, H. 2013, Astrobiology, 13, 899

Wagner, P. J., Kosnik, M. A., & Lidgard, S. 2006, Science, 314, 1289

Walker, J. C. G., Hays, P. B., & Kasting, J. F. 1981, Journal of Geophysical Research, 86, 9776

Walker, S. I., Cronin, L., Drew, A., et al. 2020, Planetary Astrobiology, 477

Walsh, M., England, T., Dyke, T., & Howard, B. 1987, Chemical physics letters, 142, 265

Walters, D., Baran, A. J., Boutle, I., et al. 2019, Geoscientific Model Development, 12, 1909

Wang, W.-C., & Stone, P. H. 1980, Journal of Atmospheric Sciences, 37, 545

Ward, P. D., & Brownlee, D. 2003, Rare Earth: Why complex life is uncommon in the universe (Springer Science & Business Media)

Warke, M. R., Di Rocco, T., Zerkle, A. L., et al. 2020, Proceedings of the National Academy of Sciences, 117, 13314

Watanabe, Y., Tajika, E., & Kadoya, S. 2012, Proceedings of the International Astronomical Union, 8, 333

Way, M., Ernst, R. E., & Scargle, J. D. 2022, The Planetary Science Journal, 3, 92

Way, M. J., & Del Genio, A. D. 2020, Journal of Geophysical Research: Planets, 125, e2019JE006276

Way, M. J., Del Genio, A. D., Kiang, N. Y., et al. 2016, Geophysical Research Letters, 43, 8376

Way, M. J., Aleinov, I., Amundsen, D. S., et al. 2017, The Astrophysical Journal Supplement Series, 231, 12

Weissbart, E. J., & Rimstidt, J. D. 2000, Geochimica et Cosmochimica Acta, 64, 4007

Welch, S., & Ullman, W. 1996, Geochimica et Cosmochimica Acta, 60, 2939

Wendland, M., Hasse, H., & Maurer, G. 1999, Journal of chemical & engineering data, 44, 901

West, A. J. 2012, Geology, 40, 811

West, A. J., Galy, A., & Bickle, M. 2005, Earth and Planetary Science Letters, 235, 211

White, A. F., & Brantley, S. L. 2003, Chemical Geology, 202, 479

Wien, W. 1897, The London, Edinburgh, and Dublin Philosophical Magazine and Journal of Science, 43, 214

Willenbring, J. K., & Von Blanckenburg, F. 2010, nature, 465, 211

Winnick, M. J., & Maher, K. 2018, Earth and Planetary Science Letters, 485, 111

Wittmann, A. C., & Pörtner, H.-O. 2013, Nature Climate Change, 3, 995

Wolf, E., Haqq-Misra, J., & Toon, O. 2018, Journal of Geophysical Research: Atmospheres, 123, 11

Wolf, E., & Toon, O. 2014, Geophysical Research Letters, 41, 167

—. 2015, Journal of Geophysical Research, 120, 5775

Wordsworth, R. 2021, The Astrophysical Journal Letters, 912, L14

Wordsworth, R., Forget, F., & Eymet, V. 2010a, Icarus, 210, 992

Wordsworth, R., Forget, F., Millour, E., et al. 2013, Icarus, 222, 1

Wordsworth, R., Forget, F., Selsis, F., et al. 2010b, Astronomy & Astrophysics, 522, A22

Wordsworth, R. D., & Pierrehumbert, R. T. 2013, The Astrophysical Journal, 778, 154

Wu, Y., Chu, D., Tong, J., et al. 2021, Nature communications, 12, 1

Xie, P. P., & Arkin, P. A. 1997, Bulletin of the American Meteorological Society, 78, 2539

Xiong, J., Yang, J., & Liu, J. 2022, Geophysical Research Letters, 49, e2022GL099599

Yan, Y., Brook, E. J., Kurbatov, A. V., Severinghaus, J. P., & Higgins, J. A. 2021, Science advances, 7, eabj9341

Yang, H., Komacek, T. D., & Abbot, D. S. 2019a, The Astrophysical Journal Letters, 876, L27

Yang, J., Boué, G., Fabrycky, D. C., & Abbot, D. S. 2014, Astrophysical Journal Letters, 787

Yang, J., Cowan, N. B., & Abbot, D. S. 2013, Astrophysical Journal Letters, 771

Yang, J., Leconte, J., Wolf, E. T., et al. 2019b, The Astrophysical Journal, 875, 46

Yang, J., Peltier, W. R., & Hu, Y. 2012, Climate of the Past, 8, 907

Zakharov, D., Bindeman, I., Slabunov, A., et al. 2017, Geology, 45, 667

Zeebe, R., & Wolf-Gladrow, D. 2001, Elsevier Oceanography Series, Vol. 65, CO_2 in seawater: equilibrium, kinetics, isotopoes (Elsevier)

Zeebe, R. E., & Caldeira, K. 2008, Nature Geoscience, 1, 312

Zeng, L., Jacobsen, S. B., Sasselov, D. D., et al. 2019, Proc. Nat. Acad. Sci. USA, 116, 9723, doi: 10.1073/pnas.1812905116

Zsom, A. 2015, The Astrophysical Journal, 813, 9